# Low Thermal Noise Coating for New Generation Gravitational-Wave Detectors

Alex Amato

Alex Amato. Low Thermal Noise Coating for New Generation Gravitational-Wave Detectors. Material chemistry. Université de Lyon, 2019. English. NNT : 2019LYSE1245 . tel-02475821

HAL Id: tel-02475821
https://theses.hal.science/tel-02475821v1

Submitted on 18 Jun 2020

N° d'ordre NNT : 2019LYSE1245

**THÈSE DE DOCTORAT DE L'UNIVERSITÉ DE LYON**
opérée au sein de
**l'Université Claude Bernard Lyon 1**
**École Doctorale ED52**
**(Physique et Astrophysique)**

**Spécialité de doctorat: Physique des matériaux**

Soutenue publiquement le 22/11/2019, par :
**Alex Amato**

---

# Low Thermal Noise Coating for New Generation Gravitational-Wave Detectors

---

Devant le jury composé de :

| | |
|---|---|
| Dujardin Christophe, Professeur, UCBL | Président |
| Foret Marie, Professeur, Université de Montpellier | Rapporteur |
| Galliou Serge, Professeur, ENSMM | Rapporteur |
| Fafone Viviana, Professeur, Università di Roma Tor Vergata | Examinatrice |
| Hellman Frances, Professeur, University of California | Examinatrice |
| Cagnoli Gianpietro, Professeur, UCBL | Directeur de thèse |
| Canepa Maurizio, Professeur, Università di Genova | Co-directeur de thèse |
| Granata Massimo, Ingénieur de Recherche CNRS, IP2I | Co-directeur de thèse |
| Martinez Valerie, Maître de Conférences, UCBL | Invitée |

**Résumé de la thèse:**

Le travail de thèse consiste en l'étude des propriétés mécaniques et optiques de couches minces (principalement déposées par IBS au LMA), dans le but de réduire le bruit thermique des miroirs des détecteurs des ondes gravitationnelles (GWDs) actuels et futurs. La caractérisation mécanique effectuée au LMA concerne les mesures de frottement interne et de constantes élastiques par la méthode de "ring-down" utilisant un système de suspension nodale (GeNS). La caractérisation optique a été réalisée à l'aide de l'ellipsométrie spectroscopique (SE). Grâce à une collaboration avec l'OPTMATLAB de l'Université de Gênes, j'ai pu caractériser les échantillons par SE pour une large gamme d'énergie (des NIR aux UV).

Les premiers échantillons analysés sont les couches actuellement utilisées dans les GWDs: $SiO_2$, $Ta_2O_5$ et Ti:$Ta_2O_5$. Ensuite, $Nb_2O_5$, Nb:$TiO_2$, Zr:$Ta_2O_5$, SiC et $SiN_x$ ont été caractérisés en tant que matériaux à haute indice de réfraction, tandis que $MgF_2$ et $AlF_3$ ont été étudiés pour remplacer le matériau à bas indice afin de réduire l'épaisseur totale du revêtement et donc le bruit thermique.

Parmi les couches étudiées, Zr:$Ta_2O_5$ et $SiN_x$ ont fourni les résultats les plus prometteurs en terme de dissipation.

Des résultats importants ont été obtenus concernant la théorie de la dissipation dans les oxydes et lors de la caractérisation optique et mécanique des échantillons.

Mots-clés: couches minces, frottement interne, bruit thermique, ellipsométrie, énergie d'Urbach, ondes gravitationnelles

* * *

**Thesis abstract:**

The work of this thesis is the study of mechanical and optical properties of coatings (mainly deposited by IBS technique at LMA), with the purpose of finding a new possible material with the aim of reduce the coating thermal noise in current and in future gravitational-wave detectors (GWDs). The mechanical characterization done at LMA regards measurements of internal friction and elastic constants by the ring-down method using a Gentle Nodal Suspension (GeNS) system. The optical characterization has been done using spectroscopic ellipsometry (SE). Thanks to a collaboration with the OPTMATLAB of the University of Genova, I was able to characterize the samples using SE in a wide-range energy region (from UV to NIR).

The first analysed samples are the coatings currently used in GWDs, $SiO_2$, $Ta_2O_5$ and Ti:$Ta_2O_5$. Then, $Nb_2O_5$, Nb:$TiO_2$, Zr:$Ta_2O_5$, SiC and $SiN_x$ have been characterized as high-refractive index coatings, whereas $MgF_2$ and $AlF_3$ have been studied with the purpose of replace the low-refractive index, reducing the total coating thickness, hence the coating thermal noise.

Among the investigated coatings, Zr:$Ta_2O_5$ and $SiN_x$ provided the most promising results in term of internal friction.

Important finding have been achieved regarding the theory of the internal friction of amorphous oxides and the optical and mechanical characterization of the samples.

Key-words: thin films, internal friction, thermal noise, ellipsometry, Urbach energy, gravitational waves

**Résumé substantiel:**
En septembre 2015, la première observation directe des ondes gravitationnelles, provenant d'un système binaire de trous noirs, a été enregistrée. L'une des caractéristiques de la radiation gravitationnelle est son amplitude extrêmement faible; ce n'est que grâce à la grande amélioration technologique qu'il a été possible de réaliser la première détection, en développant des interféromètres laser géants, fonctionnant à 1064 nm.

Ces interféromètres très sensibles se caractérisent par des bras kilométriques, des cavités résonantes Fabry-Pérot et de grands miroirs de Bragg hautement réfléchissants. Un réseau de détecteurs est actuellement opérationnel et d'autres détecteurs sont en construction. En particulier, les détecteurs jumeaux Advanced LIGO opèrent aux USA, Advanced Virgo opère en Europe tandis que KAGRA est en mis au point au Japon et participera aux prochaines missions d'observation vers la fin de cette année 2019.

Bien que de multiples détections aient déjà eu lieu, les détecteurs des ondes gravitationnelles (GWDs) doivent entrer maintenant dans une phase d'amélioration. L'un des principaux objectifs est de réduire le bruit thermique des couches réfléchissantes, qui limite la zone centrale et plus sensible de la bande de détection, autour de 200 Hz. L'équilibre thermique est un équilibre dynamique, dans lequel il existe un échange continu entre deux niveaux, provoquant le bruit thermique. C'est l'idée du système à deux niveaux (Two-level System, TLS). Une sollicitation mécanique externe modifie l'asymétrie d'un TLS, modifiant sa population en conséquence, et donc les constantes élastiques du solide. La réponse mécanique est retardée par le processus de relaxation qui se produit afin de rétablir l'équilibre dans le système, ce qui provoque la dissipation. Selon le théorème de fluctuation-dissipation, les deux phénomènes de bruit thermique et de dissipation d'énergie mécanique sont intimement liés.

Les revêtements réfléchissants actuellement utilisés sont des multicouches de tantale dopé à l'oxyde de titane (Ti:$Ta_2O_5$, le matériau à haut indice) et de silice ($SiO_2$, le matériau à bas indice) déposés par pulvérisation ionique (IBS) dans le Laboratoire des Matériaux Avancés (LMA) de Lyon, sur des substrats de silice fondue, massive et de grande surface. Les couches de Ti:$Ta_2O_5$ sont reconnues comme étant la principale source de bruit thermique dans les revêtements. Pour cette raison, il est important de trouver un nouveau matériau à haut indice avec un frottement interne (directement lié au bruit thermique) plus faible que le Ti:$Ta_2O_5$.

Dans ce contexte, la thèse consiste en l'étude des propriétés mécaniques et optiques de couches minces (principalement déposées par IBS au LMA), dans le but de trouver un nouveau matériau qui permette de réduire le bruit thermique des miroirs des GWDs actuels et futurs. La caractérisation mécanique effectuée au LMA concerne les mesures de frottement interne et de constantes élastiques par la méthode de « ring-down » utilisant un système de suspension nodale (Gentle Nodal Suspension, GeNS). La caractérisation optique a été réalisée à l'aide de l'ellipsométrie spectroscopique (SE), une technique efficace pour étudier les propriétés optiques des matériaux et l'épaisseur des couches minces. Grâce à une collaboration avec l'OPTMATLAB de l'Université de Gênes, j'ai pu caractériser les échantillons par SE pour une large gamme d'énergie (des UV aux NIR).

Les premiers échantillons analysés sont les couches actuellement utilisées dans les GWDs: $SiO_2$, $Ta_2O_5$ et Ti:$Ta_2O_5$. Ensuite, $Nb_2O_5$, Nb:$TiO_2$, Zr:$Ta_2O_5$, SiC et $SiN_x$ ont été caractérisés en tant que matériaux à haute indice de réfraction, tandis que $MgF_2$ et $AlF_3$ ont été étudiés pour remplacer le matériau à bas indice afin d'augmenter le contraste d'indice, réduisant ainsi l'épaisseur totale du revêtement et donc le bruit thermique.

Parmi les couches étudiées, Zr:$Ta_2O_5$ et $SiN_x$ ont fourni les résultats les plus prometteurs en terme de dissipation, en particulier à 100 Hz, où les GWDs sont limités par le bruit thermique des revêtements réfléchissants. Par ailleurs, ces deux matériaux ayant une température de cristallisation nettement plus élevée que le Ti:$Ta_2O_5$, ils peuvent subir un traitement thermique à plus haute température, ce qui est favorable pour leurs propriétés mécaniques et optiques. De plus, un recuit à plus haute température est bénéfique également pour les couches de silice, ce qui permet de réduire l'angle de perte total des revêtements.

Zr:$Ta_2O_5$ présente des constantes optiques et élastiques similaires à celles du Ti:$Ta_2O_5$; pour cette raison, il pourrait être un bon candidat pour les détecteurs à température ambiante. Toutefois, des tests supplémentaires sur un empilement optimisé Zr:$Ta_2O_5$/$SiO_2$ sont nécessaires.

$SiN_x$ présente des pertes $\sim 3$ fois plus faibles de celles du Ti:$Ta_2O_5$. Cependant, il réside le problème lié à l'absorption à 1064 nm, bien plus élevée que celle des couches actuellement utilisées dans les GWDs. Toutefois, d'autres améliorations de SiNx pourraient diminuer l'absorption optique; un test sur un empilement optimisé $SiN_x$/$SiO_2$ est nécessaire. Le bruit thermique dépend également de la différence entre les modules d'élasticité du substrat et du revêtement, donc le module de Young de $SiN_x$, supérieur à celui du substrat, pourrait limiter son utilisation dans les détecteurs à température ambiante. Toutefois, les futurs GWDs cryogéniques pourraient avoir un substrat en saphir, dont le module de Young est supérieur à celui de la silice. Pour ces raisons, le $SiN_x$ pourrait être une solution valable pour les détecteurs cryogéniques.

**L'une des nouveautés de ce travail concerne le calcul analytique du frottement interne dans un TLS, en considérant une expression générale de la barrière de potentiel.** L'angle de perte obtenu est en accord avec les résultats connus dans la littérature sur la silice, en utilisant un potentiel exponentiel. Pour confirmer la validité générale de ce calcul, d'autres comparaisons avec d'autres angles de perte mesurés seront nécessaires.

D'autres résultats importants ont été obtenus lors des caractérisations optique et mécanique des échantillons. En particulier, l'analyse des couches de silice a permis d'observer un angle de perte mécanique supplémentaire du bord des échantillons. **Un modèle qui tient compte de cet effet du bord a été développé au cours de cette thèse.** Cet effet est en concurrence avec le modèle "bulk and shear", et il pourrait masquer la dissipation intrinsèque de la couche s'il n'est pas pris en compte pendant l'analyse. Par ailleurs, afin d'atténuer l'effet du bord et de définir les meilleurs traitements pour tous les échantillons, un protocole de mesure et de conservation a été établi, concernant le recuit post-dépôt et le stockage sous vide des échantillons.

De plus, **une méthode non destructive, basée sur l'ajustement des simulations par éléments finis aux mesures effectuées à l'aide de GeNS, a été développée pour évaluer la constante élastique des couches.**

Enfin, au cours de cette thèse, les propriétés optiques, liées à la densité des états électroniques, et les propriétés mécaniques, relatives à la dissipation, ont été analysées en relation avec l'organisation structurale des couches à courte et moyenne distance. En particulier, **pour la première fois, une corrélation entre l'énergie d'Urbach, liée au comportement exponentiel du bord de l'absorption, et la dissipation, liée aux propriétés mécaniques, a été trouvée**. Cette corrélation est observée pour différents oxydes, ce qui suggère sa validité générale.

# ACKNOWLEDGEMENTS

I have invested a lot of effort in the fulfilment of this thesis work and despite my constant commitment, I know that I owe this accomplishment, followed by personal and professional growth, to the support of many people who have guided me along this path.

In primis, I would like to thank prof. Gianpietro Cagnoli (Geppo). He was not only my supervisor but above all a mentor as well as an outstanding scientist to be inspired by. A special thanks is addressed to Massimo Granata, my co-supervisor at Laboratoire des Matériaux Avancés (LMA), who has helped me a lot to grow as a researcher and in making me become independent in my work. I would also like to thank prof. Maurizio Canepa, my co-supervisor at the University of Genova (IT). It is thanks to him that I was able to take this path and that allowed me to get in contact with the people of LMA.

In addition, a great thanks is reserved to Prof. Silvana Terreni, who has given me a fundamental help in understanding some key aspects of the topics here discussed.

I would also like to thank all the LMA members. They were always ready to help me with any problems in the laboratory and also to settle in a new country... Merci!

Thanks also to the people of OPTMATLAB of the University of Genova. I consider most of them friends more than colleagues.

I would also like to thank the ILM group and in particular Valérie Martinez, who have helped me a lot.

I'd like to thank my family from the bottom of my heart. They supported all the choices I made during this journey and allowed me to complete my studies, without ever mentioning the sacrifices and difficulties that they certainly had to face in order to let all of this happen... È indescrivibile il bene che vi voglio.

Furthermore, I would like to thank all my friends. Fortunately there are so many that they probably cannot fit into this page if named individually. You've successfully managed to make these last years truly unforgettable... Grazie, merci, gracias, thanks, děkuji !!!

Finally, a very warm and special thanks is addressed to Sara. Thank you for supporting me during the final and most stressful part of this path. ♡

# CONTENTS

# ACRONYMS

**AdV** Advanced Virgo.

**ADWP** asymmetric double-well potential.

**AFM** atomic force microscopy.

**aLIGO** Advanced LIGO.

**CL** Cody-Lorentz.

**CM** center of the mass.

**CTN** coating thermal noise.

**CVD** chemical vapour deposition.

**DIBS** double IBS.

**DOS** density of states.

**DPOs** double-paddle oscillators.

**EDX** energy-dispersive X-ray.

**EMA** effective medium approximations.

**ESA** European Space Agency.

**ET** Einstein Telescope.

**ETM** end test-mass.

**F-D** fluctuation-dissipation.

**GC** Grand Coater.

**GeNS** Gentle Nodal Suspension.

**GW** gravitational-wave.

**GWDs** gravitational-wave detectors.

**HOA** harmonic oscillator approximation.

**HR** high-reflective.

**HREM** High Resolution Electron Microscopy.

**IBS** Ion Beam Sputtering or Ion Beam Sputtered.

**ILM** Institut Lumière Matière.

**IP** inverted pendulum.

**IPR** inverse participation ratio.

**IR** infrared.

**ITM** input test-mass.

**JDOS** joint density of states.

**KAGRA** Kamioka Gravitational Wave Detector.

**KK** Kramers-Kronig.

**LHI** linear, homogeneous and isotropic.

**LIGO** Laser Interferometer Gravitational-Wave Observatory.

**LISA** Laser Interferometer Space Antenna.

**LL** Lorentz-Lorentz.

**LMA** Laboratoire des Matériaux Avancés.

**LMI** Laboratoire des Multimatériaux et Interfaces.

**LPCVD** low-pressure chemical-vapor deposited.

**LRO** long-range (translational) order.

**LSC** LIGO Scientific Community.

**LVC** LIGO-Virgo Collaboration.

**LZH** Laser Zentrum Hannover.

**MD** molecular dinamycs.

**MG** Maxwell-Garnett.

**MIT** Massachusetts Institute of Technology.

**MSE** Mean Square Error.

**NIR** near-infrared.

**OPTMATLAB** Optics Materials Laboratory.

**PRM** power recycling mirror.

**PSEMI** parameterized semiconductor.

**PSU** Primary Structural Units.

**RAE** rotating analyzer ellipsometer.

**RBS** Rutherford back-scattering.

**RCE** rotating compensator ellipsometer.

**RDF** radial distribution function.

**RMS** root mean square.

**SA** super attenuators.

**SE** spectroscopic ellipsometry.

**SEM** Scanning Electron Microscopy.

**SRM** signal recycling mirror.

**SRO** short-range order.

**TB** tight binding.

**TE** transverse-electric.

**TEM** transmission electron microscopy.

**TL** Tauc-Lorentz.

**TLS** two level system.

**TM** transverse-magnetic.

**UEM** Ultrafast Electron Microscopy.

**UV** ultraviolet.

**WKB** Wentzel-Kramers-Brillouin.

# INTRODUCTION

> *"If I have seen further than others, it is by standing upon the shoulders of giants."*
>
> Isaac Newton
>
> Letter to Robert Hooke, Cambridge, February 5 (1676)

In 1916 Albert Einstein observed that light-speed transversal waves are solution of the linearised equations of general relativity. One characteristic of the gravitational radiation is the extremely weak amplitude, which makes them nearly impossible to be detected from sources created in laboratory. For this reason, astrophysical sources have to be considered in order to obtain detectable signals. With the observation of the binary system PSR B1913+16 [1, 2], it was possible to demonstrate indirectly for the first time the existence of gravitational-wave (GW).

Almost 33 years later, in September 2015, the first direct observation of GW originated from a black-hole binary system was recorded [3]. It was only thanks to the great technological improvement that it was possible to achieve the first detection, developing giant ground-based laser interferometers detectors. These high-sensitive interferometers are characterized by kilometric arms, Fabry-Perot resonant cavities and high-reflective large mirrors. After more than 20 years of research and development, the advanced-detectors started GW astronomy. A detectors network is already working and other detectors are under construction. In particular, the twins Advanced Laser Interferometer Gravitational-Wave Observatory (LIGO) are operating in USA, Advanced Virgo is working in Italy for an European collaboration whereas Kamioka Gravitational Wave Detector (KAGRA) is under construction in Japan and will join the next observation runs at the end of the year. Nowadays, we are in the middle of the "O3" observing run and the network is detecting an average of four signals per months.

While multiple detections already occurred, the gravitational-wave detectors (GWDs) are now entering an upgrading phase. One of the main goals is to reduce the so-called coating thermal noise (CTN) which limits the central and most sensitive region of the detection band, around 200 Hz. CTN arises from fluctuations of the mirror surface under thermally activated transitions between equilibrium configurations of structure in coatings [4]. Its amplitude is linked to the amount of internal friction within the mirror materials, via the fluctuation-dissipation theorem [5]: the higher the loss, the higher the thermal noise level. Fostering higher sensitivity in the next generation of GWDs, necessary to investigate deeper portions of the universe, calls for a lowering of CTN and a better knowledge of the structure of amorphous oxides coatings at the molecular level [6]. Furthermore, the reduction of CTN would be beneficial also for future GWDs and precision experiments using high-finesse optical cavities, such as frequency standards for laser stabilization [7], atomic clocks [8] and opto-mechanical resonators [9].

Current coatings are Ion Beam Sputtering or Ion Beam Sputtered (IBS) multilayers made of titania-doped tantala (Ti:$Ta_2O_5$, the high-index material) and silica ($SiO_2$, the low-index material) deposited by the Laboratoire des Matériaux Avancés (LMA) of Lyon[1], on massive, large-area fused silica substrates [10]. Ti:$Ta_2O_5$ was recognized as the dominant source of thermal noise in coatings [11]. For this reason, there is interest in finding new possible high-index material with lower internal friction than Ti:$Ta_2O_5$. Adding to this, new material with higher refractive index would allow to reduce the total thickness of the coating and hence to decrease the total CTN [12].

Within this context, the work of this thesis concerned the study of mechanical and optical properties of coatings, mainly deposited by IBS technique at LMA, with the purpose of finding a new possible material for current and possibly for future GWDs. The mechanical characterization done at LMA regards internal friction and elastic constants. The optical characterization has been done using spectroscopic ellipsometry (SE), a useful method to investigate optical properties and thickness of thin film materials. Thanks to a collaboration with the Optics Materials Laboratory (OPTMATLAB) of the University of Genova, I was able to characterize the samples using SE in a wide-range energy region (from ultraviolet (UV) to near-infrared (NIR)).

### Outline of the Thesis

- **Chapter 1** introduces the theory of GW and their interferometric detection. The first part is dedicated to the gravitational radiation; the different sources are listed, showing all the detected signals obtained since the first one in September 2015. The second part is dedicated to detectors, explaining the benefit of using km-scale interferometers and the need of a network to localize the sources. The main part of this chapter concerns the detectors sensitivity, explaining the need of improvement towards a new generation. Particular attention is directed to the CTN problem, which is the motivation of this work.

- **Chapter 2** gives a fundamental understanding of the atomic arrangement in amorphous structure, which is characterised by static and dynamic features and determines the optical and mechanical properties of solids. In the first part are described the static properties. The absorption of amorphous solids is defined by three different region regarding the optical absorption edge: the main absorption region involves band-like states and it is described by the Tauc-Lorentz and Cody-Lorentz models; the absorption threshold involves transitions between localized tails and extended states, described by the exponential Urbach behaviour, and the transitions which involve only localized states inside the energy gap, near the Fermi level, described by an exponential behaviour. Regarding the mechanical behaviour, the interatomic forces and the structure of a glass determine its vibrational properties and hence its elastic constants. It is possible to demonstrate that the elastic moduli of amorphous solids depend on Gaussian deformation of the structure.

  The second part treats the dynamic properties of solids. Raman spectroscopy allows to obtain informations of atomic organizations by the scattering process related to the interaction of light with the solid. Thermal equilibrium is a dynamical equilibrium, where a continuous exchange between two levels exists, causing the thermal noise. This is the idea of the two level system (TLS). An external mechanical solicitation modifies the asymmetry of a TLS, changing consequentially

---

[1] http://lma.in2p3.fr/

its population, hence the elastic constant of the solid. The mechanical response is delayed by the relaxing process that occurs in order to bring the system back to the equilibrium, causing the dissipation. Following the fluctuation-dissipation theorem [5] the two phenomena of thermal noise and mechanical dissipation are the two aspects of the same phenomenon: irreversible processes in the solid structure.

**The novelty presented in this chapter regards the analytical calculation of the internal friction in a TLS, considering a general expression of the potential barrier.**

- **Chapter 3** describes the methods adopted to characterize the samples. In SE the change in polarization of reflected or transmitted light is probed, when it interacts with the sample. I used two different ellipsometers, covering complementary and partially overlapping spectral regions, obtaining information related to a broad wavelength range from 190 to 1680 nm (0.7 - 6.5 eV). The different optical models are listed, regarding the transparent region, which gives preliminary results including the wavelength of interest 1064 nm and 1550 nm, and the absorption region.

  The mechanical properties have been characterized by the ring-down method using a Gentle Nodal Suspension (GeNS) system. Remarkably, the dilution factor − the energy stored in the coating to the total energy of the system −, which allow to estimate the coating loss angle, can now be measured with a GeNS system. **A non-destructive method to estimate the elastic constant of coatings has been developed, based on fitting the measured dilution factors with a model based on finite-element analysis.**

- **Chapter 4** presents the mechanical and optical investigation on coatings. A brief introduction describes the coating deposition method and on the different coaters used to deposit all the samples.

  During the mechanical characterization, unexpected behaviour of the loss angle highlighted the impact of the edge of the samples affecting the coating loss. **For this reason, a model which includes the extra mechanical loss of the edge and a protocol to mitigate this problem have been developed during this thesis.**

  The mechanical and optical properties of coatings are studied under different post-deposition treatments and the doping. As first, we analyse the standard coatings silica ($SiO_2$), tantala ($Ta_2O_5$) and titania-doped tantala ($Ti{:}Ta_2O_5$). Combining Raman and loss angle measurements on different post-deposition annealed samples, it has been possible to find a correlation between the structure organization and the coating loss angle for $SiO_2$ coating. Furthermore, the optical properties, related to the electronic density of states, and mechanical properties, regarding the internal friction, have been compared by their relationship with the structure organization in a short- to medium-range order. In particular, **for the first time a correlation between the Urbach energy, related to the exponential behaviour of the absorption edge, and the internal friction has been found.** The correlation is observed analysing different oxide coating materials, suggesting a general validity of such property.

  The mechanical and optical properties of $Nb_2O_5$, $Nb{:}TiO_2$, $Zr{:}Ta_2O_5$, $MgF_2$, $AlF_3$, SiC and $SiN_x$ as new possible coating materials have been analysed and compared in order to determine the best candidate for future GWDs.

# CHAPTER 1

# GRAVITATIONAL-WAVE DETECTORS

*"One must still have chaos in oneself to be able to give birth to a dancing star."*

Friedrich Nietzsche
Thus spoke Zarathustra, p.9 (1883)

Giants ears to listen to the universe. This first chapter introduces the theory of gravitational waves, showing the detectors used for all the recent detections and the upcoming improvements with the aim of a better sensitivity.

The first part is dedicated to the gravitational radiation, ripples in space and time which are solutions of the gravitational field equations in the weak-field approximation. The different sources are listed, showing all the detected signals obtained since the first one in September 2015.

The second part is dedicated to gravitational-wave detectors, explaining the benefit of using km-scale interferometers and the need of a network to localize the gravitational-wave sources. A major part concerns the detectors sensitivity, explaining the need of detectors improvement towards a new generation.

Particular attention is directed to the coating thermal noise problem, which is the motivation of this work.

## 1.1 Space-Time Curvature

General Relativity conceived in 1916 by Albert Einstein gives a new way of thinking. The main change introduced by this theory is the possibility of a curved space-time in which objects can move, so that the idea of gravitational attracting force, settled by Newton in 1687, is replaced by the concept of falling masses in a curved space. More precisely, the space-time is influenced by the presence of massive objects and, as a consequence, the matter moves according to lowest energy condition. In this sense John Wheeler stated *"Space-time tells matter how to move; matter tells space-time how to curve."*

### 1.1.1 Gravitational-Wave Equation

To obtain the expression of gravitational wave equations we have to study the weak-field solutions of the field equations [13]

$$R_{\mu\nu} - \frac{1}{2} R g_{\mu\nu} = \frac{8\pi G}{c^4} T_{\mu\nu} \,, \tag{1.1}$$

where $R_{\mu\nu}$ is the Ricci tensor, $R$ the Ricci scalar, $G$ the Newton gravitational constant, $T_{\mu\nu}$ the energy-momentum tensor, $c$ the speed of light and $g_{\mu\nu}$ is the metric-tensor such that

$$ds^2 = g_{\mu\nu} dx^\mu dx^\nu \,. \tag{1.2}$$

Following equations (1.1), each variation of $T_{\mu\nu}$ modifies the gravitational field corresponding to a variation of the metric tensor $g_{\mu\nu}$ and *vice versa*. Starting from Minkowski space, where the metric tensor is

$$g_{\mu\nu} = \eta_{\mu\nu} = \begin{pmatrix} -1 & 0 & 0 & 0 \\ 0 & 1 & 0 & 0 \\ 0 & 0 & 1 & 0 \\ 0 & 0 & 0 & 1 \end{pmatrix} , \tag{1.3}$$

and considering a weak perturbation, $g_{\mu\nu}$ is modified by a small quantity $h_{\mu\nu}$,

$$g_{\mu\nu} = \eta_{\mu\nu} + h_{\mu\nu} \,, \qquad |h_{\mu\nu}| \ll 1 \,. \tag{1.4}$$

If we now consider the Hilbert gauge[1] $\partial_\mu h_{\mu\nu} = 0$, we obtain the following equations

$$\partial^\lambda \partial_\lambda h_{\mu\nu} = \left( \nabla^2 - \frac{1}{c^2} \frac{\partial^2}{\partial t^2} \right) h_{\mu\nu} = 0 \,, \tag{1.5}$$

which describe plane-wave radiation travelling at the speed of light $c$

$$h_{\mu\nu} = \epsilon_{\mu\nu} e^{i(k_\lambda x^\lambda)} \,, \tag{1.6}$$

where $\hat{\epsilon}$ is the polarization tensor. It can been shown that under a particular gauge [14] i.e. transverse-traceless gauge (TT gaue), it is possible to reduce $\hat{\epsilon}$ to a linear combination of two independent components $\hat{\epsilon}_+$ and $\hat{\epsilon}_\times$,

$$\hat{\epsilon} = h_+ \hat{\epsilon}_+ + h_\times \hat{\epsilon}_\times = h_+ \begin{pmatrix} 0 & 0 & 0 & 0 \\ 0 & 1 & 0 & 0 \\ 0 & 0 & -1 & 0 \\ 0 & 0 & 0 & 0 \end{pmatrix} + h_\times \begin{pmatrix} 0 & 0 & 0 & 0 \\ 0 & 0 & 1 & 0 \\ 0 & 1 & 0 & 0 \\ 0 & 0 & 0 & 0 \end{pmatrix} . \tag{1.7}$$

Only the spatial components of the $\hat{h}$ tensor perpendicular to the direction of propagation have non-zero values and the sum of the diagonal terms is zero (traceless). In this sense, taking a ring of masses in the $xy$-plane (figure 1.1), a gravitational wave travelling in the $z$-direction affects only the components along $\hat{x}$ and $\hat{y}$.

---

[1] It is equivalent to the Lorentz gauge for the electromagnetism.

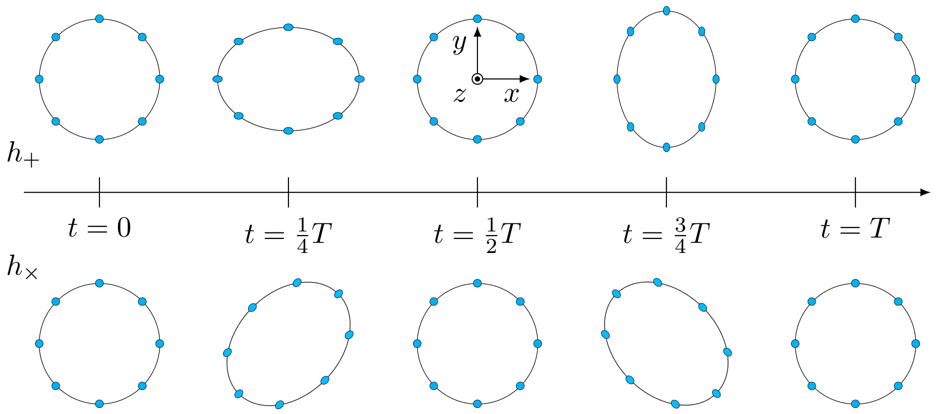

**Figure 1.1:** Ring of test masses in the $xy$-plane under the effect of a gravitational wave travelling along the $z$-axis. $\hat{\epsilon}_+$ and $\hat{\epsilon}_\times$ polarizations, having the same modulo over a period $T = 2\pi/\omega$, differ only by a rotation of 45°.

### 1.1.2 Gravitational-Wave Sources

To understand which mechanisms generate gravitational radiation, it is useful to start making some considerations about the analogy with the electromagnetic radiation. The emission by a slow variation of charge distribution can be expressed in a series of multipoles, where the strongest electromagnetic radiation would be expected for the lowest-order pole radiation, i.e. the electric dipole, followed by the magnetic dipole and electric quadrupole. In the same way, for gravitational waves, the mass conservation will exclude the monopole radiation. Furthermore, since the mass is always a positive quantity, the linear and angular momentum conservation exclude the dipolar gravitational radiation. It follows that gravitational radiation is at least quadrupolar and is directly linked to the quadrupole moment of the mass distribution, which in TT gauge reads [14]

$$Q_{\mu\nu} = \int dV \left( x_\mu x_\nu - \frac{1}{3}\delta_{\mu\nu} r^2 \right) \rho(\mathbf{r}) \,, \tag{1.8}$$

where $\rho(\mathbf{r})$ is the mass density in a volume $V$. In 1918 Einstein expressed the amplitude $h_{\mu\nu}$ as second-order temporal variation of the quadrupole moment,

$$h_{\mu\nu} = \frac{2G}{rc^4} \ddot{Q}_{\mu\nu} \,. \tag{1.9}$$

Using this relation it is possible to obtain the order of magnitude for the wave amplitude $h$ [15]. If we imagine to create a gravitational-wave source in laboratory, by spinning at 1 $kHz$ a dumbbell system of two masses of 1 ton each separated by a rod 2 meters long, the amplitude of the waves generated by this device at the distance of one wavelength would be $h_{\text{lab}} \approx 10^{-39}$, which is practically impossible to detect. More massive sources moving at relativistic speed are needed, in order to emit detectable gravitational radiation.

For astrophysical sources (like binary systems or supernova explosion, which emit, as we will see, in the detection band of ground-based detectors, from 10 to $10^4$ $Hz$), the amplitude is $h \approx 10^{-21}$, which is higher than the current experimental detection limit. The main expected sources of gravitational waves are:

**Binary System:** Compact object binaries consist of pairs of neutron stars (NS/NS), black holes (BH/BH) or neutron star/black hole pairs (NS/BH) falling one into the other in inspiral orbits. Gravitational waves are emitted during the coalescence. Typical signal frequency lies in the acoustic band probed by current ground-based detector Advanced Virgo, Advanced LIGO and KAGRA. In figure 1.2 all the signals detected in last years are listed [16], obtained from black holes or neutron stars binary system.

**Pulsar:** Neutron stars in rapid rotation can emit gravitational radiation if they lose the spherical symmetry in their mass distribution. Electromagnetic radiation is emitted with the same period of rotation. Despite the easy localization of these objects due to the electromagnetic signal, the extreme stability of the frequency radiation suggests a very small loss of energy, therefore a weak gravitational wave signal.

**Supernovae:** Gravitational radiation can be emitted during the gravitational collapse of certain types of stars. Supernovae are stars in which a gravitational collapse generates a violent explosion. If the collapse is not spherically symmetric, gravitational radiation can be emitted.

## 1.2 Interferometric Gravitational-Wave Detectors

The nature of gravitational wave radiation is to modify the space-time in the plane perpendicularly to the propagation direction. The two polarizations $\hat{\epsilon}_+$ and $\hat{\epsilon}_\times$ act in differential way, so that it is possible to detect the gravitational wave by measuring the differences of the space deformation along the two perpendicular directions of the polarizations. A particular instrument suitable for this kind of measure is the Michelson interferometer, where the differential displacement of the mirrors is measured by the interference of laser beams. The interference term is proportional to the phase shift $\phi_0$ of the beam electric fields

$$E_{1,2} = \mp\frac{1}{2}E_0 e^{-i\omega_{\text{GWD}}(t+2L_{1,2}/c)} , \tag{1.10}$$

where $\omega_{\text{GWD}} = 2\pi c/\lambda_{\text{GWD}}$ is the frequency of the laser having wavelength $\lambda_{\text{GWD}}$ and $L_{1,2}$ the length of the 1,2 arm. Under this respect, the power read by the photodiode at the output of the detector is

$$\begin{aligned} P &\sim |E_{\text{out}}|^2 = |E_1 + E_2|^2 , \\ P &= P_0 \sin^2 \Delta\phi_0 , \end{aligned} \tag{1.11}$$

where $\Delta\phi_0 = 2\pi(L_1 - L_2)/\lambda_{\text{GWD}}$. In the next session we will see how the detected phase is modified by the presence of gravitational radiation.

### 1.2.1 Detection Principle

In order to use the interferometer as gravitational wave detector, the mirrors must play the role of gravitational field probes. One can suppose a detector having free test-mass mirrors in the $xy$-plane and calculate the phase shift caused by a gravitational wave travelling along the $z$-direction, having polarization $\hat{\epsilon}_+$ and time function

$$h_+(t) = h_0 \cos(\omega_{\text{gw}} t) , \tag{1.12}$$

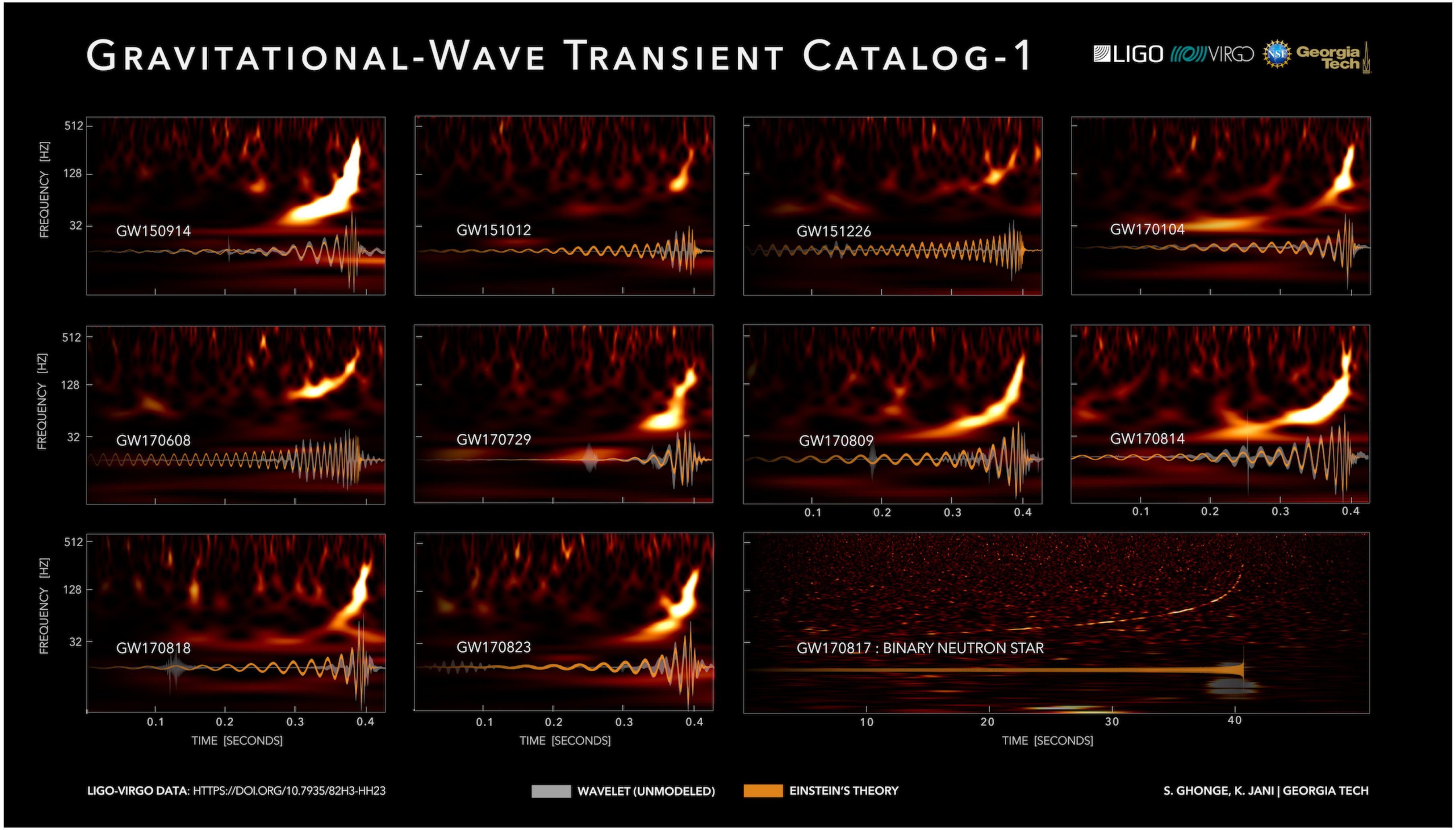

**Figure 1.2:** Waveforms of all gravitational-wave signals detected by Advanced LIGO and Advanced Virgo during the last years [16]. The evolution of wavelength, frequency and amplitude are observed during time. It is clearly visible the differences between binary black-holes system, where amplitude and frequency increase in time giving the *chirp* signal, and neutron stars merging, where the coalescence lasts more time.

where $h_0$ is the amplitude and $\omega_{\text{gw}}$ the frequency of the gravitational wave. The interval between two close space-time events linked by the laser beam is given by

$$\begin{aligned} ds^2 &= g_{\mu\nu} dx^\mu dx^\nu \\ &= (\eta_{\mu\nu} + h_{\mu\nu}) dx^\mu dx^\nu \\ &= -c^2 dt^2 + (1 + h_+(t)) dx^2 + (1 - h_+(t)) dy^2 = 0\,. \end{aligned} \tag{1.13}$$

Taking only the $x$-direction we obtain

$$ds^2 = -c^2 dt^2 + (1 + h_+(t)) dx^2 = 0\,, \tag{1.14}$$

therefore

$$dx = \pm \frac{c dt}{\sqrt{1 + h_+(t)}} \sim \pm c dt \left(1 - \frac{1}{2} h_+(t)\right)\,. \tag{1.15}$$

Gravitational radiation perturbs the metric $\eta_{\mu\nu}$ modifying the space-time. This can be observed as a delay of the laser beam in travelling along the arms of the interferometer. Considering the light travel time $\tau_{Lx}$ from the beam splitter to the end of the $L$-long $x$ arm, the integration of relation (1.15) reads

$$L = c\tau_{Lx} - \frac{c}{2} \int_0^{\tau_{Lx}} h_+(t) dt\,. \tag{1.16}$$

Considering the time $\tau_{2Lx}$ for the total round trip long $2L$ we obtain

$$2L = c\tau_{2Lx} - \frac{c}{2} \int_0^{\tau_{2Lx}} h_+(t) dt\,. \tag{1.17}$$

From equation (1.17) it is evident that the time $\tau_{2Lx}$ for a round trip is $2L/c$ plus a correction of the order of $h_0$. Since $h_+(t)$ depends already on $h_0$ and we neglect terms $O(h_0^2)$ we obtain from (1.17)

$$\begin{aligned} \tau_{2Lx} &= \frac{2L}{c} + \frac{1}{2} \int_0^{2L/c} h_0 \cos(\omega_{\text{gw}} t) dt \\ &= \frac{2L}{c} + \frac{h_0 L}{c} \frac{\sin(\omega_{\text{gw}} L/c)}{(\omega_{\text{gw}} L/c)} \cos(\omega_{\text{gw}} L/c) \\ &= \frac{2L}{c} + \frac{L}{c} h(t = L/c) \text{sinc}(\omega_{\text{gw}} L/c)\,. \end{aligned} \tag{1.18}$$

The same consideration can be done for the $y$ direction

$$\tau_{2Ly} = \frac{2L}{c} - \frac{L}{c} h(L/c) \text{sinc}(\omega_{\text{gw}} L/c)\,. \tag{1.19}$$

From relations (1.18) and (1.19) it is possible to obtain the total travel time difference between the two arms

$$\Delta\tau = \tau_{2Lx} - \tau_{2Ly} = \frac{2L}{c} h(L/c) \text{sinc}(\omega_{\text{gw}} L/c)\,, \tag{1.20}$$

which gives the following phase shift in the interferometer

$$\Delta\phi = \omega_{\text{GWD}} \Delta\tau = \frac{4\pi L}{\lambda_{\text{GWD}}} h(L/c) \text{sinc}(\omega_{\text{gw}} L/c)\,. \tag{1.21}$$

According to relation (1.11), the power observed at the photodetector is modulated by the gravitational wave signal as

$$P = P_0 \sin^2(\phi_0 + \Delta\phi)\,. \tag{1.22}$$

**(a)** Advanced Virgo. **(b)** Advanced LIGO.

**Figure 1.3:** Advanced VIRGO interferometer in Cascina, Italy on the left *(The Virgo collaboration (CC0 1.0))*. Twin Advanced LIGO interferometers in Livingston, Lousiana, and in Hanford, Washington on the right *(Courtesy CaltechMITLIGO Laboratory)*.

### 1.2.2 Large Ground-Based Interferometer

In order to obtain a detectable phase shift, it follows from the relation (1.21) that the interferometer should have very long arms. For this reason, as showed in figure 1.3, Advanced Virgo and Advanced LIGO interferometers have arms 3 and 4 km long.

In order to increase the detector sensitivity, several cavities are applied to the interferometer [17]. Looking at equation (1.21), the sensitivity increases with the arms length. For this reason, as can be observed in figure 1.4, Fabry-Perot cavities are applied to the interferometry arms. The key feature of a Fabry-Perot resonator is the *finesse* $\mathcal{F}$, i.e. the spectral resolution. The sensitivity to a phase shift for a Fabry-Perot interferometer $\Delta\phi_{\mathrm{FP}}$ is enhanced by a factor

$$\frac{\Delta\phi_{\mathrm{FP}}}{\Delta\phi} = \frac{2\mathcal{F}}{\pi} \,. \tag{1.23}$$

In presence of gravitational waves, the phase shift in a Fabry-Perot interferometer can be written as [13]

$$|\Delta\phi_{\mathrm{FP}}| \simeq h_0 \frac{8\mathcal{F}}{\lambda_{\mathrm{GWD}}} L \frac{1}{\sqrt{1 + (f_{gw}/f_p)^2}} \,, \tag{1.24}$$

where $f_{gw} = \omega_{gw}/2\pi$ is the frequency of the gravitational wave and $f_p \simeq c/(4\mathcal{F}L)$ is the frequency related to the storage time of the cavity. This formula holds as long as $\omega_{gw}L/c \ll 1$, otherwise the $\mathrm{sinc}(\omega_{\mathrm{gw}}L/c)$ in relation (1.21) cuts the response further, reflecting the fact that in each round-trip the gravitational wave have time to reverse its sign.

Furthermore, to increase the signal to noise ratio one mirror (the *power recycling mirror*) is added at the input of the detector to create the *power recycling cavity* with the rest of the interferometer and use the signal sent backwards to increase the power circulating in the interferometer [18]. In the same way, a mirror (the *signal recycling mirror*) is added at the end of the detector, before the photodiode, to create the *signal recycling cavity* and increase the sensitivity [18].

## 1.3 Past, Present and Future Detectors

Large ground-based interferometer requires extreme effort to control the many degrees of freedom with extraordinary accuracy. Under this respect, the accomplishment of the

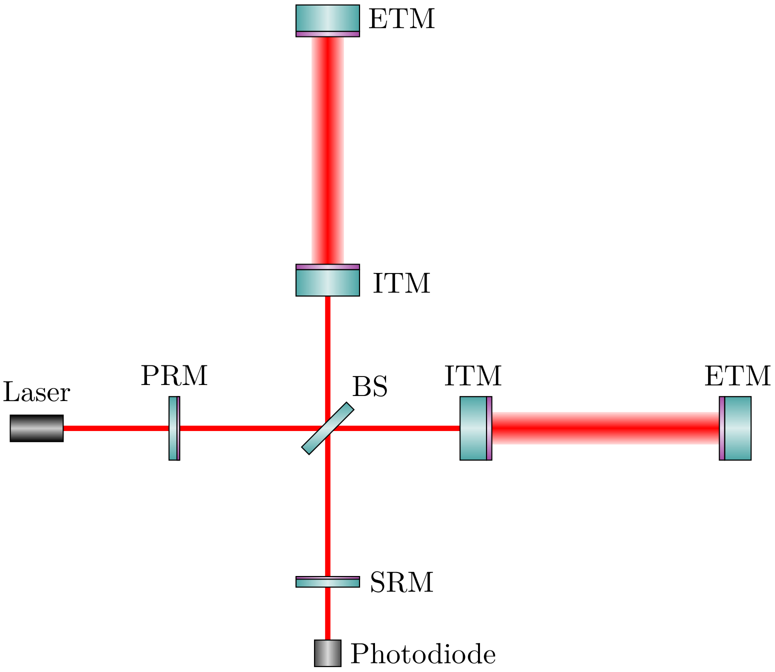

**Figure 1.4:** Sketch of the interferometric detector highlighting the cavities. The beam splitter (BS) allows to obtain the Michelson interferometer. The Fabry-Perot cavities are between the input test-mass (ITM) and the end test-mass (ETM). The power recycling cavity is made on the power recycling mirror (PRM) and the rest of the interferometer. The signal recycling cavity is made on the signal recycling mirror (SRM) and the rest of the interferometer.

firsts detectors needed the building up of large collaborations and more than 30 years of technological improvement.

The Virgo collaboration, which started as scientific collaboration between Italy and France now extended to several European countries, inaugurated the Virgo project in 2003; a power-recycled Fabry-Perot interferometer located in Cascina, Italy, with arms of 3 km.

The LIGO collaboration has scientists members of the LIGO Scientific Community (LSC) and runs two detectors in US with arms of 4 km since 2005, one located in Hanford (Washington State) and one in Livingstone (Louisiana).

Beside these large detectors, GEO600 is an interferometer with 600-m long arms, located in Hannover, Germany. The members of GEO600 are also members of the LSC.

If we refer only to binary system sources, the predicted rate of detection for these interferometers is of the order of $10^{-3}$/yr. In practice, despite the several joint observational runs, the above interferometers never detected a gravitational wave signal.

### 1.3.1 To the First Detection and Beyond

A tenfold improvement of the first detectors' sensitivity would increase the volume of the Universe probed by a factor $\sim 10^3$, increasing correspondingly the expected detection rate. This was the motivation of the proposal of a second generation of interferometers: Advanced LIGO (aLIGO) [19] and Advanced Virgo (AdV) [20], currently operational, and KAGRA [21], a Japanese interferometer which will join the next observational runs. The main improvement included the adoption of signal-recycling cavity, the increase of input laser power, silica wires to suspend the optics and new high-reflective coatings.

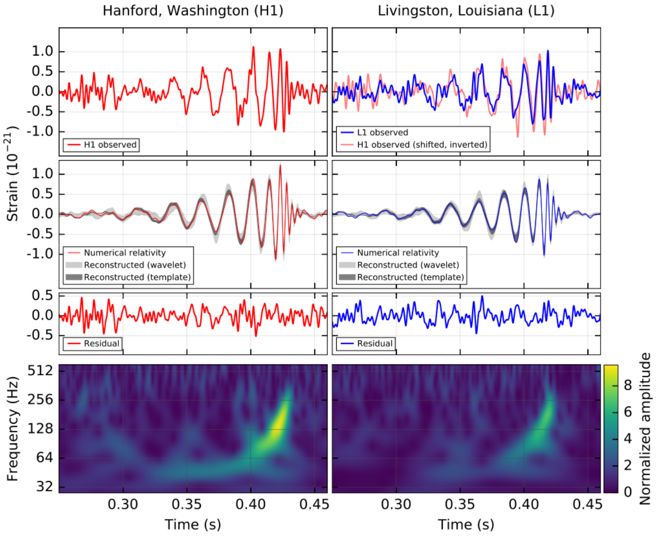

**Figure 1.5:** The gravitational-wave event GW150914 observed by the LIGO Hanford (H1, left column panels) and Livingston (L1, right column panels) detectors [22]. First row: GW150914 signal. Second row: Solid lines show a numerical relativity waveform for a system with parameters consistent with those recovered from GW150914. Third row: Residuals after subtracting the filtered numerical relativity waveform from the filtered detector time series. Bottom row: A time-frequency representation of the strain data, showing the signal frequency increasing over time.

On the 14th of September 2015, a gravitational wave was detected for the first time by aLIGO [22]. This was the first direct detection of gravitational waves and the first observation of a binary black hole merger. The detected signal is illustrated in figure 1.5. After this great achievement, the gravitational-wave detectors accomplished several detections [16] listed in figure 1.2.

After having accomplished a first stage of successful measurements, the largest ground-based interferometric detectors are presently undergoing a major technical upgrade towards a significant sensitivity improvement over the whole detection band. In figure 1.6, the sensitivity improvement for Virgo and LIGO interferometers is showed. The projects are identified by the appellative “+” and regard different technical aspect of the detectors. LIGO and Virgo collaboration are planning to increase the detector sensitivity in the central region of the detection band, where Brownian coating thermal noise dominates.

### Detector Network

A single detector allows to observe the transit of gravitational waves without the possibility to localize the sources. Similarly to what happens for an earthquake, at least three detectors with similar sensitivity are needed to localize the source. As showed in figure 1.7, there are four ground-based interferometers currently operational around the globe: aLIGO Hanford, aLIGO Livingstone, AdV and GEO600 [23].

The localization of a source is extremely important because by knowing the exact position of the source it is possible to observe also the electromagnetic counterpart of the signal. Indeed, thanks to the first triple detection by aLIGO and AdV, it was possible to localize a binary neutron-star merging system and to coordinate with others optical astronomy facilities [24], giving birth to the multi-messenger astronomic observation

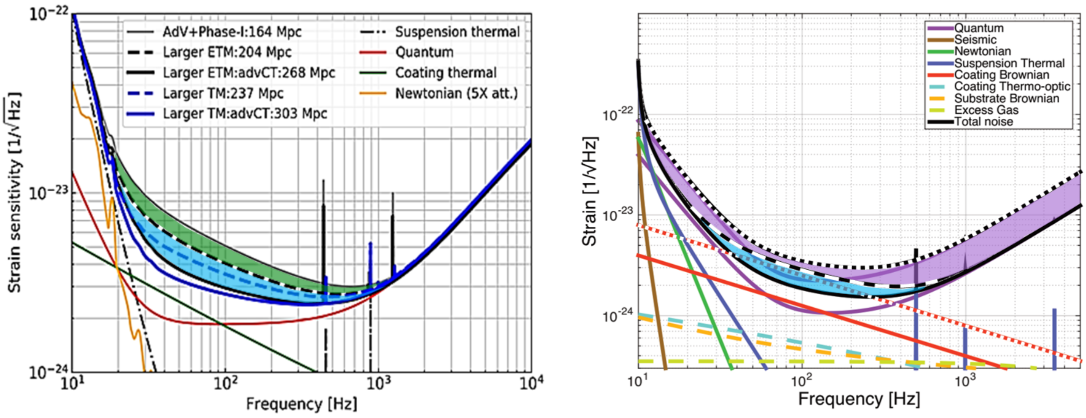

**(a)** Advanced Virgo +.

**(b)** Advanced LIGO +.

**Figure 1.6:** Detector sensitivity for (a) advance Virgo + and for (b) advanced LIGO +. The green area refer to noise budget reduced by the laser beam size, the violet by the frequency-dependent squeezing and the blue by lower coating loss angle.

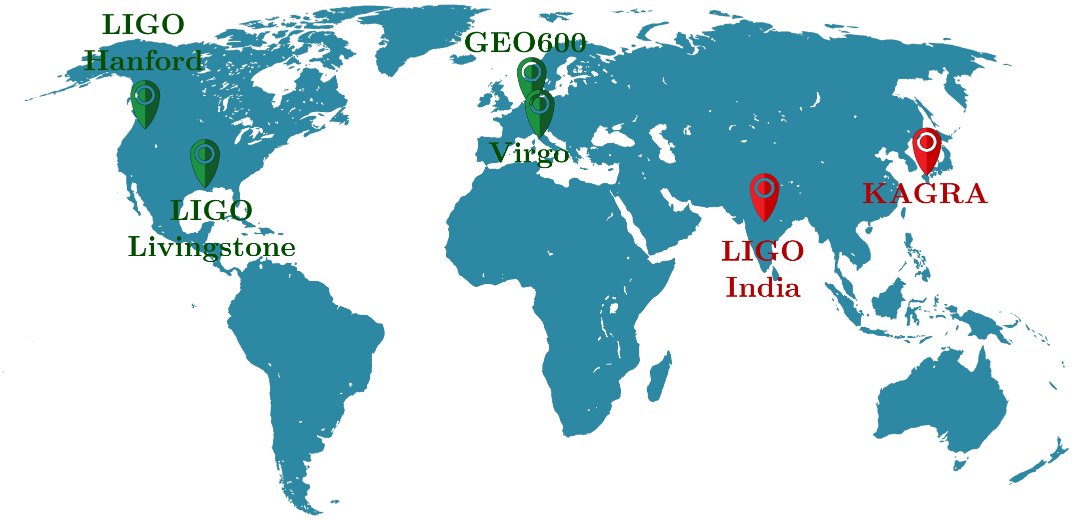

**Figure 1.7:** Current ground-based gravitational-wave detectors' network on the Earth. In green, the operational interferometers: Advanced LIGO (USA), Advanced Virgo (Italy) and GEO600 (Germany). In red, the cryogenic interferometer under construction KAGRA (Japan) and the replica of Advacned LIGO interferometer to be built in India.

era. In figure 1.8a the localization of the signal is showed. Figure 1.8b shows the skymap of all the gravitational wave detections using the ground-based interferometers. It is clearly visible that the localizations made by the three detectors LIGO and Virgo are more accurate than the others.

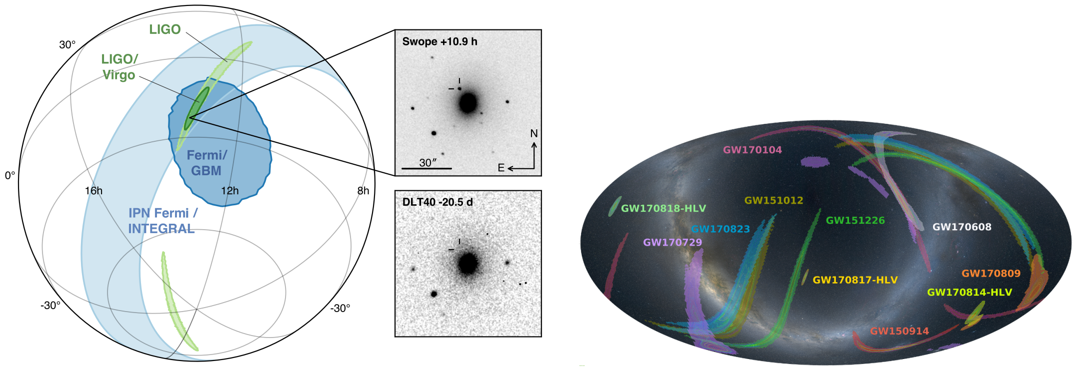

**(a)** GW170817-HLV. **(b)** Skymap.

**Figure 1.8:** (a) Localization from the LIGO-Virgo 3-detectors global network (green) of the gravitational-wave detected on the 17th of August, 2017. The position overlaps with the gamma-ray and optical signals (blue) detected by the Fermi/INTEGRAL satellites and the Swope discovery image respectively. The inset shows the location of the apparent known galaxy NGC4993: In the image on top, recorded almost 11 hours after the gravitational-wave and gamma-ray signals had been detected, a new source (marked by a reticle) is visible. That source was not there in the bottom image, taken about three weeks before the event. (b) Sky localization of all the gravitational wave detection. The HLV acronym at the end of the signal name stands for Hanford, Livingstone (LIGO) and Virgo to indicate the triple detection.

In order to improve the localization, another aLIGO interferometer is planned to be built in India [25]. Furthermore, the Japanese detector KAGRA will operate at cryogenic temperature, at the end of 2019.

### 1.3.2 Next Generation Detectors

The next generation gravitational wave detector Einstein Telescope (ET) [26], will be an underground cryogenic detector planned to be operating in the 2030 decade with 10 km arm length. ET will combine three detectors in a triangle shape operating at different frequency bands, with the aim of improving the detection bandwidth and increasing the sensitivity with respect to the gravitational wave polarization.

Lowering the temperature is also an update proposed for the current Advanced LIGO detectors. Cosmic Explorer [27] is a cryogenic detector with 40 km arms.

Laser Interferometer Space Antenna (LISA) [28] is a space-based detector, with the aim to detect from $10^{-4}$ to $10^{-1}$ Hz, started under the coordination of the European Space Agency (ESA). LISA will be a space giant interferometer in which three spacecraft are separated by 2.5 million km, orbiting behind the Earth as we orbit the Sun.

## 1.4 The Limits to the Gravitational-Wave Detection

In this section the main sources of noise limiting the detector sensitivity are described. For gravitational-wave interferometers, lowering the noise would allow to detect weaker signals from farther sources, thus increasing the detection horizon, i.e. the radius of the accessible volume of the Universe.

The sensitivity curve of Advanced detectors is the envelop of all the noises contributions, assumed to be statistically independent, expressed in equivalent amplitude of the gravitational-waves signal as function of frequency. The output of the detector $\phi(t)$, in arbitrary unit, will contain contributions from both gravitational wave strain and from various noise sources. By assuming a linear response, it is possible to write $\phi(t)$ as

$$\phi(t) = \int T_{h\to\phi}(t,t')h_{\text{eff}}(t')dt' + N_\phi(t)\,, \tag{1.25}$$

where $N_\phi(t)$ is the additive noise contribution and $T_{h\to\phi}(t,t')$ is the transfer function, which connect the effective strain $h_{\text{eff}}$ to the detected signal. By assuming stationary condition for the interferometer, where time invariance occurs, the response function will not depend independently on $t$ and $t'$ but on their difference, $t-t'$. By doing this, it is possible to perform the Fourier transform, going to the frequency domain $f$,

$$\tilde{\phi}(f) = \tilde{T}_{h\to\phi}(f)\tilde{h}_{\text{eff}}(f) + \tilde{N}_\phi(f)\,. \tag{1.26}$$

For example, it is possible to rewrite equation (1.24) as $|\Delta\phi_{\text{FP}}| = T_{h\to\phi}h_0$, where

$$T_{h\to\phi} \simeq \frac{8\mathcal{F}}{\lambda_{\text{GWD}}}L\frac{1}{\sqrt{1+(f_{gw}/f_p)^2}}\,, \tag{1.27}$$

is the transfer function of the Fabry-Perot interferometer. It is possible to use the transfer function in order to express the noise in a quantity comparable to the gravitational wave signal $h_{\text{eff}}(f)$

$$\tilde{N}_h(f) \equiv \tilde{T}^{-1}_{h\to\phi}(f)\tilde{N}_\phi(f)\,, \tag{1.28}$$

Assuming that $\tilde{N}_h(f)$ is related to stochastic stationary processes, it can be expressed by its power $S_h(f)$ [29]

$$S_h(f)\delta(f-f') = \langle\tilde{N}_h(f')\tilde{N}_h(f)\rangle\,. \tag{1.29}$$

The square root of this quantity, having the unit of $1/\sqrt{Hz}$, represents the *spectral strain sensitivity* for the noise under consideration and can be compared to the gravitational wave amplitude

$$\tilde{h}(f) = \sqrt{S_h(f)}\,. \tag{1.30}$$

Thus, a gravitational wave signal having amplitude higher than the sensitivity curve can be detected.

From equation (1.11) it is clear that the interferometer is sensitive to the fluctuation of the laser power and phase shift, which can be observed as variation in arms length $\Delta L = L_1 - L_2$ thus as the displacement of the optical components in the arms.

The sensitivity curve of Advanced Virgo is showed in figure 1.9. It can be observed that three main noise curves limit the sensitivity in different frequency region. The quantum noise is related to the fluctuation of the power and limits the detector sensitivity at both lower and higher frequencies. At lower frequencies the sensitivity is limited by the suspension thermal noise whereas in the central and most sensitive region there is coating thermal noise, which is a displacement noise. It has to be noted that, in a Fabry-Perot interferometer, the noise sources inside the resonant cavity dominate the others because they are amplified by the finesse of the cavity.

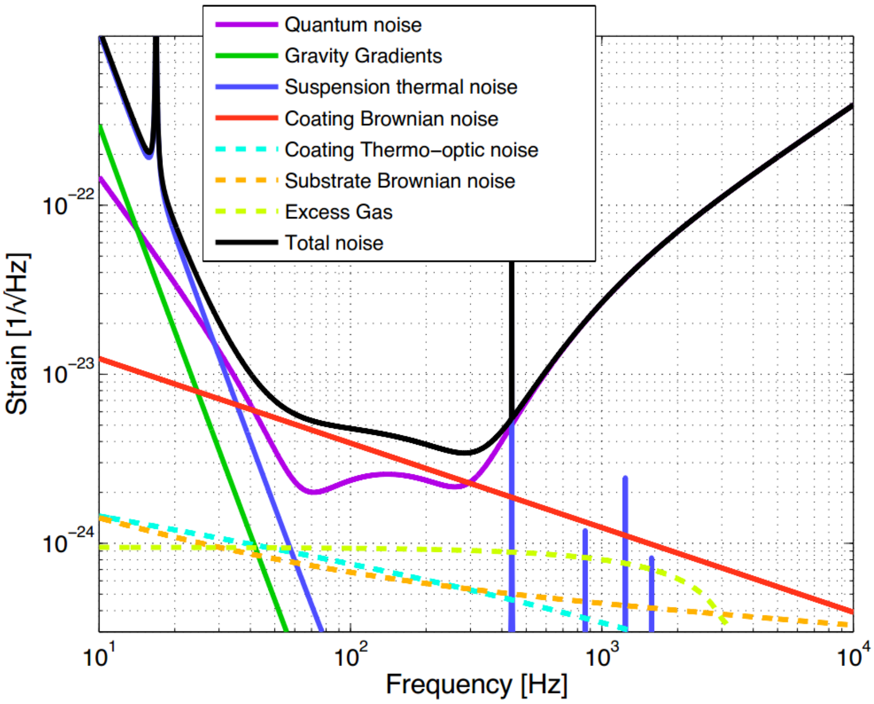

**Figure 1.9:** The Advanced Virgo reference sensitivity (black) obtained as envelop of different noise sources. The sensitivity is limited by the suspension thermal noise at low frequency, by the shot noise at high frequency (*quantum noise*) and by the coating thermal noise in the intermediate region.

### 1.4.1 Quantum Noise

The incident laser light on the photodetector can be seen as a set of photons. The effect of the discrete quanta can be observed in the laser power and sets a quantum limits in the measurement. The spectral strain density of this quantum noise is made on two components

$$h(f)_{\mathrm{QN}} = h(f)_{\mathrm{shot}} + h(f)_{\mathrm{rad}} \,, \tag{1.31}$$

where $h(f)_{\mathrm{shot}}$ is the shot noise and $h(f)_{\mathrm{rad}}$ is the radiation pressure noise.

**Shot Noise**

The shot noise is due to the fact that the incident laser light on the photodetector is a set of photons characterized by a Poisson distribution [30]. The incidence of one photon is independent from the others and the spectral density of the phase shift is then frequency independent [13]

$$S_{\Delta\phi}^{1/2} = \left(\frac{2\hbar\omega_{\mathrm{GWD}}}{P}\right)^{1/2} \,, \tag{1.32}$$

where $\hbar$ is the reduced Planck constant and $P$ the average incoming power. Therefore, the shot noise can be reduced by increasing the laser power $P$. In order to obtain the spectral strain noise and comparing it to the effective strain of gravitational wave signals, equation (1.32) must be divided by the transfer function (1.27)

$$\begin{aligned} h_{\text{shot}}(f) &= \tilde{T}^{-1}_{h\to\phi}(f)\sqrt{S_{\Delta\phi}} \\ &= \frac{1}{8\mathcal{F}L}\left(\frac{4\pi\hbar\lambda_{\text{GWD}}c}{P}\right)^{1/2}\sqrt{1+(f/f_p)^2}\,. \end{aligned} \tag{1.33}$$

**Radiation Pressure**

We observed that the shot noise is reduced by increasing the light power. However, when photons hit an optical element they impart a recoil of the object, disturbing the measure that we are performing. Considering the force $F = 2P/c$ that a beam of power $P$ exerts on the mirror of mass $M$, the spectral density of the displacement of the mirror is [13]

$$S_x^{1/2}(f) = \frac{2}{M(2\pi f)^2}\left(\frac{2\hbar\omega_{\text{GWD}}P}{c^2}\right)^{1/2}\,. \tag{1.34}$$

The second term under the square root is related to the fluctuation of the number of photons which is independent of the frequency, the first term is related to the Fourier transform of the stochastic force $F = M\ddot{x}$ acting on the mirror. A given displacement of a mirror results in a phase shift which is increased by the presence of the finesse in the transfer function. However, in order to compare with the effect of a gravitational wave, we must divide by the transfer function of the Fabry-Perot interferometer, so the two effects cancel. Actually, the fluctuation of the electric field inside the cavity is enhanced by a factor $2\mathcal{F}/\pi$. Furthermore, if the mirror vibrates at a frequency f, the power inside the cavity is reduced by a factor $(1+(f/f_p)^2)$. With this in mind and considering the transfer function of a simple Michelson interferometer $\tilde{T}_{\text{Mich}} = L$, we obtain

$$h(f)_{\text{rad}} = \frac{16\sqrt{2}\mathcal{F}}{ML(2\pi f)^2}\left(\frac{\hbar P}{2\pi\lambda_{\text{GWD}}c}\right)^{1/2}\frac{1}{\sqrt{1+(f/f_p)^2}}\,. \tag{1.35}$$

### 1.4.2 Seismic Noise

The first problem to face in order to use interferometer as gravitational-wave detector is the isolation of the mirrors from the ground, because of the seismic noise. For this purpose, a suspensions system called super attenuators (SA) is adopted on Advanced Virgo (figure 1.10). It is made of three fundamental parts:

- The inverted pendulum (IP), which consists in three aluminium legs 6 m long. In such a pendulum the gravity acts as an anti-spring and the resonant frequency can be lowered by increasing the mass, suppressing a large part of the input horizontal seismic noise.
- The chain seismic filters, made on five horizontal and vertical passive filters, connected by a 8 m long suspension wire. With this chain a very large attenuation of the seismic noise horizontal component can be obtained at a frequency above the highest pendulum resonance.
- The mirror payload, the last stage of the suspension system, including the actuators for the active isolation and alignment. This guarantees that the mirrors in cavities are always at a position to assure the resonant condition.

The super attenuators allow to reduce the seismic noise well under the limit of the detector sensitivity.

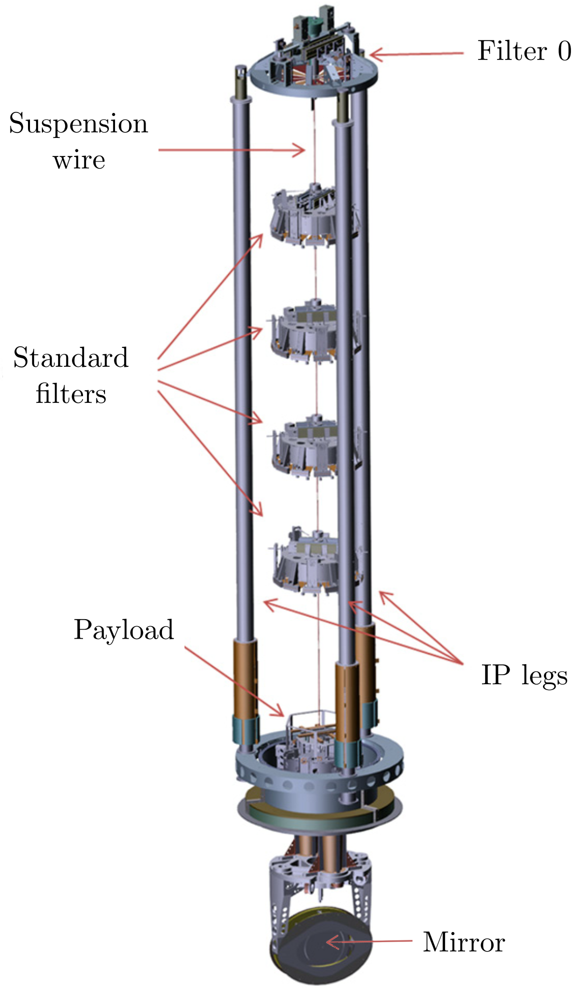

**Figure 1.10:** The Advanced Virgo SA. We can distinguish the three legs of the inverted pendulum, the set of filters and the mirror.

### 1.4.3 Thermal Noise

The central part of the detection band (30 Hz to 300 Hz) is limited by the thermal noise, arising from a thermally induced dissipation mechanisms of suspension elements and high-reflecting coatings. The comprehension of such noise lies in the so-called fluctuation-dissipation (F-D) theorem [5] (appendix A). Since the frequency of the detector is always less than $10^4$ Hz, the F-D theorem is considered in its classical limit even at cryogenic temperature and we can express equation (A.9) as

$$S(\omega, T) = \frac{4k_B T}{\omega^2}\Re\left[\mathcal{Y}(\omega)\right] \ . \tag{1.36}$$

**Suspension Thermal Noise**

The pendulum thermal noise and the violin modes' noise are the main contributions to the suspension thermal noise, are expressed by the same function but act in different frequency bands. The pendulum thermal noise is related to the thermally activated oscillation of the suspension, causing a displacement of the test masses [31]. The violin modes noise is related to the transversal oscillations which induce longitudinal displacement of the test masses [4]. To reduce the suspension thermal noise, a monolithic suspension made of four fused silica wires, 400 $\mu m$ thick, are fixed to the mirror using silicate bonding [32]. However, this noise still dominant at frequency below 30 $Hz$.

**Mirror Thermal Noise**

Mirror thermal noise is composed of several terms, due to different dissipative processes. The dissipation of mirror is treated in appendix A, and from (A.9) we obtain the general power spectral density [33]

$$S(\omega, T) = \frac{4k_BT}{\omega}\frac{W_{\text{diss}}}{F_0^2\pi} \, . \tag{1.37}$$

The main mirror thermal noise contributions are:

- Brownian thermal noise: such noise is caused by the internal friction of both coating and substrate, having the same spectral density [34]:

  $$S(f, T) = \frac{2k_BT}{\pi^{\frac{3}{2}}\mathrm{w}f}\frac{(1-\sigma^2)}{Y}\phi \, , \tag{1.38}$$

  where w is the laser beam size on the mirror, $\sigma$ is the Poisson ratio, $Y$ the Young's modulus and $\phi$ is the loss angle, which differ for substrate and coating.

  The main contribution to the mirror thermal noise is the Brownian **coating thermal noise** (CTN) [35]. In a Fabry-Perot cavity like those of GW interferometers, the frequency-dependent coating thermal noise reads [35]

  $$\begin{aligned} S(f, T)_{\text{CTN}} =& \frac{2k_BT}{\pi^{\frac{3}{2}}\mathrm{w}f}\frac{(1-\sigma^2)}{Y}\phi_c^{\text{tot}} \\ =& \frac{2k_BTt_c}{\pi^2\mathrm{w}^2f}\frac{(1-\sigma^2)}{Y}\left(\frac{Y'(1+\sigma)(1-2\sigma)^2 + Y\sigma'(1+\sigma')(1-2\sigma)}{Y(1+\sigma')(1-\sigma')(1-\sigma)}\phi_{\parallel}\right. \\ &\left. + \frac{Y(1+\sigma')(1-2\sigma') - Y'\sigma'(1+\sigma)(1-2\sigma)}{Y'(1+\sigma)(1-\sigma')(1-\sigma)}\phi_{\perp}\right) \, , \end{aligned} \tag{1.39}$$

  where $t_c$ is the total coating thickness, $Y$, $\sigma$ are the Young's modulus and Poisson's ratio of the substrate, $Y'$, $\sigma'$ are the Young's modulus and Poisson's ratio of the high-reflecting coating and $\phi_{\parallel}$,$\phi_{\perp}$ are the coating loss angles associated to the parallel and perpendicular coating strain.

- Thermo-elastic noise: in linear approximation, the thermal expansion coefficient $\alpha(T)$ induce a deformation proportional to the temperature fluctuation. If there are thermal gradients, some stress may induce dissipation processes in the solid. In this sense, the spectral density of such noise for the substrate [36] and for the coating [37] is then related to the temperature, to the coefficient $\alpha(T)$ and to the elastic moduli of the solid.

- Thermo-refractive noise: considering the coating, thermal gradient induces fluctuation in the refractive index with the quantity $\beta(T) = dn(T)/dT$, which causes noise in the output phase of the interferometer. Such noise is related to the structure and the material of the coating [38].

## 1.5 Thesis Goal: Coatings for Future Detectors

The technological challenge in creating high-reflecting coatings with low thermal noise lies in obtaining outstanding optical and mechanical properties at the same time, i.e.

mainly low optical absorption and low internal friction. The reduction of coating thermal noise is of fundamental importance in order to increase the detection horizon (i.e. the radius of the accessible volume of the Universe) and hence of the expected detection rate [39] of present and future detectors like the Einstein Telescope [40]. More generally, lowering such noise would be highly beneficial also for other precision experiments using optical cavities such as optomechanical resonators [9] and references for laser frequency stabilization [41].

It is clear from equation (1.39) that there are several parameters involved in the coating thermal noise: the total coating thickness, the coating loss angle, the elastic constant of the materials, the temperature and the laser beam size.

The coating thickness is a monotonically decreasing function of the refractive index contrast $c = n_H - n_L$ in the Bragg reflectors. An higher contrast $c$ allows to reduce the total stack thickness, hence the coating thermal noise, without altering the reflectivity. As a consequence, the optimal coating materials would feature the lowest loss and the largest refractive index contrast at the same time.

Several options can be considered in order to reduce the coating loss angle. First of all, it depends on the coating material. Current oxide coatings can be also further optimize to reduce the thermal noise: tuning of the sputtering ion beam, co-sputtering (also referred to as *doping*), substrate heating during deposition, post-deposition annealing; in principle, these techniques could be also combined to cumulate their benefits. Otherwise, other alternative materials may be selected and then potentially further improved. Indeed, crystalline coatings present very low loss angle [42, 43] but there are difficulties in the deposition on large substrate. A more exotic solution is nano-structuring of silicon waveguides [44], characterized by promising optical properties but limited to small substrate.

The work in this thesis consist in finding a possible solution to the coating thermal noise issue, studying the optical and mechanical properties of coatings.

### 1.5.1 The Current Picture

The advanced detectors impose some requirements that coatings must fulfil. On one hand, coatings have to minimize the optical losses in order to avoid power issue in the Fabry-Perot cavities and limit the shot noise. On the other hand, coatings must have a low loss angle in order to minimize the Brownian thermal noise.

From an optical point of view, coatings for gravitational-wave detectors have high reflectivity, low optical absorption and low scattering. The two first conditions increase the power in the arm cavities, whereas the last one minimizes an additional phase noise related to the reflection of scattered light on vibrating elements (optics, vacuum tubes).

From the mechanical point of view, in order to reduce the coating thermal noise, thin coating with low internal friction must be adopted. Furthermore, the Young's modulus of coating should match the Young's modulus of substrate. In table 1.1 the technical requirements for Fabry-Perot cavities and mirrors are summarised.

#### Substrate

The 40 kg substrates play the role of the test masses in gravitational-wave detectors. The main properties which define the choice of the material are the low optical absorption at the operational laser wavelength, the homogeneity of the refractive index and the low internal friction. Several studies have determined that the fused silica Suprasil® (3001 and 3002) is the best material to use at room temperature for a 1064 nm laser wavelength [46, 47].

| **Fabry-Perot Cavity** | | |
|---|---|---|
| **Geometry** | **ITM** | **ETM** |
| ∅ Beam $[mm]$ | 48.7 | 58.0 |
| **Optics** | **ITM** | **ETM** |
| Transmission | 1.4% | 1 $ppm$ |
| Finesse | 443 | |
| Losses $[ppm]$ | $< 75$ | |

**(a)** Measured values of Fabry-Perot arm cavities.

| **Coatings** | **ITM** | **ETM** |
|---|---|---|
| # layers | 16 | 38 |
| Thicnkess $[\mu m]$ | 2.8 | 5.9 |
| Absorption $[ppm]$ | 0.2 | 0.2 |
| Diffusion $[ppm]$ | 3 | 4 |
| Roughness RMS $[nm]$ | 0.1 | 0.1 |
| Planarity RMS $[nm]$ | 0.3 | 0.5 |
| Loss Angle $\phi$ $[10^{-4}]$ | 1.7 | 2.4 |

**(b)** Measured values of coatings properties.

**Table 1.1:** Parameters of Advanced Virgo, for the input test masses (ITM) and end test masses (ETM) in the arm cavities [45].

### Coating

In order to obtain high reflectivity, quarter-wave Bragg reflectors have been historically chosen as mirror coatings. We can consider for instance a stack made of $m+1$ layers, as shown in figure 1.11, where $j=0$ and $j=m+1$ are the ambient and the substrate[2]. If we assume that the stack is made of $N$ doublets of material having high- and low-refractive index ($n_H$ and $n_L$), the reflectivity of the stack reads [48]

$$R = \left| \frac{n_s - \left(\frac{n_H}{n_L}\right)^{2N}}{n_s + \left(\frac{n_H}{n_L}\right)^{2N}} \right|^2 \simeq 1 - 4n_s \left(\frac{n_L}{n_H}\right)^{2N} , \tag{1.40}$$

where $n_s$ is the refractive index of the substrate. Considering the absorption and the scattering negligible, we obtain the transmissivity

$$T = 1 - R = 4n_s \left(\frac{n_L}{n_H}\right)^{2N} . \tag{1.41}$$

It is easy to observe that for $N \to \infty$ then $R \to 1$ and $T \to 0$.

Nowadays, the thickness of each layer has been optimized in order to reduce the thickness of the high index layers, hence the coating thermal noise, without altering the reflectivity [49].

The main characteristics of the coatings are summarised in table 1.1b. In order to keep a low optical absorption, the Bragg reflectors were historically made of alternate ion-beam sputtered layers of silica ($SiO_2$) and tantala ($Ta_2O_5$), deposited at Laboratoire des Matériaux Avancés (LMA) as low- and high-refractive index materials respectively [50, 51]. Titania-doped tantala ($Ti:Ta_2O_5$) has been then developed in LMA in order to minimize the loss angle, obtaining a value lower than $Ta_2O_5$ layer [52].

### 1.5.2 Objective of the Thesis

In a scenario of further upgrade of advanced detectors and of development of next generation detectors, an intense research is devoted to decrease the coating loss angle in order to reduce the coating thermal noise. The work presented in this thesis takes

---

[2] We consider linear, homogeneous and isotropic materials.

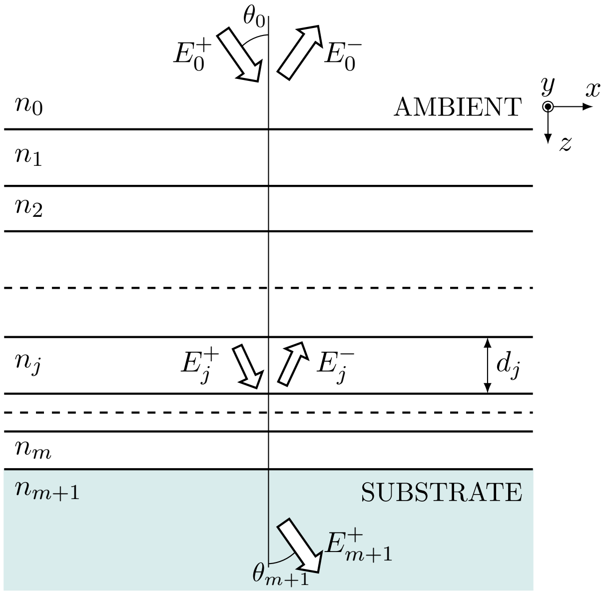

**Figure 1.11:** Sketch of a multilayer. The surface of the mirror is perpendicular to the $z$ direction. in each $j$-th layer, $E_j^+$ and $E_j^-$ are the overlap of the multiple reflection for the transmitted and reflected electric field.

place in this context and is intended to be a contribution to the development of present and future detectors with higher sensitivity. Indeed, this research is not limited to the upgrade on current detector but candidate coatings for future cryogenic detectors KAGRA, Cosmic Explorer and Einstein Telescope, are also investigated.

Since the coatings must fulfil very stringent optical and mechanical requirements, a deep optical and mechanical characterization have been made on several materials. The analysis regards the standard materials currently adopted in advanced detectors; oxides, carbides and nitrides in order to replace the high-refractive index material; fluorides to investigate their possible application as low-refractive index material.

# CHAPTER 2

# AMORPHOUS SOLIDS

*"Crystals are like people: it is the defects in them which tend to make them interesting!"*

Colin J. Humphreys

Introduction to analytical electron microscopy, p.305 (1979)

This chapter gives a fundamental understanding of the atomic arrangement in amorphous structure that determines the macroscopic optical and mechanical properties of the solid and marks the difference with respect to crystals. The structure of amorphous materials is characterised by static and dynamic features.

The optical absorption of amorphous solids is determined by the structure arrangement, hence by the static properties, and is defined by three different regions of the absorption edge: (i) The main absorption region, described by the Tauc-Lorentz and Cody-Lorentz models; (ii) The absorption threshold, around the energy gap, described by the exponential Urbach behaviour. The extension of such tails gives information about the structure organization of the solid; (iii) The transitions which involve localized states inside the energy gap, near the Fermi's level, described by an exponential behaviour similar to the Urbach theory.

The structure of amorphous solids gives also important macroscopic mechanical properties. The interatomic forces and the structure of a glass determines its vibrational properties and hence its elastic constants.

The study of dynamic properties of solids can be performed by exploiting atomic vibrations to study the structure. Raman spectroscopy allows to obtain informations of atomic organization via the scattering process of light in the solid.

The structure of amorphous solids allows many equilibrium configurations in which atoms can be disposed. Thermal equilibrium is a dynamical equilibrium, where a continuous exchange between two levels exists, causing the thermal noise: this is the two-level system (TLS) model, where all the possible energy minima in the atomic configurations are represented by an asymmetric double-well potential. An external mechanical solicitation modifies the asymmetry of a TLS, changing its population, hence the elastic constants of the solid. The mechanical response is delayed by the relaxing process that occurs in order to bring the system back to equilibrium, causing dissipation which gives rise to thermal noise [5].

**The novelty presented in this chapter regards the calculus of the internal friction in a TLS, considering a general expression of the potential barrier.**

## 2.1 Structure

It is of fundamental importance to understand how to distinguish crystals from amorphous solids. There can be a considerable amount of confusion concerning the term 'disorder' as a definition of amorphous materials. In fact, in principle also crystalline solids have a disordered structure at any finite temperature, where the random motion of atoms about their equilibrium positions destroys the perfect periodicity of the lattice. Indeed, the concept of perfect crystal is valid only at absolute zero temperature. However, atoms at finite temperature are vibrating about their equilibrium crystalline positions and can not be considered as topologically disordered, where they should present differences from the equilibrium crystalline positions even at absolute zero temperature. In the following we will try to built a model to represent the structure of amorphous solids, considering that there are as yet no universally accepted definitions.

### 2.1.1 Topological Disorder

The main property that define the amorphous solids is the absence of a periodicity i.e. long-range (translational) order (LRO) of atomic structure. however, one may recognise a short-range order (SRO) preserved. This means that the local coordination in amorphous solid is similar to the corresponding crystal; the value of the first neighbour distance, coordination number or binding energy is more or less the same in the amorphous and crystalline phase [53]. Under this assumption it is possible to create two models to describe amorphous solids: the random network and the polycrystallite structure (figure 2.1).

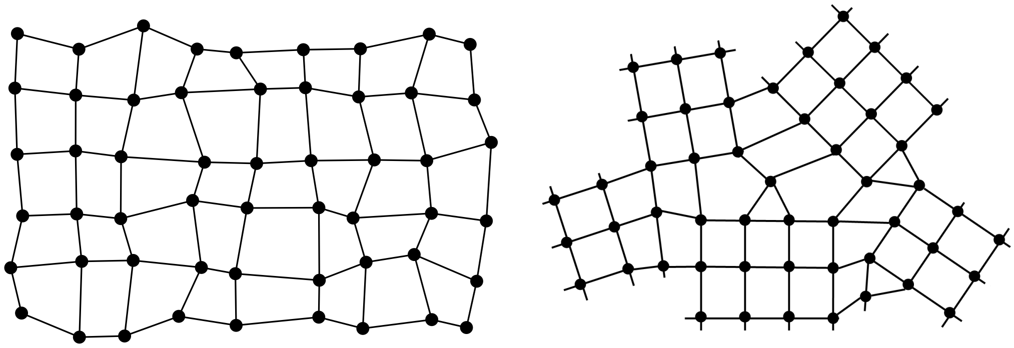

**(a)** Random Network. **(b)** Polycrystallite materials.

**Figure 2.1:** Possible representation of amorphous solids. Random network structure on the left and polycrystalline structure on the right.

**Random network:** This model is represented by a Gaussian distribution of the atomic positions around the crystalline mean value, varying distances and bonding angles. The resulting structure is a random distortion of the corresponding crystalline structure (figure 2.1a). This concept is interesting since it allows to develop the idea of a perfect amorphous solid; the distortions related to the Gaussian distributions of angles and distance give rise to the perfect amorphous solid, whereas the imperfections not related to the distributions, such as substitutional defects or dangling bonds, affect the ideal structure. In this sense, as happens for crystals, some properties are to associated to the ideal amorphous solid and the others are related to the imperfections [54].

**Polycrystallite:** In this model the structure is described by several crystalline grains, randomly oriented in different part of the lattice. The disordered connection between the crystalline domain breaks the LRO and the macroscopic properties of the solid depend to the properties of every single crystal. The size of the grains define the material as microcrystalline or nanocrystalline.

In both model the main feature is the absence of the LRO, however it is possible to recognise a SRO. In fact, X-ray or neutron diffraction measurements show a distribution of first-neighbours atoms positions around a mean value.

### 2.1.2 Radial Distribution Function

The technique that can be employed to obtain structural information for solids is the diffraction pattern, obtained by the scattering of neutron or X-ray when they interact with matter. As observed in figure 2.2a, in the presence of periodicity in atomic positions, if the incident beam has a wavelength comparable to the atomic dimensions, a constructive interference occurs for the scattered beam under the Bragg condition, giving information on the atomic positions. In amorphous solids the diffraction pattern should not give information about the structure because there is not a LRO, however, as observed in figures 2.2b and 2.2c, it is possible to recognize a SRO. The difference between polycrystalline and random network structure lies in their electron diffraction patters (sharpness and spottiness of rings) as well as in High Resolution Electron Microscopy (HREM). In order to quantify the information behind the diffraction pattern, a radial distribution function (RDF) can be defined as the average number of atoms lying between $r$ and $r + dr$ from the center of an arbitrary origin atom

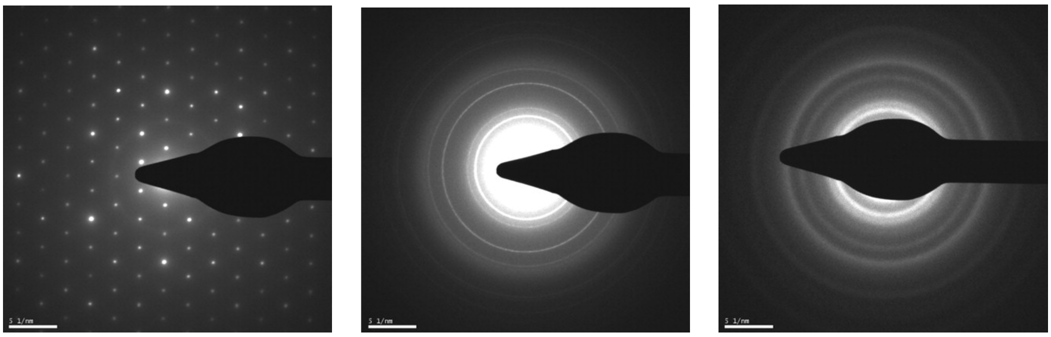

**(a)** Single-crystal gold. **(b)** Polycrystalline aluminum. **(c)** Amorphous carbon.

**Figure 2.2:** Ultrafast Electron Microscopy (UEM) diffraction patterns for single-crystal gold (a), polycrystalline aluminium (b) and amorphous carbon (c) [55].

$$J(r)dr = 4\pi r^2 \rho(r) dr \ , \tag{2.1}$$

where $\rho(r)$ is essentially a *pair correlation function*, which is large for distances where there are on average many atoms from a given origin atom, and small otherwise. In figure 2.3a there is a two-dimensional representation of $\rho(r)$ for an amorphous structure. It can be observed that the first peak corresponds to the first shell of atoms, the second peak to the second shell, and so on. It is important to note that both $\rho(r)$ and RDF (figure 2.3b) are a two-dimensional representation of a three-dimensional structure and then they can only carry a limited amount of structural information. The importance of the RDF is that the area under a given peak is related to the effective coordination

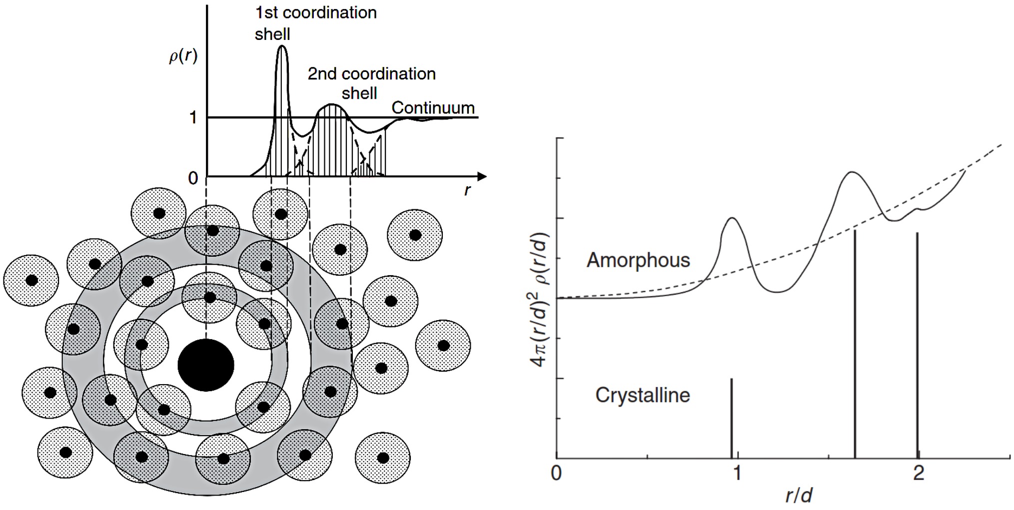

**(a)** Pair correlation function. **(b)** RDF.

**Figure 2.3:** a) the meaning of the pair correlation function $\rho(r)$ as function of radial distance from a given origin atom [56]. b) the RDF for amorphous and crystalline silicon with $sp^3$ configuration [57].

number of that particular shell. The position of the first peak gives a value for the nearest-neighbour bond length, furthermore, a broadened peak is related to the random distribution of atom positions around a mean value in amorphous solids or to the thermal vibrations in perfect crystals.

## 2.2 Properties Related to Structure

Once understood what are the elements that differ amorphous solids from crystals, it is possible to concentrate about the properties related to the random atomic positions, where the translational symmetry disappear but a SRO can be observed. In the following we will concentrate about properties related simply to the static of amorphous semiconductors structure.

### 2.2.1 Electronic Density of States

The lack of LRO breaks the translational symmetry so that the Block theorem is no longer valid, resulting in the wavevector k not being a good quantum number. In principle, the wavefunctions of electrons should not be extended in the whole lattice but limited to localized regions [58]. Under these considerations, one should suppose that the concept of energy bands is meaningless in amorphous solids. However, even if the LRO does not characterize amorphous materials it is possible to recognise a SRO. For covalent bond materials it is possible to assume that within the SRO a tight binding (TB) approximation is still valid, where the superposition of electronic orbitals are described by the first-neighbours distance and the extension of electronic wavefunctions. Using a TB approach, the bonding and antibonding states create a situation similar to the valence and conduction bands of a crystalline solid. These states are so closed to obtain quasi-continuum states called delocalized stated or extended states, separated by a gap. However, weak and strained bonds create bonding and anti-bonding states which lie close to the valence and conduction extended state edges respectively. Under this respect, the band edges broaden due to the disordered structure, creating tails inside the energy gap called Urbach tails. The first evidence of such localized tails states was observed by Urbach in absorption measurements [59] and then included in the electronic density of states (DOS) expressed by Mott [60]. Since the bonds related to the Urbach tails are strained and larger than those related to the extended states, the resulting states may not form quasi-continuum band, remaining localized. The edge separating the extended states and tail states is called the mobility edge. As the tail states are localized energy states, at 0°K conduction can only occur when excited electrons are in the extended states above the conduction tail states, and that defines the mobility edge [61].

In figure 2.4 there is a comparison of the DOS for crystalline and amorphous solids, where the mobility shows the localized stated in the case of amorphous solids.

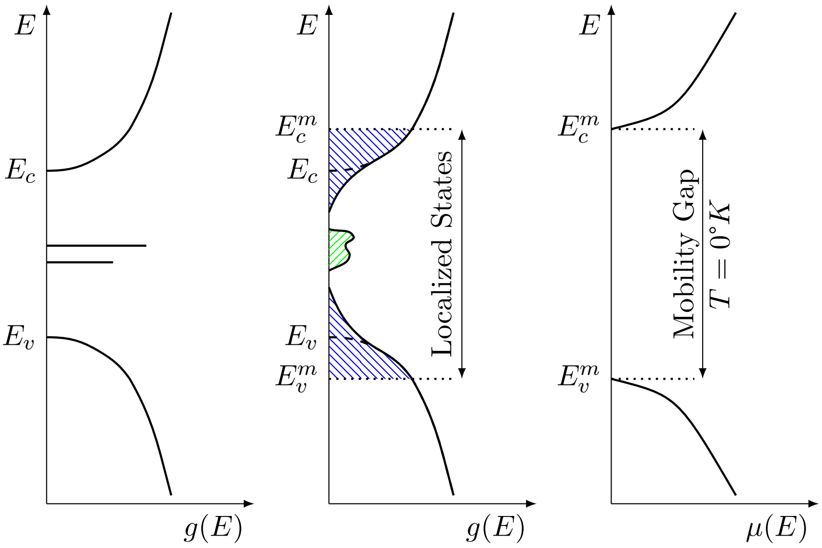

**(a)** Crystalline. **(b)** Amorphous. **(c)** Mobility.

**Figure 2.4:** DOS and mobility representation of amorphous semiconductor. On the left a) the DOS for crystalline solids, in the middle b) for amorphous solids. On the right c) the mobility related to each electronic state at 0°K is showed. Note that the conductivity depends on the position of the Fermi level. The features related to amorphous solids are exaggerated to obtain a more clear representation.

There are two mobility edges, electron mobility edge at the bottom of the conduction extended states $E_c^m$ and hole mobility edge at the top of valence extended states $E_v^m$. It is evident that amorphous solids presents localized states which extend into the gap due to the disorder, creating the Urbach tails (blue area in figure 2.4b). Furthermore, as it happens for crystals, local defects in amorphous solids like dangling bonds or substitutional atoms create states near the Fermi level at the centre of the gap (green area in figure 2.4b), which are localized and broadened due to the disorder. In this sense, since the disorder related to the Urbach tails creates states far from the Fermi level and near the extended states, it must be non-local and more complex with respect to the simple random atomic dispositions.

### 2.2.2 Optical Response

In order to understand the optical response of solids and obtain important properties like the refractive index or the absorption, the theory of propagation of light in matter must be introduced [62]. Starting from Maxwell equation in linear, homogeneous and isotropic (LHI) media and assuming $\mu_r = 1$, the electromagnetic-wave equation reads

$$\vec{\nabla}^2 \vec{E} = \frac{\varepsilon}{c^2}\frac{\partial^2 \vec{E}}{\partial^2 t} + \frac{\sigma}{\varepsilon_0 c^2}\frac{\partial \vec{E}}{\partial t} \, , \tag{2.2}$$

where $c = 1/\sqrt{\varepsilon_0 \mu_0}$ is the speed of light in vacuum, $\varepsilon_0 = 8.85 \cdot 10^{-12} C^2/Nm^2$ and $\mu_0 = 4\pi \cdot 10^{-7} Ns^2/C^2$ are the electric and magnetic permittivity in vacuum respectively, $\varepsilon$ is the relative dielectric function and $\sigma$ the electric conductivity. By assuming monochromatic plane-waves

$$\vec{E}(\vec{r}, t) = \vec{E}_0 e^{i(\omega t - \vec{q}\cdot\vec{r} + \delta)} \, , \tag{2.3}$$

where $\omega = 2\pi\nu$ is the radiation angular frequency and $\delta$ is the phase. From equation (2.2) one obtains the dispersion relation

$$q^2 = \left(\frac{\omega}{c}\right)^2 \left[\varepsilon - i\left(\frac{\sigma}{\varepsilon_0 \omega}\right)\right] = \left(\frac{\omega}{c}\right)^2 \tilde{\varepsilon} \, , \tag{2.4}$$

where $\tilde{\varepsilon} = \tilde{\varepsilon}_1 - i\tilde{\varepsilon}_2$ is the complex dielectric function and describes the macroscopic optical properties of matter. From equation (2.4) it is clear that $\tilde{\varepsilon}$ consists in two terms. The first, related to the electric charge described by the Lorentz model, can be expressed as

$$\varepsilon = 1 + \frac{P}{\varepsilon_0 E} = 1 + \chi \, , \tag{2.5}$$

where $P$ is the polarization and $\chi$ the electric susceptibility. The second term $\left(\frac{\sigma}{\varepsilon_0 \omega}\right)$ is related to the free carrier described by the Drude model.

In order to describe the propagation and absorption phenomena it is useful to use a complex quantity strictly linked to the dielectric function, which is made on measurable quantity. This complex quantity is the refractive index

$$N = n - ik = \sqrt{\tilde{\varepsilon}} = \sqrt{\varepsilon - i\left(\frac{\sigma}{\varepsilon_0 \omega}\right)} \, , \tag{2.6}$$

where $n$ is the real part of the refractive index and $k$ is the extinction coefficient. It is possible to express the real and imaginary part of $\tilde{\varepsilon}$ in term of $n$ and $k$:

$$\tilde{\varepsilon}_1 = n^2 - k^2 \, , \tag{2.7a}$$

$$\tilde{\varepsilon}_2 = 2nk \, . \tag{2.7b}$$

Usually the models describe the quantity $\tilde{\varepsilon}_2$ and it is possible to demonstrate that $\tilde{\varepsilon}_1$ can be derived from $\tilde{\varepsilon}_2$. This can be done using the Kramers-Kronig relations [63]

$$\tilde{\varepsilon}_1(\omega) = 1 + \frac{2}{\pi}\mathcal{P}\int_0^\infty \frac{\omega' \tilde{\varepsilon}_2(\omega')}{\omega'^2 - \omega^2} d\omega' \, , \tag{2.8a}$$

$$\tilde{\varepsilon}_2(\omega) = -\frac{2\omega}{\pi}\mathcal{P}\int_0^\infty \frac{\tilde{\varepsilon}_1(\omega') - 1}{\omega'^2 - \omega^2} d\omega' \, , \tag{2.8b}$$

where $\mathcal{P}$ denotes the Cauchy principal value

$$\mathcal{P}\int_0^\infty d\omega' \equiv \lim_{\delta \to 0}\left(\int_0^{\omega-\delta} d\omega' + \int_{\omega+\delta}^\infty d\omega'\right) \, . \tag{2.9}$$

### 2.2.3 Optical Absorption

The optical and conduction properties of solids are characterized by the behaviour of the DOS. Indeed, the localized states are crucial not only for the conductivity but also for the optical absorption. Since the optical transitions regard also localized states, they are useful in order to study the DOS of amorphous solids. Indeed, it is almost impossible to study the individual contribution of the elements that cause the disorder and for that reason, it is useful to study the quantity which gives information related to the population of the localized states like the absorption coefficient. In the case of amorphous solids, the theory of optical transitions due to the absorption of photons is similar to the crystalline solids, with the constraint that $k$ is no longer a good quantum number and only direct transitions are allowed. In figure 2.5 there is the typical behaviour of the absorption near the absorption edge for an amorphous solid.

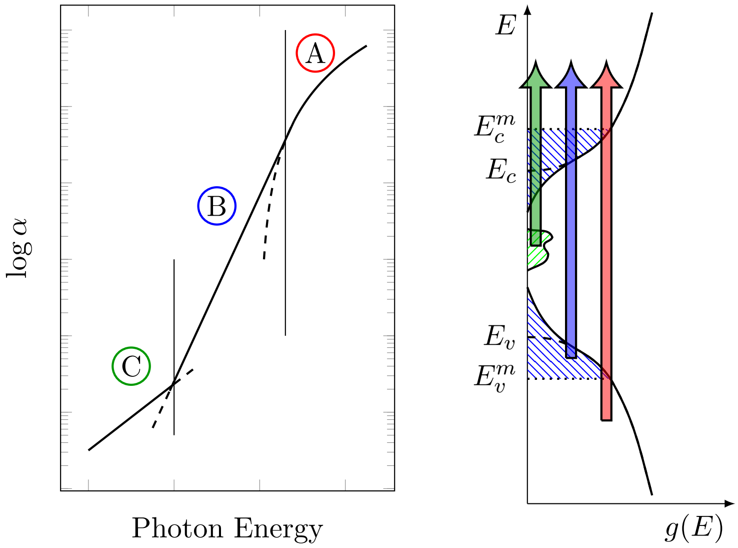

**(a)** Absorption. **(b)** Optical transitions.

**Figure 2.5:** (a) Typical behaviour of the absorption for amorphous solids in logarithmic scale. The three regions A, B and C are associated to the transitions involving different energy states. (b) The different allowed transitions. The red arrow highlights the transition contributing to the region A of the absorption, the blue one the region B and the green one the region C.

looking at figure 2.5a it is possible to distinguish three different regions [54] which are associated to the transitions between different states, as pointed out in figure 2.5b. Note that the transitions involving only localized states gives a very low optical absorption and are not discussed here.

### Region A

In the high energy region the absorption is produced by the transitions between extended states. Since $\vec{k}$ is not a good quantum number, in order to obtain the expression of one photon absorption $\alpha$, we should consider only the energy and momentum conservation laws. Considering the expression of the electric potential vector

$$\vec{A} = A\hat{e}, \text{ with } A = -\frac{F}{2q}(e^{i(\vec{q}\cdot\vec{r}-\omega t)} + c.c.) \,, \tag{2.10}$$

where $\hat{e}$ is the polarization and $F$ the electric field modulus, the absorbed power $W$ over the unit volume, can be expressed as a variation of the intensity $I = (nF)^2/(8\pi)$ over the time

$$W = R\hbar\omega = -\frac{dI(x)}{dt} = -\frac{dI(x)}{dx}\frac{dx}{dt} = \alpha\frac{c}{n}I\,, \tag{2.11}$$

where $c$ is the speed of light, $c/n$ is the phase velocity of the radiation in matter and $R$ is the probability of the transition. This probability can be obtained by the Fermi's golden rule, expressed as function of the photon energy $E = \hbar\omega$,

$$R = \frac{2\pi}{\hbar\Omega}\sum_{E'_c,E'_v}\left|\left\langle 1, E'_c|\hat{H}_I|0, E'_v\right\rangle\right|^2 \delta(E'_c - E'_v - E)\,, \tag{2.12}$$

where $\Omega$ is the irradiated volume, $E'_v$ and $E'_c$ are the two energy states where the transition occurs and $\hat{H}_I$ is the Hamiltonian of the interaction

$$\hat{H}_I = -\frac{e}{m_e^* c}\vec{A}\cdot\vec{p}\,, \tag{2.13}$$

where $\vec{p}$ the momentum for an electron of effective mass $m_e^*$. Under this consideration, equation (2.12) reads

$$R = \frac{2\pi}{\hbar\Omega}\left(\frac{e}{m_e^*\omega}\right)^2\left(\frac{F}{2}\right)^2\sum_{E'_c,E'_v}\left|\langle 1, E'_c|\hat{e}\cdot\vec{p}|0, E'_v\rangle\right|^2 \delta(E'_c - E'_v - E)\,. \tag{2.14}$$

It is now possible to express the absorption

$$\alpha = \frac{R\hbar\omega}{I(c/n)} = \frac{1}{nc}\left(\frac{2\pi e}{m_e^*}\right)^2\left(\frac{1}{\Omega\omega}\right)\sum_{E'_c,E'_v}|p_{cv}|^2\,\delta(E'_c - E'_v - E)\,, \tag{2.15}$$

where $|p_{cv}| = |\langle 1, E'_c|\hat{e}\cdot\vec{p}|0, E'_v\rangle|$ is the matrix dipole element. By considering all the possible states

$$\alpha = \frac{1}{nc}\left(\frac{2\pi e}{m_e^*}\right)^2\left(\frac{1}{\Omega\omega}\right)\int_{E_c}^{E_v+E} g_c(E'_c)\int_{E-E_v}^{E_v} g_v(E'_v)\,|p_{cv}|^2\,\delta(E'_c - E'_v - E)dE'_v dE'_c\,, \tag{2.16}$$

where $g_c(E'_c)$ and $g_v(E'_v)$ are the DOS of the conduction and valence band respectively. If we assume that the matrix element does not depend on the initial and final states, $|p_{cv}|$ can be considered constant. Considering the delta function we can integrate over the valence states to get

$$\alpha = \frac{1}{nc}\left(\frac{2\pi e}{m_e^*}\right)^2\left(\frac{1}{\Omega\omega}\right)|p_{cv}|^2\int_{E_c}^{E_v+E} g_c(E'_c)g_v(E'_c - E)dE'_c\,. \tag{2.17}$$

Furthermore, assuming a dependence of $g(E)$ by some power of $E$ [64]

$$g_c(E) = \frac{(E - E_c)^{r_1}}{(E_c^m - E_c)^{r_1}}g_c^0 \tag{2.18}$$

$$g_v(E) = \frac{(E_v - E)^{r_2}}{(E_v - E_v^m)^{r_2}}g_v^0\,, \tag{2.19}$$

where $E_c^m - E_c = E_v - E_v^m = \Delta E$ is the band-tail width in the extended states due to disorder. In the case of identical bands $r_1 = r_2 = r$, we obtain[1]

$$\alpha = \frac{1}{nc}\left(\frac{2\pi e}{m_e^*}\right)^2\left(\frac{1}{\Omega\omega}\right)|p_{cv}|^2\frac{g_c^0 g_v^0}{\Delta E^{2r}}\int_{E_c}^{E_v+E}(E' - E_c)^r(E_v + E - E')^r dE'\,. \tag{2.20}$$

---

[1] We changed the name of the variable to integrate $E'_c \to E'$.

The integral can be calculated using the Eulero's Gamma function, $\Gamma(n) = (n-1)!$,

$$\alpha = \frac{1}{nc}\left(\frac{2\pi e}{m_e^*}\right)^2\left(\frac{1}{\Omega\omega}\right)|p_{cv}|^2\, g_c^0 g_v^0 \frac{(E-E_g)^{2r+1}}{\Delta E^{2r}}\frac{(\Gamma(r+1))^2}{\Gamma(2r+2)}\,. \tag{2.21}$$

Assuming parabolic bands ($r = 1/2$), we obtain the Tauc model [54]

$$\alpha(E)n(E) \propto \frac{(E-E_g)^2}{E}\,, \tag{2.22}$$

where $E = \hbar\omega$. Using equation (2.22), it is possible to evaluate the so called *Tauc Plot* $(\alpha(E)n(E)E)^{1/2}$ as function of the energy $E$. In other words, the Tauc Plot is based on the linearization of equation (2.22) and allows to determine the energy gap $E_g$. In some experiments it has been observed that there are materials which do not follow the Tauc behaviour but that can be represented by a cubic law [65] [66]. In this case, the Davis-Mott model can be used in order to represent the absorption, where $r = 1$

$$\alpha(E)n(E) \propto \frac{(E-E_g)^3}{E}\,. \tag{2.23}$$

It has to be noticed that the expressions (2.22) and (2.23) have been derived by assuming the matrix element $|p_{cv}|$ not dependent on the photon energy, even though the matrix element $|p_{cv}|$ has the dimension of momentum, and therefore it does not appear to be justified to assume it independent of momentum and energy. However, there are two methods to evaluate the matrix element. In Mott and Davis (1979) [61] method it appears to be justified to assume $|p_{cv}|$ constant, obtaining the Tauc behaviour. On the other hand Cody *et al.* (1984) [67] have demonstrated that it is not independent from the photon energy. Under this respect, it is possible to obtain the absorption by using the conjugate of the operator momentum [67]

$$\vec{p} = i\frac{m_e^*}{\hbar}[\hat{H},\vec{x}]\,, \tag{2.24}$$

and it can be shown that the momentum matrix element $|p_{cv}|$ depends on the initial and final energy

$$\begin{aligned} p_{cv} &= \left\langle 1, E_c'|\hat{e}\cdot\vec{p}|0, E_v'\right\rangle \\ &= i\frac{m_e^*}{\hbar}\left(\left\langle 1, E_c'|\hat{H}\hat{e}\cdot\vec{x}|0, E_v'\right\rangle - \left\langle 1, E_c'|\hat{e}\cdot\vec{x}\hat{H}|0, E_v'\right\rangle\right) \\ &= i\frac{m_e^*}{\hbar}(E_c' - E_v')\left\langle 1, E_c'|\hat{e}\cdot\vec{x}|0, E_v'\right\rangle \\ &= i\frac{m_e^*}{\hbar}(E_c' - E_v')x_{cv}\,, \end{aligned} \tag{2.25}$$

where $x_{cv}$ is the dipole matrix element. In this sense, the dipole matrix element can be treated as independent to the energy, following the Cody model. If we consider parabolic bands, the absorption obtained from equation (2.16) reads

$$\alpha(E)n(E) \propto E(E-E_g)^2\,. \tag{2.26}$$

Using equation (2.26) we can evaluate the *Cody Plot* $(\alpha(E)n(E)/E)^{1/2}$ where the energy gap $E_g$ can be extrapolated.

Two different methods can be used to evaluate the absorption behaviour for amorphous solids in the main absorption region. In both cases a parabolic trend of the DOS is considered. Furthermore, the constant momentum matrix element is assumed by the Tauc model, whereas the constant dipole matrix element is assumed by the Cody model. Considering the relation between the imaginary part of the dielectric function and the absorption $\varepsilon_2 = cn\alpha/\omega$, where $n$ is the refractive index, we obtain

$$\text{TAUC} \qquad \varepsilon_2(E) \propto \frac{(E-E_g)^2}{E^2} \,, \tag{2.27a}$$

$$\text{CODY} \qquad \varepsilon_2(E) \propto (E-E_g)^2 \,. \tag{2.27b}$$

The distinction between $(\alpha/E)^{1/2}$ and $(\alpha E)^{1/2}$ as a definition of $E_g$ is important only when films of widely differing thicknesses are compared. These two formulas give identical results if one considers only changes in $E_g$ for the same film [67].

**Region B**

A seminal work by F. Urbach pointed out a near-edge exponential increase of the absorption coefficient with the photon energy [59]. Such so-called Urbach edge is related to Gaussian distribution of disorder in the structure (bond lengths and angles) giving an exponential broadening of the DOS and the creation of localized electronic states (Anderson's states [58]) routinely observed by optical absorption in crystalline and amorphous semiconductors [68]. The Urbach behaviour of the absorption edge in amorphous semiconductors is assigned to transitions between localized and delocalized electronic state. The typical optical transitions observed by our system in the DOS, regard the transitions between the initial localized state in the exponential valence band tail and the extended state in the conduction band. The exponential absorption edge can be obtained from equation (2.17), where the DOS has an exponential trend [54]

$$g_t(E) = g_t^0 e^{(E-E_0^m)/E_U} \,, \tag{2.28}$$

where $g_t^0$ is defined by the continuity condition $g_t^0 = g(E_0^m)$, with $g(E_0^m)$ the density of state of continuous band evaluated at the mobility edge $E_0^m$ and the Urbach energy $E_U$ characterizes the energy spread of the tail decay into the gap due to lattice disorder. Assuming the Mott and Davis (1979) [61] theory for the matrix element $|p_{cv}|$ and parabolic conduction band, the absorption coefficient which describes this transition reads

$$\alpha(E) \propto e^{(E-E_0^m)/E_U} \,. \tag{2.29}$$

Recent works [69, 70] have pointed out a relation between Urbach broadening and the topological organization emerging of defects, where weakly-strained regions are clustered. The Urbach energy is usually considered as made on three terms [71]

$$E_U = (E_U)_T + (E_U)_X + (E_U)_C \,, \tag{2.30}$$

where $(E_U)_T$, $(E_U)_X$ and $(E_U)_C$ are the contributions of the temperature disordering, structural disordering, and compositional disordering, respectively. The temperature disordering is mainly caused by the lattice thermal vibrations. The structural disordering can be related to intrinsic defects of structure, e.g. vacancies or dislocations, or induced by deviation from stoichiometry, doping, ion implantation, hydrogenation, etc. The compositional disordering is caused by atomic substitution in mixed crystals.

Ab-initio structural simulation in amorphous Silicon highlighted the atomistic origin of Urbach tails [69, 72] associated to the existence of particularly extended atomic topological organization and more interestingly, such structural topological organization is connected to structural relaxation in the presence of disorder. Some theoretical works investigate the correlation between Urbach tails, electronic DOS, atomic structure and morphology. Interesting results are obtained by atomistic modelling of amorphous silicon [69]: molecular dynamics methods show that the reorganization of the simulated structure, after artificially introducing a defect, generates an exponential valence tail in the electronic DOS. In order to observe the extension of the electronic state, the inverse participation ratio (IPR) quantifies the number of single atom wave functions needed to create the Anderson state. Under this respect, near the valence and conduction band edge, the energetic levels refer to more complex and extended structural organization whereas, approaching the Fermi level, the energetic levels refer to more localized defects. Therefore, less-organized structure presents topological defects extended in a medium-long range and the Urbach tails are more broadened. This means that by measuring the extension of the Urbach tails it is possible to obtain information about the structure organisation at medium-long range. In this view, Urbach tails represent a simple, meaningful way to visualize the impact of defects disorder, in a multi-range perspective not limited to short-range or medium-range, on amorphous oxide coatings.

**Region C**

This region is characterized by the optical transitions between localized and extended states, not involving the Urbach tails. The levels involved are near the Fermi levels corresponding to very localized defects such as dangling bond or variation in coordination number. Also in that case, the absorption has exponential behaviour

$$\alpha \propto e^{E/E_d} \, , \tag{2.31}$$

where $E_d$ is always higher than $E_U$ and is strictly related to the short-range organization of the structure.

### 2.2.4 Elastic Response

The elastic response of solids can be studied considering the deformation of the solid under an external solicitation. Under this condition, as observed in figure 2.6, the generic point $P$, identified by the vector $\vec{r} = (x_1, x_2, x_3)$, will move to the point $P'$, identified by the vector $\vec{r}' = (x'_1, x'_2, x'_3)$ [73]. The vector $\vec{u} = \vec{r}' - \vec{r}$ is called *displacement vector*.

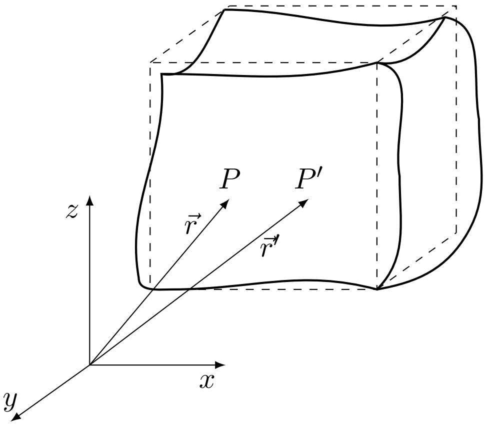

**Figure 2.6:** Deformation of the solid under external force. During the deformation, the point $p$ will move to the point $P'$.

Considering a second point $Q$ close to $P$, it is possible to evaluate the distance $PQ$ after the deformation. If we call $dx_i$ and $dx'_i$ $(i = 1, 2, 3)$ the difference between the coordinates of $P$ and $Q$ before and after the deformation, respectively, we obtain[2]

$$dl^2 = dx_i^2 \qquad\qquad dl'^2 = dx_i'^2 = (dx_i + du_i)^2 \, ,$$

via the change in coordinates $du_i = \frac{\partial u_i}{\partial x_k} dx_k$, we obtain

$$dl'^2 = dl^2 + \frac{\partial u_i}{\partial x_k}\frac{\partial u_i}{\partial x_l} dx_k dx_l + \frac{\partial u_i}{\partial x_k} dx_i dx_k + \frac{\partial u_k}{\partial x_i} dx_i dx_k = dl^2 + 2u_{ik} dx_i dx_k \, ,$$

where $u_{ik}$ is the so-called *strain tensor*

$$u_{ik} = \frac{1}{2}\left(\frac{\partial u_i}{\partial x_k} + \frac{\partial u_k}{\partial x_i} + \frac{\partial u_l}{\partial x_i}\frac{\partial u_l}{\partial x_k}\right) \, . \tag{2.32}$$

Under the small deformations condition, the relation (2.32) can be written considering only the linear terms

$$u_{ik} = \frac{1}{2}\left(\frac{\partial u_i}{\partial x_k} + \frac{\partial u_k}{\partial x_i}\right) \, . \tag{2.33}$$

After the deformation, if the solid were in equilibrium, internal forces appear in order to bring the system back to the equilibrium. These forces are called *internal stress* and are due to the molecular interactions[3]. The action-reaction principle states that each internal stress has to be balanced. For this reason, the total force on the solid consists of superficial forces only, which can be expressed by the gradient of a high-order tensor, so that

$$\int_V F_i dV = \int_V \frac{\partial \sigma_{ik}}{\partial x_k} dV = \oint_A \sigma_{ik} n_k dA \, , \tag{2.34}$$

where $n_i$ are the normal components to the surfaces and $\sigma_{ik}$ is the so-called *stress tensor*. In order to obtain the link between the strain and the stress tensors, it is useful to introduce the free energy of the system $F = \mathfrak{E} - TS$, where $T$ is the temperature, $S$ the entropy and $\mathfrak{E}$ the internal energy

$$d\mathfrak{E} = TdS - dL = Tds + \sigma_{ik} du_{ik} \, . \tag{2.35}$$

We can then write

$$dF = \sigma_{ik} du_{ik} - SdT \, . \tag{2.36}$$

From the relation (2.35) and (2.36) we obtain

$$\sigma_{ik} = \left(\frac{\partial \mathfrak{E}}{\partial u_{ik}}\right)_S = \left(\frac{\partial F}{\partial u_{ik}}\right)_T \, . \tag{2.37}$$

We obtained that the stress is related to the change of the internal energy of the system with respect to the deformation. It is possible to show that if we express the free energy in power of $u_{ik}$, we can discriminate between two terms related only to *shear* deformation and *hydrostatic compression* (i.e. bulk deformations)

$$F = F_0 + \frac{\lambda}{2} u_{ii}^2 + \mu u_{ik}^2 \, , \tag{2.38}$$

where $\lambda$ and $\mu$ are the *Lamé coefficients.* In particular we can discriminate between:

- *Shear:* $u_{ii} = 0$ :
  Change the shape but not the volume (figure (2.7a)).
- *Compression:* $u_{ik} \propto \delta_{ik}$ :
  Change the volume but not the shape (figure (2.7b)).

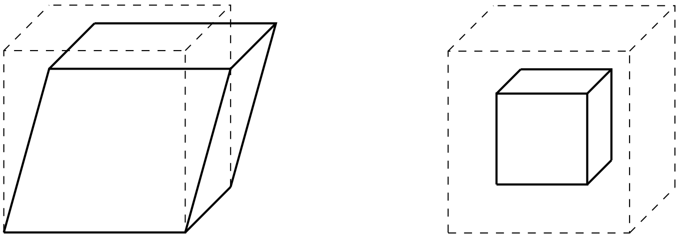

**(a)** Shear. **(b)** Compression.

**Figure 2.7:** (a) Example of shear deformation. (b) Example of bulk deformation.

Therefore, the strain tensor can be expressed by

$$u_{ik} = (u_{ik} - \frac{1}{3}\delta_{ik}u_{ll}) + \frac{1}{3}\delta_{ik}u_{ll} \, , \tag{2.39}$$

where the first term is the pure shear deformation and the second is the bulk term. Using the relation (2.39) in (2.38) we obtain

$$\begin{aligned} F &= F_0 + \frac{\lambda}{2}u_{ii}^2 + \mu(u_{ik} - \frac{1}{3}\delta_{ik}u_{ll})^2 + \frac{1}{9}(\delta_{ik}u_{ll})^2 \\ &= F_0 + \mu(u_{ik} - \frac{1}{3}\delta_{ik}u_{ll})^2 + \frac{1}{2}(\lambda + \frac{2}{3}\mu)u_{ll}^2 \\ &= F_0 + \mu(u_{ik} - \frac{1}{3}\delta_{ik}u_{ll})^2 + \frac{1}{2}Ku_{ll}^2 \, , \end{aligned} \tag{2.40}$$

where $\mu$ are $K$ are the *shear modulus* and the *bulk modulus*, respectively. From equation (2.40) it is possible to obtain the stress tensor as function of the strain tensor[4]

$$\begin{aligned} dF &= 2\mu(u_{ik} - \frac{1}{3}\delta_{ik}u_{ll})d(u_{ik} - \frac{1}{3}\delta_{ik}u_{ll}) + Ku_{ll}du_{ll} \\ &= 2\mu(u_{ik} - \frac{1}{3}\delta_{ik}u_{ll})du_{ik} + Ku_{ll}du_{ll} \\ &= [2\mu(u_{ik} - \frac{1}{3}\delta_{ik}u_{ll}) + Ku_{ll}\delta_{ik}]du_{ik} \, , \end{aligned} \tag{2.41}$$

and finally

$$\sigma_{ik} = 2\mu(u_{ik} - \frac{1}{3}\delta_{ik}u_{ll}) + Ku_{ll}\delta_{ik} \, , \tag{2.42}$$

which defines the stress tensor for isotropic solids. We can use the relation (2.42) in order to express the strain tensor as function of the stress

$$u_{ik} = \frac{1}{9K}\delta_{ik}\sigma_{ll} + \frac{1}{2\mu}(\sigma_{ik} - \frac{1}{3}\delta_{ik}\sigma_{ll}) \, . \tag{2.43}$$

The equation (2.43) is the well known Hooke's law, where the strain is proportional to the applied force.

### Homogeneous Deformations

During a homogeneous deformation, the tensor $u_{ik}$ is constant over all the volume of the solid. We can consider a simple extension of a rod, represented in figure (2.8). If

---

[2] The sum over repeated index is adopted: $dl^2 = dx_i^2 = dx_1^2 + dx_2^2 + dx_3^2$.

[3] Usually, the deformations under consideration are small with respect to the macroscopic system and large with respect to the atomic interactions.

[4] The arbitrary constant term $F_0$ has been put to zero.

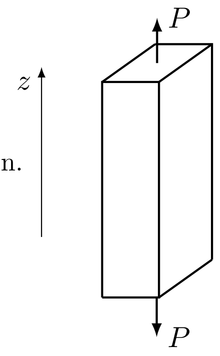

**Figure 2.8:** Traction of a rod along the $z$-direction.

we consider only the force along the $n_z$ direction, represented by a uniform force on unit area $p$, it follows that all the components $\sigma_{ki}$ except $\sigma_{zz}$ are zero

$$\sigma_{zi} n_i = p \qquad \Rightarrow \qquad \sigma_{zz} = p \, . \tag{2.44}$$

From equation (2.43) we obtain

$$u_{ik} = 0 \quad \text{per } i \neq k \tag{2.45a}$$

$$u_{xx} = u_{yy} = -\frac{1}{3} p \left( \frac{1}{2\mu} - \frac{1}{3K} \right) \tag{2.45b}$$

$$u_{zz} = \frac{1}{3} p \left( \frac{1}{\mu} + \frac{1}{3K} \right) \, . \tag{2.45c}$$

The term along the $z$-direction (2.45c) of the strain tensor defines the relative lengthening of the rod,

$$u_{zz} = \frac{p}{Y} \qquad \text{with} \qquad Y = \frac{9K\mu}{3K + \mu} \, , \tag{2.46}$$

where $Y$ is the so-called *Young's modulus*. The $x$ and $y$ terms (2.45b) represent the relative compression of the rod in the transverse directions. The ratio of the transverse compression to the longitudinal extension is called *Poisson's ratio*:

$$\sigma = -\frac{u_{xx}}{u_{zz}} = -\frac{u_{yy}}{u_{zz}} = \frac{1}{2} \frac{3K - 2\mu}{3K + \mu} \, . \tag{2.47}$$

From equation (2.46) and (2.47) it is possible to express the Lamé coefficient as function of $Y$ and $\sigma$,

$$\begin{aligned} \mu &= \frac{Y}{2(1+\sigma)} \\ K &= \frac{Y}{3(1-2\sigma)} \, . \end{aligned} \tag{2.48}$$

Therefore, the expression (2.43) can be written as

$$u_{ik} = \frac{1}{Y} \left[ (1+\sigma) \sigma_{ik} - \sigma \sigma_{ll} \delta_{ik} \right] , \tag{2.49}$$

which in matrix notation is $\hat{u} = \mathbf{J} \hat{\sigma}$,

$$\begin{pmatrix} u_{xx} \\ u_{yy} \\ u_{zz} \\ u_{yz} \\ u_{zx} \\ u_{xy} \end{pmatrix} = \begin{pmatrix} \frac{1}{Y} & -\frac{\sigma}{Y} & -\frac{\sigma}{Y} & 0 & 0 & 0 \\ -\frac{\sigma}{Y} & \frac{1}{Y} & -\frac{\sigma}{Y} & 0 & 0 & 0 \\ -\frac{\sigma}{Y} & -\frac{\sigma}{Y} & \frac{1}{Y} & 0 & 0 & 0 \\ 0 & 0 & 0 & \frac{1+\sigma}{Y} & 0 & 0 \\ 0 & 0 & 0 & 0 & \frac{1+\sigma}{Y} & 0 \\ 0 & 0 & 0 & 0 & 0 & \frac{1+\sigma}{Y} \end{pmatrix} \begin{pmatrix} \sigma_{xx} \\ \sigma_{yy} \\ \sigma_{zz} \\ \sigma_{yz} \\ \sigma_{zx} \\ \sigma_{xy} \end{pmatrix} , \tag{2.50}$$

where **J** is the so-called *compliance* and the ratio $\frac{1+\sigma}{Y}$ is the inverse of the shear modulus $G = 1/2\mu$. For non-isotropic solids

$$\begin{pmatrix} u_{xx} \\ u_{yy} \\ u_{zz} \\ u_{yz} \\ u_{zx} \\ u_{xy} \end{pmatrix} = \begin{pmatrix} \frac{1}{Y_x} & -\frac{\sigma_{xy}}{Y_y} & -\frac{\sigma_{zx}}{Y_z} & 0 & 0 & 0 \\ -\frac{\sigma_{xy}}{Y_x} & \frac{1}{Y_y} & -\frac{\sigma_{yz}}{Y_z} & 0 & 0 & 0 \\ -\frac{\sigma_{zx}}{Y_x} & -\frac{\sigma_{yz}}{Y_y} & \frac{1}{Y_z} & 0 & 0 & 0 \\ 0 & 0 & 0 & G_{yz} & 0 & 0 \\ 0 & 0 & 0 & 0 & G_{zx} & 0 \\ 0 & 0 & 0 & 0 & 0 & G_{xy} \end{pmatrix} \begin{pmatrix} \sigma_{xx} \\ \sigma_{yy} \\ \sigma_{zz} \\ \sigma_{yz} \\ \sigma_{zx} \\ \sigma_{xy} \end{pmatrix} . \tag{2.51}$$

**Structural Changes**

The interatomic forces and the structure of a glass determine its vibrational properties and hence its elastic constants. The Poisson's ratio is directly related to the bulk and shear modulus ratio, as expressed by the equation (2.47), which is found to decrease after structural relaxation and increase under pressure. Under this respect, the behaviour of $K/\mu$ of a metallic glass indicates a very different change of the structure. It has been demonstrated that this ratio depends on microscopic and macroscopic properties. A model based on a Gaussian distribution for the nearest-neighbour atomic distance has been used to describe qualitatively the structural changes responsible for the Poisson's ratio behaviour [74]. The approach is based on the assumption of a Gaussian radial distribution function (RDF) for the atomic positions and that the elastic properties are determined by the immediate surroundings of the atoms, without considering the contributions of the atomic configuration further than the first shell

$$RDF(r) = \frac{r}{(2\pi)^{1/2}} \frac{N_1}{r_1\gamma_1} \left( \exp\left[ -\frac{(r-r_1)^2}{2\gamma_1^2} \right] \right) , \tag{2.52}$$

where $N_1$ is the number of atoms, $r_1$ the mean position and $\gamma_1$ the the width of the Gaussian for the atoms in the first shell, around a central atom.

To describe the macroscopic properties, an interatomic potential with harmonic and anharmonic terms has been used

$$U(r) = a(r-r_m)^2 + b(r-r_m)^3 , \tag{2.53}$$

where $a > 0$, $b < 0$ and $r_m$ the position of the minimum. In particular, the region of interest in order to use $U(r)$ and $RDF(r)$ is within the interval $r_m - \gamma_1 < r < r_m + \gamma_1$.

Finally, the bulk and shear ratio becomes [74]

$$\frac{K}{\mu} = \frac{5}{3} \left[ 1 + \frac{3}{2} \frac{\langle \sum r_k U'(r_k) \rangle}{\langle \sum r_k^2 U''(r_k) \rangle} \right]^{-1} , \tag{2.54}$$

where

$$\left\langle \sum r_k U'(r_k) \right\rangle = \int_0^\infty rU'(r)RDF(r)dr \tag{2.55}$$

$$\left\langle \sum r_k^2 U''(r_k) \right\rangle = \int_0^\infty r^2U''(r)RDF(r)dr \tag{2.56}$$

and $r_k$ is the position of a central atom $k$ in the undeformed situation.

## 2.3 Structure Dynamics

In the previous section we analysed the response of an amorphous solid related to the static properties of its structure. In this section we are going to analyse how the response is related to the dynamic properties of the structure. We will see how the interaction of light with a vibrating structure, allows to obtain information about the structure of solids. Furthermore, we will see how the elasticity of amorphous solids relaxation phenomena and in particular how the mechanical losses and, consequently, the thermal noise, depend on these relaxations.

### 2.3.1 Vibrational Spectroscopy

The interaction of light with matter can be mainly described by absorption and scattering. The former has been explained in section 2.2, the latter occurs when the light interacts and distorts the cloud of electrons round the nuclei, with a consequently released energy in the form of scattered radiation. In particular, Rayleigh scattering, occurs when the electron cloud relaxes without any nuclear movement. This is essentially an elastic process and there is no appreciable change in energy. Raman scattering on the other hand occurs when the light and the electrons interact and the nuclei begin to move at the same time. In this case the nuclei are much heavier than the electrons, hence there is an appreciable change in energy of the molecule. The final photon energy will be lower for Stokes scattering, where the process starts with a molecule in the ground state and obtains vibrational energy from the radiation, or higher for anti-Stokes scattering, where the excited molecule transfers its energy to the photon when it returns to its fundamental state. The relative intensities of the two processes depend on the population of the various states of the molecule and at room temperature, the number of molecules expected to be in an excited vibrational state will be small and it is possible to verify that the intensity related to Stokes radiation is higher than that of Anti-Stokes, explaining why Stokes radiation is usually used.

In Raman spectroscopy a monochromatic radiation is focussed on the sample and the intensity of the scattered radiation is detected as function of frequency. Raman spectrum gives the frequencies of the resonant modes of the structure at the molecular level (at least all the modes that are Raman active). A model needs to be developed in order to identify the specific modes from the frequency detected by the Raman spectrum. Usually, the intensity in a Raman spectrum is plotted as function of the Raman shift expressed in $cm^{-1}$, which corresponds to the difference in frequency between the scattered light $\nu_s$ and the incident radiation $\nu_0$, normalized by the speed of light $c$

$$\text{Raman shift} = \frac{\nu_0 - \nu_s}{c} \, . \tag{2.57}$$

### 2.3.2 Two-Level Systems

We will see here how the disorder is able to determine the elastic and anelastic response of an amorphous solid.

Mechanical response of ideal solids is described by the Hooke law. This instantaneous reaction to external solicitations does not manifest entirely in real solids, where relaxation of some internal quantity take place [75]. In amorphous solids the structure allows several equilibrium configurations giving interesting characteristics which differ from crystals, like the specific heat and thermal conductivity at low temperature [76–78]. The study of these several configurations is based on a pure theoretical representation known as two-level system (TLS), where two different asymmetric local minimum of the energy landscape separated by a barrier energy are considered and the system will be able to switch between these levels thanks to certain given energy, such as the temperature, or by tunnelling effect at low temperature. In this sense, the two equilibrium states are described by an asymmetric double-well potential (ADWP) [79] showed in figure 2.9

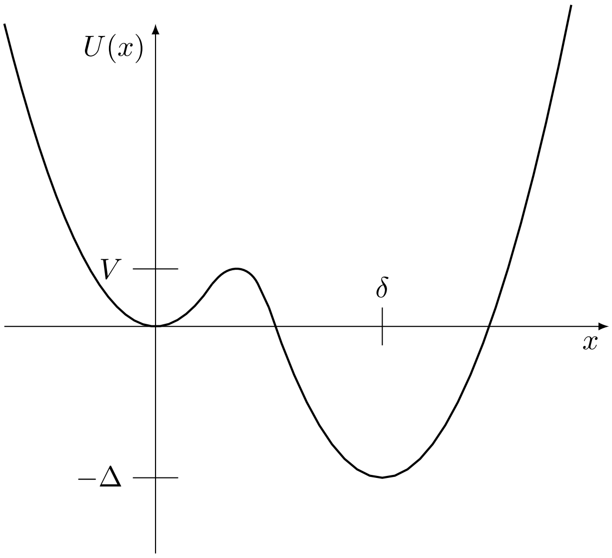

**Figure 2.9:** Double-well potential with an asymmetry $\Delta$, a potential barrier $V$ and width $\delta$.

In order to represent the complexity of the solid, different TLS having a distribution of the potential $V$ and asymmetry $\Delta$ are usually considered. For sake of clarity, here we will se the contribution of one TLS. Under thermal equilibrium the population of the two minima in a TLS is described by the statistic of Boltzmann and it is possible to relate the elastic response of the material to the population of the two systems [80].

The elastic constants express the dependence of the free energy from strain [73]. Therefore, in order to obtain the relation between the TLS and the mechanical loss, it is essential to evaluate the free energy for a Gibbs distribution

$$F = -k_B T \ln Z \,, \tag{2.58}$$

where $k_B$ is the Boltzmann constant, $T$ is the temperature of the system and $Z$ is the partition function

$$Z = \sum_n e^{-E_n/k_B T} = \mathrm{Tr}\{e^{-\hat{H}/k_B T}\} \,, \tag{2.59}$$

over the eigenvalues $E_n$ of the Hamiltonian $\hat{H}$ of the system. Such system can be described by a combination of the eigenstates $\varphi_L(x)$ and $\varphi_R(x)$ of the left ($L$) and right ($R$) local minima, treated as independent and with the same characteristic frequency $\omega_0$. In this case, the Hamiltonian related to the potential $U(x)$ is

$$\hat{H}_U = \begin{pmatrix} 0 & -\frac{\Delta_0}{2} \\ -\frac{\Delta_0}{2} & -\Delta \end{pmatrix} \,, \tag{2.60}$$

where $\Delta$ is the energy difference between the minima of the double-well potential and $\Delta_0$ is a parameter which describes the coupling between the two states. By introducing the tunnelling parameter[5]

$$\lambda = \frac{1}{2}\frac{\delta}{\hbar}\sqrt{2mV} \,, \tag{2.61}$$

---

[5] We are not saying here that the transition is made through quantum tunneling.

where $\delta$ is the separation between wells and $m$ is the mass of the system, it is possible to express $\Delta_0$ using the Wentzel-Kramers-Brillouin (WKB) approximation

$$\Delta_0 = \hbar\omega_0 e^{-\lambda} \, . \tag{2.62}$$

The easier way to find the eigenvalues is to work on the base where $\hat{H}_U$ does not have off-diagonal therm. Using the unitary matrix

$$\hat{U} = \hat{U}^{-1} = \frac{\Delta_0}{\sqrt{\Delta_0^2 + (\Delta - \varepsilon)^2}} \begin{pmatrix} 1 & \frac{\Delta-\varepsilon}{\Delta_0} \\ \frac{\Delta-\varepsilon}{\Delta_0} & -1 \end{pmatrix} , \tag{2.63}$$

one can diagonalize $\hat{H}_U$ as

$$\hat{H}'_U = \hat{U}\hat{H}_U\hat{U}^{-1} = \frac{1}{2}\begin{pmatrix} -\Delta + \varepsilon & 0 \\ 0 & -\Delta - \varepsilon \end{pmatrix} , \tag{2.64}$$

where $\varepsilon = \sqrt{\Delta^2 + \Delta_0^2}$. In this sense, the Hamiltonian of the system will be the sum of the Hamiltonian related to non-interacting wells with energy $1/2\hbar\omega_0$ and $\hat{H}'_U$, than

$$\hat{H}' = \frac{1}{2}\begin{pmatrix} \hbar\omega_0 & 0 \\ 0 & \hbar\omega_0 \end{pmatrix} + \frac{1}{2}\begin{pmatrix} -\Delta + \varepsilon & 0 \\ 0 & -\Delta - \varepsilon \end{pmatrix} , \tag{2.65}$$

and the energies of the two levels which can be called "up" (↑) and "down" (↓) are

$$E_\uparrow = \frac{1}{2}\left(\hbar\omega_0 - \Delta + \varepsilon\right) , \tag{2.66a}$$
$$E_\downarrow = \frac{1}{2}\left(\hbar\omega_0 - \Delta - \varepsilon\right) . \tag{2.66b}$$

Using equations (2.66) and (2.58) it is possible to evaluate the free energy $F$ of the system

$$F = \frac{1}{2}(\hbar\omega_0 - \Delta) - k_B T \ln\left(2\cosh\left(\frac{\sqrt{\Delta^2 + \Delta_0^2}}{2k_B T}\right)\right) = F_0 + F_U , \tag{2.67}$$

where $F_0$ is the free energy of the non-interacting wells and $F_U$ is the free energy for the double-well potential.

### Interaction with phonon

Once we found the free energy for a double-well potential we need to consider the interaction between such system and its surroundings. In doing this, we consider the phonon relaxation attenuation caused by TLS, in which the energy splitting will have a periodic modulation at phonon frequency, related to the elastic stress [81]. Considering a weak external field, the interaction with the TLS can be treated using perturbation theory. Furthermore, the wavelengths of corresponding frequencies phonon modes, which induce resonant transition from one level to the other, are typically larger than the separation of the wells and the local perturbation field is taken as uniform. This perturbation affects the energy $U(x)$ leaving the height of the barrier unaltered and changing the asymmetry energy by a linear function [82]

$$\Delta(u) = \Delta + \gamma_{ik}u_{ik} , \tag{2.68}$$

where $\gamma_{ik} = d\Delta/du_{ik}$ is the so-called *deformation potential* and

$$u_{ik} = \frac{1}{2}\left(\frac{\partial u_i}{\partial x_k} + \frac{\partial u_k}{\partial x_i} + \frac{\partial u_l}{\partial x_i}\frac{\partial u_l}{\partial x_k}\right) \tag{2.69}$$

is the deformation field[6]. Thanks to the isotropy of amorphous solids the two-level system interacts only with longitudinal phonon and $\gamma_{ik} = \gamma\delta_{ik}$. In this case, the Hamiltonian related to the perturbed potential is

$$\hat{H}_U = \begin{pmatrix} 0 & -\frac{\Delta_0}{2} \\ -\frac{\Delta_0}{2} & -\Delta \end{pmatrix} + \gamma u_{ii} \begin{pmatrix} 0 & 0 \\ 0 & -1 \end{pmatrix} , \tag{2.70}$$

and following the same procedure, the free energy becomes

$$F = F_0 - \frac{1}{2}\gamma u_{ii} - k_B T \ln\left(2\cosh\left(\frac{\sqrt{(\Delta + \gamma u_{ii})^2 + \Delta_0^2}}{2k_B T}\right)\right) . \tag{2.71}$$

Since we are interested to the interaction with phonon, we have to consider the thermal energy region $k_B T > \varepsilon \gg \hbar\omega$ where the temperature is more important than tunnelling effect. Furthermore, for weak perturbation we can neglect all non-linear therms in $\gamma u_{ii}$ and the free energy is

$$\begin{aligned} F \approx& F_0 - \frac{1}{2}\gamma u_{ii} - k_B T \ln\left(2\cosh\left(\frac{\sqrt{\varepsilon^2 + 2\gamma u_{ii}\Delta}}{2k_B T}\right)\right) \\ \approx& F_0 - \frac{1}{2}\gamma u_{ii} - k_B T \ln\left(2\cosh\left(\frac{\varepsilon\sqrt{1 + 2\frac{\gamma u_{ii}\Delta}{\varepsilon^2}}}{2k_B T}\right)\right) \\ \approx& F_0 - \frac{1}{2}\gamma u_{ii} - k_B T \ln\left(2\cosh\left(\frac{\varepsilon(1 + \frac{\gamma u_{ii}\Delta}{\varepsilon^2})}{2k_B T}\right)\right) . \end{aligned} \tag{2.72}$$

Since $\sqrt{1+x} \approx 1 + x/2$ for $x \ll 1$. Furthermore, $\Delta \gg \Delta_0$ and $\varepsilon/\varepsilon^2 \approx 1/\Delta$, hence

$$F = F_0 - \frac{1}{2}\gamma u_{ii} - k_B T \ln\left(2\cosh\left(\frac{\varepsilon + \gamma u_{ii}}{2k_B T}\right)\right) , \tag{2.73}$$

which can be simplified by the assumption $\varepsilon = \sqrt{\Delta^2 + \Delta_0^2} \approx \Delta$

$$F \approx F_0 - \frac{1}{2}\gamma u_{ii} - k_B T \ln\left(2\cosh\left(\frac{\Delta + \gamma u_{ii}}{2k_B T}\right)\right) . \tag{2.74}$$

## 2.4 Properties Related to Structure Dynamics

### 2.4.1 Mechanical Response of Anelastic Solids

In order to understand the behaviour of anelastics solids is useful to look at the differences from ideal elastic materials [75]. If we apply the stress $\sigma(t)$ to the solid, the strain $u(t)$ is modified following the linear-response theory

$$u(t) = \int_{-\infty}^{t} j(t - t')\sigma(t')dt' , \tag{2.75}$$

where $j(t)$ is the response function (impulse response), which depends on elastic parameters of the solid such as the *Young's modulus*, *Poisson's ratio* and *Shear modulus*. The output is therefore the convolution of the input and the response function. We

---

[6] Notation of sum over repeated index is used.

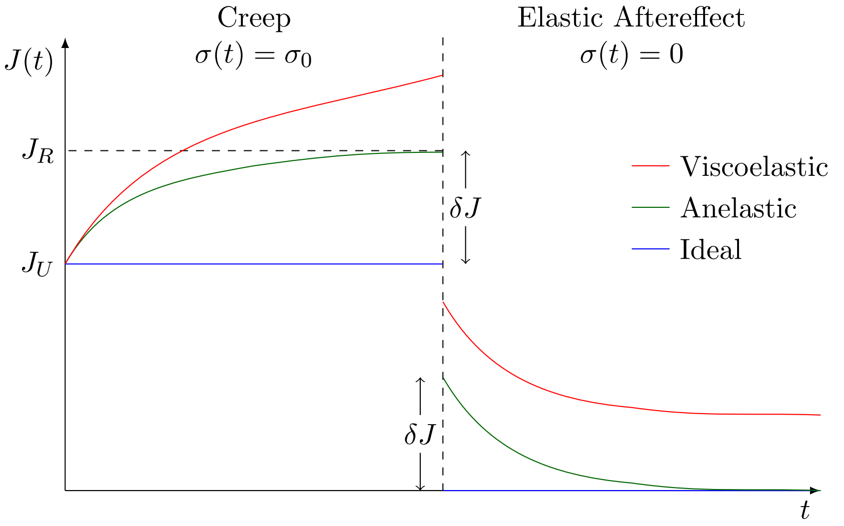

**Figure 2.10:** Creep function for ideal solid (blue line), anelastic solid (green line) and viscoelastic solid (red line).

can imagine to apply a constant stress at $t = 0$ so that $\sigma(t) = \sigma_0\theta(t)$, where $\theta(t)$ is the Heaviside function. For this kind of perturbations, using equation (2.75) we found

$$J(t) = \frac{u(t)}{\sigma_0} = \int_0^t j(t-t')dt' \,, \tag{2.76}$$

which is known as *compliance* and can be seen as the response to a constant perturbation. Since $\sigma_0$ is applied, elastic solid shows a constant response function $J(t) = J_U$ which is called *unrelaxed compliance*, whereas anelastic solid shows a creep response and for that reason $J(t)$ is known as *creep function*. In figure 2.10 there is the behaviour of the creep function for different materials. After a transient period, for the viscoelastic solid, $J(t)$ increases linearly with time, representing steady-state viscous creep. On the other hand, for anelastic solid the creep function or the strain, since $\sigma(t)$ is constant, approaches asymptotically to an equilibrium value $J_R$ called *relaxed compliance*. The difference $\delta J = J_R - J_U$ is the reason of the difference between elastic and anelastic solid after the stress is removed in the so called *elastic aftereffect*. In contrast with elastic solid the strain of anelastic solid does not returns instantaneously to its initial equilibrium value but to $\delta J\sigma_0$ and reaches the initial value only after a certain period of time. A similar behaviour can be found for viscoelastic solid with the difference that the final strain value is different from the initial one.

The compliance is useful in order to study the deformation of the solid after the applied stress. If we are interested in the dynamic of the system, it is useful to study the internal stress as consequence of the deformation. Indeed, if we imagine to apply a strain to the solid in equilibrium, internal stress would appear in order to bring back the system to the equilibrium. Supposing a weak perturbation, one may suppose a linear response

$$\sigma(t) = \int_{-\infty}^t m(t-t')u(t')dt' \,, \tag{2.77}$$

where $m(t)$ is the response function of the solid at applied strain. Following the approach used in the creep experiment, if we imagine to apply a constant strain at $t = 0$ so that $u(t) = u_0\theta(t)$ we obtain

$$M(t) = \frac{\sigma(t)}{u_0} = \int_0^t m(t-t')dt' \,, \tag{2.78}$$

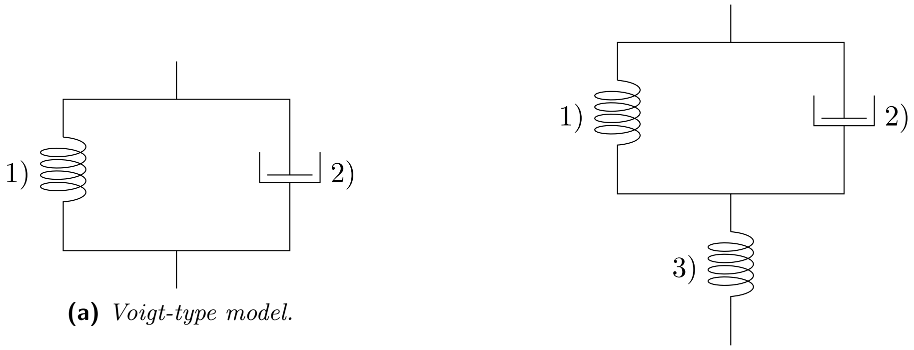

**(a)** *Voigt-type model.*

**(b)** *Three-phase model.*

**Figure 2.11:** Representation of Voigt-type model (a) and three-phase model (b).

where $M(t)$ is known as the *modulus function*. In this sense, since $u_0$ is applied we can introduce the *unrelaxed modulus* $M_U$ related to ideal elastic material response, the *relaxed modulus* $M_R$ representing the stress of anelastic solid reached at infinite time since $u(t) = u_0$ and $\delta M = M_U - M_R$ which represents the difference between modulus functions of elastic and anelastic solid when the last one approach to the value $M_R$.

Even if the meaning of equation (2.75) sometime is more easier to understand than (2.77), it is more convenient to work with the modulus function. For that reason, it is useful to express the relation between the different response functions. Applying the Laplace transform at equations (2.75), (2.76), (2.77) and (2.78) we obtain

$$u(s) = j(s)\sigma(s) \;, \tag{2.79a}$$
$$J(s) = j(s)/s \;, \tag{2.79b}$$
$$\sigma(s) = m(s)u(s) \;, \tag{2.79c}$$
$$M(s) = m(s)/s \;, \tag{2.79d}$$

where we can derive the relation between the two response functions $m(s) = j^{-1}(s)$ and $s^2M(s) = J^{-1}(s)$. It is now clear that the elastic moduli are the response of the solids to an external solicitation. This reaction can be compared to the reaction of a spring. If we apply a force or a strain to the spring its response will try to bring the system back to the equilibrium and will oppose to the external solicitation.

### Debye functions

In order to evaluate $m(t)$, we can build a model which describes the creep function. As first, we may represent anelastic solid with a system composed by parallel coupling of one spring, which describes the elastic part of the solid, and one dash-pot, which damp the spring. This model, called *Voigt-type model*, is illustrated in figure 2.11a. In such a system the stress is distributed in the two elements whereas the strain is the same

$$\sigma_{tot} = \sigma_1 + \sigma_2 \;, \qquad u = u_1 = u_2 \;, \tag{2.80}$$

where

$$u_1 = \delta J \sigma_1 \qquad \text{and} \qquad \dot{u}_2 = \delta J \sigma_2 / \tau_\sigma \;, \tag{2.81}$$

where $\tau_\sigma$ is the relaxation time constant related to the presence of the dash-pot. Despite the presence of the dash-spot which allows to reproduce the behaviour of $J(t)$ during and after the applied stress, the Voigt-type model does not describe the discontinuity of the creep function when $\sigma_0$ is removed. In order to include this gap, it is necessary to introduce another element describing the elastic behaviour, such as a spring. This *three-phase model* is illustrated in figure 2.11b and allows to describe anelastic solids. Now, the total strain contains two terms, one is related to the Voigt-type model and the other is the third spring, whereas the total stress is the same

$$\sigma_{tot} = \sigma_1 + \sigma_2 = \sigma_3 \,, \qquad\qquad u = u_1 + u_3 \,, \tag{2.82}$$

and

$$u_2 = u_1 = \delta J \sigma_1 \,, \qquad \dot{u}_2 = \delta J \sigma_2 / \tau_\sigma \qquad \text{and} \qquad u_3 = J_U \sigma_3 \,, \tag{2.83}$$

where $\tau_\sigma$ is the *retardation time* of the deformation, due to the presence of the dash-pot when a stress is applied. Using relations (2.82) and (2.83) it is easy to find

$$J_R \sigma + J_U \dot{\sigma} \tau_\sigma = u + \dot{u} \tau_\sigma \,, \tag{2.84}$$

which represents the equation of motion for such system. In the case of a creep experiment, we may solve the equation (2.84) under the conditions

$$\sigma(t) = \sigma_0 \,, \qquad \dot{\sigma}(t) = 0 \qquad \text{for } t \geq 0 \,, \tag{2.85a}$$

$$u(t) = J_U \sigma_0 \qquad \text{for } t = 0 \,. \tag{2.85b}$$

In this sense, the equation (2.84) becomes

$$\frac{J_R \sigma_0}{\tau_\sigma} = u + \dot{u} \,, \tag{2.86}$$

whit the solution

$$u(t) = e^{-\int_0^t 1/\tau_\sigma ds} \left( J_U \sigma_0 + \int_0^t \frac{J_R \sigma_0}{\tau_\sigma} e^{\int_0^s 1/\tau_\sigma dl} ds \right) \,, \tag{2.87}$$

which yields the compliance in the case of a creep experiment

$$J(t) = \frac{u(t)}{\sigma_0} = J_U + \delta J \left( 1 - e^{-t/\tau_\sigma} \right) \,. \tag{2.88}$$

In order to obtain the modulus function it is useful to use the Laplace transform

$$\mathscr{L}(J(t)) = J(s) = J_U s^{-1} + \delta J \left( s^{-1} - \frac{\tau_\sigma}{1 + s\tau_\sigma} \right) \,, \tag{2.89}$$

which yields the modulus function by using the relations (2.79b) and (2.79d)

$$M(s) = \frac{1}{s^2 J(s)} = \frac{1 + s\tau_\sigma}{s J_R \left( 1 + \frac{J_U}{J_R} s \tau_\sigma \right)} \,. \tag{2.90}$$

If we introduce a new time constant for the modulus function $\tau_u = \tau_\sigma J_U / J_R$, we obtain

$$M(s) = \frac{1}{s J_R} - \frac{\delta J}{J_U J_R} \frac{\tau_u}{1 + s\tau_u} \,, \tag{2.91}$$

therefore

$$\mathscr{L}^{-1}(M(s)) = M(t) = M_R + \delta M e^{-t/\tau_u} \,, \tag{2.92}$$

where $M_R = J_R^{-1}$ and $\delta M = \delta J / (J_U J_R)$. In the figure 2.12 there is the behaviour of the modulus function. By using the time constant $\tau_u$, known as *relaxation time*

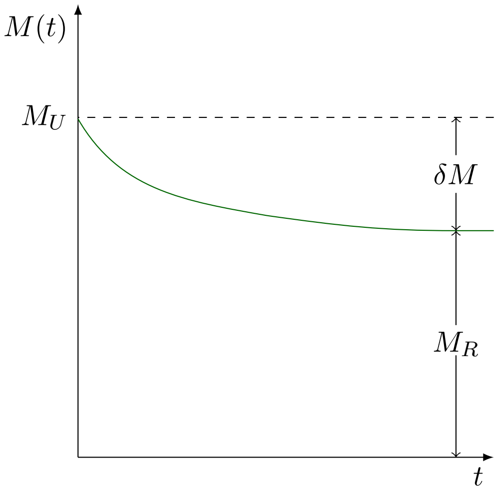

**Figure 2.12:** Modulus function of anelastic solid.

at constant strain, it is possible to rewrite the equation of motion (2.84) in term of modulus function

$$\sigma + \dot{\sigma}\tau_u = M_R u + M_U \dot{u}\tau_u \,. \tag{2.93}$$

Since we are interesting to the dynamic response, we can assume a periodic strain

$$u = u_0 e^{i\omega t}, \qquad \sigma = (\sigma_1 + i\sigma_2)e^{i\omega t} \tag{2.94}$$

into equation (2.93) and call $M_1 = \sigma_1/u_0$, $M_2 = \sigma_2/u_0$. Using the real and the imaginary part of the equation so obtained, we can evaluate the *Debye equations*

$$M_1 = M_R + \delta M \frac{\omega^2\tau_u^2}{1+\omega^2\tau_u^2} \,, \tag{2.95a}$$

$$M_2 = \delta M \frac{\omega\tau_u}{1+\omega^2\tau_u^2} \,. \tag{2.95b}$$

The Debye equations are routinely obtained in relaxation processes[7] and describe the elastic modulus as function of frequency; The quantity $M_1$ goes from $M_R$ at high frequencies ($\omega\tau_u \gg 1$) to $M_U$ at low frequencies ($\omega\tau_u \ll 1$). The quantity $M_2$ has small values at both high and low frequencies and is called *Debye peak.*

**Loss angle**

We will see now the physical meaning of the Debye equations. Using equation (2.77) it is possible to relate the stress to strain

$$\sigma = (M_1 + iM_2)u \,, \tag{2.96}$$

that using the Debye equations (2.95a) and (2.95b), for a periodic strain reads

$$\sigma = \left(M_R + \delta M \frac{\omega^2\tau_u^2}{1+\omega^2\tau_u^2}\right) u_0 \cos(\omega t) - \left(\delta M \frac{\omega\tau_u}{1+\omega^2\tau_u^2}\right) u_0 \sin(\omega t) \,, \tag{2.97}$$

In figure 2.13 the hysteresis shows that there are two symmetrical moments where the work is positive (blue curves) and two where it is negative (red curves). Furthermore the area of the ellipse represents the dissipated energy over a cycle. It is possible to

---

[7] the Debye equations were first derived by P. Debye for the case of dielectric relaxation phenomena.

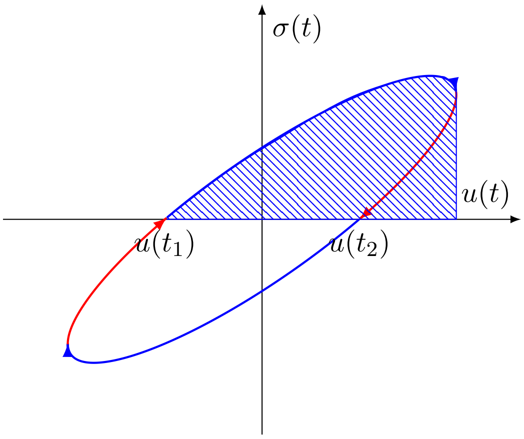

**Figure 2.13:** Hysteresis cycle for the stress versus the strain. The blue area represents the maximum energy stored by the system during a cycle.

demonstrate that the dissipated energy is associated to the area under the hysteresis curve. The dissipated power reads

$$P(t) = \sigma(t)\dot{u}(t) \,, \tag{2.98}$$

so that the dissipated energy over a period $T$ is

$$E_{\text{diss}} = \int_0^T P(t)dt, \qquad \text{with } \omega T = 2\pi \,. \tag{2.99}$$

We note that

$$u(t) = u_o \Re[e^{i\omega t}] \,, \tag{2.100}$$
$$\dot{u}(t) = -u_0\omega \sin\omega t \,, \tag{2.101}$$
$$\sigma(t) = u_o \Re[M(\omega)e^{i\omega t}] = u_o(M_1 \cos\omega t - M_2 \sin\omega t) \,, \tag{2.102}$$

and equation (2.98) becomes

$$P(t) = u_0^2\omega \left(M_2 \sin^2\omega t - M_1 \sin\omega t \cos\omega t\right) \,, \tag{2.103}$$

so that the dissipated energy is

$$\begin{aligned} E_{\text{diss}} &= u_0^2\omega \left(M_2 \int_0^T \sin^2\omega t dt - M_1 \int_0^T \sin\omega t \cos\omega t dt\right) \,, \\ E_{\text{diss}} &= u_0^2 \pi M_2 \,. \end{aligned} \tag{2.104}$$

In other words, the dissipated energy depends on the imaginary part of the elastic modulus function. It is also possible to evaluate the maximum stored energy in the system, which corresponds to the area under the positive work curve in figure 2.13

$$E_{\text{max}} = \int_{t_1}^{t_2} P(t)dt \,. \tag{2.105}$$

In order to obtain $t_1$ and $t_2$ we need to find the condition for having null stress $\sigma(t) = 0$ and the maximum of the strain $max(u(t))$, which corresponds to the zero of the function $\dot{u}(t)$. In other words, we need to find the maximum of the energy which is

$$E_{\text{max}} = max\left(\int P(t)dt\right) \rightarrow P(t) = \sigma(t)\dot{u}(t) = 0 \,. \tag{2.106}$$

From $\sigma(t) = 0$ we obtain $\tan(\omega t) = M_1/M_2$, that in the presence of quasi-ideal solid, where $M_1 >> M_2$, is verified for $t \cong \pm\pi/2\omega$. From $\dot{u}(t) = 0$ we obtain $t = k\pi/\omega$ with $k \in \mathbb{Z}$. Under this consideration, the maximum stored energy is

$$\begin{aligned} E_{\max} &= \int_{-\frac{\pi}{2\omega}}^{0} P(t)dt \\ &= u_0^2\omega \left( M_2 \int_{-\frac{\pi}{2\omega}}^{0} \sin^2 \omega t dt - M_1 \int_{-\frac{\pi}{2\omega}}^{0} \sin \omega t \cos \omega t dt \right) \\ &= \frac{1}{2} u_0^2 (M_1 + M_2/2) \,. \end{aligned} \tag{2.107}$$

Since $M_1 >> M_2$ we can assume that the maximum stored energy is $E_{\max} = u_0^2 M_1/2$ so that

$$\begin{aligned} E_T &= u_0^2 \pi M_2 \\ &= u_0^2 \pi \frac{M_2}{M_1} M_1 \\ &= 2\pi \frac{M_2}{M_1} E_{\max} \\ &= 2\pi\phi E_{\max} \,, \end{aligned} \tag{2.108}$$

where $\phi$ is the so-called *loss angle* of the system.

### 2.4.2 Internal Friction and Relaxations

Now it remains to understand how to obtain the loss angle from the creep and the relaxation time. The relaxation is related to a transition of the solid from a state at higher energy to a state at lower energy. As we have seen in the section 2.3.2, in the case of amorphous solids, the relaxation may be related to the multiple metastable configurations of the structure at different energies. If we consider the asymmetric double-well potential, the relaxation is due to the transition from the state $E_\uparrow$ to $E_\downarrow$, and at room temperature, this phenomena is ensured by the thermal energy. In this sense, if we have an asymmetric double-well potential with asymmetry energy $\Delta$ and energy barrier $V$, as shown in figure 2.9, the probability to change state using the thermal energy is

$$p^{\uparrow\downarrow} = p_0^{\uparrow\downarrow} e^{-\frac{V}{k_B T}} , \qquad p^{\downarrow\uparrow} = p_0^{\downarrow\uparrow} e^{-\frac{V+\Delta}{k_B T}} \,, \tag{2.109}$$

where $p^{\uparrow\downarrow}$ is the probability to switch from the state up to the state down and $p^{\downarrow\uparrow}$ vice versa. Using the probability (2.109), the relaxation time[8] is

$$\tau = \frac{1}{p^{\uparrow\downarrow} + p^{\downarrow\uparrow}} \tag{2.110a}$$

$$= \tau_0 \frac{e^{V/k_B T}}{1 + e^{-\Delta/k_B T}} \tag{2.110b}$$

$$= \tau_0' e^{V/k_B T} \,, \tag{2.110c}$$

which follows the Arrhenius' law and where $1/(1 + e^{-\Delta/k_B T})$ goes from 1/2 to 1. The thermal noise of the amorphous solids is related to the imaginary part of modulus function $M_2$ expressed by relation (2.95b). In reality, amorphous solids are well described

---

[8] From now on the subscript on $\tau$ is omitted, since $\tau_\sigma$ and $\tau_u$ are equal if $M_R \sim M_U$.

by a distribution of asymmetric double-well potential and equation (2.95b) must be implemented [80]

$$M_2 = \int_0^\infty \int_0^\infty \delta M \frac{\omega\tau}{1+\omega^2\tau^2} g(\Delta) f(V) d\Delta dV \,, \tag{2.111}$$

where $f(V)dV$ is the number of wells with barrier between $V$ and $V+dV$, while $g(\Delta)d\Delta$ is the number of wells with asymmetry between $\Delta$ and $\Delta + d\Delta$ and $\delta M$ is evaluated in appendix B.

**Exponential Behaviour of $f(V)$**

There are evidence of an exponential behaviour of the distribution function $f(V)$ for materials like silica [83, 84]

$$f(V) = \frac{1}{V_0} e^{-V/V_0} \,, \tag{2.112}$$

where $V_0$ is a constant which depends on the material. Furthermore, considering equation (B.7) we obtain

$$\int_0^\infty \frac{\omega\tau}{1+\omega^2\tau^2} f(V) dV = \int_0^\infty \frac{f(V)dV}{2\cosh\left(V/k_BT + \ln(\omega\tau_0')\right)} \,. \tag{2.113}$$

In this respect we can solve the integral

$$\begin{aligned}
\int_0^\infty \frac{f(V)dV}{2\cosh\left(V/k_BT + \ln(\omega\tau_0')\right)} &= \frac{k_BT}{2} \int_{\ln(\omega\tau_0')}^\infty \frac{f\left(k_BT(x-\ln(\omega\tau_0'))\right)}{\cosh x} dx \\
&= \frac{k_BT}{2} \int_{\ln(\omega\tau_0')}^\infty \frac{\frac{n}{V_0} e^{-\frac{k_BT}{V_0}x} e^{\ln(\omega\tau_0')\frac{k_BT}{V_0}}}{\cosh x} dx \\
&= \frac{n}{V_0}\frac{k_BT}{2} (\omega\tau_0')^{\frac{k_BT}{V_0}} \int_{\ln(\omega\tau_0')}^\infty \frac{e^{-\frac{k_BT}{V_0}x}}{\cosh x} dx \,.
\end{aligned} \tag{2.114}$$

From experimental data it can be observed $\tau_0 \cong 10^{-13}s$ for glasses and $\omega\tau_0' \ll 1$, so that $\ln(\omega\tau_0') \to -\infty$. Furthermore, if we compare $e^{-\frac{k_BT}{V_0}x}$ and $\cosh x$ (figure 2.14) it is clearly evident that the key of such integral is the parameter $\frac{k_BT}{V_0}$. Indeed, $V_0$ depends on the temperature and it is possible to obtain $k_BT \ll V_0$ especially at low temperature. In this sense, if we consider the case $k_BT \ll V_0$ the function $e^{-\frac{k_BT}{V_0}x}$ can be considered as constant with respect to $1/\cosh x$ and

$$\frac{e^{-\frac{k_BT}{V_0}x}}{\cosh x} \sim \frac{1}{\cosh x} \,. \tag{2.115}$$

We can now integrate

$$\begin{aligned}
\int_0^\infty \frac{f(V)dV}{2\cosh\left(V/k_BT + \ln(\omega\tau_0')\right)} &= \frac{n}{V_0}\frac{k_BT}{2} (\omega\tau_0')^{\frac{k_BT}{V_0}} \int_{-\infty}^\infty \frac{1}{\cosh x} dx \\
&= \frac{n}{V_0}\frac{k_BT}{2} (\omega\tau_0')^{\frac{k_BT}{V_0}} \pi \,.
\end{aligned} \tag{2.116}$$

Once the integration in $V$ is done, the integral in $\Delta$ must be solved and equation (2.111) becomes

$$M_2 = \int_0^\infty \delta M \frac{n}{V_0}\frac{k_BT}{2} (\omega\tau_0')^{\frac{k_BT}{V_0}} \pi g(\Delta) d\Delta \,. \tag{2.117}$$

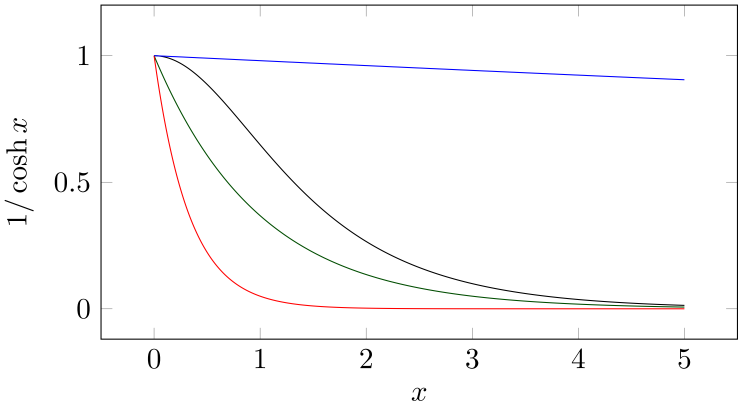

**Figure 2.14:** Comparison of $1/\cosh x$ (black) and $e^{-\frac{k_BT}{V_0}x}$ functions. The comparison regards three cases of the exponential factor: $k_BT \gg V_0$ in red, $k_BT \simeq V_0$ in green and $k_BT \ll V_0$ in blue.

The asymmetry $\Delta$ must be of the order of the energy available to the glass transition. For this reason, under the glass transition temperature the function $g(\Delta)$ can be considered as a constant $g_0$. furthermore, considering the normalization

$$\int_0^\infty g(\Delta)d\Delta = 1$$

$$g_0\Delta_0 = 1\,, \tag{2.118}$$

where we can observe that $g(\Delta)$ has dimension of Joule$^{-1}$. In this respect, considering equation (B.5), we obtain

$$M_2 = \frac{n}{V_0}\frac{k_BT}{2\Delta_0}(\omega\tau_0)^{\frac{k_BT}{V_0}}\pi\int_0^\infty \frac{\delta M}{(1+e^{-\Delta/k_BT})^{\frac{k_BT}{V_0}}}d\Delta\,. \tag{2.119}$$

Considering $\delta M$ as obtained in appendix B, we obtain

$$\begin{aligned} M_2 &= \frac{n}{V_0\Delta_0}\frac{\pi\gamma^2}{8}(\omega\tau_0)^{\frac{k_BT}{V_0}}\int_0^\infty \frac{\operatorname{sech}^2\left(\frac{\Delta}{2k_BT}\right)}{(1+e^{-\Delta/k_BT})^{\frac{k_BT}{V_0}}}d\Delta \\ &= \frac{n}{V_0\Delta_0}\frac{\pi\gamma^2}{8}(\omega\tau_0)^{\frac{k_BT}{V_0}}\int_0^\infty 4\frac{e^{-\frac{\Delta}{k_BT}}}{(1+e^{-\Delta/k_BT})^{(2+\frac{k_BT}{V_0})}}d\Delta\,. \end{aligned} \tag{2.120}$$

If we consider $k_BT \ll V_0$

$$\begin{aligned} M_2 &\sim \frac{n}{V_0\Delta_0}\frac{\pi\gamma^2}{8}(\omega\tau_0)^{\frac{k_BT}{V_0}}\int_0^\infty 4\frac{e^{-\frac{\Delta}{k_BT}}}{(1+e^{-\Delta/k_BT})^2}d\Delta \\ M_2 &= \frac{n}{V_0\Delta_0}\frac{\pi\gamma^2}{8}(\omega\tau_0)^{\frac{k_BT}{V_0}}\int_0^\infty \operatorname{sech}^2\left(\frac{\Delta}{2k_BT}\right)d\Delta\,, \end{aligned} \tag{2.121}$$

and eventually[9]

$$M_2 = \frac{\pi\gamma^2}{4}k_BT\frac{n}{V_0\Delta_0}(\omega\tau_0)^{\frac{k_BT}{V_0}}\,. \tag{2.122}$$

---

[9] To solve the integral the change of coordinates via $s = e^{(\frac{\Delta}{2k_BT})}$ may help, so that

$$4k_BT\int_1^\infty \frac{ds}{(s+1)^2} = 2k_BT\,.$$

It is now possible to obtain the expression of the loss angle.

Considering the Debye equations (2.95), under the condition of quasi-ideal solid $M_2 \ll M_1$ we can assume that $M_1 \simeq M_R$. Using equation (2.108) it is possible to express the loss angle in the case of harmonic analysis

$$\begin{aligned}\phi &= M_2/M_1 = M_2/M_R \\ &= \frac{\pi\gamma^2}{4M_R} k_B T \frac{n}{V_0\Delta_0} (\omega\tau_0)^{\frac{k_B T}{V_0}} ,\end{aligned} \tag{2.123}$$

where $M_R$ is constant. From equation (2.123) we observe that the loss angle should depend on frequency by a power law.

**General $f(V)$**

It is clear that the parameter $k_B T$ is important in order to evaluate the validity of the function for the distribution $f(V)$. In the case where $k_B T$ is small, the Debye function acts like a delta and we can expand the function $f(V)$ in term of $(V + k_B T \ln(\omega\tau_0'))$

$$f(V) = f(-k_B T \ln(\omega\tau_0')) + \sum_{n=1}^{\infty} \frac{(V + k_B T \ln(\omega\tau_0'))^n}{n!} f^{(n)}(-k_B T \ln(\omega\tau_0')) , \tag{2.124}$$

furthermore, since the imaginary part of the Debye equation acts like a delta function, we obtain

$$\begin{aligned}\int_0^{\infty} \frac{f(V)dV}{2\cosh\left(V/k_B T + \ln(\omega\tau_0')\right)} &= f(-k_B T \ln(\omega\tau_0')) \int_0^{\infty} \frac{dV}{2\cosh\left(V/k_B T + \ln(\omega\tau_0')\right)} + \\ &+ \sum_{n=1}^{\infty} \frac{f^{(n)}(-k_B T \ln(\omega\tau_0'))}{n!} \int_0^{\infty} \frac{(V + k_B T \ln(\omega\tau_0'))^n dV}{\cosh\left(V/k_B T + \ln(\omega\tau_0')\right)} .\end{aligned} \tag{2.125}$$

We transform the integral by a change of coordinates via

$$x = V/k_B T + \ln(\omega\tau_0') , \qquad dx = dV/k_B T , \tag{2.126}$$

so that the integration reads

$$\frac{k_B T}{2} f(-k_B T \ln(\omega\tau_0')) \int_{\ln(\omega\tau_0')}^{\infty} \frac{dx}{\cosh x} + \sum_{n=1}^{\infty} \frac{f^{(n)}(-k_B T \ln(\omega\tau_0'))}{n!} (k_B T)^n \int_{\ln(\omega\tau_0')}^{\infty} \frac{x^n dx}{\cosh x} . \tag{2.127}$$

For $\omega\tau_0' << 1$, $\ln(\omega\tau_0') \longrightarrow -\infty$ hence[10]

$$\frac{\pi k_B T}{2} f(-k_B T \ln(\omega\tau_0')) + \sum_{n=1}^{\infty} \frac{f^{(n)}(-k_B T \ln(\omega\tau_0'))}{n!} (k_B T)^n \int_{-\infty}^{\infty} \frac{x^n dx}{\cosh x} . \tag{2.128}$$

For odd values of $n$ the integral from $-\infty$ to $\infty$ is zero because $x^n$ is an odd function while $1/\cosh x$ is an even function. For $n = 2k$ with $k \in \mathbb{N}^+$ we obtain

$$\frac{1}{n!} \int_{-\infty}^{\infty} \frac{x^n dx}{\cosh x} = \frac{2}{n!} \int_0^{\infty} \frac{x^n dx}{\cosh x} \sim 4 , \tag{2.129}$$

---

[10] We remember that

$$\int_{-\infty}^{\infty} \frac{dx}{\cosh x} = \pi .$$

and then

$$\frac{\pi k_B T}{2} f(-k_B T \ln(\omega\tau_0')) + 4 \sum_{n=2k} f^{(n)}(-k_B T \ln(\omega\tau_0'))(k_B T)^n \,. \tag{2.130}$$

Once the integration in $V$ is done, the integral in $\Delta$ must be solved and equation (2.111) becomes

$$\begin{aligned} M_2 = & \int_0^\infty \delta M \frac{\pi k_B T}{2} f(-k_B T \ln(\omega\tau_0')) g(\Delta) d\Delta + \\ & + 4 \int_0^\infty \delta M \sum_{n=2k} f^{(n)}(-k_B T \ln(\omega\tau_0'))(k_B T)^n g(\Delta) d\Delta \,. \end{aligned} \tag{2.131}$$

We can do the previous observation for the asymmetry $\Delta$ and consider that $g(\Delta) \sim 1/\Delta_0$. Furthermore, considering $k_B T \ll V_0$ regarding $\tau_0'$ and $\delta M$, using equation (2.118) and (B.5) we obtain

$$\begin{aligned} M_2 = & \frac{\gamma^2\pi}{8\Delta_0} f(-k_B T \ln(\omega\tau_0)) \int_0^\infty \operatorname{sech}^2(\frac{\Delta}{2k_B T}) d\Delta + \\ & + \frac{\gamma^2\pi}{\Delta_0} \sum_{n=2k} (k_B T)^{(n-1)} f^{(n)}(-k_B T \ln(\omega\tau_0)) \int_0^\infty \operatorname{sech}^2(\frac{\Delta}{2k_B T}) d\Delta \,, \end{aligned} \tag{2.132}$$

and finally

$$M_2 = \frac{\gamma^2\pi}{4\Delta_0}(k_B T) f(-k_B T \ln(\omega\tau_0)) + \frac{2\gamma^2\pi}{\Delta_0} \sum_{n=2k} (k_B T)^n f^{(n)}(-k_B T \ln(\omega\tau_0)) \,. \tag{2.133}$$

Under the condition of quasi-ideal solid $M_1 \simeq M_R$ and using equation (2.108) it is possible to use the harmonic analysis to express the loss angle

$$\phi = \frac{\gamma^2\pi}{4\Delta_0 M_R}(k_B T) f(-k_B T \ln(\omega\tau_0)) + \frac{2\gamma^2\pi}{\Delta_0 M_R} \sum_{n=2k} (k_B T)^n f^{(n)}(-k_B T \ln(\omega\tau_0)), \tag{2.134}$$

where $M_R$ is constant. Finally, using equation (2.112) the loss angle reads

$$\phi = \frac{\gamma^2\pi}{4\Delta_0 M_R} \frac{k_B T}{V_0} (\omega\tau_0)^{\frac{k_B T}{V_0}} \left[ 1 + 8 \sum_{n=2k} \frac{(k_B T)^{n-1}}{V_0^n} \right] \quad \text{with } k \in \mathbb{N}^+ \,, \tag{2.135}$$

where it is clear that the relation is valid only in the case where $k_B T \ll V_0$.

# CHAPTER 3

# METROLOGY

> *"Quelli che s'innamorano di pratica sanza scienzia son come 'l nocchier ch'entra in navilio senza timone o bussola, che mai ha certezza dove si vada."*
>
> Leonardo da Vinci
>
> Trattato della pittura, parte II. 77 (the 16th century)

In this chapter the methods adopted to characterize the samples are illustrated. Spectroscopic ellipsometry (SE) is a suitable method to investigate optical properties and thickness of thin film materials. We used two different ellipsometers, covering complementary and partially overlapping spectral regions, thus obtaining information related to a broad wavelength range extended from 190 to 1680 nm (0.7 - 6.5 eV).

It is known that the optical properties of amorphous solids depend on microstructure and morphology; the optical models for amorphous oxide solids are here illustrated. Since the coating materials are amorphous, the models describing the absorption edge are the well-known Tauc-Lorentz (TL) and Cody-Lorentz Cody-Lorentz (CL). In order to describe the possible roughness of the coating surface, a model to describe mixture of materials is here illustrated.

We characterized the mechanical properties by the ring-down method: the sample is forced to vibrate at one of its resonance frequencies then the oscillations are free to decay after the excitation is removed. The characteristic decay time is measured and then the loss angle of the sample is worked out. We used a Gentle Nodal Suspension (GeNS) in order to suspend the sample without clamping.

To estimate the coating loss angle it is necessary to know the dilution factor, i.e. the ratio of the energy stored in the coating to the energy stored in the total system. **With a GeNS system, the dilution factor is measured via the shift of the resonance frequencies due to the coating deposition. By fitting the measured dilution factor with the numerical values from the finite element simulations, it is possible to estimate the elastic constants of the coating.**

## 3.1 Introduction to Ellipsometry

When the light interacts with a solid having a refractive index which differs from the medium where the radiation is propagating, reflection and transmission occur. The reflected and transmitted beams obtained by the interaction of a solid with an incident light beam are linked by suitable boundary conditions. The Snell's laws give the relation between the incident $\theta_i$ and reflection $\theta_r$ angle of the light beam

$$\theta_i = \theta_r = \theta_1 \ , \tag{3.1}$$

which can be related to the transmission angle $\theta_t$

$$\sin\theta_t = \sin\theta_2 = \frac{N_1}{N_2}\sin\theta_1 \ , \tag{3.2}$$

where $N_1$ and $N_2$ are the refractive indices of the two media.

Since a randomly polarized light can be seen as a superposition of two linear polarizations, it is convenient to study two different cases of transmission and reflection. Following figure 3.1, polarization can be classified as p-like (from parallel) and s-like (from senkrecht, German for perpendicular) depending on the direction of the oscillating electric fields with respect to the *plane of incidence*, which is defined by the incoming propagation direction and the vector perpendicular to the plane of the interface of the sample. As shown in figure 3.1a, in the case of p-polarization, the electric fields of incident, reflected and transmitted radiation oscillate in the plane of incidence. On the other hand, in figure 3.1b is shown that for s-polarization the electric fields are perpendicular to the plane of incidence.

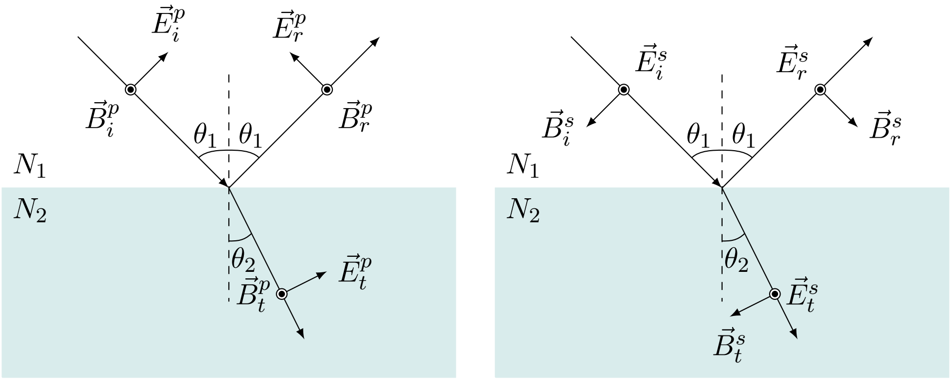

**(a)** p-polarization. **(b)** s-polarization.

**Figure 3.1:** Electric $\vec{E}$ and magnetic $\vec{B}$ fields of the incident, reflected and transmitted light beam represented over the plane of incidence. a) the $\vec{B}$ fields are transverse to the plane of incidence, and p-polarization is commonly referred to as transverse-magnetic (TM). b) the $\vec{E}$ fields are transverse and s-polarization is commonly referred to as transverse-electric (TE).

Using the boundary conditions for the electric and magnetic fields at the interface, the Fresnel's equations are obtained for the two polarizations

$$r_p \equiv \frac{\left|\vec{E}_r^p\right|}{\left|\vec{E}_i^p\right|} = \frac{N_2\cos\theta_1 - N_1\cos\theta_2}{N_2\cos\theta_1 + N_1\cos\theta_2}\,, \tag{3.3a}$$

$$t_p \equiv \frac{\left|\vec{E}_t^p\right|}{\left|\vec{E}_i^p\right|} = \frac{2N_1\cos\theta_1}{N_2\cos\theta_1 + N_1\cos\theta_2}\,, \tag{3.3b}$$

$$r_s \equiv \frac{\left|\vec{E}_r^s\right|}{\left|\vec{E}_i^s\right|} = \frac{N_1\cos\theta_1 - N_2\cos\theta_2}{N_1\cos\theta_1 + N_2\cos\theta_2}\,, \tag{3.3c}$$

$$t_s \equiv \frac{\left|\vec{E}_t^s\right|}{\left|\vec{E}_i^s\right|} = \frac{2N_1\cos\theta_1}{N_1\cos\theta_1 + N_2\cos\theta_2}\,. \tag{3.3d}$$

Since the refractive index $N$ is a complex quantity, it is possible to express the Fresnel coefficients as

$$r = |r|\,e^{i\delta_r}\,, \tag{3.4a}$$

$$t = |t|\,e^{i\delta_t}\,, \tag{3.4b}$$

$$\delta_r = \arg r = \arctan\left(\Im(r)/\Re(r)\right)\,, \tag{3.4c}$$

$$\delta_t = \arg t = \arctan\left(\Im(t)/\Re(t)\right)\,, \tag{3.4d}$$

which help to describe the reflected and transmitted beam in term of change in amplitude and phase.

With ellipsometry it is possible to measure the change in polarization state of light reflected or transmitted from the surface of a sample [85]. The sketch shown in figure 3.2 represents the particular case with linearly polarized incident beam, where the phase of p- and s-polarization are equal.

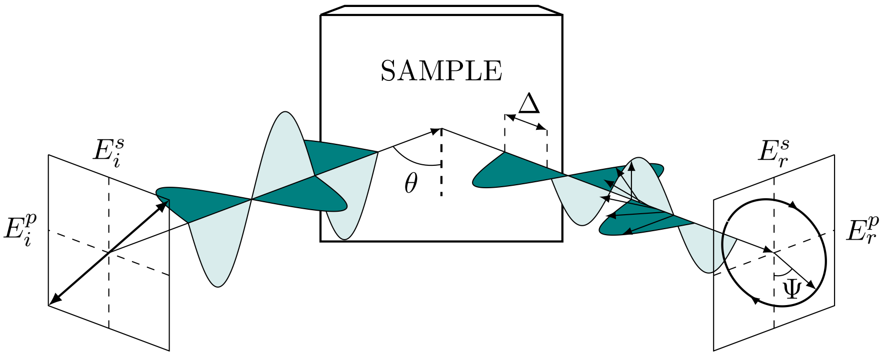

**Figure 3.2:** Sketch of reflection ellipsometry technique.

When the radiation interacts with the sample, the reflected beam is characterized by a change in amplitude and phase for both p- and s-polarization, giving different $r_p$ and $r_s$. The fundamental equation of ellipsometry connects the two angles $\Psi$ and $\Delta$, shown in figure 3.2, to the amplitude and the phase difference of p- and s-polarization

$$\rho \equiv \frac{r_p}{r_s} \equiv \frac{|r_p|}{|r_s|}e^{i(\delta_r^p - \delta_r^s)} \equiv \tan\Psi e^{i\Delta}\,, \tag{3.5}$$

where

$$\Psi = \tan^{-1}(|\rho|) = \tan^{-1}\left(\frac{|r_p|}{|r_s|}\right) , \tag{3.6}$$

$$\Delta = \delta_r^p - \delta_r^s . \tag{3.7}$$

From ($\Psi$, $\Delta$) data, thanks to equation (3.5) it is possible to compute the Fresnel's coefficients and hence the refractive index of the sample. In order to increase the sensitivity of ellipsometric measurements, it is recommended to collect the data around the Brewster angle for the incident light beam. In fact, at the Brewster angle the coefficient $r_p$ is zero for transparent samples[1] and the differences between $r_p$ and $r_s$ is maximised.

### 3.1.1 Spectroscopic Ellipsometers

Optical properties and thickness of coating layers have been obtained using spectroscopic ellipsometry. In particular, two different J.A. Woollam Co. ellipsometers have been used, covering complementary and overlapping spectral regions: the VASE showed in figure 3.3a for the interval 190 nm − 1100 nm, and the M-2000 showed in figure 3.3b for the interval 245 nm − 1680 nm. The main differences between the two ellipsometers are the configuration and the measurement method.

**(a)** VASE®.

**(b)** M-2000®.

**Figure 3.3:** Ellipsometers adopted for optical characterisation. a) The VASE, whit a vertical sample mount. b) The M-2000, featuring a horizontal sample mount. *(© J.A. Woollam Co.)*

**VASE**

J.A.Woollam VASE ellipsometer is a wide spectral range (UV-Vis-NIR) variable angle spectroscopic ellipsometer. It features a rotating analyzer ellipsometer (RAE) shown in figure 3.4, which consists of an input linear polarizer and a rotating output analyzer[2] allowing to convert the unknown polarized light coming from the sample in a linear polarized light.

Furthermore, a monochromator allows to select the wavelength of input light source, in order to perform a spectroscopic analysis changing ideally a single wavelength at time. Another interesting characteristic is the size of the light beam, which is of the order of some tens of millimeter, avoiding depolarization effects due to a possible

---

[1] For absorbing sample $r_p$ is not zero but has a minimum.

[2] Usually the analyzer is a polarizer which has a different name because of its function.

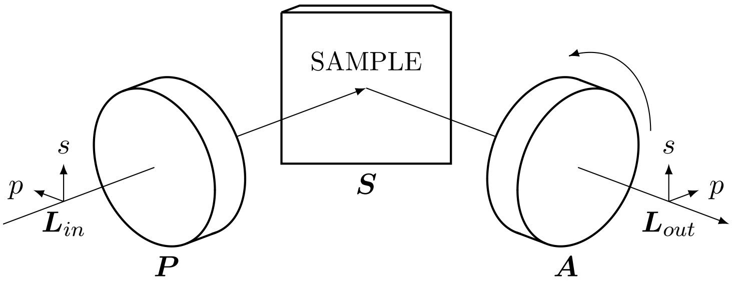

**Figure 3.4:** Sketch of a rotating analyzer ellipsometer (RAE).

thickness non homogeneity when probing a small area. The depolarization transforms the totally polarized light used as a probe into partially polarized light, increasing the error of the instrument. This will occur when the sample is extremely rough or exhibits back-surface effects, when a film on the sample is non-uniform or patterned, and when monochromator bandwidth or angular spread effects are significant.

The output light beam for a RAE, expressed with the Jones matrices for the optical components, reads

$$\boldsymbol{L}_{out} = \boldsymbol{A}\boldsymbol{R}(A(t))\boldsymbol{S}\boldsymbol{R}(-P)\boldsymbol{P}\boldsymbol{L}_{in} \, , \tag{3.8}$$

where $\boldsymbol{L}_{in}$ and $\boldsymbol{L}_{out}$ are the Jones vectors[3] of the incident and reflected beam respectively, $\boldsymbol{S}$ matrix represents the sample, $\boldsymbol{R}(-P)\boldsymbol{P}$ represents the light that transmits the polarizer $\boldsymbol{P}$, having the angular position $P$ with respect to their polarization axis and expressed by the rotating matrix $\boldsymbol{R}(-P)$ (the same notation is adopted for the analyser, where the angular position is a function of time $A(t)$). In this sense we obtain

$$\begin{aligned}\begin{pmatrix} E_{out} \\ 0 \end{pmatrix} = \begin{pmatrix} 1 & 0 \\ 0 & 0 \end{pmatrix} \begin{pmatrix} \cos(\omega t) & \sin(\omega t) \\ -\sin(\omega t) & \cos(\omega t) \end{pmatrix} \begin{pmatrix} \sin\Psi e^{(i\Delta)} & 0 \\ 0 & \cos\Psi \end{pmatrix} \\ \times \begin{pmatrix} \cos P & -\sin P \\ \sin P & \cos P \end{pmatrix} \begin{pmatrix} 1 & 0 \\ 0 & 0 \end{pmatrix} \begin{pmatrix} 1 \\ 0 \end{pmatrix} \, ,\end{aligned} \tag{3.9}$$

and the intensity of the reflected beam at the detector is

$$\begin{aligned} I_{out} &= |E_{out}|^2 \\ &= \frac{I_{in}}{4}[(1 - \cos 2P \cos 2\Psi) + (\cos 2P - \cos 2\Psi)\cos 2\omega t + (\sin 2P \sin 2\Psi \cos\Delta)\sin 2\omega t] \\ &= \frac{I_{in}}{4}[1 - \alpha\cos 2\omega t + \beta \sin 2\omega t] \, , \end{aligned} \tag{3.10}$$

where

$$\alpha = \frac{\tan^2\Psi - \tan^2 P}{\tan^2\Psi + \tan^2 P} \qquad \beta = \frac{2\tan\Psi\cos\Delta\tan P}{\tan^2\Psi + \tan^2 P} \, . \tag{3.11}$$

Therefore, with a RAE it is possible to evaluate ($\alpha$, $\beta$) by performing a Fourier analysis of the measured $I_{out}$ and eventually to obtain ($\Psi$, $\Delta$) from equation (3.11)

$$\tan\Psi = \sqrt{\frac{1+\alpha}{1-\alpha}}\,|\tan P| \qquad \cos\Delta = \frac{\beta}{\sqrt{1-\alpha^2}} \, . \tag{3.12}$$

---

[3] The Jones vector is defined by the electric field vectors in the x and y directions, for a wave travelling along the z direction. In the case of linear polarized light beam, the vector will have the component only along one direction.

Finally, since in RAE the polarization state of reflected light is determined from a variation of light intensity with the analyzer angle, left-circular polarization cannot be distinguished from right-circular polarization; these polarizations show the same light intensity variation versus the analyzer angle.

### M-2000

The M-2000 ellipsometer is made of an analyser fixed in a certain position and another rotating optical element named compensator, which converts a linear polarization in a circular polarization. For this reason the ellipsometer is a rotating compensator ellipsometer (RCE) and in figure 3.5 it is shown a sketch of its operation principle.

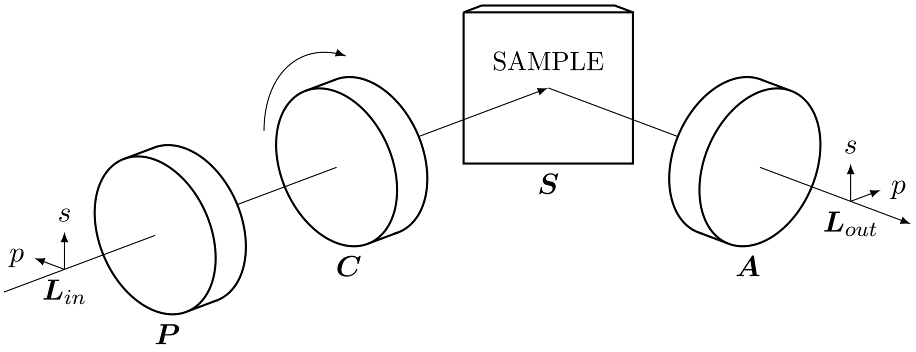

**Figure 3.5:** ketch of a rotating compensator ellipsometer (RCE). P and A are fixed linear polarizers while C convert the linear polarization into a circular one.

Using the Jones formalism, the detected light is

$$\boldsymbol{L}_{out} = \boldsymbol{A}\boldsymbol{R}(A)\boldsymbol{S}\boldsymbol{R}(-C(t))\boldsymbol{C}\boldsymbol{R}(C(t))\boldsymbol{R}(-P)\boldsymbol{P}\boldsymbol{L}_{in} \,, \tag{3.13}$$

hence

$$\begin{aligned}\begin{pmatrix} E_{out} \\ 0 \end{pmatrix} &= \begin{pmatrix} 1 & 0 \\ 0 & 0 \end{pmatrix} \begin{pmatrix} \cos A & \sin A \\ -\sin A & \cos A \end{pmatrix} \begin{pmatrix} \sin\Psi e^{(i\Delta)} & 0 \\ 0 & \cos\Psi \end{pmatrix} \\ &\times \begin{pmatrix} \cos(\omega t) & -\sin(\omega t) \\ \sin(\omega t) & \cos(\omega t) \end{pmatrix} \begin{pmatrix} 1 & 0 \\ 0 & e^{i\phi} \end{pmatrix} \begin{pmatrix} \cos(\omega t) & \sin(\omega t) \\ -\sin(\omega t) & \cos(\omega t) \end{pmatrix} \\ &\times \begin{pmatrix} \cos P & -\sin P \\ \sin P & \cos P \end{pmatrix} \begin{pmatrix} 1 & 0 \\ 0 & 0 \end{pmatrix} \boldsymbol{L}_{in} \,, \end{aligned} \tag{3.14}$$

where $\phi$ represents the phase shift related to the compensator $\boldsymbol{C}$. The intensity on the detector is then [86]

$$I_{out} = I_{in}(\alpha_0 + \alpha_2 \cos 2\omega t + \beta_2 \sin 2\omega t + \alpha_4 \cos 4\omega t + \beta_4 \sin 4\omega t) \,, \tag{3.15}$$

where the angle of the rotating compensator is described as $C = \omega t$ and the normalized

Fourier coefficients read

$$
\begin{aligned}
\alpha_0 =&1 + \frac{1}{2}(1 + \cos\phi)(\cos 2A \cos 2P - \cos 2P \cos 2\Psi + \sin 2A \sin 2P \sin 2\Psi \cos\Delta) \\
&- \cos 2A \cos 2\Psi \\
\alpha_2 =& - \sin 2A \sin 2P \sin\phi \sin 2\Psi \sin\Delta \\
\beta_2 =& \sin 2A \cos 2P \sin\phi \sin 2\Psi \sin\Delta \\
\alpha_4 =&\frac{1}{2}(1 - \cos\phi)(\cos 2A \cos 2P - \cos 2P \cos 2\Psi - \sin 2A \sin 2P \sin 2\Psi \cos\Delta) \\
\beta_4 =&\frac{1}{2}(1 - \cos\phi)(\cos 2A \cos 2P - \cos 2P \cos 2\Psi + \sin 2A \sin 2P \sin 2\Psi \cos\Delta)
\end{aligned}
\tag{3.16}
$$

An important characteristic related to the angle of the compensator $C$ with respect to the light intensity variation period, is that the light intensity variation of left-circular polarization versus C becomes opposite to that of right-circular polarization. The signs of the normalized Fourier coefficient $\alpha_2$ are reversed and left- and right-circular polarizations are distinguished in RCE measurement. Another characteristic which differs from VASE ellipsometer is that the M-2000 does not use the monochromator and the measurements are done by acquiring all the analysed wavelengths simultaneously, reducing the measurement time. Furthermore, the light beam of M-2000 is larger than the VASE one, probing larger surface area. In order to reduce depolarization effects related to the large investigated area it is possible to reduce the beam light size using an iris. However, a smaller light spot implies a smaller intensity of the detected signal and a compromise is needed to find the right beam size and the intensity of the output signal.

### 3.1.2 Optical Models

In spectroscopic ellipsometry, the dielectric constants of the material are worked out from ($\Delta$, $\Psi$) parameters through a model which represents the material optical response. The dielectric function of the coating is then obtained by using a method called *mathematical inversion* after the comparison of the experimental data with the model. This is the most significant limit of ellipsometric measurements: indeed, no matter how complex and realistic it is, each model represents just an approximation of the real system. However, once the model is validated, spectroscopic ellipsometry allows accurate and fast characterizations.

Several models exist to represent the electric function of the sample. In figure 3.6 the most common models used in spectroscopic ellipsometry are shown.

In principle, we can distinguish two regions of photon energy. At high energies, from the visible to ultraviolet (UV-Vis), there is the absorption edge, described by several models such as the Cody-Lorentz, Tauc-Lorentz or harmonic oscillator approximation (HOA). Most of them are a Lorentz model extension. At lower energies, in the infrared (IR) region, amorphous oxides do not present strong absorption and models for transparent region such as Sellmeier or Cauchy are adopted. Finally, if the absorption is related to free electrons, it is convenient to adopt the Drude model. In the following these models will be described in detail.

**Lorentz Oscillator**

The Lorentz model is a classic model which describes the optical properties of linear and homogeneous dielectric materials, without considering free electrons.

In this model the dielectric solid is considered as a viscous solid described by multiple spring-mass systems. The single spring-mass system is illustrated in figure

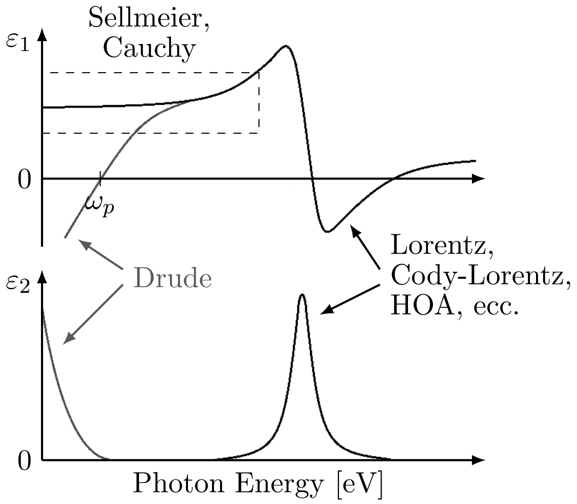

**Figure 3.6:** Most common optical models.

3.7.

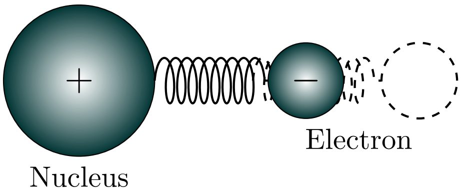

**Figure 3.7:** Oscillating dipole.

When an external oscillating electric field is applied to the system, the charges polarize along the field direction and start to oscillate around their equilibrium positions. Since the nucleus is much more massive than the electron, if the frequency of the oscillating field is high, it is possible to assume the nucleus motionless and consider only the motion of the electron. If the electric field $\vec{E}$ oscillates along the $x$ direction, we obtain

$$m_e\ddot{x} = -m_e\Gamma\dot{x} - m_e\omega_0^2 x - eE_0 e^{i\omega t}\,, \tag{3.17}$$

where $m_e$ is the mass of the electron with charge $e$, $\Gamma$ the viscous damping coefficient and $\omega_0$ the resonance frequency. The total force described by equation (3.17) is made on three terms. The first term is related to the viscosity of the system, where the force is proportional to the electron velocity in under-dumped condition, the second represents the elastic force described by the Hooke's law, the third is the Coulomb's force.

Since the electron has the same frequency as the electric field $E = E_0 e^{i\omega t}$, it is possible to assume as solution $x(t) = ae^{i\omega t}$ and from equation (3.17)

$$a = -\frac{eE_0}{m_e}\frac{1}{(\omega_0^2 - \omega^2) + i\Gamma\omega}\,. \tag{3.18}$$

Considering $N_e$ electrons we obtain the polarization

$$P = -eN_e x(t) = -eN_e a e^{i\omega t}\,, \tag{3.19}$$

which is useful to obtain the dielectric function of the Lorentz model using equation

(2.5)

$$\varepsilon = 1 + \frac{A}{(\omega_0^2 - \omega^2) + i\Gamma\omega} \, , \tag{3.20}$$

where $A = (e^2 N_e)/(\varepsilon_0 m_e)$ and the real and imaginary parts read

$$\varepsilon_1 = 1 + A \frac{(\omega_0^2 - \omega^2)}{(\omega_0^2 - \omega^2)^2 + (\Gamma\omega)^2} \, , \tag{3.21a}$$

$$\varepsilon_2 = A \frac{\Gamma\omega}{(\omega_0^2 - \omega^2)^2 + (\Gamma\omega)^2} \, . \tag{3.21b}$$

In figure 3.8 the real and imaginary part of the dielectric function are shown. The curves represent the typical behaviour of the linear theory response function. Indeed, the Lorentz model is Kramers-Kronig consistent. Under this consideration, the physical model will represents the imaginary part $\varepsilon_2$ and real part $\varepsilon_1$ is then obtained from the Kramers-Kronig relations (2.8).

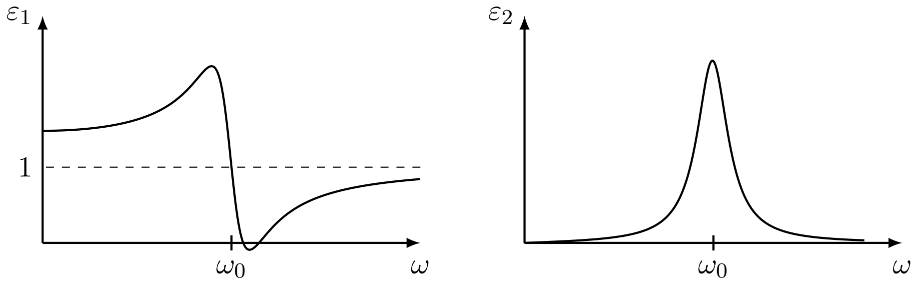

**(a)** Real part. **(b)** Imaginary part.

**Figure 3.8:** Dielectric function of Lorentz model. (a) The real part of the dielectric function $\varepsilon$, (b) the imaginary part.

If we now consider the general case where multiple oscillators are involved, different resonance frequencies associated to different energetic levels of the solid must be considered. In this sense, the dielectric function is made by the superposition of several oscillators

$$\varepsilon = 1 + \sum_n \varepsilon_n \, , \quad \text{where} \quad \varepsilon_n = \frac{A}{(\omega_n^2 - \omega^2) + i(\Gamma_n \omega)} \, . \tag{3.22}$$

In order to analyse the experimental data it is useful to express the dielectric function $\varepsilon_n$ as function of the photon energy

$$\varepsilon_{n2} = A\hbar^2 \frac{Br_n E}{(E_n^2 - E^2)^2 + (Br_n E)^2} = \frac{A_n E_n Br_n E}{(E_n^2 - E^2)^2 + (Br_n E)^2} \, , \tag{3.23}$$

where the three parameters $A_n = (A\hbar^2)/(E_n)$, $E_n = \hbar\omega_n$ and $Br_n = \hbar\Gamma_n$ have the dimension of the energy in $eV$ and they are referred to the amplitude of the n-th oscillator, its energy position and the resonance peak width, respectively. In figure 3.9 an example of the $\varepsilon_1$ behaviour considering multiple oscillator is shown.

If we consider only the n-th oscillator, the real part of the dielectric function $\varepsilon_n$ will have an offset $\varepsilon_{1\text{off}}$ which accounts for the presence of resonances at lower energies.

### Transparent Region

For reasons that will be clear later we first analyse the transparent region where the absorption is considered null as well as $\varepsilon_2$. A model describing the transparent region

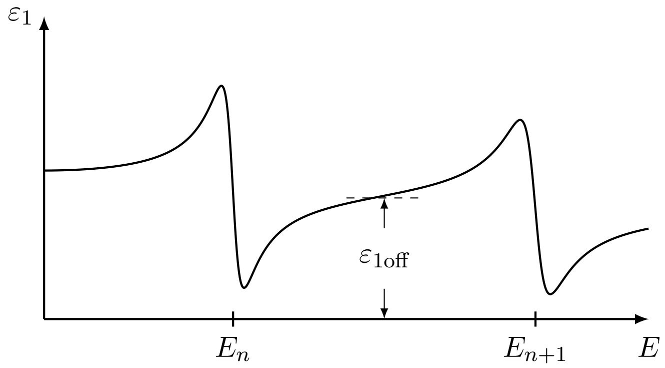

**Figure 3.9:** Real part of the dielectric function for the Lorentz oscillator.

can be derived from the Lorentz model. If we consider energies far from the resonance frequency, the width $\Gamma \to 0$ and $\varepsilon_2 \sim 0$. Using the relation $\omega/c = 2\pi/\lambda$, from equation (3.21a) we obtain

$$\varepsilon_1 = 1 + \frac{e^2 N_e}{\varepsilon_0 m_e (2\pi c)^2} \frac{\lambda_0^2 \lambda^2}{\lambda^2 - \lambda_0^2} = 1 + B \frac{\lambda_0^2 \lambda^2}{\lambda^2 - \lambda_0^2} \,, \tag{3.24}$$

which represents the Sellmeier model. In the presence of several oscillators

$$\varepsilon_2 = 0 \qquad \varepsilon_1 = n^2 = A + \sum_n B_n \frac{\lambda^2}{\lambda^2 - \lambda_n^2} \,, \tag{3.25}$$

where $A$ is the constant value of $\varepsilon_1$ to be ascribed to the oscillators at higher energies.

Considering a single oscillator, it is possible to derive a basic model which describes the refractive index. If we assume $\lambda \gg \lambda_0$, equation (3.24) can be written as

$$n = A + B_0 \frac{1}{1 - \left(\frac{\lambda_0}{\lambda}\right)^2} \,, \tag{3.26}$$

which can be expressed in the series expansion

$$n = A + \frac{B}{\lambda^2} + \frac{C}{\lambda^4} + ... \qquad k = 0 \,, \tag{3.27}$$

where $A, B$ and $C$ are the coefficients of the series. Equation (3.27) represents the Cauchy model. In figure 3.10 the Cauchy model derived from the Lorentz oscillator is shown. In particular, the refractive index $n$ approaches the constant $A$ as we get far from the resonance, at lower frequencies. On the other hand, $B$ and $C$ parameters rule the shape of the curve. Furthermore, since $A$ is the constant parameter of $n$, the offset $\varepsilon_{1\mathrm{off}}$ is included in the model.

Another model which describes the refractive index in the transparent region takes into account the absorptions in the two limits of the considered energy region. Despite this model is not obtained from physical considerations, it represents well the behaviour of the refractive index in the whole transparent region of interest. This model uses two poles to describe the real part of the dielectric function

$$\varepsilon_2 = 0, \quad \varepsilon_1 = \sum_n \varepsilon_{polo\_n} = \sum_n \frac{A_n}{E_n^2 - E^2} \quad n = 1, 2 \,, \tag{3.28}$$

where $A_n$ is the amplitude in $(eV)^2$ and $E_n$ the energy position of the n-th pole. Since there are only parameters that define the shape of the refractive index, the value $\varepsilon_{1\mathrm{off}}$

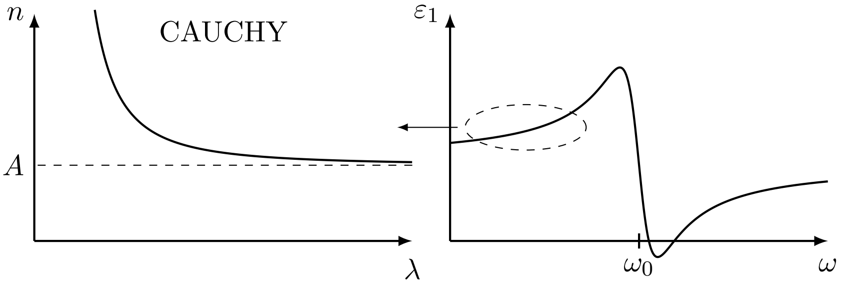

**Figure 3.10:** Cauchy model on the left and Lorentz model on the right. In the Lorentz model the transparent region described by the Cauchy model is highlighted.

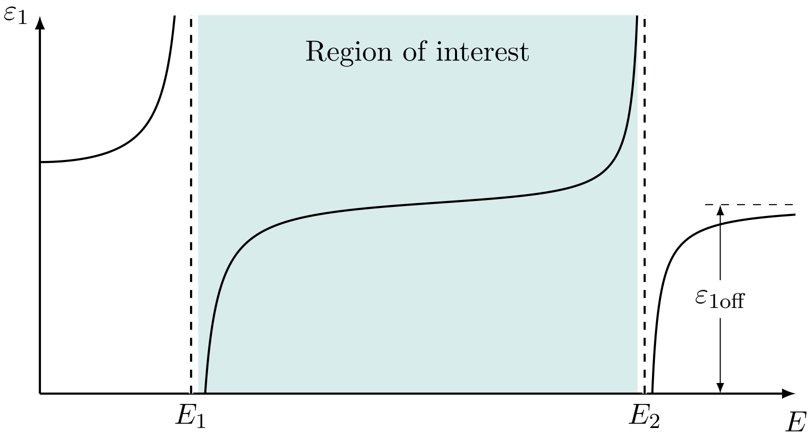

**Figure 3.11:** Two-poles model, with poles in $E_1$ and $E_2$.

is included in the model to consider the presence of resonances at higher energies. In figure 3.11, $\varepsilon_1$ obtained by the two-poles model is shown

Since the described models for transparent region consider $k \cong 0$ and are limited to a restricted region, they are not Kramers-Kronig consistent from a strictly mathematical point of view.

The models describing the transparent region are useful in order to perform a preliminary investigation of optical properties in the IR region, where the amorphous oxides show an extremely low absorption. For this reason, for each sample the transparent region has been at first investigated to obtain preliminaries informations about the coating thickness and refractive index, then the analysis has been extended to the UV region using models which describe the absorption edge. The Lorentz model is not suitable to describe the absorption of amorphous solids, for this reason a model which include Tauc or Cody behaviour is needed.

### Tauc-Lorentz and Cody-Lorentz models

The Tauc-Lorentz model developed by Jellison [87] combines the absorption edge described by Tauc (chapter 2) with the Lorentz oscillator in order to describe the joint density of states (JDOS) of amorphous solids. In this sense, we obtain a parametrization of the imaginary part of the dielectric function

$$\varepsilon_2 = \begin{cases} L(E)G_T(E), & E > E_g\,, \\ 0, & E \leq E_g\,, \end{cases} \tag{3.29}$$

where $L(E)$ is the Lorentz oscillator (3.23) and $G_T(E)$ represents the absorption edge described by Tauc

$$G_T(E) = \frac{(E - E_g)^2}{E^2} \, . \tag{3.30}$$

Hence, outside the gap $E_g$ we obtain

$$\varepsilon_2 = \frac{AE_0C(E - E_g)^2}{(E^2 - E_0^2)^2 + C^2E^2} \frac{1}{E} \, , \tag{3.31}$$

where $A$ is the amplitude, $E_0$ the transition energy and $C$ the peak width, expressed in $eV$. In figure 3.12, the $\varepsilon_2$ behaviour for Tauc-Lorentz model is shown.

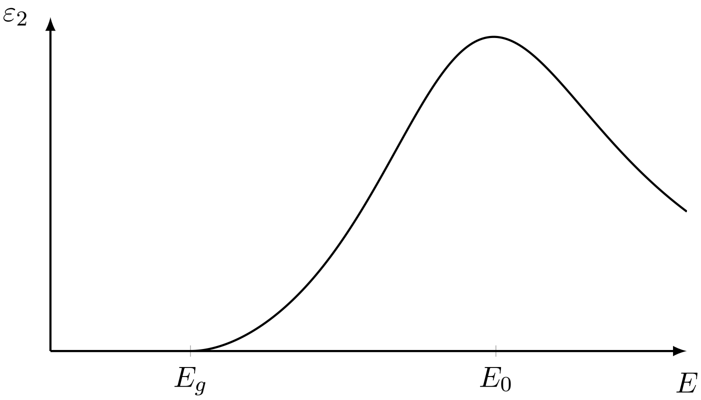

**Figure 3.12:** Imaginary part of the dielectric function $\varepsilon_2$ described by Tauc-Lorentz model.

This model is well known in literature and describes successfully the absorption edge of amorphous solids. However, $\varepsilon_2 = 0$ does not allow to describe the presence of defects as well as the distortions represented by the Urbach tails provide transition including states within the gap, giving a non zero $\varepsilon_2$.

As an alternative to the Tauc-Lorentz model, the Cody-Lorentz model developed by Ferlauto *et al.* [88] includes the urbach tails transitions. Furthermore, it is similar to the Tauc-Lorentz in the strong absorption region, where the Lorentz oscillator is modulated by the Cody behaviour of the absorption edge for amorphous solids

$$\varepsilon_2 = \begin{cases} L(E)G_C(E), & E > E_t \, , \\ \dfrac{E_1}{E} e^{(E - E_t)/E_u}, & E \leq E_t \, , \end{cases} \tag{3.32}$$

where $E_1$ is defined by the continuity condition $E_1 = E_t L(E_t) G_C(E_t)$ , $E_u$ represents the extension of the Urbach tails and $E_t$ is the transition energy between localized-extended and extended-extended transitions. As observed in (3.29) and (3.32), the difference in the strong absorption region resides in the choice of the function multiplied by the Lorentz oscillator. In the case of Cody behaviour, the expression $\varepsilon_2 \propto (E - E_g)^2$ can not be applied to $G_C(E)$ because it diverges with the energy. For this reason the following expression is adopted

$$G_C(E) = \frac{(E - E_g)^2}{(E - E_g)^2 + E_p^2} \, , \tag{3.33}$$

where $E_p$ is the limit energy between the Cody behaviour and the Lorentz oscillator. It can be shown that if $E \approx E_g$ then $G_C(E)$ follows the Cody behaviour, whereas if $E \gg E_p$ then $G_C(E) \to 1$.

Following Ferlauto *et al.* [88], the absolute value of $E_t$ is used in the model. However, the analysis in the following chapter are done by considering $E_t \rightarrow (E_g + E_t)$, and than inside the gap we obtain

$$\varepsilon_2 = \frac{E_1}{E} e^{(E-(E_g+E_t))/E_u} \,. \tag{3.34}$$

In figure 3.13, the imaginary part of the dielectric function for the Cody-Lorentz model is shown, where a zoom highlights the energy transitions separating the different trends.

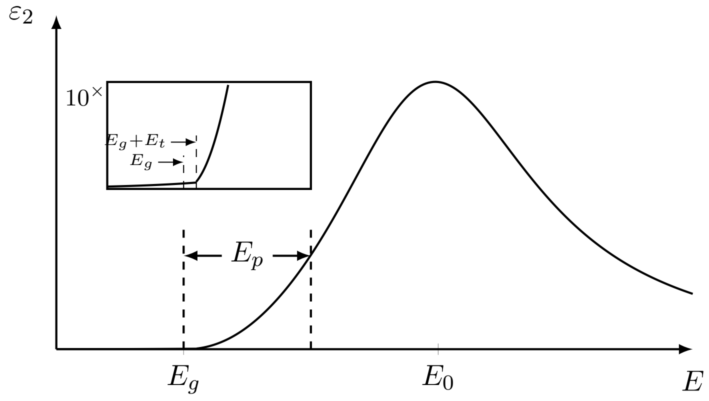

**Figure 3.13:** Imaginary part of the dielectric function $\varepsilon_2$ for the Cody-Lorentz model. In the zoom, the energy transition $E_g+E_t$ are showed.

$\varepsilon_1$ can be obtained starting from $\varepsilon_2$ using Kramers-Kronig integrals (2.8). However, the TL and CL formulae define $\varepsilon_2$ through peace-wise functions. Some authors discuss the limitations that this fact involves regarding the full Kramers-Kronig consistency of these models [89, 90].

### Parametric Model

Another method to describe the optical properties of solids is to reproduce the dielectric function with an analytical expression, based on parametric functions. In this respect, Herzinger *et al.* developed the so-called parameterized semiconductor (PSEMI) oscillator, a parametric model which describes the absorption of semiconductors [91]. It has to be noticed that the parameters used in this model do not have a direct physical meaning; it is the behaviour of the dielectric function which is important. In figure 3.14 the PSEMI function is shown, which is similar to a Gaussian oscillator, where four polynomial functions ($F_I$, $F_{II}$, $F_{III}$, $F_{IV}$) are connected respected continuity.

In the generic model developed by Herzinger and Johs, 12 parameters are needed to obtain the dielectric function. Three of them $E_0$, $A$ and $B$ are the energy of the oscillator, the amplitude and the peak width respectively. Furthermore, other parameters modify the shape of the oscillator. In particular, $W_L$, $P_L$, $A_L$ and $O2_L$ are the width of the left region of the absorption, the energy position of the connecting point between $W_L$ and $E_0$, the amplitude of the connecting point and the second order parameter for the $F_I$ and $F_{II}$ polynomials. In the same way, $W_R$, $P_R$, $A_R$ and $O2_R$ parameters are related to the right region of the absorption. The last parameter $Disc$ rules the discontinuity. However, the PSEMI model used for the analysis in the following section is one of the five PSEMI type available from J. A. Woollam Co.[4] models, which allows to modify only 7 parameters and $Disc$ is set to zero. In table 3.1 the seven models are listed, highlighting the editable parameters.

---

[4] jawoollam.com

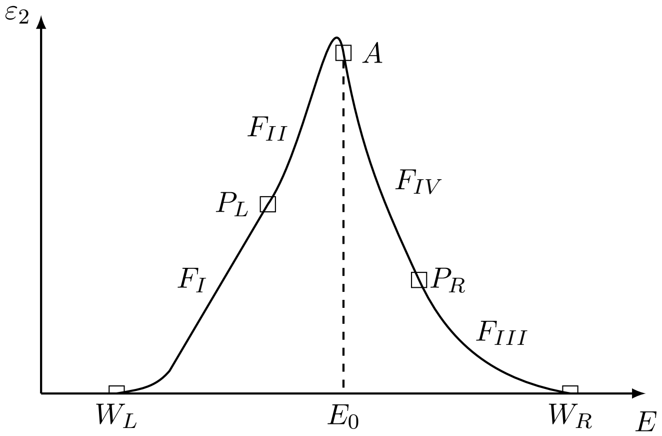

**Figure 3.14:** Example of PSEMI oscillator.

| **Psemi** | $E_0$ | $A$ | $B$ | $W_L$ | $W_R$ | $P_L$ | $A_L$ | $P_R$ | $A_R$ | $O2_L$ | $O2_R$ |
|---|---|---|---|---|---|---|---|---|---|---|---|
| PSM0 | ✓ | ✓ | ✓ | 0 | ✓ | 0.5 | 0.5 | ✓ | ✓ | 0 | ✓ |
| PSM1 | ✓ | ✓ | ✓ | ✓ | ✓ | 0.75 | ✓ | 0.5 | ✓ | 1 | 0 |
| PSM2 | ✓ | ✓ | ✓ | ✓ | ✓ | 0.5 | ✓ | 0.75 | ✓ | 0 | 1 |
| PSM3 | ✓ | ✓ | ✓ | ✓ | 0 | ✓ | ✓ | 0.5 | 0.5 | ✓ | 0 |
| PSTRI | ✓ | ✓ | ✓ | ✓ | ✓ | 0.5 | ✓ | 0.5 | ✓ | 0 | 0 |

**Table 3.1:** Editable parameters of PSEMI models available from J. A. Woollam Co.

### Mixtures

Sometimes the sample is not homogeneous and is characterised by a mix of several materials or presents regions with different density. In order to represent this kind of sample it is useful to use an effective medium approximations (EMA). In order to represent the optical properties of such system, it is convenient to relate the macroscopic properties of the system such as the dielectric function $\varepsilon$, with the microscopic properties, such as the atomic polarization $\alpha$. This relation is given by the Clausius-Mossotti [92] formula

$$\frac{\varepsilon - 1}{1 + (\varepsilon - 1)L} = \frac{N\alpha}{\varepsilon_0} \,, \tag{3.35}$$

where $N$ is the atomic density and $L$ is the depolarization factor which takes into account the geometry of the system[5]. If we consider $j$ different materials, we can assume, as first approximation, that a linear combination of the several polarizations gives the total one

$$\frac{\varepsilon - 1}{1 + (\varepsilon - 1)L} = \sum_j \frac{N_j \alpha_j}{\varepsilon_0} \,. \tag{3.36}$$

Using the relation (3.35)

$$\frac{\varepsilon - 1}{1 + (\varepsilon - 1)L} = \sum_j f_j \frac{\varepsilon_j - 1}{1 + (\varepsilon_j - 1)L} \,, \tag{3.37}$$

---

[5] In the case of a sphere, the depolarization factor is $L = 1/3$.

where $f_j$ is the volume covered by the $j$-th component with respect to the total volume. If we have a medium surrounded by a host dielectric having $\varepsilon_h$, relation (3.37) reads

$$\frac{\varepsilon - \varepsilon_h}{\varepsilon_h + (\varepsilon - \varepsilon_h)L} = \sum_j f_j \frac{\varepsilon_j - \varepsilon_h}{\varepsilon_h + (\varepsilon_j - \varepsilon_h)L} \,, \tag{3.38}$$

where the dielectric function of the entire mixed system $\varepsilon$ depends on the dielectric functions of the individual component, the relative covered volume and their morphology.

In the Maxwell-Garnett (MG) EMA, the relation (3.38) considers the $l$-th material as the host (figure 3.15a). In this respect we obtain

$$\frac{\varepsilon - \varepsilon_l}{\varepsilon_l + (\varepsilon - \varepsilon_l)L} = \sum_{j \neq l} f_j \frac{\varepsilon_j - \varepsilon_l}{\varepsilon_l + (\varepsilon_j - \varepsilon_l)L} \,. \tag{3.39}$$

This model is largely used to represent voids inclusion in the material or to describe the roughness of the sample surface. In particular, the surface is described by a thin layer having the dielectric function of the material at the top of the sample under investigation, including 50% of voids.

The Bruggeman EMA considers the host material as the mixing itself $\varepsilon = \varepsilon_h$ (figure 3.15b), so that

$$0 = \sum_{j \neq l} f_j \frac{\varepsilon_j - \varepsilon}{\varepsilon + (\varepsilon_j - \varepsilon)L} \,. \tag{3.40}$$

This model is used in case of homogeneous mixed materials, where it is not possible to recognise the host material. During the analysis of our coating, this model is used to represent the surface roughness, mixing the coating optical properties with air.

Finally, in the presence of a porous sample, the system is described by the Lorentz-Lorentz (LL) EMA, where the host material has $\varepsilon_h = 1$

$$\frac{\varepsilon - 1}{1 + (\varepsilon - 1)L} = \sum_j f_j \frac{\varepsilon_j - 1}{1 + (\varepsilon_j - 1)L} \,. \tag{3.41}$$

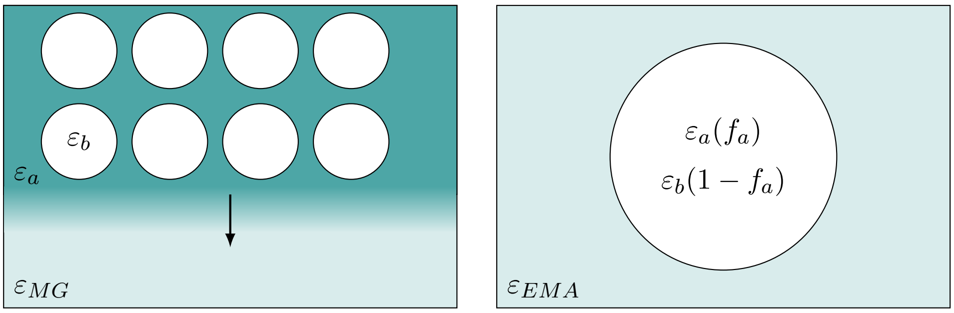

**(a)** Maxwell-Garnett. **(b)** Bruggeman.

**Figure 3.15:** Spherical inclusions in two materials. a) The Maxwell-Garnet model, b) The Bruggeman model.

### Non-ideal Model

When we create a model, it represents the ideal physical features which determine the optical properties of the sample. In the real case, the sample could present non ideal characteristics which cause depolarization of light and affect the measurement. For example, a coating thickness non uniformity may refract differently the wavelength of the light beam which has a finite size and cover a certain area of the coating surface. Another parameter can be related to the ellipsometer. The bandwidth of the monochromator or the diffraction grating has a finite value and when we select a wavelength there is the possibility to select also the adjacent one. All this parameters should be included in the model if necessary.

### 3.1.3 Analysis Procedure

The protocol adopted to analyse the sample is described by the diagram in figure 3.16. When we are interested on coatings properties, the substrate must be characterised with previous dedicated measurements so that its optical properties can be used to develop the model for the coated sample. For each sample, the first step is to measure all the energies probed by the ellipsometers. Usually, measurements are done at different angles 55°, 60° and 65° around the Brewster's angle ($\theta_B \sim 55.3°$ for silica and $\theta_B \sim 63.7°$ for tantala). This is useful in order to increase the sensitivity to $\Delta$.

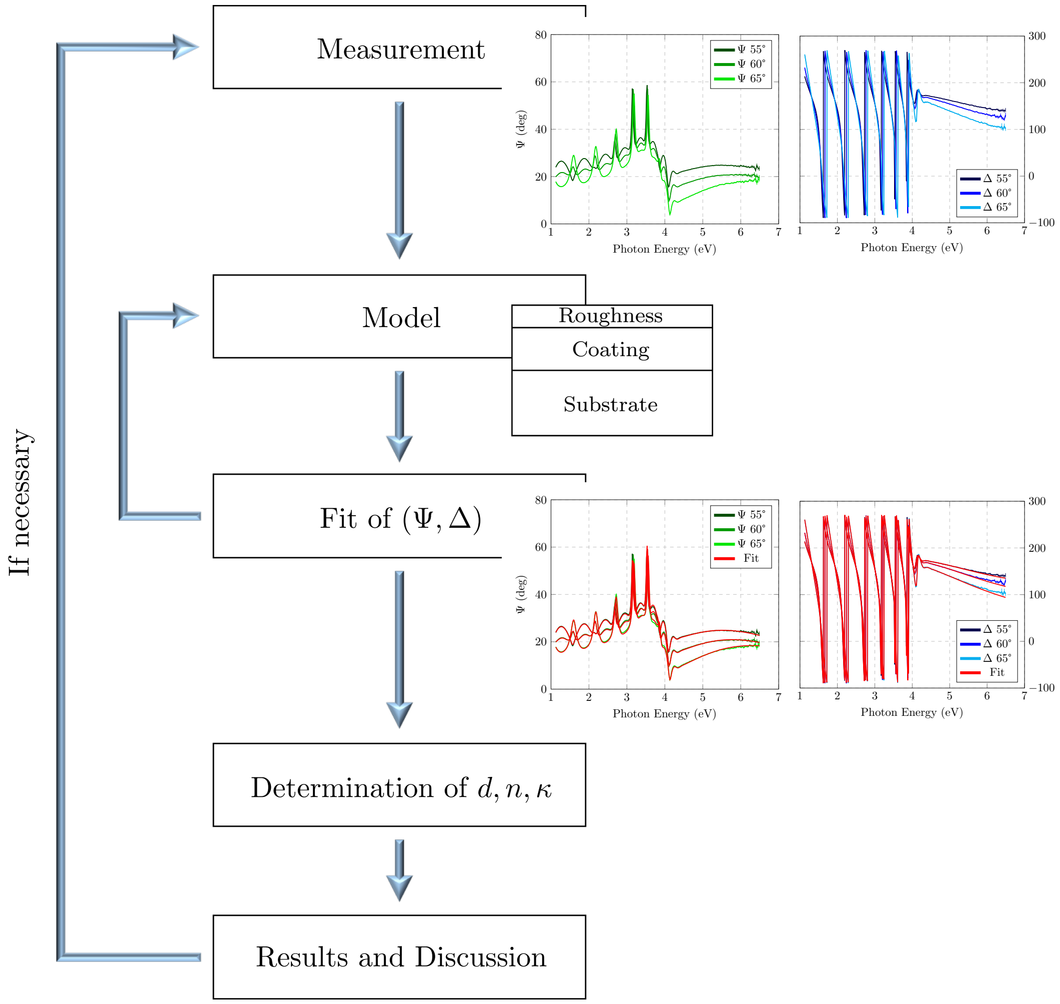

**Figure 3.16:** Diagram of the protocol for spectroscopic ellipsometry measurements.

In order to obtain information about the coating optical properties we have to create a model to describe the dielectric function and hence, using equation (3.5), to reproduce the $(\psi, \Delta)$ data. The model simulates $(\psi, \Delta)$ data which have to be compared to the experimental curves. If the fit is not satisfactory, the model should be improved. Usually it is possible to develop different adequate models and eventually obtain comparable results, for this reason the final optical properties should take into account all the possible representations. Finally, the results must be discussed and considered to define the most appropriate optical properties and thickness of coating materials.

This protocol is applied in measurements done with both VASE and M-2000 ellipsometers. Since they are based on different technologies, they produce different experimental data. For that reason, the analysis done independently with the two instruments must be compared to obtain the best and most adequate results. Furthermore, VASE ellipsometer is more appropriate than M-2000 to analyse the coating presented in this work. In fact, VASE probes a restricted surface area and has a small bandwidth, making this ellipsometer a convenient instrument to investigate the absorption edge in the UV region.

By combining the data obtained from the two instruments, it is possible to investigate a wide energy region, 0.7 - 6.5 eV. The two ellipsometers cover an overlapping energy region where comparable results can be obtained. The extended energy region contains the absorption edge of the investigated samples in the UV region and the transparent region in the Vis-NIR, including the 1064 nm wavelength used in gravitational-wave detectors. To obtain more accurate results, a preliminary analysis is done in the transparent region in order to obtain information about thickness and refractive index. The analysis is then extended to the whole energy region, trying to create a general model which gives comparable results in the transparent region. This model should be as simple as possible, representing the physics of the system. Finally, when it is necessary, the model could be refined including non-ideal effects which cause depolarization, such as the finite bandwidth of the ellipsometers.

The consistency of the model is checked by the minimization of the Mean Square Error (MSE). This parameter represents the quadratic difference between the experimental data and simulations

$$MSE = \frac{1}{2N - M} \sum_{i=1}^{N} \left[ \left| \frac{\Psi_i^{mod} - \Psi_i^{exp}}{\sigma_{\Psi,i}^{exp}} \right|^2 + \left| \frac{\Delta_i^{mod} - \Delta_i^{exp}}{\sigma_{\Delta,i}^{exp}} \right|^2 \right] , \tag{3.42}$$

where $i$ is the photon wavelength or energy index ($N$ is the total number of $(\Psi^{exp}, \Delta^{exp})$ experimental points[6]), $M$ the number of parameters included in the model, $(\Psi^{mod}, \Delta^{mod})$ the simulated quantities and $\sigma^{exp}$ the standard deviation of the experimental data.

There are several possibilities to reduce the standard deviation such as the precision of the angle of incidence, the calibration of the ellipsometer or reducing the depolarization effects. Furthermore, In order to reduce $\sigma$ it is possible to increase the number of revolutions of the rotating element of the ellipsometers so that the measurement corresponds to an average done on several periods.

## 3.2 The Resonant Method

In chapter 2 anelastic properties of amorphous solids have been treated in details. One possible method to study the elastic properties of solids is the observation of the compliance during the relaxation after an external excitation. In this respect, the resonance method [75] is a valid option. If a periodic stress is applied to the sample

$$\sigma = \sigma_0 e^{i\omega t} , \tag{3.43}$$

---

[6] It has to be noted that the MSE is calculated for both the $\Psi$ and $\Delta$ data at the same time.

where $\sigma_0$ is the amplitude and $\omega$ the angular frequency, the deformation should be periodic with the same frequency

$$\varepsilon = \varepsilon_0 e^{i(\omega t - \phi)} \,, \tag{3.44}$$

where $\varepsilon_0$ is the amplitude of the deformation and $\phi$ is the so-called loss angle. The compliance $J$ will be then composed of a real and an imaginary term

$$\begin{aligned} J(\omega) &= \frac{\varepsilon}{\sigma} = |J|\, e^{-i\phi(\omega)} \\ &= J_1(\omega) + iJ_2(\omega) \,. \end{aligned} \tag{3.45}$$

In the case of an ideal elastic solid, the loss angle must be zero ($\phi \to 0$).

For a better understanding of $J_1$ and $J_2$, it can be useful to make some comments about the energy of the system during the vibration. From equation (B.4) we can obtain the dissipated energy (per unit volume) during a cycle

$$\Delta E = \oint \sigma d\varepsilon = \pi J_2 \sigma_0^2 \,, \tag{3.46}$$

while the maximum stored energy density reads

$$E = \int_{\omega t=0}^{\pi/2} \sigma d\varepsilon = \frac{1}{2} J_1 \sigma_0^2 \,. \tag{3.47}$$

It is now clear that the real part of the compliance $J$ is related to the stored energy in the solid, while the imaginary part to the dissipation. Furthermore accordingly with equation (2.108), using equations (3.45), (3.46) and (3.47) it is possible to obtain the loss angle

$$\tan\phi = \frac{J_2}{J_1} = \frac{1}{2\pi} \frac{\Delta E}{E} = \mathcal{Q}^{-1} \,, \tag{3.48}$$

where $\mathcal{Q}$ is the mechanical *quality factor*. From equation (3.48) it can be observed that $\tan\phi$ quantifies the dissipated internal energy for an anelastic deformation. For this reason, the loss angle is also called internal friction.

To measure $\phi(\omega)$ it is necessary to put the system in resonance at frequency $\omega$ and to evaluate the amplitude of the deformation with the relative phase. During the oscillations, the differential equation describing the energy during time is

$$\frac{dE}{dt} = \Delta E / T \,, \tag{3.49}$$

where $T$ is the period of the oscillations. From equation (3.48) the energy variation (under the small oscillation condition, i.e. $\tan\phi \sim \phi$) is

$$\frac{\Delta E}{E} = 2\pi\phi \,, \tag{3.50}$$

with the energy $E(t) = E_0 e^{-2t/\tau}$ and the decay time

$$\tau = T/(\pi\phi) \,. \tag{3.51}$$

Since the energy is quadratic in the strain $\varepsilon$ (see equation (2.38)), we obtain

$$\varepsilon(t) = \varepsilon_0 e^{-t/\tau} \,. \tag{3.52}$$

In figure 3.17 the strain is plotted over the time.

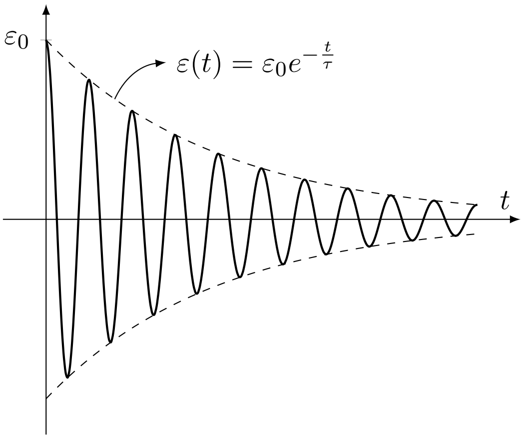

**Figure 3.17:** Strain $\varepsilon(t)$ as function of the time $t$.

Considering $T = 2\pi/\omega = 1/\nu_0$, where $\nu_0$ is the resonance frequency, we obtain

$$\phi^{-1} = \mathcal{Q} = (\pi\nu_0\tau) . \tag{3.53}$$

In the general case, we have to consider several resonance modes $j$

$$\phi_j = \mathcal{Q}_j^{-1} = (\pi\nu_j\tau_j)^{-1} . \tag{3.54}$$

Thus, in order to evaluate the loss angle, it is convenient to excite the sample with a periodic stress and then to measure the decay time for a mode having resonance frequency $\nu_j$, after the excitation is removed.

### 3.2.1 Gentle Nodal Suspension (GeNS)

It is of fundamental importance that the energy during the loss measurement is dissipated only by the internal friction of the sample, and not by any other different mechanism. One of the usual suspension system is clamping of cantilever blades [93] (figure 3.18a); with this system, measurements could be easily spoiled by the friction at the contact surface between the sample and the clamp.

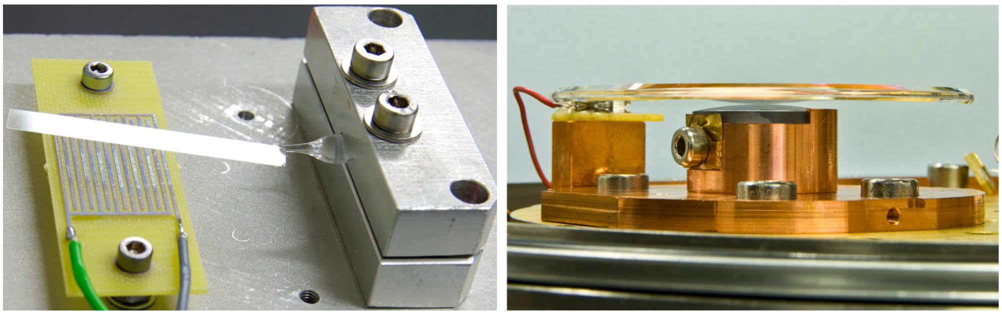

**(a)** Cantilever blade. **(b)** GeNS.

**Figure 3.18:** Suspension systems for the mechanical loss characterization: a) clamping of a fused-silica cantilever blade; b) spherical support of GeNS with a fused-silica disk on top [94].

If we change the suspension system, clamping can be avoided. Most of the resonance modes of disk-shaped resonators present a nodal point at the center, as it can

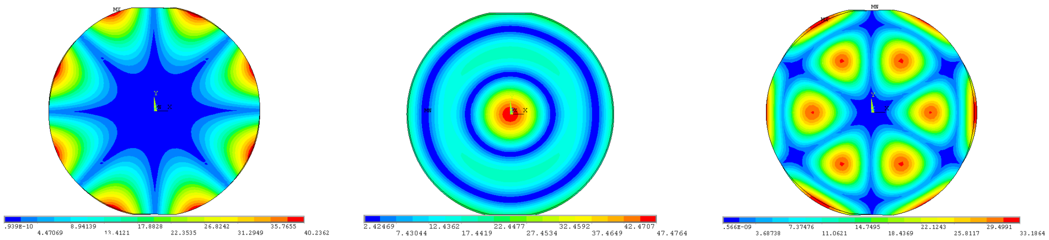

**Figure 3.19:** Vector displacement sum of disk-shape resonance mode for a finite element simulation. The displacement goes from zero (blue) to the maximum of the deformation during the vibration (red). The three examples show modes (n,m) with n radial nodes and m azimuthal nodes: mode (0,4) on the left, mode (2,0) in the middle and mode (1,3) on the right.

be seen by looking at finite element simulations of silica disks, for instance, shown in figure 3.19. Therefore, it is possible to suspend the sample from the center, using the Gentle Nodal Suspension [94–97] (GeNS) system. However, a drawback is that modes vibrating at the center can not be measured because of the central contact point.

As shown in figure 3.18b, GeNS is made of a spherical support which allows ideally one-point contact at the center of the disk. In figure 3.20 a sketch of GeNS system shows the disk suspended on a sphere, having the possibility of rolling motion. In a pure rolling condition, the vertical position $h(\theta)$ of the center of the mass (CM) can be expressed as function of the angular position of the disk $\theta$

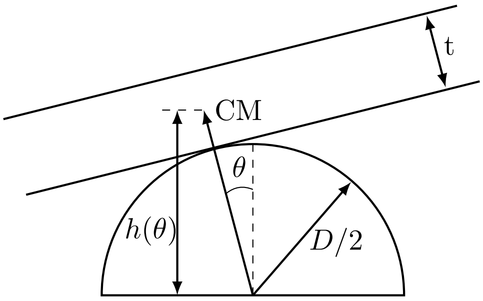

**Figure 3.20:** Sketch of the GeNS support with a disk suspended.

$$2h(\theta) = D\cos(\theta) + D\theta\sin(\theta) + t\cos(\theta)\ , \tag{3.55}$$

where $D$ is the diameter of the sphere and $t$ is the thickness of the disk. Assuming a static friction coefficient $\mu_s$ sufficiently high to avoid any slipping during the motion around the equilibrium position, it possible to show that the equilibrium condition is achieved when $D > t$ [95]. In figure 3.21 three particular conditions are shown: only when $D > t$ we have a minimum in $h(\theta)$.

The GeNS used in this work is made of a silicon lens having 6 cm radius of curvature in a copper mount, for cryogenic operation [97]. Since the samples are dielectric, the mechanical excitation is generated through the electrical polarization of the material. In particular, the vibrational modes $\nu_k$ of the resonator are excited with an AC voltage applied through a comb-shaped capacitor, placed at about 1 millimeter away from the surface of the sample [98] in order to avoid any contact (visible in figure 3.18a). In turn, each mode $k$ is excited well above its ambient noise level; then the excitation is turned off, leaving the resonator free to ring down.

The amplitude of the resonating mode is continuously read out through an optical-lever system, where a He-Ne laser is reflected at the surface of the sample towards a

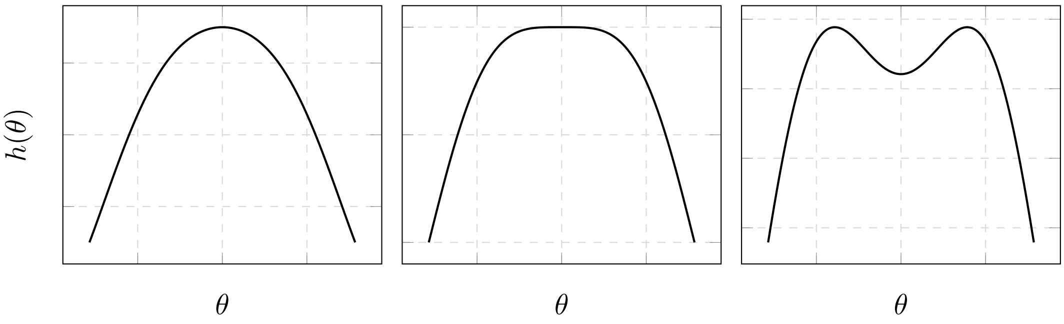

**(a)** $D < t$. **(b)** $D = t$ **(c)** $D > t$

**Figure 3.21:** Vertical position of the CM $h(\theta)$ as function of $\theta$ (in arbitrary unit): a) non-equilibrium condition $D < t$; b) limit condition $D = t$; c) equilibrium condition $D > t$.

photodiode used as a displacement sensor. The measurements are performed using a custom-developed software based on LabVIEW. The software allows to

1. Acquire the signal of the photodiode.
2. Perform the fast Fourier transform of the acquired signal and filter it with a narrow (1 Hz) band-pass filter, centered around the mode frequency.
3. Compute the exponential fit of the envelope $A(t) = A_0 e^{-\frac{t}{\tau_j}}$ of the free decay amplitude of the filtered signal.
4. Calculate the ring-down time $\tau_j$ and the corresponding loss angle $\phi_j = (\pi \nu_j \tau_j)^{-1}$.

The system is installed in a vacuum tank in order to do measurements at $p \leq 10^{-6}$ mbar, to prevent residual-gas damping.

### 3.2.2 Dilution Factor

When we consider a heterogeneous sample, composed by different parts like the substrate and the coating, the total dissipated energy density is the sum of those dissipated in each part. Moreover, energy can be dissipated through several processes and each dissipated energy is proportional to a specific stored energy. Therefore, we have a heterogeneity that comes from the resonator composition but also from the dissipation mechanism involved. Here we are dealing with all kinds of heterogeneity. In one cycle, each part $i$ of the system will dissipate the stored energies, giving rise to different loss angles. Thus, the energy dissipated in one cycle is $E_i = 2\pi E_{\text{tot},i}\phi_i$, where $\phi_i$ and $E_{\text{tot},i}$ are the total loss angle and the total energy stored in the $i$ part of the system, respectively. $E_i$ depends on the stored energies $E_j$ ($j = 1, 2, ...$) dissipated by different mechanisms $\phi_m$,

$$E_i = 2\pi \sum_j E_{j,i} \sum_m \phi_{m,i} \, . \tag{3.56}$$

We can now introduce the definition of the dilution factor $D_{j,i}$ as the ratio between the stored energy $E_{j,i}$ and the total energy $E_i$ of the system, so that

$$\phi_i = \sum_j D_{j,i} \sum_m \phi_{m,i} \, , \tag{3.57}$$

and for the total system

$$\phi_{\mathrm{tot}} = \sum_i \sum_j D_{j,i} \cdot \sum_m \phi_{m,i} \, . \tag{3.58}$$

The previous expression is the most general one that applies to all kind of composed resonators. Now we consider our system composed by a substrate and a coating, both homogeneous and isotropic. Equation 3.58 leads to

$$\phi_{\mathrm{tot}} = D_s \phi_s + D_c \phi_c \, , \tag{3.59}$$

where $\phi_s$ and $\phi_c$ are the loss angles associated to the total energy stored in the substrate and the coating respectively, and $D_s$ and $D_c$ are the dilution factors of the substrate and of the coating, respectively. Since the total energy $E_{\mathrm{tot}}$ is entirely distributed between the two parts $s$ and $c$, we can write

$$\phi_{\mathrm{tot}} = (1 - D)\phi_s + D\phi_c \, , \tag{3.60}$$

where $D = E_c/E_{\mathrm{tot}}$ and $E_{\mathrm{tot}} = E_c + E_s$. Therefore, the coating loss angle reads

$$\phi_c = \frac{\phi_{\mathrm{tot}} - (1 - D)\phi_s}{D} \, . \tag{3.61}$$

Thus, in order to estimate the internal friction of the coating, it is necessary to measure the sample before and after the coating deposition. It is important to highlight the fact that both $\phi_s$ and $\phi_c$ should present a frequency dependence without sharp variations, as predicted by the theory described in chapter 2; we will see in the following that this is not the case. As first approximation, $D$ can be considered constant; however, we will see that it actually depends on the resonant mode shape and hence on frequency.

Following the theory of elasticity of isotropic materials, the energy density in each infinitesimal volume of the disk-shaped resonator reads

$$\begin{aligned} dE = \frac{Y}{1+\nu} \Bigg\{ \frac{1}{2(1-\nu)} \left( \frac{\partial^2 w}{\partial r^2} + \frac{1}{r}\frac{\partial w}{\partial r} + \frac{1}{r^2}\frac{\partial^2 w}{\partial \theta^2} \right)^2 - \\ + \Bigg[ \frac{\partial^2 w}{\partial r^2} \left( \frac{1}{r}\frac{\partial w}{\partial r} + \frac{1}{r^2}\frac{\partial^2 w}{\partial \theta^2} \right) - \\ + \left( \frac{\partial}{\partial r} \left( \frac{1}{r}\frac{\partial w}{\partial \theta} \right) \right)^2 \Bigg] \Bigg\} z^2 dz r dr d\theta \, , \end{aligned} \tag{3.62}$$

where $Y$, $\nu$ are the Young's modulus and Poisson's ratio respectively. $w$ is the function expressing the off-plane displacements of the disk and hence it gives the shape of the resonant mode. Although we assume that the shape modes are the same for the samples before and after the coating deposition, the elastic energy as given by equation (3.62) is divided in two parts whose ratio is fixed by the Poisson's ratio $\nu$. Therefore, if the Poisson's ratio of coating and substrate are the same, the dilution factor is mode independent; otherwise, the dilution factor is similar to the example of figure 3.22. The Poisson's ratio is affecting the repartition of the total elastic energy into bulk and shear components. It is clearly visible that, when the Poisson's ratio of the coating differs from the one of the substrate, the dilution factor as function of frequency presents sharp variations which depend on resonant mode shapes.

Usually, dilution factors are computed (either analytically or through finite-element simulations) by making assumptions on the coating Young's modulus, Poisson's ratio and thickness. This is a rather important limitation, because most of the times the coating parameters are not known. **In this thesis we developed a method to measure the coating dilution factor $D$ through the shift of resonance frequencies**

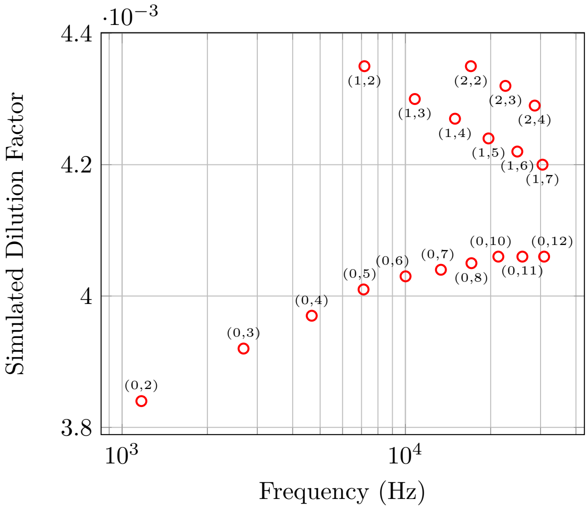

**Figure 3.22:** Simulated dilution factors of $Ta_2O_5$ coating ($\nu = 0.3$) on silica substrate ($\nu = 0.16$). The two curves highlight the separation of (0,m) and (1,m) family modes.

**and mass variations after deposition. In this way the dilution factor can be worked out without any prior knowledge of the coating parameters.** In the following, the basic theory of this method is explained.

When the disc is free to oscillate in one of its resonant modes, its elastic energy must be equal to the kinetic energy,

$$K = \frac{1}{2}\rho\omega^2 \int \dot{w}(r,\theta,t)^2 dzrdrd\theta \,, \tag{3.63}$$

where $\rho$ is the mass density, $\omega$ the angular frequency and $w(r,\theta,t)$ the time-dependent mode shape in circular coordinates during time. By solving the integral for the bare substrate thickness $h$ along $z$, we obtain

$$K_s = \frac{1}{2}\rho_s h\omega_s^2 \int \dot{w}_s(r,\theta,t)^2 rdrd\theta \,, \tag{3.64}$$

whereas for a sample coated on both sides, with a coating thickness $t$,

$$K_{\text{tot}} = \frac{1}{2}\rho_{\text{tot}}(h+2t)\omega_{\text{tot}}^2 \int \dot{w}_{\text{tot}}(r,\theta,t)^2 rdrd\theta \,. \tag{3.65}$$

Since the kinetic energy must be equal to the elastic energy, it is possible to write

$$\begin{cases} \frac{1}{2}\rho_s h\omega_s^2 \int \dot{w}_s(r,\theta,t)^2 rdrd\theta = E_s \,, \\ \frac{1}{2}\rho_{\text{tot}}(h+2t)\omega_{\text{tot}}^2 \int \dot{w}_{\text{tot}}(r,\theta,t)^2 rdrd\theta = E_{\text{tot}} \,. \end{cases} \tag{3.66}$$

The integrals in equations (3.66) depend on the mode shape $w(r,\theta,t)$ of the disk[7]. In the following we assume that the mode shape of the coated disc $w_{\text{tot}}$ is equal to that of the bare disc $w_s$. This implies also that the neutral plane – the imaginary surface

---

[7] The elastic energy of the substrate $E_S$ and of the coated sample $E_{\text{tot}}$ are evaluated analytically in the appendix C for the simple disc geometry, applying the definition of the energy density (3.62).

that has zero deformation all the times during the oscillation − remains in the same position. Under this assumption, dividing each members of equations (3.66) we obtain

$$\frac{\rho_s h}{\rho_{\text{tot}}(h+2t)}\left(\frac{\omega_s}{\omega_{\text{tot}}}\right) = \frac{E_s}{E_{\text{tot}}} \ . \tag{3.67}$$

Considering that $E_{\text{tot}} = E_s + E_c$ and that $A\rho_s h = m_s$ and $A\rho_{\text{tot}}(h+2t) = m_{\text{tot}}$, where $A$ is the area of the disk and $m_s$, $m_{\text{tot}}$ the mass of the disk before and after the coating deposition, respectively, we obtain

$$D = 1 - \frac{m_s}{m_{\text{tot}}}\left(\frac{\omega_s}{\omega_{\text{tot}}}\right)^2 \ . \tag{3.68}$$

where $D = E_c/E_{\text{tot}}$ is the dilution factor. This relation is very important because it gives the dilution factor as a function of measurable parameters, without any prior knowledge of coating elastic constants or thickness. The masses and frequencies after coating deposition are significantly different from those of bare substrates, so that they can be measured with an analytical balance and a GeNS system, respectively. The validity of equation (3.68) is based on the homogeneity of the coating on the entire surface of the substrate and on the fact that the deposition should not add stress on the system which are not intrinsic to the coating. For this reason, the same coating must be deposited on both sides of the substrate, avoiding additional stress and bending of the sample [97].

### 3.2.3 Measurement of Coating Elastic Constant

The dilution factor can be obtained by measurements, using equation (3.68), and also by finite-elements simulations [99]. This means that, in order to estimate the elastic constants of the coating, it is possible to fit the measured dilution factor $D_k^{\text{meas}}$ with finite-elements simulations $D_k^{\text{sim}}$ for each $k$ resonance mode, to minimize the least-square merit function

$$m_D = \sum_k \left(\frac{D_k^{\text{meas}} - D_k^{\text{sim}}}{\sigma_k^{\text{meas}}}\right)^2 \ , \tag{3.69}$$

where $\sigma_k^{\text{meas}}$ is the statistical uncertainty on the dilution factor measurement.

In order to carefully reproduce the real system, we measured the geometry of the sample. The model of the coated samples was composed of a three-dimensional structural elements for the substrates and two-dimensional structural elements for the coatings [94]. In figure 3.23 a typical geometry of the sample and the meshing is reproduced using ANSYS[8].

In this method, knowledge of the substrate parameters is critical: diameters are measured, values of density ($\rho = 2202$ g/cm$^3$), Young's modulus ($Y_s = 73.2$ GPa) and Poisson's ratio ($\nu_s = 0.17$) of fused silica have been taken from the literature [100]; in a dedicated subset of simulations of the bare substrates, thickness $t$ has been fitted to the measured mode frequencies. For few disks, we have independently measured $t$ with a micrometer and found that the discrepancy with the fitted values is less than 2%.

In figure 3.24a an example of the fitting of the dilution factor measured for tantala coating is shown and the relative merit function is in figure 3.24b. Dilution factors of modes with a different number of radial nodes lie on distinct curves, which we have called *mode families*; thus, for example, modes with $(0,\ \text{a})_k$ and modes with $(1,\ \text{a})_k$ belong to two different families (called butterfly and mixed modes, respectively). For

---

[8] ansys.com

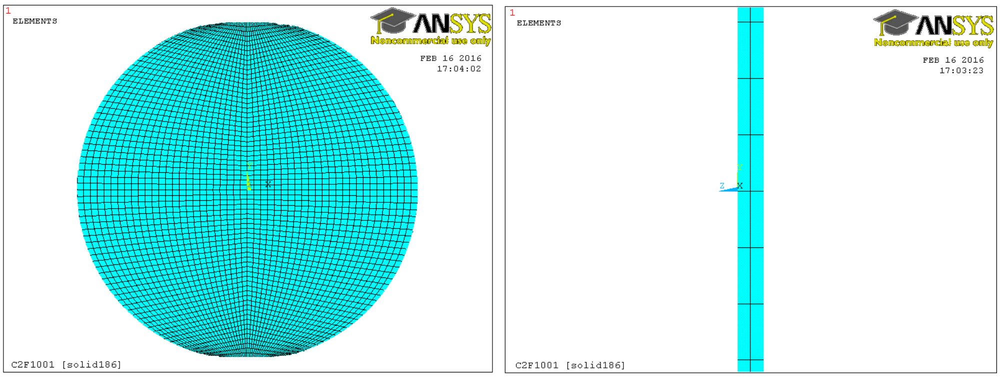

**(a)** Surface.

**(b)** Profile.

**Figure 3.23:** Typical geometry of finite-element simulated sample. The mesh size was set to 1 mm for in-plane surface and volume elements. a) Front view of the circular sample with flats. b) Zoom on the profile in order to show the finite elements along the thickness.

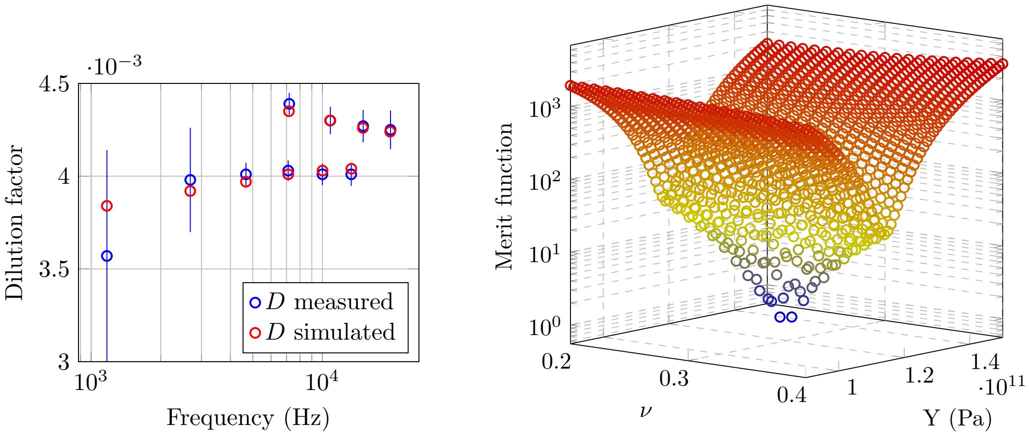

**(a)** Dilution factor.

**(b)** Merit function.

**Figure 3.24:** Fitting procedure for tantala coating currently used in GWDs ($Y = 121 \pm 1$ GPa and $\nu = 0.30 \pm 0.01$). a) Best fit of measured dilution factor with simulation. b) Minimization of merit function.

a given substrate, dilution factors are determined by the coating elastic constants: their average value depends on the $Y_c/Y_s$ ratio, whereas the separation between mode families increases along with the difference $|\nu_c - \nu_s|$.

# CHAPTER 4

# RESULTS

*"A scientist in his laboratory is not a mere technician:*
*he is also a child confronting natural phenomena that*
*impress him as though they were fairy tales."*
Marie Curie
*Madame Curie* A Biography by Eve Curie (1937)

In this chapter the mechanical and optical characterization on coatings for present and future gravitational-wave detectors is presented.

A brief introduction describes the coating deposition method and the different coaters used to deposit all the samples.

During the mechanical characterization of substrates, an unexpected behaviour of the loss angle highlighted the impact of the unpolished edge of the samples on the mechanical loss. A similar effect affects also the coating. For this reason, **a model that includes the extra mechanical loss related to the edge has been developed during this thesis.**

The mechanical and optical properties of coatings are studied under different post-deposition treatments and mixing ratios. As first, the analysis of silica ($SiO_2$), tantala ($Ta_2O_5$) and titania-doped tantala ($Ti{:}Ta_2O_5$), currently used in gravitational-wave detectors, allowed a better comprehension of amorphous oxide coatings, obtaining new results: a "structural limit" for annealed $Ta_2O_5$ coatings, a correlation between the structure organization and the coating loss angle for $SiO_2$ coating.

The optical and mechanical properties have been associated to the structure organization in a short- to medium-range order: **a correlation between the Urbach energy and the internal friction has been found**. The correlation is observed for different oxide coating materials, suggesting its general validity for this kind of coating materials.

Finally, **we characterised alternative coating materials ($Nb_2O_5$, $NbTiO_2$, $Zr{:}Ta_2O_5$, $MgF_2$, $AlF_3$, SiC and $SiN_x$)** to develop low-noise mirrors for gravitational-wave detectors.

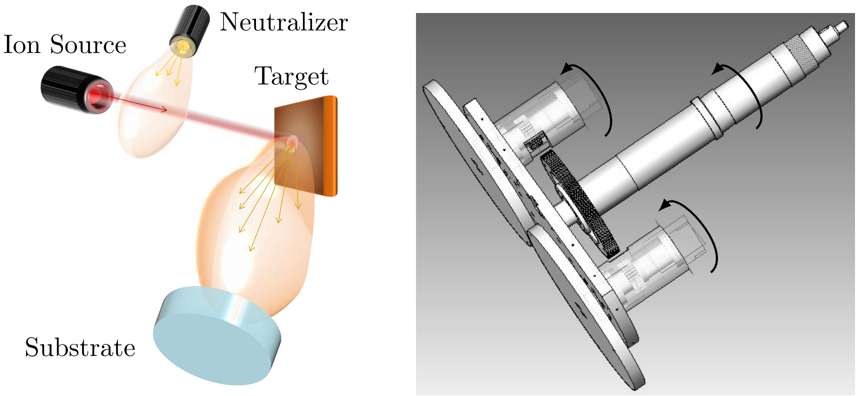

**(a)** IBS deposition. **(b)** Substrate holder.

**Figure 4.1:** (a) Sketch of IBS deposition method. (b) Planetary motion holder.

## 4.1 Deposition Method

High-reflective coatings for gravitational-wave detectors are deposited by ion beam sputtering (IBS) at Laboratoire des Matériaux Avancés (LMA) in Lyon. The IBS deposition method is schematically illustrated in figure 4.1a. An ion source focuses an ion beam over a target made on the material that has to be deposited. Because of the energy of the ions and the highly collimated beam, it is possible to obtain precise thickness control and deposition of very dense coatings. The high ions energy pulverises the surface of the target and ejects the target as a "plume" of particles, which will be deposited on the substrate. Usually the ions are made of inert gas such as $Ar^+$ in order to be accelerated from the source and directed to the target. To prevent the impact of charged particles on the target, a neutraliser diffuses electrons in order to neutralize the ion beam before it collides on the target. A flux of Oxygen is injected in the chamber, in order to deposit oxide coatings. In order to better control the deposition plume profile, the deposition is done at low pressure $p \simeq 10^{-4}$ mb.

The usual methods for improving the thickness uniformity in coating systems is to include some kind of simple or planetary substrate rotation, together with moving or stationary masks, to modify the deposition plume profile, which is approximately Gaussian. As illustrated in figure 4.1b, the planetary motion support allows the simple rotation of the substrate coupled with the motion around another rotation axis.

The IBS facilities used to deposit the coatings for this work are the Veeco's SPECTOR®, the double IBS (DIBS)[1] and the Grand Coater (GC). In particular, the SPECTOR (figure 4.2a) is a commercially available facility, with the possibility to use a second ion source for substrate precleaning and bombardment of the oxide films during the deposition, the DIBS (figure 4.2b) is one of the first IBS coaters developed in Europe. Finally, the GC is one of the largest IBS coater in the world (figure 4.2c), developed in order to deposit high-reflective coatings for the large mirrors of gravitational-wave detectors. The GC allows to deposit coatings on two large ($\varnothing = 35$ cm) massive substrates in planetary motion in order to obtain two paired high-quality mirrors. In figure 4.2d one pair of mirrors used for the gravitational-wave detectors of Advanced LIGO is shown.

---

[1] Only one ion source has been used.

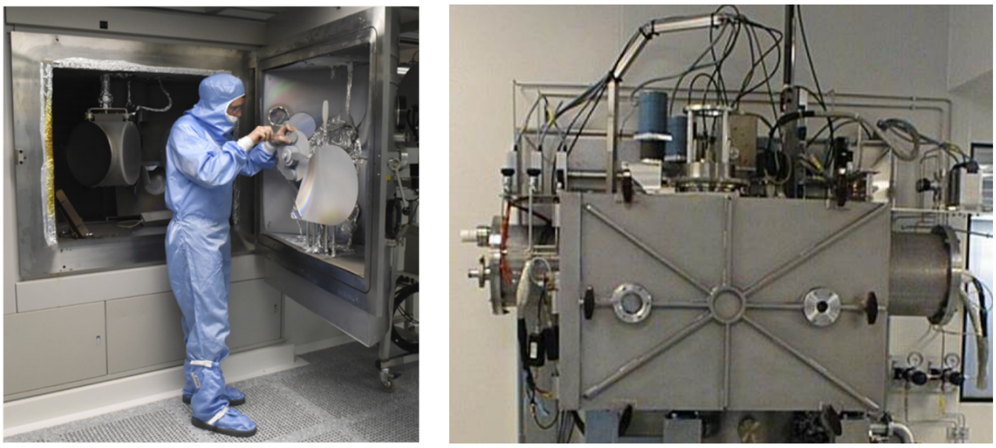

**(a)** SPECTOR. **(b)** DIBS.

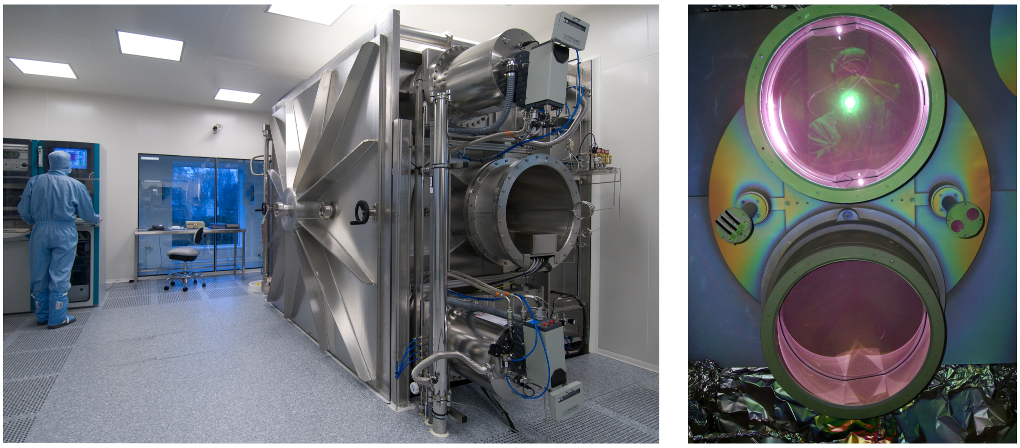

**(c)** Grand Coater. **(d)** Mirrors.

**Figure 4.2:** (a)Veeco's SPECTOR®. (b) DIBS. (c) Grand Coater. The dimension of GC can be compared with the height of a man. (d) A set of high-reflective mirrors used for the first detection of Advanced LIGO, right after the deposition.

## 4.2 Substrates for Optical Characterization

In reflective ellipsometry, a reflective substrate (high index of refraction) is to be preferred to transparent materials (e.g. silica), to increase the reflected signal. For this reason, silicon wafer is adopted as substrate. Furthermore, the silicon substrate may have the unpolished bottom surface, avoiding problems arising with backside reflections. In figure 4.3 the $(\Psi, \Delta)$ data of VASE for a representative substrate are shown. The M-2000 ellipsometer provided similar data.

Creating a model that reproduces well the optical properties of the substrate is extremely important for the analysis of the coating. In fact, any unknown feature of the substrate will introduce uncertainties in the analysis of the optical properties of coating materials. The substrate model is set as bottom layer in the analysis of the coating samples. In the case of silicon wafers the model consists of two layers. The first includes several oscillators centred at critical points of the joint-density of state [101]; the other one is an ultra-thin layer, of the order of 2 nm, representing the native thermal oxide and described by library optical properties [102]. The model based on critical points in JDOS is illustrated in figure 4.4. In figure 4.4a the critical points in the JDOS

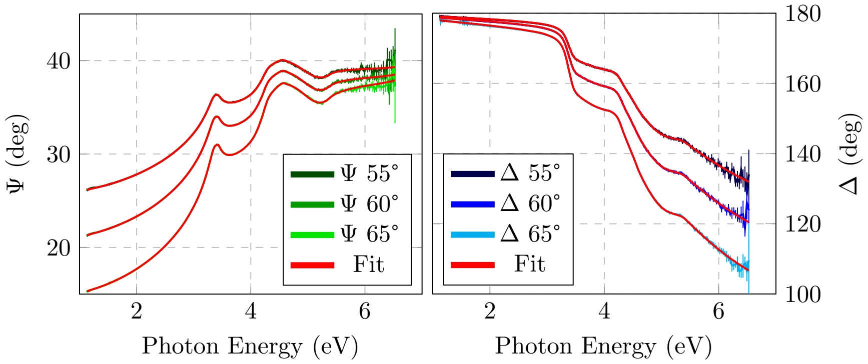

**(a)** Psi. **(b)** Delta.

**Figure 4.3:** $\Psi$ (a) and $\Delta$ (b) data of VASE ellipsometer at different angles of incidence, compared with the fit curves, for a bare silicon wafer.

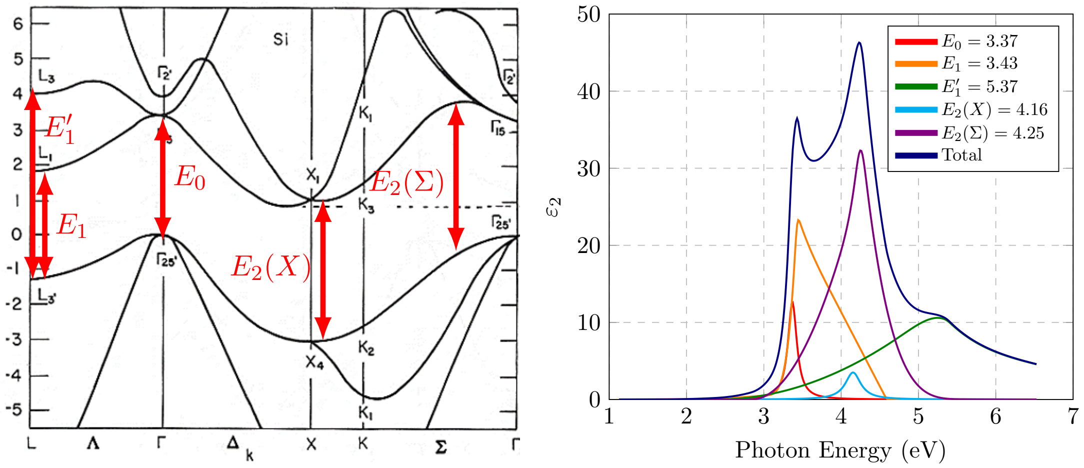

**(a)** JDOS. **(b)** Model.

**Figure 4.4:** (a) Critical points in JDOS of silicon that would affect $\varepsilon_2$ at $T = 296$ K. (b) The $\varepsilon_2$ of silicon substrate made on several oscillators centered at critical points in JDOS. The energies are in eV.

are highlighted, showing the direct inter-band transitions. In figure 4.4b the imaginary part of the dielectric constant $\varepsilon_2$ is made on the overlap of several oscillators, centered at critical points in JDOS. The result is a curve with 3 main peaks around 3.4 eV, 4.2 eV and 5.3 eV. The fitting curves obtained with this model are shown in figure 4.3.

The data acquired by the two ellipsometers have been analysed independently using the same method and, as showed in figure 4.5, the results are equivalent within the fitting errors.

## 4.3 Substrates for Mechanical Characterization

The substrates used for mechanical characterizations are fused-silica disks (⌀ 3” or ⌀ 2”) of Corning 7980, of a nominal thickness of 1 mm, optically polished on both surfaces. The purpose of such high-quality polishing is to test the coatings on substrates with specifications as close as possible to those of substrates of gravitational-wave

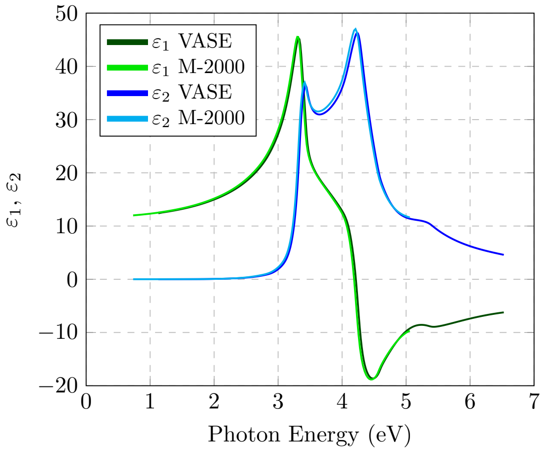

**Figure 4.5:** Real $\varepsilon_1$ and imaginary $\varepsilon_2$ part of the silicon dielectric function, obtained by the analysis done on $(\Psi, \Delta)$ acquired by VASE and M-2000 ellipsometers.

interferometers.

A perfect circular geometry gives resonance modes degeneration in which modes with azimuthal nodes have "twin" modes rotated by $\pi/2n$, where $n$ is the radial node number, with the same elastic energy. This creates beating in the vibration and in order to avoid it, two small symmetrical and diametrically opposite flats are cut from the sample.

Samples are coated on both sides in order to avoid curvatures of the substrate related to the stress applied on the system when a coating is deposited. Coating on one side would change the neutral line of the disk and cause bending. This effect makes impossible the direct measurement of dilution factor as given by equation (3.68).

### 4.3.1 Edge Effect on Substrates

In a recent work it has been shown that for silica disk-shaped resonators, the measured loss angle is affected by spurious losses at the edge of the sample [103]. This might be due to the adsorption of contaminants by the unpolished edge. As a result, the internal friction of different resonance modes does not lie on a single curve, following the frequency dependence discussed in chapter 2, but modes that vibrate more at the edge have higher loss angle, separating in mode families. In particular, the deformation is smaller at the edge for modes with only azimuthal nodes m and gets higher for modes having more radial nodes n. In figure 4.6 there is the measured loss angle for each resonant modes for one representative 3" silica disk, annealed at for 24 hours at 900°C and unpolished at the edge (blue dots). The measurements show separation between modes with different azimuthal and angular nodes. In particular, modes with only azimuthal nodes (0,m) lie in the curve with higher loss angle.

The spurious loss of the edge is well described by considering the system as composed of a barrel and a disk [103]. Using the model illustrated in figure 4.7, one can consider the system as composed by two different part having their own dissipation mechanisms. From equation (3.56), the substrate $s$ loss angle reads

$$E_s\phi_s = E_d\phi_d + E_B\phi_B \ , \tag{4.1}$$

where $\phi_d$ and $E_d$ ($\phi_B$ and $E_B$) refer to the loss angle and the energy stored in the

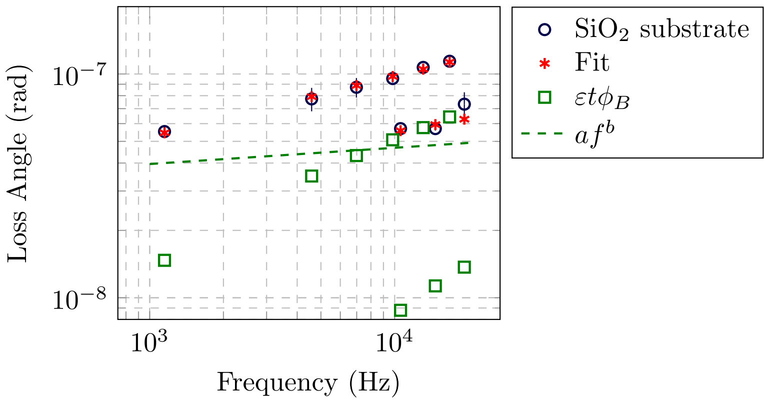

**Figure 4.6:** Measurement (blue) of silica disk (3" of diameter and 1 mm thick) and fit (red). The simulation is made on two contribution, one related to the extra loss on the edge (green squares) and the other to the frequency dependence of the silica loss angle (dashed green line).

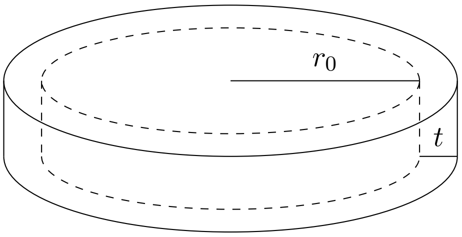

**Figure 4.7:** Model based on barrel of thickness $t$.

central part of the disk $d$ (in the barrel $B$), respectively. In particular,

$$E_B = \left.\frac{dE_B}{dr}\right|_{r=R} t\,, \tag{4.2}$$

where $t$ is the thickness of the barrel. If we introduce the associated dilution factors, we obtain

$$\phi_s = D_d\phi_d + D_B\phi_B\,, \tag{4.3}$$

where $D_d = E_d/E_s$ and $D_B = E_B/E_s$ are the dilution factor of the disk and of the barrel, respectively. If the thickness $t$ of the barrel is $t << r_0$, where $r_0$ is the radius of the disk, we can assume that $D_d \sim 1$ and

$$D_B = \epsilon t << 1\,; \qquad D_B + D_d \cong 1\,, \tag{4.4}$$

where $\epsilon$ is the dilution factor density

$$\epsilon = \lim_{t\longrightarrow 0}\frac{1}{t}\frac{E_B}{E_s}\,, \tag{4.5}$$

as introduced in [103]. The value of $\epsilon$ can be numerically computed[2]. The values for a silica Corning 7980 ($\nu = 0.16$) disk with unitary radius are listed in table 4.1.

As shown in chapter 2, the potential used to describe the TLS in glasses leads to a power law for the internal friction [104, 105]. Using the power law for $\phi_d$, equation (4.1) can be rewritten as

$$\phi_s = af^b + \epsilon t\phi_B\,. \tag{4.6}$$

---

[2] The values are obtained from the energies $E_s$ end $E_B$ in equation (C.17), by doing the integration over the radius of the disk for $E_s$ and considering only the element $dr$ for $E_B$.

|  | m |  |  |  |  |  |  |  |  |  |  |
|---|---|---|---|---|---|---|---|---|---|---|---|
| n | 0 | 1 | 2 | 3 | 4 | 5 | 6 | 7 | 8 | 9 | 10 |
| 0 |  |  | 1.24 | 2.17 | 2.96 | 3.66 | 4.3 | 4.88 | 5.44 | 5.97 | 6.47 |
| 1 | 0.567 | 0.15 | 0.535 | 0.744 | 0.96 | 1.16 | 1.35 | 1.53 | 1.67 | - | - |
| 2 | 0.116 | 0.08 | 0.282 | 0.43 | 0.59 | 0.757 | 0.901 | 1.03 | 1.16 | - | - |

**Table 4.1:** Table of the dilution factor density $\epsilon$ for a disk ($\nu = 0.16$) with unitary radius. The value for a disk of radius $R$ can be obtained as $\epsilon/R$. n and m stand for radial and azimuthal node numbers, respectively.

| $a$ $(10^{-8})$ | $b$ | $t \cdot \phi_B$ $(10^{-10} m)$ |
|---|---|---|
| $2.40 \pm 0.08$ | $0.070 \pm 0.005$ | $4.4 \pm 0.2$ |

**Table 4.2:** Results of the fit for the coating loss model defined in equation (4.6) for the data of figure 4.6.

As shown in figure 4.8, the family separation resides in the dilution factor density of the edge.

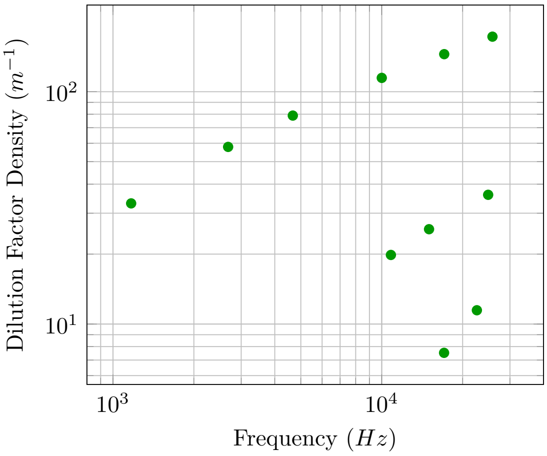

**Figure 4.8:** Dilution factor density $\epsilon$ scaled by the radius $R$ for a 3" diameter disk, for the modes usually measured on a silica disk 1 mm thick.

Using equation (4.6) it is possible to model the experimental data. In figure 4.6 it is possible to distinguish the two contributions related to the silica loss angle and the edge effect. The fit results are listed in table 4.2. It is important to observe on figure 4.6 that for this silica substrate with unpolished edge, the extra losses of the edge are of the same order of the internal friction of the substrate material. This means that, if we are interested to the intrinsic loss angle of the substrate, it is necessary to find a method to remove this *edge effect*.

The so-called *edge effect* limits the measurements not only because it limits the sensitivity, but also because it evolves during time increasing the loss angle. The edge effect is likely caused by adsorption of contaminants.

In figure 4.9a the evolution of the loss angle of a reference silica substrate (figure 4.6) can be observed. During this *ageing*, the loss angle increased especially for the first family (0,m). This affects the coating loss measurement: it is clear from equation (3.60)

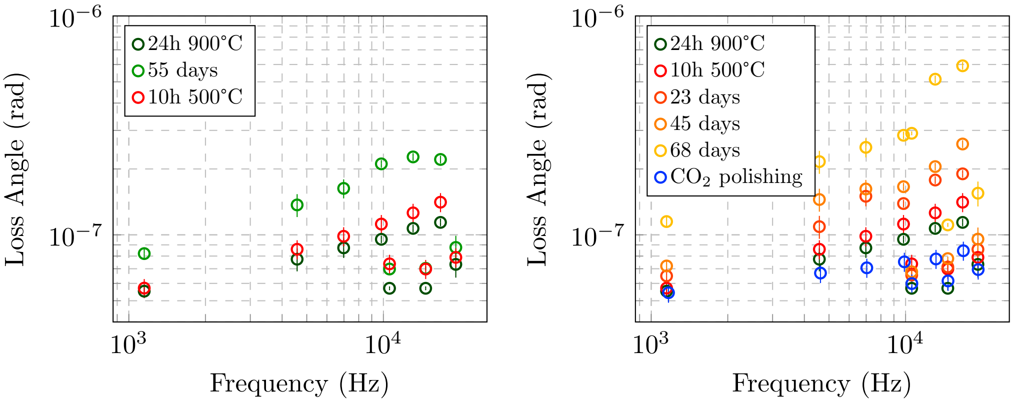

**(a)** Ageing. **(b)** Ageing after annealing.

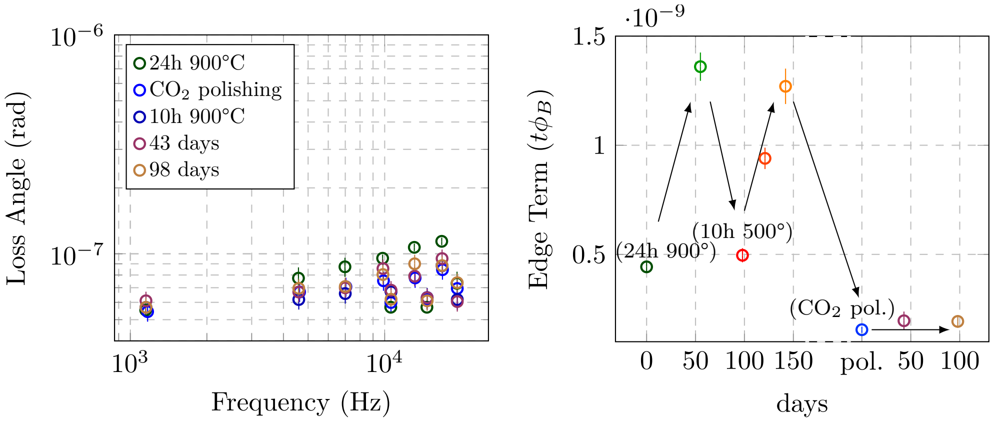

**(c)** Polishing. **(d)** Edge Term.

**Figure 4.9:** (a) Ageing of a reference silica substrate. (b) Ageing of the reference silica substrate after the annealing for 10 hours at 500°C (the reference loss value measured after the first annealing at 900°C is also shown, for comparison). (c) Evolution of the loss angle after laser polishing (the reference loss value after 900°C annealing is also shown, for comparison). (d) Evolution of the edge term $t\phi_B$ during time.

that the coating loss angle is obtained by subtraction of the substrate contribution to the total loss angle. Thus, if the substrate evolves during time, it is possible that the measured coating loss angle resulting from the subtraction is affected by a systematic uncertainty due to ageing effect of the substrate.

In figure 4.9a it can be observed that the annealing is a valid option to erase the evolution of the ageing history. After several tests, it has been observed that, at least, the annealing for 10 hours at 900°C is needed in order to obtain the initial values of loss angle. The heating treatment is a good procedure to restore the quality factor of the sample, however the ageing effect is not eliminated: in figure 4.9b the evolution of the loss angle after the annealing is shown; the ageing did not stop, even after more than two months.

After preliminary tests performed by the groups of the University of Urbino Carlo Bo, at the Virgo site, in the University of Roma Tor Vergata, has been developed a system which allows to perform a $CO_2$ laser polishing of the edge. The effect of the polishing is shown in figure 4.9b: the ageing has been erased and the difference between the first (0,m) and second (1,m) mode families is reduced. Figure 4.9c shows that the

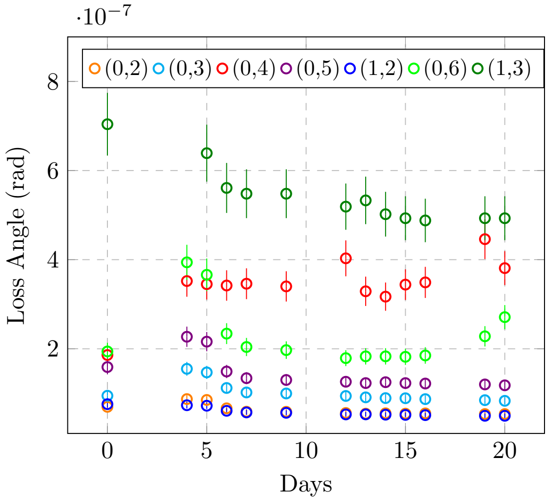

**Figure 4.10:** Loss angle for different resonant modes (n,m) of 3” silica substrate monitored in vacuum during time.

laser polishing greatly inhibits the ageing effect.

In order to quantify the effect of the ageing, the change of loss angle has been analysed using equation (4.6) and the value of edge term $t\phi_B$ is plotted in figure 4.9d. After each annealing there is an evolution of the loss angle related to the edge and the minimum of $t\phi_B$ is reached after the laser polishing. In figure 4.9d it is clearly evident that after the polishing the evolution of the edge loss is significantly reduced.

While the laser polishing system was under development and not yet available, a protocol was adopted to cope with the ageing problem. The protocol is:

- The substrates underwent a standard heating treatment for 10 hours at 900°C before the coating deposition in order to erase any ageing effect.
- The loss angle of the samples is measured just after the annealing and the coating is then deposited right after.
- The samples are stored in a vacuum tank in order to limit the ageing between each measurement and treatments.

With these precautions, we are sure that the edge loss change is negligible with respect to the coating loss angle to be measured; by using equation (3.60), it is then possible to calculate the coating loss accurately.

In order to observe the effect of the vacuum storage, the loss angle of a 3” silica substrate annealed for 10 hours at 900° C has been monitored in time, maintaining the sample at $p \sim 10^{-6}$ mb. In figure 4.10 the loss angle of several modes (n,m) have been measured as a function of time. It is evident from the figure that the vacuum prevents ageing, keeping the loss angle approximately constant over twenty days. Furthermore, the low pressure slightly lowers the loss angle during time, likely because it helps the desorption of contaminants from the sample edge.

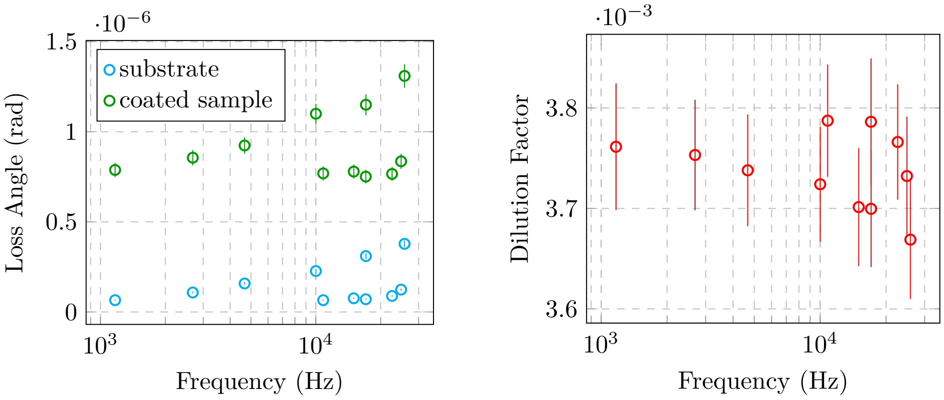

**(a)** Loss Angle. **(b)** Dilution Factor.

**Figure 4.11:** a) Loss angle of bare silica disk (blue) and after the GC $SiO_2$ coating deposition (green). The substrate has been annealed at 900°C. b) Measured dilution factor for a fused silica substrate of 3" of diameter and 1 mm thick, coated on both sides with ~700 nm of silica. The error bars are mainly due to the uncertainties on mass measurement which are dominant with respect to the uncertainties of the frequencies measurement.

## 4.4 $SiO_2$ Coating

Silica ($SiO_2$) is the low-refractive index layer in the current Bragg mirrors of gravitational-wave detectors. Historically it was chosen because of its low optical absorption at the wavelength of interest. It also shows low internal friction at room temperature.

During the mechanical characterization of silica coatings, we observed a branching of the coating loss as a function of mode shape, closely following a separation in mode families. In the following we will discuss in detail how to cope with this edge effect on coatings.

### 4.4.1 Edge Effect on Coatings

Following the procedure established by the protocol, in figure 4.11a it is possible to observe a typical measurement of the loss angle of the substrate taken right after the annealing, and of the coated sample. The substrate measurement is affected by the edge effect and presents mode families separation, as we have seen in section 4.3.1. Although the coating is much thinner than the substrate, the loss of the coated sample is dominated by the coating as it is possible to observe in figure 4.11a. Moreover, the family pattern observed in the coated disk should come from both the pattern of the bare substrate and that of the dilution factor shown in figure 4.11b. The coating loss angle can be then worked out using equation (3.61) and should depend on frequency without sharp variations between frequency modes. However, even respecting the protocol, the result of the coating loss angle $\phi_c$ of figure 4.12 still have a branching, closely following the separation in mode families due to the edge effect present on the substrate. In order to prove that this is likely related to an edge effect, the coating loss angle have been analysed using the same model used for the substrate. The fitting result of figure 4.12 confirms that the edge model can still describe the data. Surprisingly, it is possible to observe that even if the edge effect of the substrate has been removed by the $CO_2$ polishing (figure 4.13a), the coating loss angle presents family modes that can be represented by the edge effect model (figure 4.13b). This phenomenon could be caused

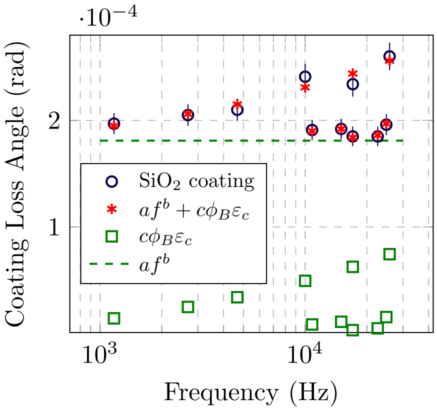

**Figure 4.12:** Measurement of SiO$_2$ GC coating (blue dots) and fit (red). The first three mode families ((0,$x$), (1,$x$) and (2,$x$)) are shown. The model is made of two contributions, one related to the extra loss on the edge (green squares) and the other to the frequency dependence of the silica coating loss angle (green line).

by spurious loss due to the coating spilling off on the substrate barrel, changing the physical condition of the material. In figure 4.14 some examples of coating deposited at the edge of samples are shown. In figure 4.15 there is a representation of the model which considers the coating deposited also on the edge of the substrate.

Let's see which are the assumptions behind this analysis. The system is represented by the composite resonator made by the substrate and the coating. The total dissipated energy is the sum of the energies lost in each part of the resonator, as expressed by equation (3.56). In particular we have

$$E_{\text{tot}}\phi_{\text{tot}} = E_s^{\text{tot}}\phi_s^{\text{tot}} + E_c(\phi_c + \phi_B c\varepsilon_c)\ , \tag{4.7}$$

where $E_{\text{tot}}$ is the total energy of the system, $E_s^{\text{tot}}$ is the contribution of the substrate, including its edge, $E_c$ is the energy stored in the coating and the last term $E_c c\varepsilon_c$ is the energy stored in the coating spilled off onto the barrel of the substrate. Geometry allows writing this edge contribution as proportional to the coating energy through the coefficient $\varepsilon_c$. Since we are dealing with and edge effect, the coefficient $\varepsilon_c$ has the same values of the dilution factor density found for the substrate $\epsilon$ (table 4.1). It has to be noted that in this case the parameter $c$ does not represent strictly the thickness of the barrel for the coating but contains also informations about the interaction between coating and substrate. The hierarchy of the energies is

$$E_{\text{tot}} \gtrsim E_s^{\text{tot}} \gg E_c \gg c\varepsilon_c E_c\ , \tag{4.8}$$

and the total energy must be

$$E_{\text{tot}} = E_s^{\text{tot}} + E_c(1 + c\varepsilon_c)\ . \tag{4.9}$$

The coating increases the resonant frequency of each mode by the contribution $E_c(1 + c\varepsilon_c)$ to the total elastic energy and, at the same time, it reduces the resonant frequency through its mass. Dividing (4.7) by $E_{\text{tot}}$ we obtain

$$\phi_{\text{tot}} = \frac{E_s^{\text{tot}}}{E^{\text{tot}}}\phi_s^{\text{tot}} + \frac{E_c}{E^{\text{tot}}}(\phi_c + \phi_B c\varepsilon_c)\ . \tag{4.10}$$

Now the question is whether or not the energy ratios of (4.10) are measured through the frequency shifts. As pointed out above, the total energy stored in coating $E_c(1 + c\varepsilon_c)$

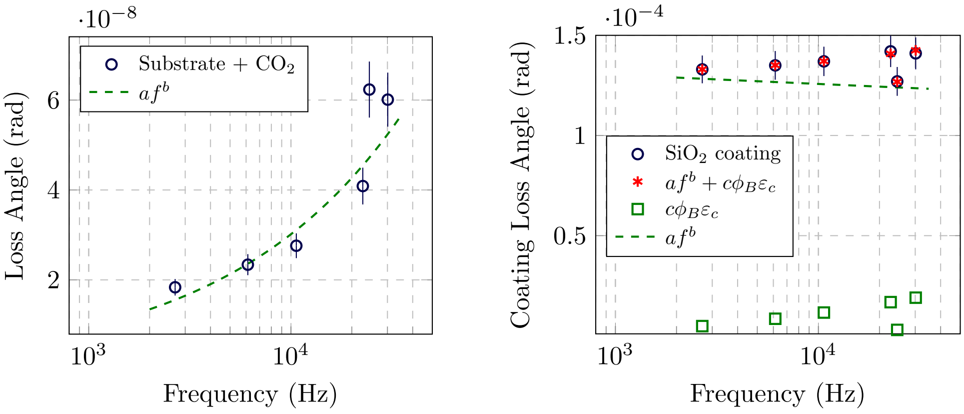

**(a)** Substrate. **(b)** Coating.

**Figure 4.13:** a) Loss angle of bare silica disk (blue), CO$_2$ polished and annealed at 900°C, and frequency dependence $af^b$ fit (green line). b) Measurement of DIBS SiO$_2$ coating (blue dots) and fit (red). The model is made of extra loss on the edge (green squares) and a frequency dependence (green line).

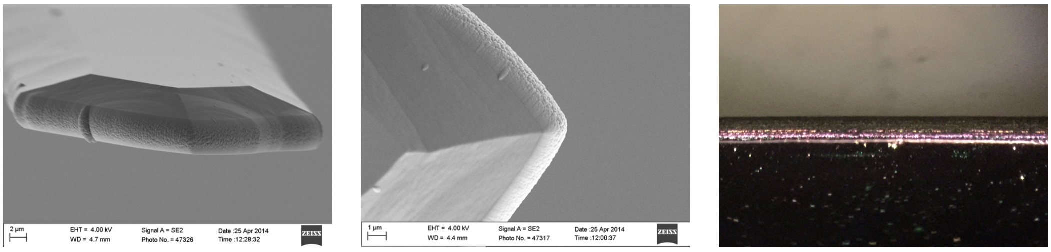

**(a)** Silicon cantilever. **(b)** Silicon cantilever. **(c)** Silicon disk.

**Figure 4.14:** Example of IBS process on the edge of different geometry substrate. (a) and (b) Scanning Electron Microscopy (SEM) image of coated cantilever silicon substrate. (c) optical microscope image of coated silicon disk. In every cases it is evident that the coating on the edge looks different from the coating on the surface of the sample.

and its total mass, included that on the barrel, determine the resonant frequencies shift. However, thanks to the hierarchy of the energy it is possible to consider that $E_c(1 + c\varepsilon_c)/E_{\text{tot}} \simeq E_c/E_{\text{tot}} = D$ and the inertia of the coating on the barrel are negligible with respect that of the coating on the flat surfaces. The dilution factor $D$ is measured as explained in the section 3.2.2. Under these considerations, we obtain

$$\begin{aligned} \phi_{\text{tot}} &= (1 - D)\phi_s^{\text{tot}} + D(\phi_c + \phi_B c\varepsilon_c) \qquad (4.11) \\ &= (1 - D)\phi_s + D\phi_c^{\text{tot}}\,, \qquad (4.12) \end{aligned}$$

where $\phi_c^{\text{tot}}$ is the total loss related to the coating deposition

$$\phi_c^{\text{tot}} = \frac{\phi_{\text{tot}} - (1 - D)\phi_s^{\text{tot}}}{D} = \phi_c + \phi_B c\varepsilon_c \qquad (4.13)$$

$$\phi_c^{\text{tot}} = af^b + \phi_B c\varepsilon_c\,. \qquad (4.14)$$

We remind again here that the useful information on coatings is inside the $\phi_c = af^b$ term only; the rest, coming from the edge effect, is a systematic error in the measurements that can be isolated through the fitting process.

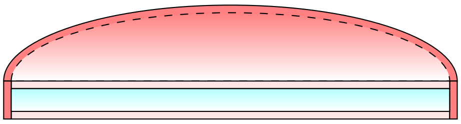

**Figure 4.15:** Sketch of the geometry used in the model based on the edge effect. For sake of clarity, the cross section of the disk is considered.

| n | m 0 | 1 | 2 | 3 | 4 | 5 | 6 | 7 | 8 | 9 |
|---|---|---|---|---|---|---|---|---|---|---|
| 0 | | | 0.0699 | 0.1106 | 0.1376 | 0.1571 | 0.1719 | 0.1836 | 0.1931 | 0.2010 |
| 1 | - | 0.3487 | 0.3040 | 0.2845 | 0.2751 | 0.2706 | 0.2685 | 0.2678 | 0.2678 | 0.2683 |
| 2 | - | 0.3276 | 0.3151 | 0.3064 | 0.3004 | 0.2962 | 0.2932 | 0.2911 | 0.2897 | 0.2887 |

**Table 4.3:** Table of the dilatation dilution factor for a disk ($\nu = 0.16$) with unitary radius. n and m stand for radial and azimuthal node numbers, respectively.

In figure 4.12 and 4.13b there are the comparisons between the data (blue dots) and the fitted model (red dots) for SiO$_2$ deposited in different conditions.

### Edge effect vs Bulk/Shear losses

Every deformation of a solid can be decomposed in two contributions, one related to the change in volume and the other to shear deformations. This means that the energy of the system is made of two terms that depend on bulk and shear moduli, which in principle will be related to different dissipation mechanisms. Since the samples under investigation are amorphous coatings, it is reasonable to describe the mechanical properties using only two quantities, the Young's modulus and the Poisson's ratio, and hence to assume that there are two loss angles that dissipate the total energy of the system. Then, the total loss angle of the coating is

$$\phi_c^{\mathrm{tot}} = \phi_c^{bulk} D_{dil} + \phi_c^{shear} D_{shear} + \phi_B c \varepsilon_c \tag{4.15}$$

$$= A_1 f^{B_1} D_{dil} + A_2 f^{B_2}(1 - D_{dil}) + \phi_B c \varepsilon_c \, , \tag{4.16}$$

where $A_i$, $B_i$ are coefficients of the frequency dependence of the loss angle and $D_{dil}$, $D_{shear} = 1 - D_{dil}$ are the bulk and shear dilution factors.

The bulk dilution factor is the ratio of the energy stored in the system in which the volume changes during the deformations to the total energy of the system[3]. The values of bulk dilution factor for a disk with $\nu = 0.16$ are listed in table 4.3. In figure 4.16 the values of the shear and bulk dilution factors for different resonance modes are shown. Equation 4.16 describes all the physical factors involved in the dissipation mechanisms of the coating and should be considered in the analysis. However, it is not possible to obtain accurate results. If we compare the dilution factors 4.8 of the edge effect and 4.16b of the shear, it is evident that they behave in the same way; the first family has an higher dilution factor than the others. For this reason, these quantities can not be discriminated during the analysis. This is a problem since our objective is to remove the contribution of the edge and obtain information only on the coating bulk properties.

---

[3] The bulk and shear dilution factors can be numerically computed considering the equation (C.31) for the bulk energy.

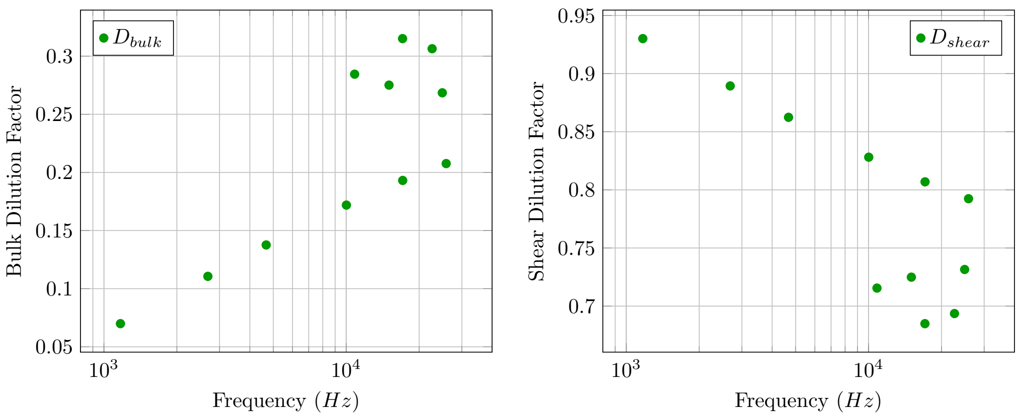

**(a)** Bulk. **(b)** Shear.

**Figure 4.16:** (a) Bulk dilution factor scaled by the radius $R$ for a 3" diameter disk. The modes are those that are measured on the silica disk. (b) Shear dilution factor obtained from $D_{shear} = 1 - D_{dil}$.

In order to evaluate which mechanism represents better the data between the shear and the edge effect, two different models have been used to fit the data. The first describes the coating considering one loss angle and the edge effect, as shown by equation 4.14, the second considers only the two loss angles ascribed to the bulk and shear, as shown by equation 4.16, without the term $\phi_B c \varepsilon_c$. In figure 4.17 the data are compared with the two model fits. The fit results are summarized in table 4.4.

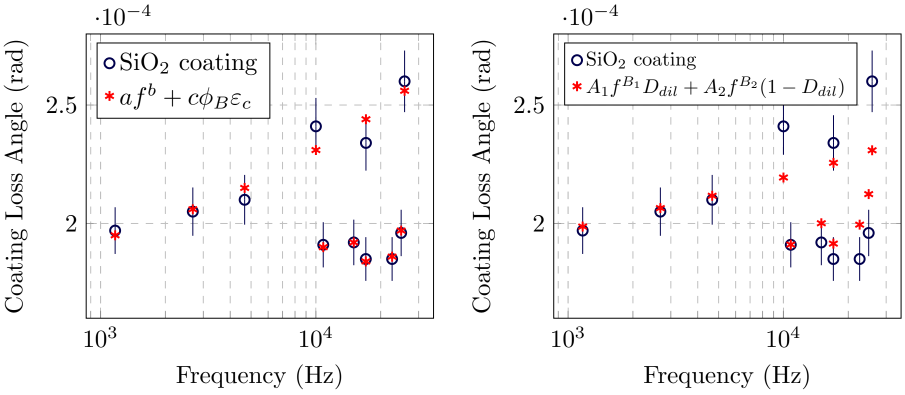

**(a)** Edge effect. **(b)** Bulk/Shear.

**Figure 4.17:** (a) GC SiO$_2$ coating data and fit obtained by the edge effect model. (b) GC SiO$_2$ coating data and fit obtained by the bulk/shear model.

It was possible to find a set of parameters to reproduce the experimental data using both models. It is clear from figure 4.17 that the edge effect model provides a better fit than the bulk/shear, as confirmed by the MSE values of the fit in table 4.4. Furthermore, in order to fit the data with the bulk/shear model, the bulk term must be null, which appears to be unlikely. We note that the two models can both fit the data but since the analysis shows better results for the edge effect, in the following the data will be analysed using only the edge effect model.

| Edge Effect | | | | Bulk/Shear | | | | |
|---|---|---|---|---|---|---|---|---|
| MSE | $a$ ($10^{-4}$) | $b$ | $c\phi^B_{\text{tot}}$ ($10^{-7}$ m) | MSE | $A_1$ | $B_1$ | $A_2$ ($10^{-4}$) | $B_2$ |
| 0.27 | $1.81 \pm 0.02$ | 0 | $4.3 \pm 0.3$ | 2.18 | 0 | – | $1.1 \pm 0.2$ | $0.10 \pm 0.02$ |

**Table 4.4:** Fit results for the edge effect and the bulk/shear models.

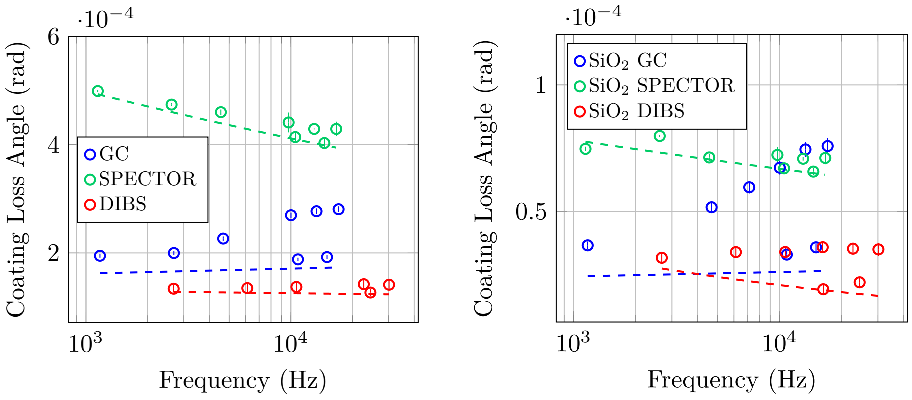

**(a)** Not annealed.

**(b)** Annealed.

**Figure 4.18:** Coating loss angle of $SiO_2$ deposited with GC, SPECTOR and DIBS. (a) The comparison before the annealing. (b) The comparison after the annealing at 500°C. Shaded regions represent uncertainties from fitting parameters of equation (4.14) to each sample set, via iterative non-linear regression; dashed curves show the behaviour of the $af^b$ term only.

### 4.4.2 Mechanical Properties

#### Deposition Conditions

Different deposition conditions entail different coating properties. In figure 4.18a the coating loss angles of silica deposited with the GC,the SPECTOR and the DIBS are shown. All the three silica are sputtered from the same material but have different losses. Deposition parameters which may have a relevant impact on the coating properties are the ion energy and current and the geometric configuration of the elements inside the chamber, i.e. the distances and the angles between the sputtering sources, the sputtered targets and the substrates to be coated. Each coater has its own specific set of values for these parameters, optimized for yielding the highest coating optical quality, resulting in a different deposition rate. However, in all the coaters the ion energy and current are of the order of 1 keV and 0.1 A, respectively. Furthermore, we found no correlation between the measured loss and the distances of targets and substrates. For this reason, the loss seems to be related to the coating deposition rate, determined by the energy and the flux of particles of the sputtering beam and by the configuration of the coating chamber. In our case, the SPECTOR provided the fastest rate (2.2 $\mathring{A}$/s) and the highest loss; however, while having the same deposition rate (within 25% experimental uncertainty) than the GC sample, the DIBS sample had the lowest loss values. This might be related to the unusually small measured density value for the DIBS sample.

When considering the $af^b$ term only, the loss of the GC sample appears fairly constant ($b \sim 0$), whereas the loss of the SPECTOR and DIBS samples showed surprisingly a weak decreasing trend ($b < 0$). This latter result could be related to a non exponential distribution of the barrier height in the TLS. The samples underwent a standard post-deposition annealing for 10 hours at 500°C. After the annealing (4.18b), the loss of all samples are reduced. The loss values of the SPECTOR and GC samples moved closer to those of the DIBS.

For all the samples, the elastic constants have been worked out by fitting the measured dilution factor $D$ with simulations. In figure 4.19 the fit results for SiO$_2$ coating deposited with the CG and annealed at 500°C is shown, as representative sample. The large residuals could be symptom of a slightly curved disk, where the curvature affects the frequency shift [97]. The final results are listed in table 4.5.

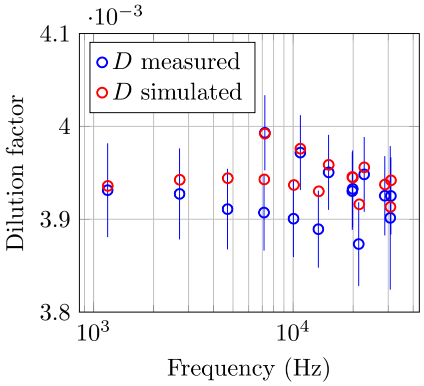

**Figure 4.19:** Fit of measured dilution factor (blue) with simulated values (red), for a SiO$_2$ coating annealed in air at 500°C during 10 hours.

| SiO$_2$ | $Y$ (GPa) | $\nu$ | $a$ ($10^{-4}$ rad Hz$^{-b}$) | $b$ | $c\phi^B_{\text{tot}}$ ($10^{-6}$ m) |
|---|---|---|---|---|---|
| GC | 66 ± 4 | 0.19 ± 0.02 | 1.37 ± 0.22 | 0.024 ± 0.019 | 3.11 ± 0.26 |
| GC 500°C | 70 ± 1 | 0.19 ± 0.01 | 0.20 ± 0.04 | 0.030 ± 0.024 | 1.41 ± 0.05 |
| SPEC. | 78 ± 1 | 0.14 ± 0.01 | 8.87 ± 0.19 | -0.083 ± 0.003 | 0.84 ± 0.11 |
| SPEC. 500°C | 78 ± 1 | 0.11 ± 0.01 | 1.26 ± 0.23 | -0.069 ± 0.024 | 0.19 ± 0.15 |
| SPEC. 900°C | - | - | 0.039 ± 0.013 | 0.10 ± 0.04 | 0.038 ± 0.006 |
| DIBS | 74 ± 2 | 0.18 ± 0.02 | 1.45 ± 0.06 | -0.016 ± 0.005 | 0.39 ± 0.03 |
| DIBS 500°C | 75 ± 2 | 0.19 ± 0.02 | 1.42 ± 0.54 | -0.208 ± 0.044 | 0.42 ± 0.05 |

**Table 4.5:** Young's modulus $Y$, Poisson ratio $\nu$, and $a$, $b$, $c\phi^B_{\text{tot}}$ parameters from equation (4.14) for SiO$_2$ coatings deposited with GC, SPECTOR and DIBS, before and after the annealing at 500°C and 900°C.

### Annealing

The post-deposition heating treatment is of fundamental importance for the purpose of reducing coating thermal noise. The problem is to find the optimal annealing temperature $T_a$ and duration $\Delta t$, avoiding coating crystallization which would increase optical loss by scattering and absorption. In figure 4.20 is shown the effect of increasing $\Delta t$ with $T_a = 500$°C constant on SiO$_2$ deposited by the SPECTOR.

SiO$_2$ loss, shown in figure 4.20a, decreases with the annealing time and, as it can be observed in figure 4.20b, this behaviour has a structural counterpart.

SiO$_2$ is composed of tetrahedral units arranged in rings of different size [106] and the area of the $D_2$ band of the Raman spectrum, near 600 cm$^{-1}$, is associated to 3-fold ring population [107]. A correlation between coating loss and $D_2$ area has been found, suggesting that $SiO_2$ loss increases with the 3-fold ring population [108]. This correlation holds for different kinds of $SiO_2$, for coatings deposited with different parameters and treated with different annealing times, and also for bulk (Fig. 4.21).

Figure 4.22 shows coating loss and structure for increasing $T_a$, with $\Delta t = 10$ hours constant. $SiO_2$ coating loss angle decreases (4.22a) and its structure evolves considerably (4.22b). The fit values for the coating annealed at 900°C are listed in table 4.5. Surprisingly, crystallization occurs at $T_a = 1000$°C, differently from fused silica whose crystallization occurs at higher temperature.

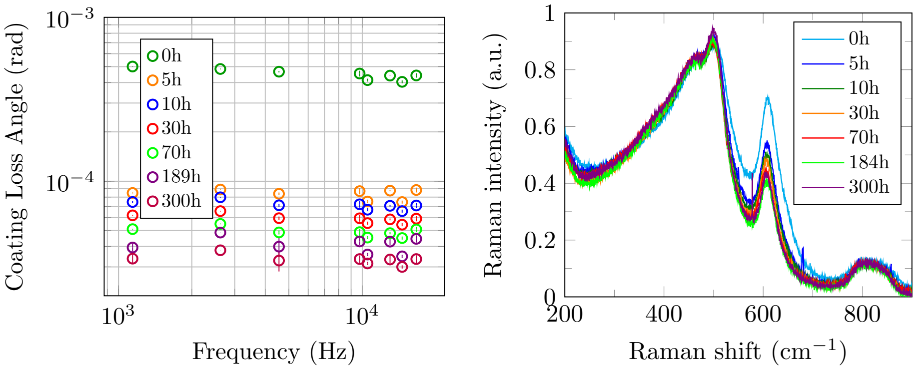

**(a)** Coating loss angle.

**(b)** Raman spectrum.

**Figure 4.20:** $SiO_2$ coating (SPECTOR) annealed at 500°C for different time $\Delta t$. (a) Evolution of coating loss angle. (b) Evolution of Raman spectrum (acquired in collaboration with Institut Lumière Matière (ILM)).

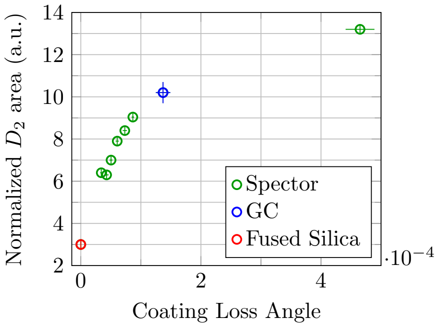

**Figure 4.21:** Normalized $D_2$ area versus coating loss angle of $SiO_2$ coatings deposited with different coaters.

### 4.4.3 Optical Properties

All the analysed coatings gave comparable results; for this reason, only one representative sample deposited with the GC will be shown. Furthermore, the analysis has been done with both ellipsometers, obtaining comparable results. For the sake of clarity, only the measurement obtained by the M-2000 ellipsometer, which extends more in the NIR region, will be shown.

After the coating deposition, the $\Psi$ data showed in figure 4.23a present oscillations that follow the bare substrate measurements. The amplitude of the oscillations depends

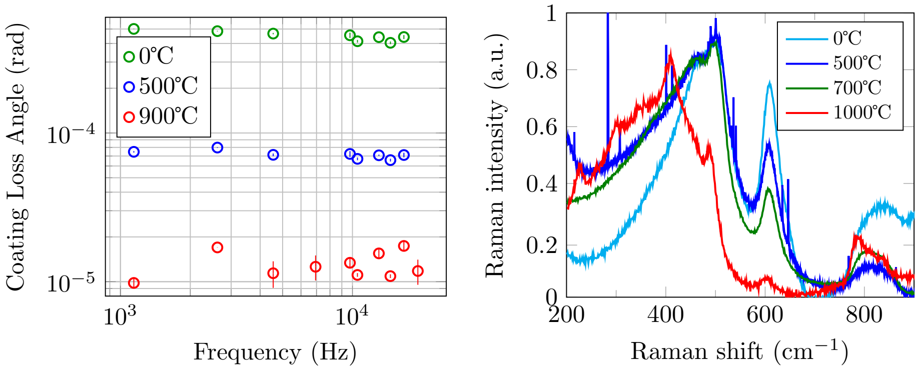

**(a)** Coating loss angle. **(b)** Raman spectrum.

**Figure 4.22:** $SiO_2$ coating (SPECTOR) annealed for $\Delta t = 10$ hours at different temperature. (a) Evolution of coating loss angle. (b) Evolution of Raman spectrum (in collaboration with ILM).

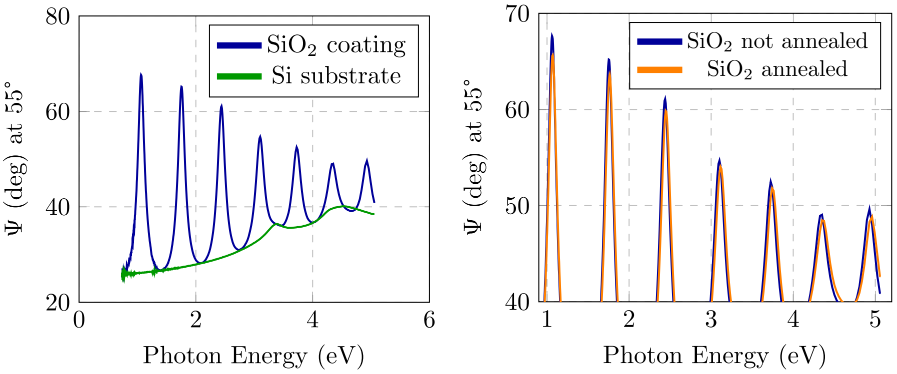

**(a)** $SiO_2$ on Silicon **(b)** $SiO_2$ zoom

**Figure 4.23:** Ψ data measured at 55°. (a) Comparison between Ψ data of Si substrate and $SiO_2$ coating. (b) Comparison between Ψ data of $SiO_2$ coating before and after the annealing at 500°C.

on the difference between the refractive index of the substrate and of the coating, whereas the distance of the minima/maxima depends on the coating thickness. Since the substrate does not evolve with the annealing, the minima of the oscillations after the annealing lie on the same curve. For this reason, in figure 4.23b the effect of the standard annealing at 500°C is shown only in the maxima of the oscillations, where the differences between the curves before and after the annealing are well visible. The annealing reduces the amplitude of the oscillations and shift the maxima positions. Under this respect, the refractive index of the coating after the annealing should be lower with a consequently change in the coating thickness.

For sake of clarity, in figure 4.24 only (Ψ, Δ) data and fit curves after the annealing are shown at different angles. It is evident from the data that the oscillations, related to the interference of the multiple reflections in the transparent film, do not stop, pointing out that any absorbing mechanism occurs in the whole energy region. Indeed, the extinction coefficient is too low to be appreciated by reflection SE.

The samples have been analysed with a three-layers model [109] including the substrate, the thin film and a surface layer. The latter was modelled through a Bruggeman

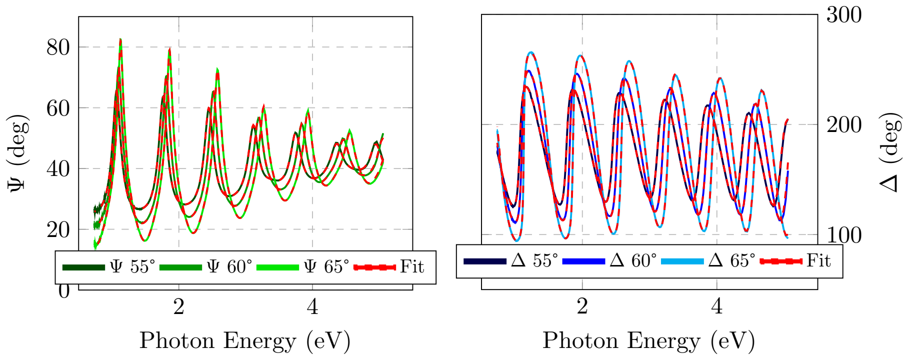

**(a)** $\Psi$ at different angles **(b)** $\Delta$ at different angles

**Figure 4.24:** Experimental data and fit curves at different angles for SiO$_2$ coating after the annealing at 500℃.

effective medium approximation (EMA) layer, which accounts for roughness. Silica is transparent in the whole measured energy region. Thus, in order to reproduce the experimental data, Cauchy or two poles function have been used as optical models for the thin film. In figure 4.24 the best fit obtained by the two poles function is compared with the ($\Psi$, $\Delta$) data.

In figure 4.25a a comparison of the refractive index of SiO$_2$ coating obtained from the sample before and after the annealing is shown. The effect of the annealing is to reduce the refractive index. The reduction at 1064 nm is of about 1%, as can been observed in table 4.6, furthermore, the annealing increases the coating thickness of about the same amount. The coating thickness has been then used to estimate the density of the material. The thickness and the density of the sample are listed in table 4.6. Remarkably, the SPECTOR sample is significantly denser and stiffer than the GC one, whose properties closely resemble to those of bulk fused silica. The resulting refractive index is comparable with previous determinations, such as those reported for a silica film deposited by dual Ar$^+$ IBS coater [110]. Furthermore, at 600 nm the refractive index of our coating is comparable to other experiments reporting on ion-beam assisted SiO$_2$ growth [111].

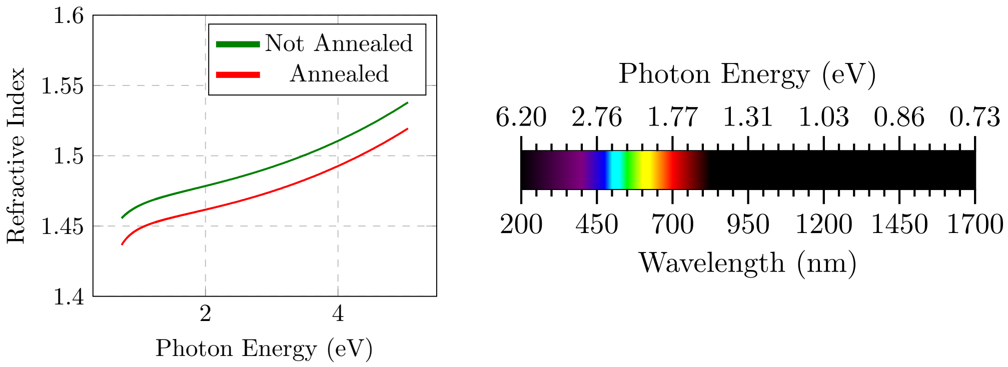

**(a)** Refractive Index. **(b)** Spectrum.

**Figure 4.25:** (a) Refractive index of SiO$_2$ coating before (green) and after (red) the annealing at 500℃. (b) Analysed wavelength region converted in photon energy.

The final results presented in table 4.6 are obtained by taking into account Cauchy

| $SiO_2$ | Thickness (nm) | $\rho$ (g/cm$^3$) | $n$@1064 nm | $n$@1550 nm |
|---|---|---|---|---|
| GC | 718 ± 2 | 2.33 ± 0.06 | 1.468 ± 0.005 | 1.46 ± 0.01 |
| GC ann. | 725 ± 2 | 2.20 ± 0.04 | 1.452 ± 0.004 | 1.45 ± 0.01 |
| SPEC. | 2961 ± 13 | 2.38 ± 0.01 | 1.480 ± 0.005 | 1.474 ± 0.005 |
| SPEC. ann. | 3000 ± 15 | 2.36 ± 0.03 | 1.467 ± 0.006 | 1.460 ± 0.006 |
| DIBS | – | 2.02 ± 0.09 | 1.44 ± 0.01 | 1.44 ± 0.02 |
| DIBS ann. | – | 1.91 ± 0.09 | 1.44 ± 0.01 | 1.44 ± 0.02 |

**Table 4.6:** Thickness, density $\rho$ and refractive index $n$ at wavelength of interest ($\lambda$ = 1064 nm for LIGO and Virgo detectors, $\lambda$ = 1550 nm of future detectors such as the Einstein Telescope) of different $SiO_2$ samples before and after the annealing at 500°C. The silica DIBS values have been obtained by transmission spectrophotometric measurements.

and poles models which give comparable and reasonable MSE, considering the measurements of both ellipsometers. From the analysis, the EMA layer on top is of the order of 3 nm.

### 4.4.4 Summary

Silica coating deposited with GC, SPECTOR and DIBS has been investigated. Silica SPECTOR is stiffer and the coating loss angle measurements suggest a dependence of the mechanical loss on the deposition rate, with the CG and DIBS yielding the lowest internal friction.

The optical characterization shows that silica SPECTOR is also significantly denser as confirmed by the higher refractive index than the one of silica GC. Furthermore, silica coating shows a lower refractive index after the annealing.

It has been observed that the coating presents spurious loss at the edge, likely related to the interaction of the sputtered material with the edge. The internal friction of silica SPECTOR has been than characterized as function of the in-air post-deposition annealing, monitoring the structure with Raman spectroscopy on analogous samples. It has been observed that the coating loss angle is reduced by the increasing of the annealing temperature and the annealing time. Furthermore, the Raman spectrum highlighted an evolution of the $D_2$ peak area, associated to the population of tetrahedral units arranged in 3-fold ring. The evolution of internal friction and structure with respect to annealing showed a correlation between the $D_2$ area and the coating loss angle. Another surprising result regards the unexpected crystallization at 1000°C.

Finally, comparing the silica coating loss angle with the loss angle of fused-silica (figure 4.26) it can be observed that at room temperature, the internal friction of silica coating obtained with the frequency trend $af^b$ at 100 Hz is higher than the one of fused-silica even after the annealing. This difference could be related to the different frequency range, which is of the order of the MHz for the fused-silica [112].

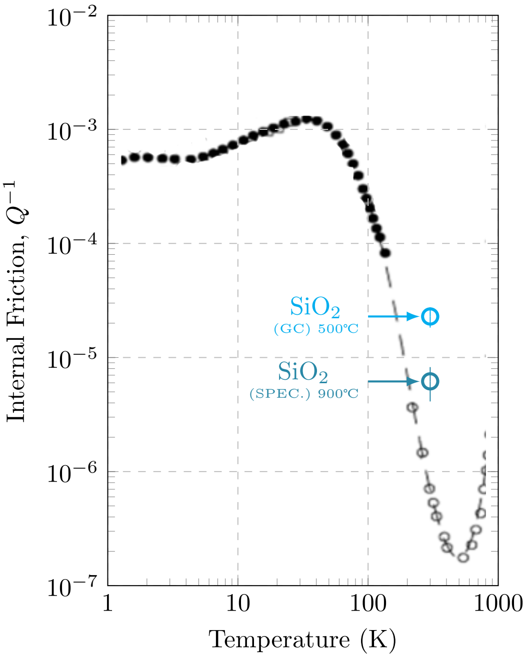

**Figure 4.26:** Internal friction of fused-silica as function of temperature [112], acquired at 1.5 MHz. The blue dots refer to the loss angle of silica coating at 100 Hz, annealed at 500℃ and 900℃.

## 4.5 Ta$_2$O$_5$ and Ti:Ta$_2$O$_5$ Coatings

The Ti:Ta$_2$O$_5$ is the high-refractive index layer in the current Bragg reflector of gravitational-wave detectors. Historically, the Ta$_2$O$_5$ was used because of its very low optical absorption. Ta$_2$O$_5$ proved to be substantially more dissipative than silica [11, 113], making it the dominant source of coating loss in the Bragg mirrors. This loss was decreased by mixing titanium dioxide (TiO$_2$, titania) with tantala, a procedure developed by the LMA [114] for the LIGO and Virgo collaborations [52]. Eventually, Ti-mixing proved to be beneficial to the optical absorption of the high-reflective (HR) coating as well [115]. In the following, we will refer at the mixing as Ti-doping, which is entered in the common language in this research field.

### 4.5.1 Mechanical Properties

**Deposition Conditions**

In figure 4.27 the coating loss angles of tantala deposited with the GC, SPECTOR and the DIBS are shown. It can be observed that it is not possible to discriminate between family modes, symptom of a negligible edge effect. Thus, the analysis has been carried out by keeping only the $af^b$ term in equation (4.14).

The GC provides the slowest rate and lowest loss values, whereas the SPECTOR the fastest rate (2.8 $\mathring{A}$/s) and the highest loss values. however, despite having the same deposition rate (within 25% experimental uncertainty), the DIBS sample has lower loss values than those of the GC sample. While this inconsistency will be subject to further investigation, we may conclude that, as a rule of thumb, the faster the deposition rate, the higher the loss. The situation changed radically after the annealing (figure 4.27b), when all the films exhibited equal and significantly lower loss, as if their deposition history had been completely erased. This outcome seems to suggest that 500℃ in-air annealing during 10 hours brings the structure of tantala coatings down to a

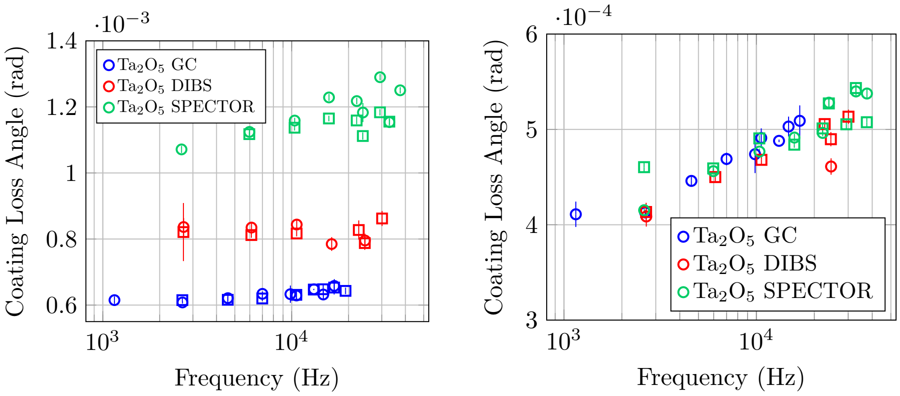

**(a)** Not annealed. **(b)** Annealed.

**Figure 4.27:** Coating loss angle of $Ta_2O_5$ deposited with the GC, SPECTOR and the DIBS. (a) The comparison before the annealing. (b) The comparison after the annealing at 500°C. The colours identifies the coater and the different markers denote distinct samples; shaded regions represent uncertainties from fitting parameters of $af^b$.

stable optimal configuration for lowest loss, in agreement with observations that higher annealing temperatures or longer duration do not decrease loss further [116]. The same erasing effect has been observed later on in an independent experiment, where sputtered tantala coatings (IBS, magnetron) had been annealed after being deposited on heated substrates [117]. The coating structure depends on the chemical composition of the sputtered particles and on their energy distribution and electrical charge, however so far there is no model available nor there are any measurements for any of our coaters about these data. A research project has been recently financed to address this issue (project ViSIONs).

For all the samples the elastic constants have been carried out by fitting the measured dilution factor $D$ with simulations. In figure 4.28 the fit result for $Ta_2O_5$ coating deposited with the CG and annealed at 500°C is shown, as representative sample. The final results are listed in table 4.7.

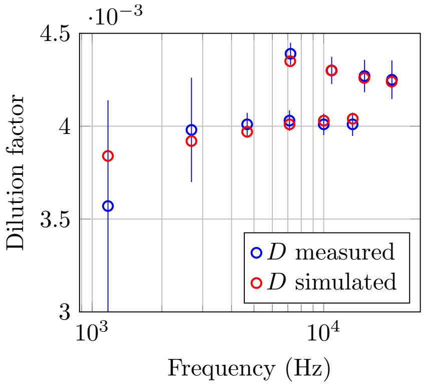

**Figure 4.28:** Fit of measured dilution factor (blue) with simulated values (red), $Ta_2O_5$ coating annealed in air at 500°C during 10 hours.

If measured via nano-indentation, the Young's modulus of IBS tantala coatings appears to be about 140 GPa [118], i.e. about 18% higher than our value. This difference could be explained by the nature of the films, deposited with different conditions,

| Ta$_2$O$_5$ | $Y$ (GPa) | $\nu$ | $a$ ($10^{-4}$ rad Hz$^{-b}$) | $b$ |
|---|---|---|---|---|
| GC | 121 ± 1 | 0.30 ± 0.01 | 4.61 ± 0.11 | 0.036 ± 0.003 |
| GC ann. | 117 ± 1 | 0.28 ± 0.01 | 1.88 ± 0.06 | 0.101 ± 0.004 |
| DIBS | 117 ± 1 | 0.27 ± 0.01 | 8.20 ± 0.24 | - |
| DIBS ann. | 115 ± 1 | 0.28 ± 0.01 | 2.27 ± 0.14 | 0.078 ± 0.007 |
| SPEC. | 121 ± 1 | 0.29 ± 0.01 | 7.60 ± 0.21 | 0.045 ± 0.003 |
| SPEC. ann. | 121 ± 2 | 0.29 ± 0.01 | 2.29 ± 0.06 | 0.079 ± 0.003 |

**Table 4.7:** Young's modulus $Y$, Poisson ratio $\nu$, and $a$, $b$ parameters of the model $af^b$ for Ta$_2$O$_5$ deposited with GC, DIBS and SPECTOR, before and after the annealing at 500°C.

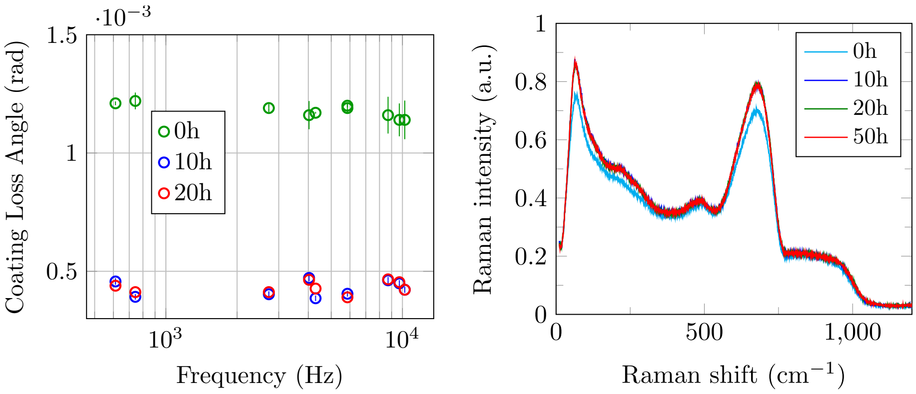

**(a)** Coating loss angle.

**(b)** Raman spectrum.

**Figure 4.29:** Ta$_2$O$_5$ coating deposited with the SPECTOR and annealed at 500°C for different time $\Delta t$. (a) Evolution of coating loss angle. (b) Evolution of Raman spectrum (acquired in collaboration with ILM).

and by the fact that results from nano-indentation are model dependent and rely on assumptions on the coating Poisson's ratio. Furthermore, nano-indentations of the same coating deposited on different substrates might give different results: our tantala SPECTOR coatings yielded a reduced coating Young's modulus of 130 ± 3 GPa on silica witness samples and of $100 \pm 3$ GPa on silicon wafers.

### Annealing

In figure 4.29 it is shown the effect of increasing $\Delta t$ with $T_a = 500$°C constant on Ta$_2$O$_5$ deposited by the SPECTOR on a 3" silica disk 0.5 mm thick. Ta$_2$O$_5$ loss, shown in figure 4.29a, decreases rapidly with the first annealing, reaching a limit value; as it can be observed in figure 4.29b, this behaviour has a structural counterpart.

Figure 4.30 shows coating loss and structure for increasing $T_a$, with $\Delta t = 10$ hours constant. Ta$_2$O$_5$ coating loss is roughly constant for $T_a > 500$°C (4.30a) and its structure does not change up to $T_a = 650$°C (4.30b), when crystallization occurs.

### Ti:Ta$_2$O$_5$ mixture

The titania content in HR coatings for gravitational-wave detectors was initially determined by analysing a set of Bragg reflectors with $\lambda/4$ layers [52], produced in the DIBS and in the GC with different titania-to-tantala mixing ratios. Since then, the structure of the HR coatings of Advanced LIGO and Advanced Virgo has evolved [94,119], while

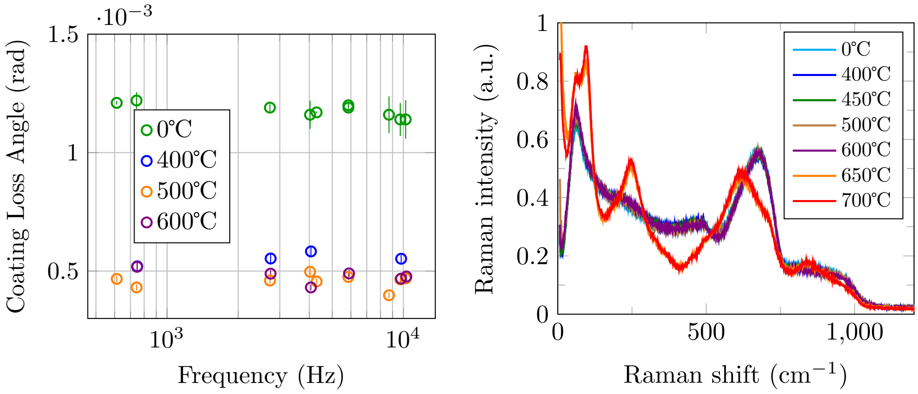

**(a)** Coating loss angle. **(b)** Raman spectrum.

**Figure 4.30:** $Ta_2O_5$ coating deposited with the SPECTOR and annealed for $\Delta t = 10$ hours at different temperature. (a) Evolution of coating loss angle. (b) Evolution of Raman spectrum (acquired in collaboration with ILM).

the Ti/Ta ratio in the Ti-doped tantala layers remained the same. This choice is now confirmed by our latest loss measurements of single titania-doped tantala films produced with the GC, which we also characterized through Rutherford back-scattering (RBS) and energy-dispersive X-ray (EDX) spectroscopy. In figure 4.31 there is the coating loss angle as function of Ti/Ta ratio: Ti/Ta= 0.27 yielded minimum loss and thereby had been chosen as optimal ratio. In the following, the standard Ti:$Ta_2O_5$ deposited by the GC with Ti/Ta= 0.27 is presented in detail.

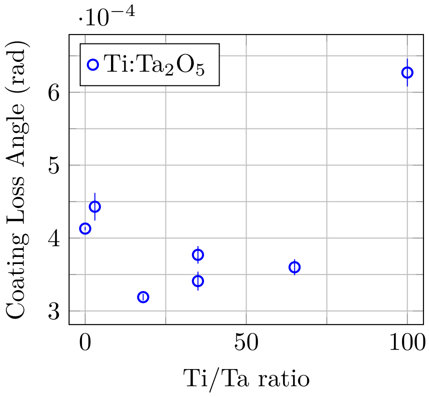

**Figure 4.31:** Coating loss angle of $Ta_2O_5$ as function of Ti/Ta ratio. For clarity, only values measured at ∼2.5 kHz are shown; the same trend has been observed at ∼10 kHz. The number of points corresponds to the number of samples. The variation of the loss angle observed on similarly doped samples is not explained, and will be subject to further investigation.

In figure 4.32a the coating loss angle before and after the post-deposition annealing at 500°C is shown. As expected, the annealing decreases the loss angle. By comparing Ti/Ta= 0.27 Ti:$Ta_2O_5$ to $Ta_2O_5$ in figure 4.32b, we observe that both coating materials feature similar loss before the annealing, whereas after the annealing Ti:$Ta_2O_5$ loss is $\sim 25\%$ lower in the whole sampled band, suggesting that the lower loss of Ti:$Ta_2O_5$ is the result of a combined effect of mixing and annealing. The $\sim 25\%$ loss reduction has

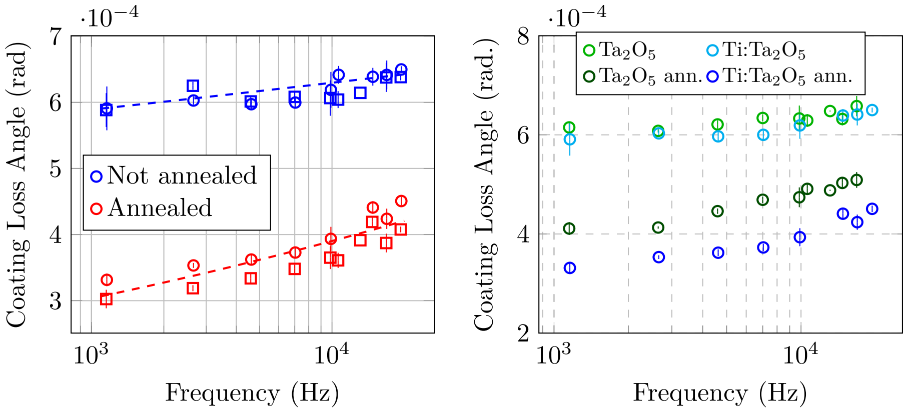

**(a)** $Ti{:}Ta_2O_5$. **(b)** $Ta_2O_5$ and $Ti{:}Ta_2O_5$.

**Figure 4.32:** (a) Coating loss angle of standard $Ti{:}Ta_2O_5$. The colours identifies the coater and the different markers denote distinct samples (b) The comparison of coating loss angle of $Ta_2O_5$ and $Ti{:}Ta_2O_5$ before and after the annealing.

been confirmed by independent coating thermal noise measurements [120].

By fitting the measured dilution factor with the simulations, the elastic constants have been obtained for the sample before and after the annealing. In table 4.8 the final results are listed. It can be observed that the Ti-doping does not affect the elastic constants and that the main difference of loss angle is after the annealing.

| $Ti{:}Ta_2O_5$ | $Y$ (GPa) | $\nu$ | $a$ ($10^{-4}$ rad Hz$^{-b}$) | $b$ |
|---|---|---|---|---|
| GC | 122 ± 1 | 0.30 ± 0.01 | 4.82 ± 0.18 | 0.029 ± 0.004 |
| GC ann. | 120 ± 4 | 0.29 ± 0.01 | 1.43 ± 0.07 | 0.109 ± 0.005 |

**Table 4.8:** Young's modulus $Y$, Poisson ratio $\nu$, and $a$, $b$ parameters of the coating loss model $af^b$ for standard $Ti{:}Ta_2O_5$ deposited with GC, before and after the annealing at 500°C.

### 4.5.2 Optical Properties

In figure 4.33 are shown the data obtained by VASE ellipsometer of $Ta_2O_5$ deposited with the GC and annealed at 500°C. For sake of clarity, only the data at 60° are shown. The oscillations related to the non-absorbing NIR region stop when approaching the UV region, highlighting the absorption threshold.

The $(\Psi, \Delta)$ data show a quality degradation in the UV region caused by the strong absorption which reduces the signal to noise ratio and and data are no longer useful for fitting purposes. The interference features, related to multiple reflections in the transparent region of the coating, stop quite sharply around 4 eV; this behaviour marks the fundamental absorption threshold. Furthermore, the amplitude of the oscillations in the visible region starts to slowly reduce approaching the absorption threshold. This could be related to the presence of the Urbach tails which are responsible of the weak absorption near the absorption edge, inside the energy gap.

From the comparison of the measurements before and after the annealing, shown in figure 4.34, it can be noted that the main difference related to the heating treatment

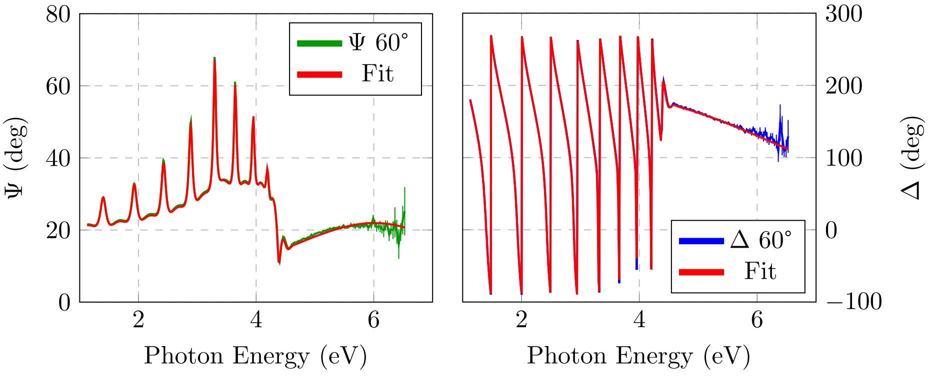

**(a)** $Ta_2O_5$, Ψ.

**(b)** $Ta_2O_5$, Δ.

**Figure 4.33:** Ψ (green), Δ (blue) data of $Ta_2O_5$ annealed coating, measured with VASE ellipsometer. The data are compared with the best fit (red) obtained with a CL model.

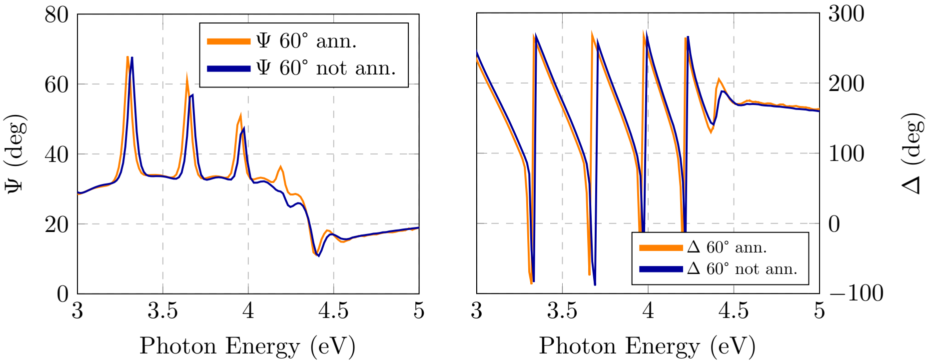

**(a)** $Ta_2O_5$, Ψ.

**(b)** $Ta_2O_5$, Δ.

**Figure 4.34:** (Ψ, Δ) data at 60° for $Ta_2O_5$ coating before (blue) and after (orange) the annealing.

is around the absorption threshold. The annealing seems not to affect the energy gap. However, it is evident that after the annealing, there are oscillations near the absorption threshold that appear. This means that the absorption, related to the Urbach tails, is slightly reduced.

The data have been analysed through a three-layers model including the substrate, the thin film and a surface layer [109]. The latter was modelled through a Bruggeman effective medium approximation (EMA) layer, which accounts for roughness. In a first step of the analysis, Cauchy and 2-poles functions have been used in order to describe the optical properties of the thin layer in the region of high transparency, below 3 eV. The values of thickness and refractive index of the coating obtained by this kind of analysis have been used as starting point in physical models aimed to reproduce data in the whole measured energy region. Although the thin film can be represented by both Cody-Lorentz (CL) and Tauc-Lorentz (TC) models, the best fit has been provided by the CL model which accounts for the Urbach tails. It has to be noticed that the analysis has been done at three angles of incident 55°, 60° and 65°, and the fit curves reproduced the (Ψ, Δ) data with the same accuracy.

In order to test the validity of the Urbach tails, the (Ψ, Δ) data of $Ta_2O_5$ coating before the annealing, which presents higher absorption in the region of interest, have been described by two CL models. The first model did not include the Urbach tails and the best fit reproduced the $(\Psi, \Delta)$ behaviour giving a mean squared error (MSE) of about 6.4. The main differences between the fit curves and the data were mainly located near the absorption edge, where the fit curves differed more than 10% from the data. The second CL model included the Urbach tails and the best fit gave comparable optical properties, especially the refractive index in the transparent region, the energy gap and thickness; however, the model reproduced the $(\Psi, \Delta)$ behaviour giving a lower MSE of about 4.0. The differences located near the absorption edge have been reduced to less than 5%, demonstrating that the Urbach tails are needed in the model to better reproduce the $(\Psi, \Delta)$ data. The same analysis has been done also for Ti:Ta$_2$O$_5$ and the same result has been obtained. For this reason, the fit curves shown in figure 4.33 and the following analysis refer to CL model including the Urbach tails.

The analysis showed that the annealing increases the coating thickness of about almost 2% from 579 ± 2 to 592 ± 2 nm. The coating thickness has been then used to estimate the density of the material, which does not change considerably with the annealing. The thickness and the density of the sample are listed in table 4.9.

| Ta$_2$O$_5$ | $n$@1064 nm | $n$@1550 nm | $\rho$ (g/cm$^3$) | $E_g$ (eV) | $E_U$ (meV) |
|---|---|---|---|---|---|
| GC | 2.07 ± 0.01 | 2.06 ± 0.01 | 7.40 ± 0.03 | 4.1 ± 0.2 | 164 ± 8 |
| GC ann. | 2.05 ± 0.01 | 2.03 ± 0.01 | 7.33 ± 0.06 | 4.0 ± 0.1 | 130 ± 10 |
| DIBS | 2.06 ± 0.01 | 2.04 ± 0.01 | 7.04 ± 0.09 | - | - |
| DIBS ann. | 2.03 ± 0.01 | 2.02 ± 0.01 | 6.94 ± 0.09 | - | - |
| SPEC. | 2.11 ± 0.01 | 2.09 ± 0.01 | 7.75 ± 0.03 | 4.1 ± 0.1 | - |
| SPEC. ann. | 2.09 ± 0.01 | 2.07 ± 0.01 | 7.47 ± 0.09 | 4.1 ± 0.1 | |

**Table 4.9:** Refractive index $n$ at wavelength of interest ($\lambda = 1064$ nm for LIGO and Virgo detectors, $\lambda = 1550$ nm of future detectors such as the Einstein Telescope), density $\rho$, energy gap $E_g$ and Urbach energy $E_U$ of different Ta$_2$O$_5$ samples before and after the annealing at 500°C. The values for the DIBS sample have been obtained by spectrophotometric measurements on Vis-NIR region and hence the values regarding the absorption threshold have not been worked out. The Ta$_2$O$_5$ SPECTOR has been deposited on silica substrate and the bad quality of data did not allow a reliable estimation of $E_U$.

The roughness obtained on these coatings is less than 1 nm and the value is comparable with atomic force microscopy (AFM) measurements of root mean square (RMS) roughness on this kind of samples [121]. Since its value is less than 1% of the coating thickness, the EMA layer does not affect substantially the coating fit optical parameters, especially in the NIR region. Furthermore, the annealing reduces the refractive index in the transparent region, as shown in figure 4.35. The values of the refractive index at wavelengths of interest 1064 nm and 1550 nm are listed in table 4.9.

In figure 4.36a the Cody Plot obtained with the CL model is shown, in order to evaluate the absorption edge. The energy gap $E_g$ is not affected by the annealing, whereas it is evident from the figure that there is a clearly change in the absorption trend before the energy gap, related to the change of the Urbach tails. Indeed, the extension of the Urbach tails, quantified by $E_U$, are reduced after the annealing. The values of the energy gap and the Urbach energies are listed in table 4.9.

In figure 4.37 the data of the standard Ti:Ta$_2$O$_5$ coating, deposited by the GC, are compared with the fit curves obtained using the CL model. Also in this case, the $(\Psi, \Delta)$ data show a quality degradation related to the strong absorption in the UV

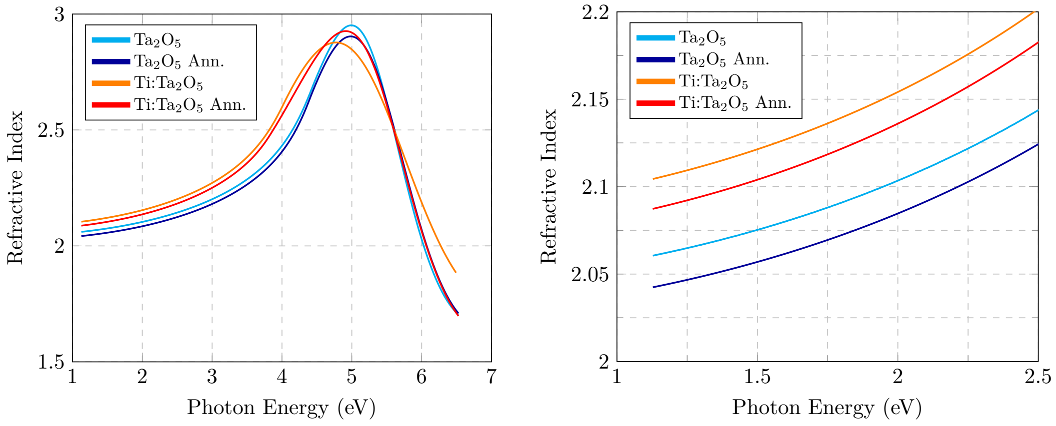

**(a)** Refractive index.

**(b)** Zoom in the NIR-Vis region.

**Figure 4.35:** a) Refractive index of $Ta_2O_5$ coating before (light blue) and after (blue) the annealing, compared to the that of Ti:$Ta_2O_5$ coating before (orange) and after (red) the annealing. b) The zoom in the NIR-Vis region.

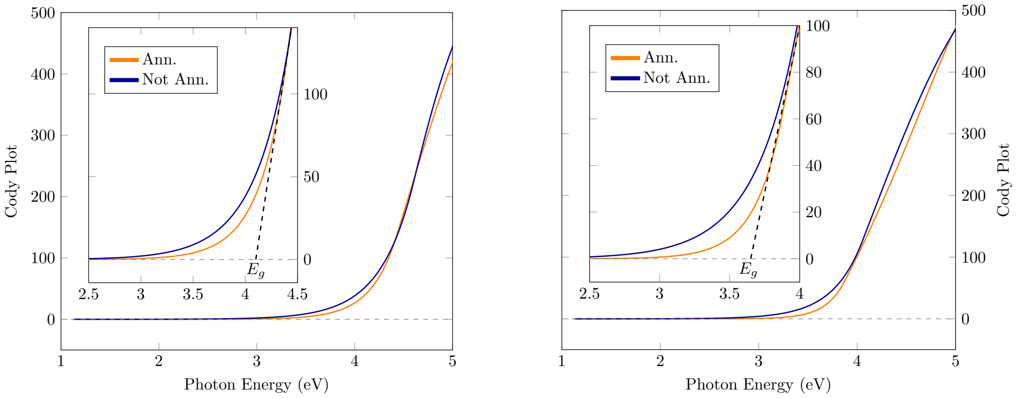

**(a)** $Ta_2O_5$.

**(b)** Ti:$Ta_2O_5$.

**Figure 4.36:** Cody plot for (a) $Ta_2O_5$ and (b) Ti:$Ta_2O_5$ before (blue) and after (orange) the annealing, obtained with the CL model. The dashed line represents the linear trend of $(\alpha(E)n(E)/E)^{1/2}$ and highlight the energy gap value. The data not covered by the linear trend, represent the Urbach tails.

region.

The annealing reduces the refractive index (figure 4.35) in the NIR region where at 1064 the reduction is almost about 1%. The coating thickness is increased instead of about 2% from $500 \pm 2$ to $509 \pm 2$. The coating thickness has been used to determine the density. The values of the refractive index at wavelengths of interest 1064 nm and 1550 nm and the density are listed in table 4.10. It can be observed that the Ti:$Ta_2O_5$ has a lower density than $Ta_2O_5$.

The oscillations in $(\Psi, \Delta)$ data, shown in figure 4.37, stop almost abruptly approaching the absorption edge. This could be related to shorter Urbach tails. The Cody plot shown in figure 4.36b highlights the effect of the heating treatment on the Ti:$Ta_2O_5$ absorption edge. The energy gap is not affected by the annealing whereas there is a clearly reduction of the Urbach tails. Furthermore, by comparing $E_g$ in table

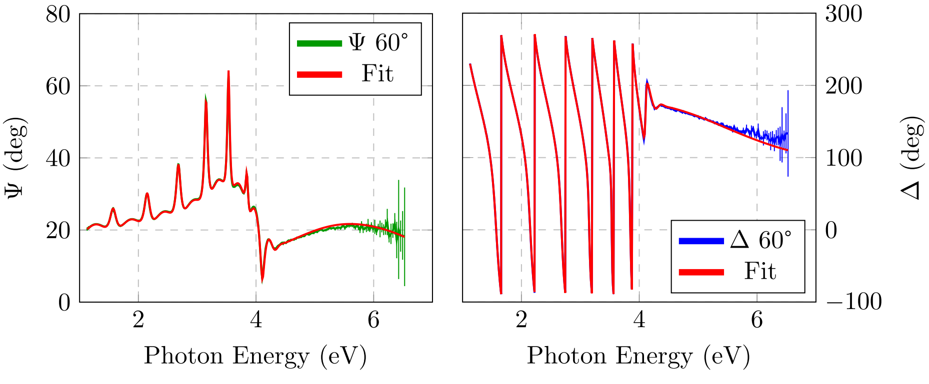

**(a)** Ti:Ta$_2$O$_5$, Ψ. **(b)** Ti:Ta$_2$O$_5$, Δ.

**Figure 4.37:** Ψ (green), Δ (blue) data of Ti:Ta$_2$O$_5$ annealed coating, measured with VASE ellipsometer. The data are compared with the best fit (red) obtained with the CL model.

| Ti:Ta$_2$O$_5$ | $n$@1064 nm | $n$@1550 nm | $\rho$ (g/cm$^3$) | $E_g$ (eV) | $E_U$ (meV) |
|---|---|---|---|---|---|
| GC | 2.11 ± 0.01 | 2.10 ± 0.01 | 6.87 ± 0.06 | 3.6 ± 0.1 | 152 ± 5 |
| GC ann. | 2.09 ± 0.01 | 2.08 ± 0.01 | 6.65 ± 0.07 | 3.6 ± 0.1 | 108 ± 5 |

**Table 4.10:** Refractive index $n$ at wavelength of interest ($\lambda = 1064$ nm for LIGO and Virgo detectors, $\lambda = 1550$ nm of future detectors such as the Einstein Telescope), density $\rho$, energy gap $E_g$ and Urbach energy $E_U$ of Ti:Ta$_2$O$_5$ samples deposited with the GC before and after the annealing at 500℃.

4.10, it is evident that the Ti-doping reduces the energy gap. This effect can be also observed directly in the $(\Psi, \Delta)$ data, comparing the figures 4.33a and 4.37a, where it is evident that the Ti-doping causes a red-shift of the energy gap.

The values of the energy gap and the Urbach energy are listed in table 4.10. The values confirm the homogeneity of the coatings since, especially for Ta$_2$O$_5$ the shift of the energy gap due to the Ti-doping, where the TiO$_2$ has been found to have an energy gap about $3.3 - 3.5$ eV [122, 123], seems in agreement with a linear combination of the energy gap of pure material considering the atomic ratio concentration of 0.27. Analysing the Urbach energy obtained by the CL model from Ta$_2$O$_5$ and Ti:Ta$_2$O$_5$ (table 4.9 and 4.10), it can be noticed that both Ti-doping and annealing reduce the Urbach energy. In particular, the impact of the annealing is more evident than those of the doping. Finally, by comparing refractive index in figure 4.35, it can be observed that the Ti-doping increases the refractive index, in the NIR region, including 1064 nm (table 4.10).

### 4.5.3 Correlation Between Urbach Energy and Internal Friction

In the context of optical measurements, so called Urbach tails [59] (usually observed by optical absorption measurements in crystalline and amorphous semiconductors [68]), describe a sub-gap exponential broadening of the absorption edge that is related to structural and thermal disorder. The concept of band-tails states finds interesting application in the study of amorphous solids [124, 125] where the structural disorder is dominant with respect to thermal one. The structural origin of the exponential tails [69]

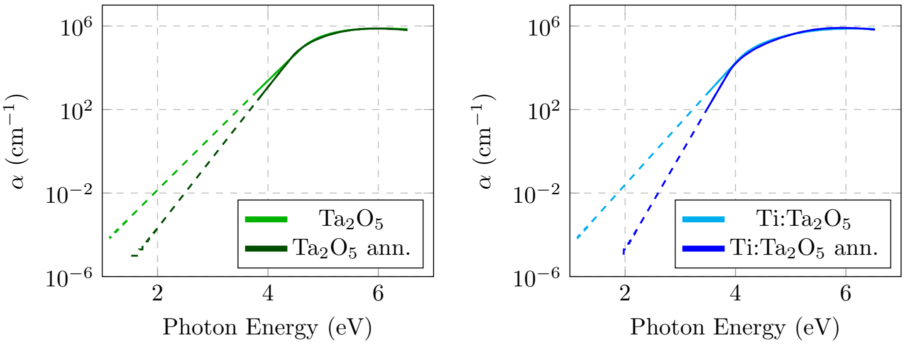

**(a)** $Ta_2O_5$. **(b)** Ti:$Ta_2O_5$.

**Figure 4.38:** Absorption coefficient of $Ta_2O_5$ and Ti:$Ta_2O_5$ before and after the annealing, obtained with the CL model. The logarithmic scale allows to distinguish better the different slopes in the region where the absorption decays exponentially with the energy $E_U$. The solid lines represent the absorption appreciated by SE analysis. The dashed lines represent an extension of the CL model to better distinguish the different slopes.

can give precious insight in atomic organization of the system involving several tens of atoms.

In recent work [126] a correlation between the mechanical coating loss angle and the short-range structural organization has been claimed. However, recent studies [127, 128] showed that the TLS giving rise to the dissipation mechanism at room temperature must involve more complex structures, regarding a medium- and even long-range structural organization.

The Urbach energy is a parameter which quantifies the homogeneity of the structure by optical absorption investigation, probing a multi-range structural organization. In figure 4.38 the absorption coefficient is shown as the function of the photon energy for the same materials analysed in previous sections. In the logarithmic scale representation chosen for $\alpha$, Urbach tails are linear functions and the inverse of the slope is proportional to $E_U$. It is clearly evident that each sample has different slope.

The results about the coating loss angle and the optical absorption coefficient, exhibit a similar trend regarding the annealing and the mixing. In this respect, it is interesting to look at figure 4.39 where the coating loss angle is reported as function of the Urbach energy $E_U$, for both $Ta_2O_5$ and Ti:$Ta_2O_5$ coating under different conditions. The linear behaviour suggests the existence of a correlation between these two quantities [129].

The observed correlation between coating loss angle and Urbach energy calls for a common physical background, to be most naturally searched in the structural ground. In this respect, interesting results were obtained on tantala and Ti-doped tantala coatings, i.e. the same system investigated here (though deposited under different conditions), by combining loss angle and transmission electron microscopy (TEM) measurements, corroborated by molecular dinamycs (MD) simulations [126]. It has been shown through radial density function (RDF) measurements on Ti:$Ta_2O_5$ coating that a decrease of the measured loss angle is accompanied by a width reduction of the main RDF peak, related to metal-oxygen distances at the short-range scale.

More recent studies [130] highlighted that the amorphous material is made of Primary Structural Units (PSU) very similar to that of the units of the crystalline state. The authors claimed that annealing favours the organization of PSUs in short

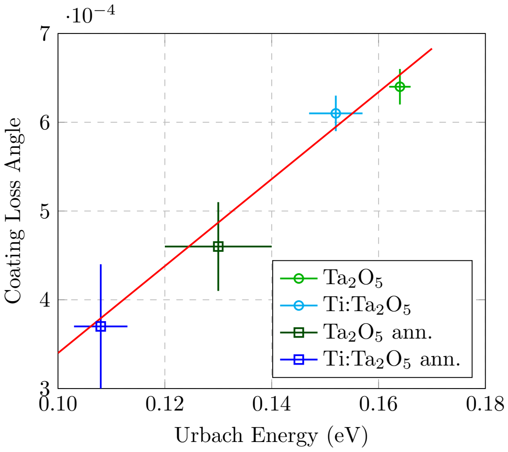

**(a)** Correlation.

| Coating | $\phi_c$ $\cdot 10^{-4}$ | $E_U$ (meV) |
|---|---|---|
| Ta$_2$O$_5$ | $6.4 \pm 0.2$ | $164 \pm 8$ |
| Ti:Ta$_2$O$_5$ | $6.1 \pm 0.2$ | $152 \pm 5$ |
| Ta$_2$O$_5$ ann. | $4.6 \pm 0.5$ | $130 \pm 10$ |
| Ti:Ta$_2$O$_5$ ann. | $3.7 \pm 0.7$ | $108 \pm 5$ |

**(b)** Data.

**Figure 4.39:** (a) Coating loss angle as a function of Urbach energy. Circles refer to as deposited samples, whereas squares to the samples after annealing. Two different coatings are considered, the Ta$_2$O$_5$ and the Ti:Ta$_2$O$_5$. Data are listed in the table (b). The reported loss angle is the average value of the data shown in figure 4.32b. The uncertainty is the maximum distance from the mean value.

1D-chains or 2D ribbons. Instead doping with Zr works in the opposite way. Further they suggest that the emergence or suppression of medium range 2D order may have important influence on mechanical properties of Ta$_2$O$_5$ coating.

A very recent paper [131] on the Zr:Ta$_2$O$_5$ system confirms that annealing produces systematic changes at the intermediate range scale; atomic modelling shows that such changes are to be related to well definite changes of the connections between PSU. These changes in the amorphous structure correlate with a reduction of mechanical losses.

In another recent work, Raman spectroscopy measurements on SiO$_2$ coating showed that extended structures such as rings made of three tetrahedrons (the PSU of SiO$_2$) are correlated to the coating loss angle [108] and have an activation energy of about 0.5 eV [132]. Furthermore, molecular dynamics of amorphous oxides such as SiO$_2$ showed that TLS with a barrier of 0.5 eV primarily involves quasi-1D chain of Si-O-Si and rings of Si-O-Si bonds [128]. The ensemble of measurements strongly suggests that at room temperature the main contribution to the loss angle is to be ascribed not only to short-range order but also to non-local structural organization.

The evidence for a relation between Urbach tails and structure is dating back to early works on the subject: Cody et al. [68] recognized that the width of the exponential tail is controlled by the amount of structural and thermal disorder in the network. More recent works [69, 70] have pointed out a relation between the presence of structural, not crystalline atomic organization on a medium range scale and the extension of Urbach tails.

Interesting results have been obtained by atomistic modelling of amorphous silicon [69]: molecular dynamics calculations show that, after the relaxation of the structure, an exponential valence tail appears in the electronic DOS. An inverse participation ratio analysis shows that the extreme tail eigenstates on amorphous semiconductors are primary localized on so-called topological filaments. In fact, while well localized defects induce mid-gap states, more complex and organized structures induces Urbach states near the valence or conduction band edge. In a-Si such structures are connected subnetworks of short bonds or long bonds [125]. Interesting, if the defects correlation is artificially destroyed, the Urbach tail is severely affected. Structural relaxation favours defects correlation and reduces the Urbach energy [69].

Post-deposition annealing generally modifies the Urbach tails. For example, Xue et al. [133] recorded the decreasing of Urbach energy in ZnO thin film with increasing annealing temperature from 600°C to 750°, whereas an inverse trend is observed exceeding 750°. This observation can help to understand Urbach tailing mechanisms, where the annealing may be used to allow a structural self-organization with a consequent lattice strain relaxation [134].

Therefore, Urbach tails can be viewed as a simple, meaningful way to visualize the occurrence of atomic organization in the amorphous structure, in a multi-range perspective. In this respect, the correlation between the Urbach tail extension and the mechanical losses could be explained through the spatial character of the Urbach tails states, related to atomic configurations that are responsible of the dissipation of mechanical energy as measured at 300 K in the acoustic band. Annealing relaxes the network and consequently this relaxation increases the spatial correlation between defects: the structure evolves from large stresses, concentrated in small regions, towards a situation where weakly strained regions are clustered around the site where the large stress were once. Urbach-type electronic states associated to medium/long range atomic configurations approach in energy the mobility edge, so that Urbach tails get narrower and Urbach energy decreases. In order to explain the impact of stress relaxation on energy loss, one has to consider that the measurement were done only at room temperature, hence, only the reduction of TLS density having a barrier height of about 0.5 eV is probed. Energy barriers of interest at room temperature correspond to equilibrium configurations formed by several PSUs, as suggested in a recent work [127, 130]. The recent observations of ref. [131] have been interpreted by the authors as due to a decrease of PSUs sharing edges in favour of corner sharing which form TLS with lower barrier heights.

The effect of Ti/Ta mixing on the reduction of the Urbach energy is less intuitive and to some extent even counter-intuitive. The investigation done in [126] points out that Ti-doping changes the $Ta_2O_5$ structure, possibly leading to an increase of short-range homogeneity. The authors showed that this is related to a low coating loss angle. In [126], reverse Monte Carlo simulation has been used to match the observed RDF and a significant fraction of $TaTiO_2$ ring fragments is formed in the doped coating. This changes the structure by modifying the angles between oxygen-metal-oxygen and metal-oxygen-metal as consequence. The considerations made above explain the reduction of the Urbach tails with the reduction of disorder in the material as a consequence of both annealing and mixing. Another mechanism could justify the modification of Urbach energy after mixing, based on the consideration that Urbach energy depends not only on static structural disorder but also on a temperature term [68, 71] that is related to the interaction of electronic states with the phonon spectrum. Although all the measurements reported here are done at room temperature, doping changes the phonon spectrum and likely the Debye temperature of the original materials. A changing in PSU connection, as found in ref. [131] is also able to change the Debye temperature. The modification of the phonon spectrum alters the relation between temperature and thermal disorder.

In any case, since the Urbach tails of doped oxides are less extended than in the undoped ones, we can infer that the local structure of the doped material is more homogeneous and that on a larger scale the material becomes organized into cluster of atoms, resulting in a lower loss angle.

The observed correlation between the energy extension of Urbach tails and the level of mechanical losses opens new perspectives. First, optical characterization of the fundamental absorption edge emerges as a tool for rapid pre-diagnostics of coating

| ITM | | | | |
|---|---|---|---|---|
| $f$ | $\phi_c$ ($10^{-4}$ rad) | $a$ ($10^{-4}$ rad $Hz^{-b}$) | $b$ | $r$ |
| 2708.1 | 1.6 ± 0.1 | 1.1 ± 0.3 | 0.05± 0.03 | 0.32 |
| 16092.6 | 1.7 ± 0.1 | | | |
| 16283.9 | 1.8 ± 0.1 | | | |
| 22423.4 | 1.7 ± 0.1 | | | |

| ETM | | | | |
|---|---|---|---|---|
| $f$ | $\phi_c$ ($10^{-4}$ rad) | $a$ ($10^{-4}$ rad $Hz^{-b}$) | $b$ | $r$ |
| 2708.6 | 2.4 ± 0.1 | 2.2 ± 0.6 | 0.01± 0.03 | 0.56 |
| 6168.3 | 2.3 ± 0.1 | | | |
| 16088.1 | 2.5 ± 0.1 | | | |
| 16297.9 | 2.4 ± 0.1 | | | |
| 22414.5 | 2.3 ± 0.1 | | | |

**Table 4.11:** Mechanical loss $\phi_c$ of Advanced LIGO and Advanced Virgo input (ITM) and end (ETM) mirror high-reflective coatings. Nominal specification of thickness ratio $r = t_H/t_L$, where $t_H$ and $t_L$ are the thickness of the high-index and low-index layers ($t_H = 727$ nm, $t_L = 2080$ nm for the ITM and $t_H = 2109$ nm, $t_L = 3766$ nm for the ETM).

mechanical quality. At the same time, the characterization of Urbach tails complements the analysis of the structure in a different spatial range. Being the Urbach energy a single value parameter, hardly it can describe the complexity of the amorphous material, whereas it is correlated to the structural homogeneity of the material at the right range for the energy loss mechanisms. Finally, the correlation has been observed on different oxides, suggesting its general validity for this kind of coating materials [129].

### 4.5.4 High-Reflective Coatings of Advanced LIGO and Advanced Virgo

The knowledge of the mechanical properties of mono-layers are commonly used to predict the loss of high-reflective coating $\phi_{\mathrm{HR}}$, which can be obtained by a linear combination of the measured loss of its constituent layers [135],

$$\phi_{\mathrm{HR}} = \frac{\sum_i t_i Y_i \phi_i}{\sum_i t_i Y_i}\ , \tag{4.17}$$

where $t_i$, $Y_i$ and $\phi_i$ are the thickness, the Young's modulus and the loss of the $i$-th layer ($i = H$ for the high-index $Ti{:}Ta_2O_5$ layers and $i = L$ for the low-index $SiO_2$ layers, for instance), respectively.

The reference loss values of the Advanced LIGO and Advanced Virgo input (ITM) and end (ETM) mirror high-reflective coatings had been previously estimated [94] by assuming $Y_c = 140$ GPa for titania-doped tantala layers [136]. These values may now be updated by using the values of Young's modulus and Poisson's ratio, $Y_c = 120$ GPa: the new estimations, listed in table 4.11, are about 10% higher than the previous ones [94] for both ITM and ETM coatings.

Figure 4.40 shows the comparison between the expected loss of equation (4.17), calculated using the values of loss and Young's modulus from this thesis, and the direct loss measurements of the HR coatings. As shown by the points, the measured loss is fairly constant over the sampled band ($2.7 - 22.4$ kHz), whereas the expectations have

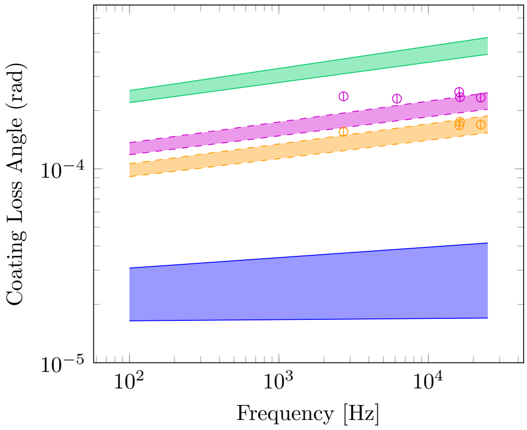

**Figure 4.40:** Mechanical loss of Advanced LIGO and Advanced Virgo input (ITM, orange) and end (ETM, purple) mirror HR coatings: comparison between the expected values (shaded regions) calculated via equation (4.17) and measured values (markers) from table 4.11. The frequency-dependent loss term $\phi_c(f) = af^b$ of $SiO_2$ (blue) and Ti:$Ta_2O_5$ (green) layers, from table table 4.5 and 4.8, is also shown for comparison.

the same frequency dependence of their dominant contribution, i.e. the titania-doped tantala layers.

When extrapolating down to 100 Hz, i.e. the frequency where Advanced LIGO and Advanced Virgo are limited by coating thermal noise, the expectations underestimate the actual measured loss of the HR coatings, of about 30% for the ITM coating and about 43% for the ETM coating.

### 4.5.5 Summary

The $Ta_2O_5$ has been studied as high-refractive-index material in Bragg reflectors. Different deposition conditions yield different coating mechanical properties. In particular, the lowest deposition ratio provides the coating with lowest loss angle. These differences disappear after the annealing at 500°C, which erases the deposition history. Indeed, the rapid decrease of coating loss angle, with the annealing at 500°C, has little structural counterpart. After 10 h, the increasing of annealing time does not affect the loss and the structure, which keeps the same configuration. On the other hand, the increase of the annealing temperature beyond 600°C causes the crystallization. The Young's modulus and Poisson's ratio is comparable for the different deposition conditions.

In order to decrease the internal friction, mixing $Ta_2O_5$ with $TiO_2$ has been investigated at several Ti% concentration. It has been confirmed that Ti/Ta= 0.27 yielded minimum loss. The mixed coating presents comparable elastic moduli but lower coating loss angle, after the annealing. The coating loss angle of Ti:$Ta_2O_5$ after the annealing at 100 Hz is almost reduced by 25% with respect to $Ta_2O_5$ coating loss (figure 4.41).

Looking at the optical properties, it has been observed that the annealing does not affect the energy gap whereas it decreases the refractive index, especially in the NIR region. However, the refractive index at 1064 nm of the Ti-doped coating after the annealing is higher almost about 2% than the one of pure tantala. The Ti-doping causes a red-shift of the energy gap which results to be in agreement with the doping atomic ratio concentration of 0.27. The effect of the annealing and the doping on the weak absorption related to the Urbach tails is remarkable. In particular, similarly to the coating loss angle, the annealing and the doping reduce the Urbach energy, hence

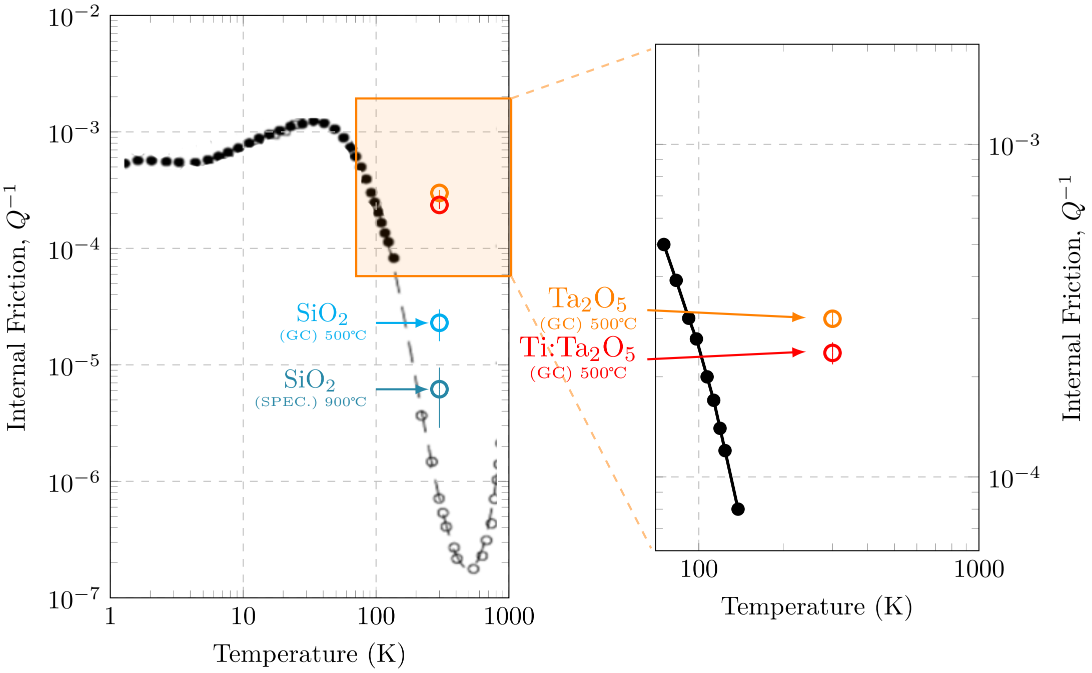

**Figure 4.41:** Comparison of $Ta_2O_5$ and Ti:$Ta_2O_5$ coating loss angle at 100 Hz after the annealing at 500℃, measured at room temperature. In the plot, also the fused-silica internal friction [112], acquired at 1.5 MHz, is showed. The zoom allows to better compare the higher dissipative materials.

leading to a correlation between the Urbach energy and the coating internal friction.

## 4.6 $Nb_2O_5$ and $Nb:TiO_2$ Coatings

Niobia ($Nb_2O_5$) has been one the first coating tested during my thesis with the purpose of replacing the high-refractive index material in the Bragg mirror. The refractive index of $Nb_2O_5$ is higher than the refractive index of $Ti:Ta_2O_5$ and this could lead to a thinner high-reflective stack, hence to a lower coating thermal noise.

The analysed coatings are oxides deposited by IBS with DIBS; the deposition is directly scalable to the Grand Coater, in order to deposit on large substrates.

Mixing with $TiO_2$ has been tested in order to obtain a coating with high refractive index. It has been observed that a modest amount of Ti-doping does not increase the refractive index but it makes possible to anneal the sample at 600℃ without crystallization. The crystallization temperature of the $Ti:NbO_2$ is therefore higher than the crystallization temperature of pure $TiO_2$, which is between 250℃ and 300℃, and of pure $Nb_2O_5$, which is about 400℃.

Then, $TiO_2$ has been doped with $Nb_2O_5$ in order to obtain a coating with a refractive index similar to pure $TiO_2$, increasing its crystallization temperature. The best result has been obtained by the $Nb:TiO_2$ with atomic ratio of Nb to Ti equal to 0.37, as measured through energy-dispersive X-ray spectroscopy (EDX), which has been tested up to 400℃.

In the following, the measurements of pure $Nb_2O_5$ and of $Nb:TiO_2$, before and after an air post-deposition annealing at 400℃ for 10 hours, are presented.

### 4.6.1 Mechanical Properties

In figure 4.42, the coating loss angle of two samples having $Nb_2O_5$ coating deposited with the DIBS (before and after the annealing) is shown. It can be observed that it is not possible to discriminate between family modes, so that the analysis has been carried out considering only the frequency trend $af^b$ (see section 2.4.2). During the analysis both samples have been considered whereas, for sake of clarity, in the following plots only one sample is shown.

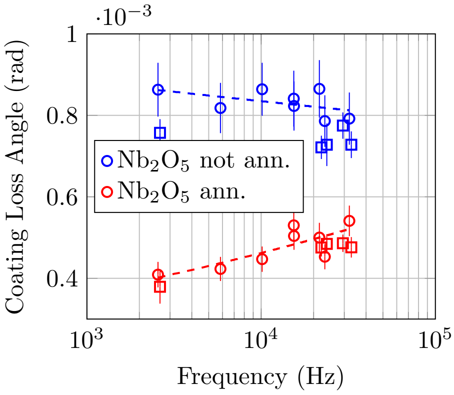

**Figure 4.42:** Coating loss angle of $Nb_2O_5$ deposited with DIBS. Comparison for the coating before (blue) and after (red) the annealing at 400℃.

The annealing has been done in air at 400℃ for 10 hours, which is a temperature lower than the standard annealing because of the crystallization starting just above 400℃. The heating treatment reduces the mechanical loss. It can be observed that the after the annealing, the coating loss angle changes trend with respect to the frequency. The exponent $b$, related to the distribution of the barrier height in TLS, goes from negative to positive value, ascribed to an exponential distribution of the barrier height.

In figure 4.43 it is shown the fit of the measured dilution factor $D$ with the simulation, to obtain the elastic constant. The results have been summarised in table 4.12.

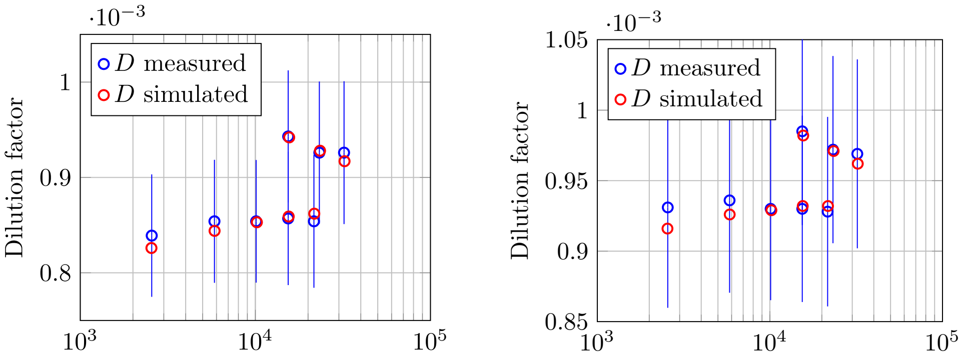

**(a)** Not annealed.

**(b)** Annealed.

**Figure 4.43:** Fit of measured dilution factors (blue) with simulated values (red) for Nb$_2$O$_5$ coating before (a) and after (b) the annealed in air at 400°C during 10 hours. From these data, the elastic constant of table 4.12 have been worked out.

Comparing the elastic moduli obtained following the procedure in section 3.2.3, it can be observed that the annealing does not affect the Young's modulus, whereas it reduces the Poisson ratio. Even if the model for the fitting of the elastic constants seems to work well, we observe that the change of $\nu$ is anomalous with respect to most of the samples analysed in this thesis work.

| Nb$_2$O$_5$ | $Y$ (GPa) | $\nu$ | $a$ ($10^{-4}$ rad Hz$^{-b}$) | $b$ |
|---|---|---|---|---|
| DIBS | 100 ± 7 | 0.295 ± 0.015 | 9.8 ± 1.9 | -0.02 ± 0.02 |
| DIBS ann. | 99 ± 1 | 0.24 ± 0.01 | 2.0 ± 0.4 | 0.09 ± 0.02 |

**Table 4.12:** Young's modulus $Y$, Poisson ratio $\nu$, and $a$, $b$ parameters of the model $af^b$ for Nb$_2$O$_5$ deposited with DIBS, before and after the annealing at 400°C.

### Doping

Nb:TiO$_2$ with atomic ratio of Nb to Ti equal to 0.37 (as measured through EDX) has been tested at 400°C.

In figure 4.44 the coating loss angle is shown with the fit. It can be observed that the data present a families separation. In particular, the second family (1,m) is more dissipative than the first (0,m) (unlike the edge effect, where the second family (1,m) is less dissipative), suggesting a considerable bulk contribution. The bulk deformation, related to pure dilatation, can be described by the model expressed by equation 4.16.

In figure 4.44 it is clearly evident that the annealing reduces the coating loss angle by reducing the shear contribution. The reduction of the shear term allows the dilatation to be the main contribution at higher frequencies. The results are summarised in table 4.13, including the Young's modulus and the Poisson ratio. The elastic constants are not significantly affected by the annealing, whereas, comparing the values of table 4.12 and 4.13, it is evident that the mixed coating Nb:TiO$_2$ has higher Young's modulus

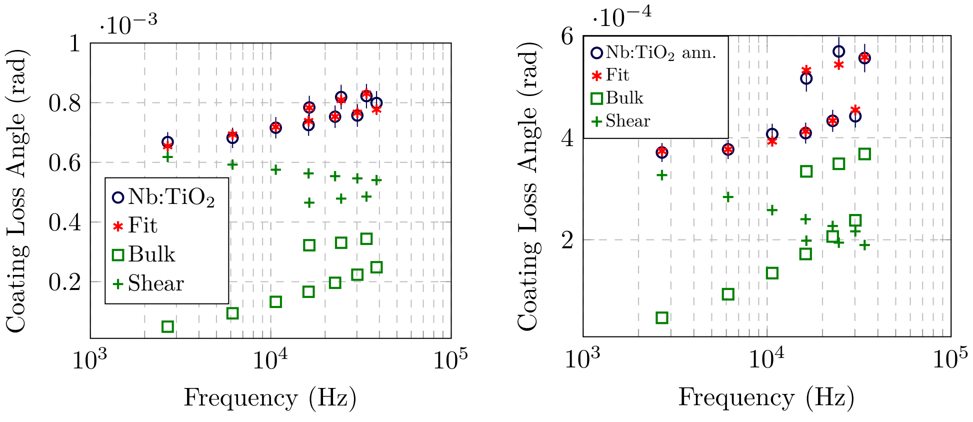

**(a)** Not annealed.

**(b)** Annealed.

**Figure 4.44:** Coating loss angle of Nb:TiO$_2$ deposited with DIBS (blue), compared with the fit (red), for the sample before and after the annealing at 400°C. The green points represent the contributions of the fit model $A_1 f^{B_1} D_{dil} + A_2 f^{B_2} D_{shear}$, where the crosses represent the shear part $A_2 f^{B_2} D_{shear}$, where $D_{shear} = 1 - D_{dil}$, and the squares represent the bulk part $A_1 f^{B_1} D_{dil}$.

| Nb:TiO$_2$ | $Y$ (GPa) | $\nu$ | $A_1$ ($10^{-4}$) | $B_1$ | $A_2$ ($10^{-4}$) | $B_2$ |
|---|---|---|---|---|---|---|
| DIBS | 120 ± 1 | 0.30 ± 0.01 | 1.2 ± 0.6 | 0.23 ± 0.05 | 6.5 ± 0.7 | - |
| DIBS ann. | 116 ± 1 | 0.29 ± 0.01 | 0.8 ± 0.7 | 0.27 ± 0.08 | 9 ± 3 | -(0.12 ± 0.04) |

**Table 4.13:** Young's modulus $Y$, Poisson ratio $\nu$, and $A_{1,2}$ expressed in rad Hz$^{-b}$, $B_{1,2}$ parameters of the model $A_1 f^{B_1} D_{dil} + A_2 f^{B_2} D_{shear}$ for Nb:TiO$_2$ deposited with DIBS, before and after the annealing at 400°C.

and Poisson ratio than the pure Nb$_2$O$_5$. To better evaluate the effect of the doping and compare it with the annealing, in figure 4.45 the coating loss angle of Nb$_2$O$_5$ and Nb:TiO$_2$ are compared. It can be observed that the annealing is the main factor which

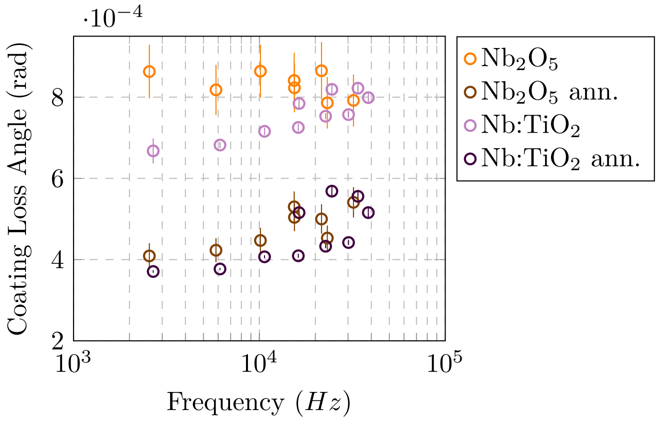

**Figure 4.45:** Coating loss angle of Nb$_2$O$_5$ and Nb:TiO$_2$, before and after the annealing in air for 10 hours at 400°C.

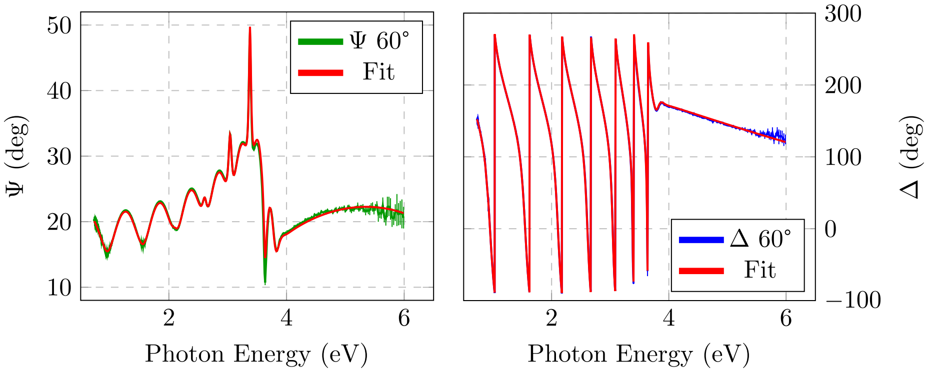

**(a)** Nb$_2$O$_5$, $\Psi$.

**(b)** Nb$_2$O$_5$, $\Delta$.

**Figure 4.46:** $\Psi$ (green), $\Delta$ (blue) data of Nb$_2$O$_5$ annealed coating, measured with VASE ellipsometer. The data are compared with the best fit (red) obtained by CL model.

reduces the coating loss angle.

### 4.6.2 Optical Properties

At least four samples have been analysed, but since they provided comparable results, we will show the analysis of one representative sample only. The measurements have been acquired with both VASE and M-2000 ellipsometers at 55°, 60° and 65°. Since the two ellipsometers and the analysis done for the three angles of incidence gave comparable results, for sake of clarity, the measurements refer only to VASE ellipsometer at 60° whereas the final results have been obtained considering all the acquired data.

In figure 4.46 the data obtained by VASE ellipsometer of Nb$_2$O$_5$ deposited with the DIBS and annealed at 400℃ are shown. The $(\Psi, \Delta)$ data show a degradation in the UV region caused by the strong absorption which reduces the signal to noise ratio and data are no longer useful for fitting purposes. For this reason, the data are shown below 6 eV.

The interference features, related to multiple reflections in the transparent region of the coating, stop quite sharply around 3.4 eV; this behaviour marks the fundamental absorption threshold. Furthermore, the amplitude of the oscillations in the Vis region starts to slowly reduce approaching the absorption threshold. This is well remarkable in figure 4.46b and could be related to the presence of Urbach tails. From the comparison of the measurements before and after the annealing, shown in figure 4.47, it can be noticed that the main difference related to the heating treatment is around the absorption threshold. As observed for the standard coatings, the annealing seems not to affect the energy gap. However, it is evident that, after the annealing, the absorption related to the Urbach tails is reduced.

Following previous analysis, the data have been analysed through a three-layers model including the substrate, the thin film and a surface roughness layer. The latter was modelled through a Bruggeman effective medium approximation (EMA) layer. Although the thin film can be represented by Cody-Lorentz (CL) the Tauc-Lorentz (TC), the best fit has been provided by the CL model which accounts for the Urbach tails. The comparison between the fit curves and the data is shown in figure 4.46. The fit curves reproduced the $(\Psi, \Delta)$ data at the three angles of incidence 55°, 60° and 65° with the same accuracy. In particular, the analysis showed that the annealing increases the coating thickness of about almost 3%, from $(470 \pm 2)$ nm to $(483 \pm 2)$

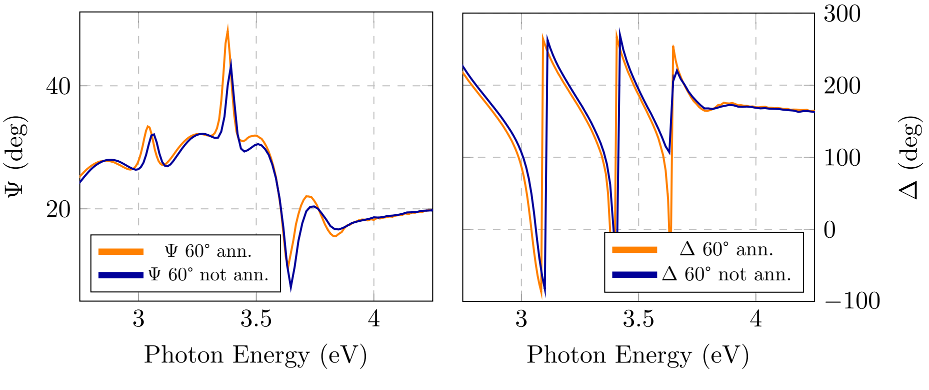

**(a)** $Nb_2O_5$, Ψ. **(b)** $Nb_2O_5$, Δ.

**Figure 4.47:** $(\Psi, \Delta)$ data at 60° for $Nb_2O_5$ coating before (blue) and after (orange) the annealing.

nm. The coating thickness has been then used to estimate the density of the material, which does not change considerably with the annealing. The thickness and the density of the sample are listed in table 4.14. Furthermore, the annealing reduces the refractive index in the transparent region, as shown in figure 4.48. The values of the refractive index at wavelengths of interest 1064 nm and 1550 nm are listed in table 4.14.

| $Nb_2O_5$ | $n$@1064 nm | $n$@1550 nm | $\rho$ (g/cm$^3$) | $E_U$ (eV) | $E_g$ (meV) |
|---|---|---|---|---|---|
| DIBS | $2.24 \pm 0.01$ | $2.22 \pm 0.01$ | $3.6 \pm 0.8$ | $110 \pm 10$ | $3.4 \pm 0.1$ |
| DIBS ann. | $2.22 \pm 0.01$ | $2.20 \pm 0.01$ | $3.5 \pm 0.8$ | $80 \pm 10$ | $3.4 \pm 0.1$ |

**Table 4.14:** Refractive index $n$ at wavelength of interest ($\lambda = 1064$ nm for LIGO and Virgo detectors, $\lambda = 1550$ nm of future detectors such as the Einstein Telescope), density $\rho$, energy gap $E_g$ and Urbach energy $E_U$ of $Nb_2O_5$ before and after the annealing at 400°C.

In figure 4.49a the Cody Plot obtained by the CL model is shown in order to evaluate the absorption edge. The energy gap $E_g$ is not affected by the annealing, whereas it is evident in the figure that a clearly change in the absorption trend occurs below the energy gap, related to the reduction of the Urbach tails. The values of the energy gap and the Urbach energies are listed in table 4.14.

In figure 4.50 the data of the standard Nb:$TiO_2$ coating, deposited by the DIBS and annealed at 400°C, are compared with the fit curves obtained using the CL model. Also in this case, the $(\Psi, \Delta)$ data show a degradation related to the strong absorption in the UV region. The annealing reduces the refractive index (figure 4.48) in the NIR region where at 1064 the reduction is almost about 1%. The coating thickness is increased instead of about 2% from $482 \pm 2$ to $490 \pm 2$ nm. The coating thickness has been used to determine the density. The values of the refractive index at wavelengths of interest 1064 nm and 1550 nm and the density are listed in table 4.15. It can be observed that the Nb:$TiO_2$ has a higher density than $Nb_2O_5$.

The Cody plot shown in figure 4.49b highlights the effect of the heating treatment on the Nb:$TiO_2$ absorption edge. It is evident that the energy gap is not affected by the annealing whereas there is a clearly reduction of the Urbach tails. Since the $TiO_2$ has almost the same energy gap than $Nb_2O_5$ ($TiO_2$ has been found to have an energy gap about $3.3 - 3.5$ eV [122, 123]), the mixing does not determine a change in energy gap,

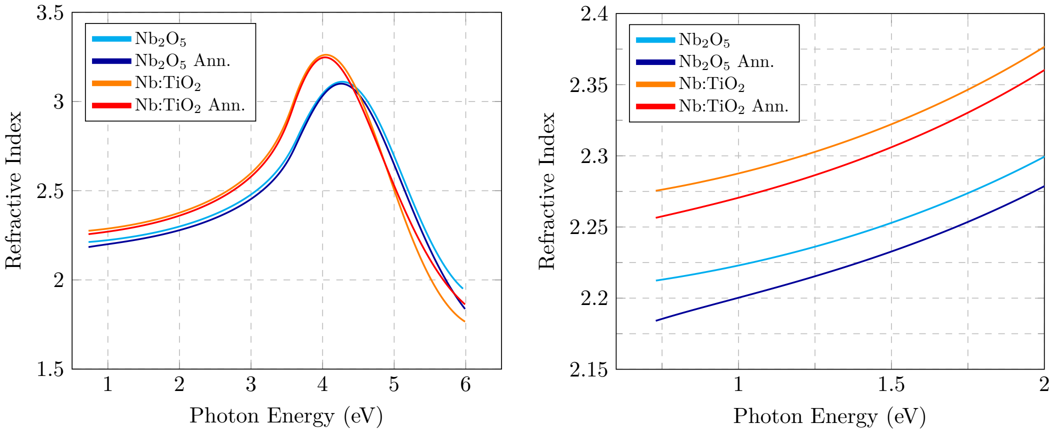

**(a)** Refractive index. **(b)** Zoom in the NIR-Vis region.

**Figure 4.48:** (a) Refractive index of Nb$_2$O$_5$ coating before (light blue) and after (blue) the annealing, compared to the that of Nb:TiO$_2$ coating before (orange) and after (red) the annealing. (b) The zoom in the NIR-Vis region.

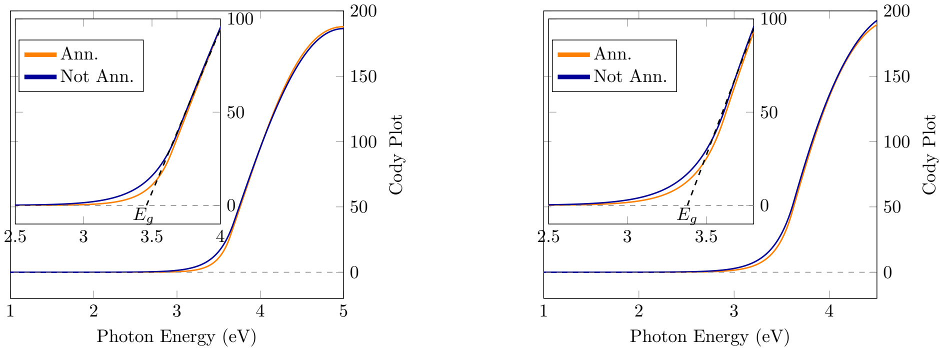

**(a)** Nb$_2$O$_5$. **(b)** Nb:TiO$_2$.

**Figure 4.49:** Cody plot for (a) Nb$_2$O$_5$ and (b) Nb:TiO$_2$ before (blue) and after (orange) the annealing, obtained by CL model. The dashed lines represent the linear trend of $(\alpha(E)n(E)/E)^{1/2}$ to better highlight the energy gap value and the beginning of the Urbach tails.

| Nb:TiO$_2$ | $n$@1064 nm | $n$@1550 nm | $\rho$ (g/cm$^3$) | $E_U$ (eV) | $E_g$ (meV) |
|---|---|---|---|---|---|
| DIBS | 2.30 ± 0.01 | 2.28 ± 0.01 | 4.26 ± 0.11 | 108 ± 5 | 3.3 ± 0.1 |
| DIBS ann. | 2.28 ± 0.01 | 2.26 ± 0.01 | 4.08 ± 0.11 | 80 ± 5 | 3.3 ± 0.1 |

**Table 4.15:** Refractive index $n$ at wavelength of interest ($\lambda = 1064$ nm for LIGO and Virgo detectors, $\lambda = 1550$ nm of future detectors such as the Einstein Telescope), density $\rho$, energy gap $E_g$ and Urbach energy $E_U$ of Nb:TiO$_2$ before and after the annealing at 400°C.

as can be observed comparing figures 4.49a and 4.49b. The values of the energy gap and the Urbach energy are listed in table 4.15. Analysing the Urbach energy obtained by the CL model from Nb$_2$O$_5$ and Nb:TiO$_2$ (table 4.14 and 4.15), it can be noticed

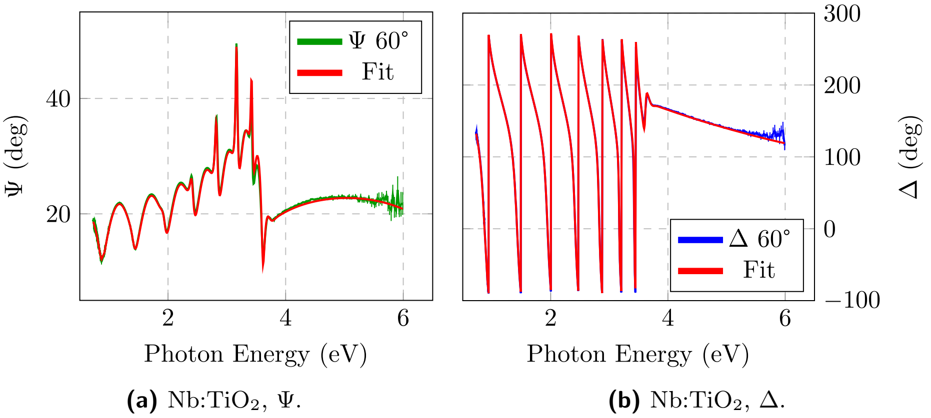

**(a)** Nb:TiO$_2$, Ψ. **(b)** Nb:TiO$_2$, Δ.

**Figure 4.50:** Ψ (green), Δ (blue) data of Nb:TiO$_2$ annealed coating, measured with VASE ellipsometer. The data are compared with the best fit (red) obtained by CL model.

that the annealing reduce the Urbach energy, whereas the doping does not change it.

Finally, by comparing refractive index in figure 4.48, it can be observed that the mixing increases the refractive index, in the NIR region, including 1064 nm.

### 4.6.3 Correlation Between Urbach Energy and Internal Friction

Similar to Ta$_2$O$_5$ and Ti:Ta$_2$O$_5$ coatings, the effect of the annealing on the coating loss angle and the Urbach energy suggests a correlation between these two quantities [129]. In figure 4.51 the absorption coefficient is shown as the function of the photon energy. In the logarithmic scale representation chosen for $\alpha$, Urbach tails have a linear appearance and the inverse of the slope is proportional to $E_U$. The different slopes for each sample is evident.

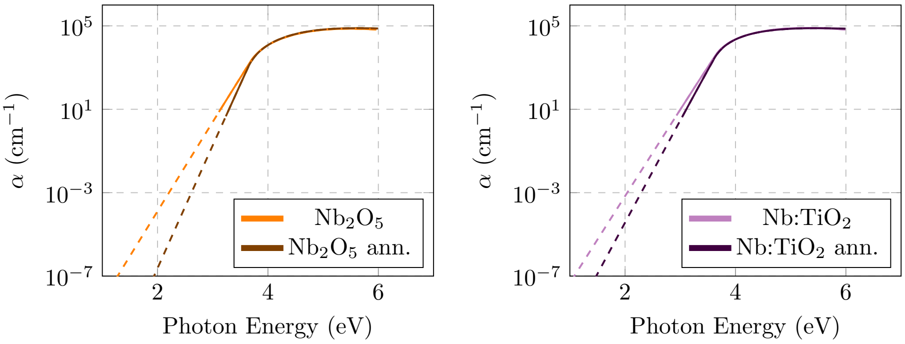

**(a)** Nb$_2$O$_5$. **(b)** Nb:TiO$_2$.

**Figure 4.51:** Absorption coefficient of Nb$_2$O$_5$ and Nb:TiO$_2$ before and after the annealing, obtained with the CL model. The logarithmic scale allows to distinguish better the different slopes in the region where the absorption decays exponentially with the energy $E_U$. The solid lines represent the absorption appreciated by SE analysis. The dashed lines represent an extension of the CL model to better distinguish the different slopes.

The coating loss angle (shown in figure 4.45) and the optical absorption coefficient

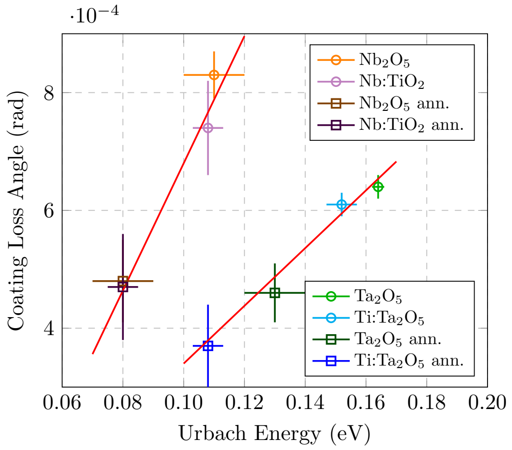

**(a)** Correlation.

| Coating | $\phi_c$ $\cdot 10^{-4}$ | $E_U$ (meV) |
|---|---|---|
| $Ta_2O_5$ | $6.4 \pm 0.2$ | $164 \pm 8$ |
| $Ti:Ta_2O_5$ | $6.1 \pm 0.2$ | $152 \pm 5$ |
| $Ta_2O_5$ ann. | $4.6 \pm 0.5$ | $130 \pm 10$ |
| $Ti:Ta_2O_5$ ann. | $3.7 \pm 0.7$ | $108 \pm 5$ |
| $Nb_2O_5$ | $8.3 \pm 0.4$ | $110 \pm 10$ |
| $Nb:TiO_2$ | $7.4 \pm 0.8$ | $108 \pm 5$ |
| $Nb_2O_5$ ann. | $4.8 \pm 0.7$ | $80 \pm 10$ |
| $Nb:TiO_2$ ann. | $4.7 \pm 0.9$ | $80 \pm 5$ |

**(b)** Data.

**Figure 4.52:** (a) Coating loss angle as function of Urbach energy. Circles refer to as deposited samples, squares to the samples after the annealing. Different coatings are considered, $Ta_2O_5$, $Ti:Ta_2O_5$, $Nb_2O_5$, $Nb:TiO_2$. The values of the data are listed in the table (b). The reported loss angle is the average value of the data shown in figure 4.32b and 4.45. The uncertainty is the maximum distance from the mean value.

exhibit a similar trend regarding the annealing and the mixing. Under this considerations, the correlation shown in figure 4.39 can be compared to figure 4.52. The correlation holds for several oxides ($Ta_2O_5$, $Ti:Ta_2O_5$, $Nb_2O_5$ and $Nb:TiO_2$), suggesting a general validity for this behaviour [129].

### 4.6.4 High-Reflective Stack

In order to measure the coating thermal noise of stacks made of $Nb_2O_5$ and $Nb:TiO_2$ layers, three stacks are currently under investigation.

In particular, one $\lambda/4$ Bragg mirror stack $Nb_2O_5/SiO_2$ with thickness ratio 0.62 and two stacks $Ti:Nb_2O_5/SiO_2$ have been deposited on fused silica witness sample (⌀ 1”, 5 mm thick). In the case of the stacks with the doped layers, one is a $\lambda/4$ mirror with thickness ratio 0.60, whereas the other one is an optimized stack [137] with thickness ratio 0.38.

The samples have been sent to the Massachusetts Institute of Technology (MIT) for measuring directly the coating thermal noise, using a folded free-space Fabry-Perot cavity [138,139] and three resonant transverse electromagnetic modes (TEM): the fundamental mode TEM00, commonly used in GW detectors, and the second order transverse mode TEM02 and TEM20. The folded cavity allows to measure samples with high reflectivity because the read-out is not located directly in transmission of the sample under investigation, while the multiple co-resonating TEMs share the same sensitivity to the laser frequency and cavity lens, so that it is possible to use the TEM00 to suppress the common noises, such as laser frequency noise, cavity length noise and substrate thermal noise. Furthermore, TEM02 and TEM20 sample different areas of the coating and hence the thermal noise seen by each of the resonant modes is largely independent.

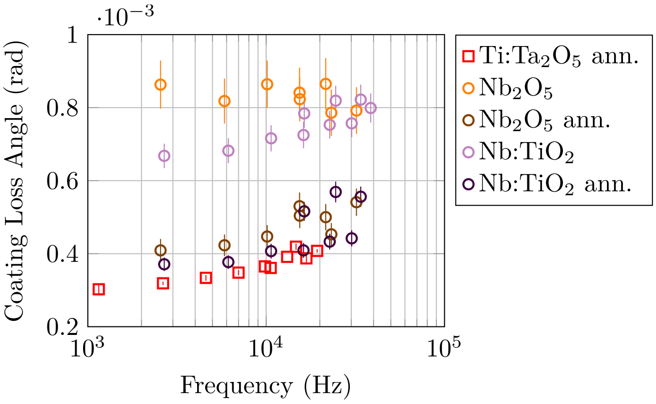

**Figure 4.53:** Coating loss angle of $Nb_2O_5$ and Nb:$TiO_2$ before and after the annealing, compared with the standard coating Ti:$Ta_2O_5$ annealed at 500°C.

### 4.6.5 Summary

A higher refractive index coating (increasing the crystallisation temperature) has been achieved from $TiO_2$ by Nb-doping. The resulting Nb:$TiO_2$ has been tested at 400°C. The Nb:$TiO_2$ presents a refractive index at 1064 nm of $2.22 \pm 0.01$, which is about 6% higher than the one of Ti:$Ta_2O_5$ ($2.09 \pm 0.01$). The elastic constants of Nb:$TiO_2$ are comparable with those of Ti:$Ta_2O_5$ ($Y \sim 120$ GPa and $\nu \sim 0.3$). However, it can be observed from figure 4.53 that the lowest coating loss angle obtained is still slightly higher than the one of Ti:$Ta_2O_5$ coating annealed at 500°C. In figure 4.54 the coating loss angle at 100 Hz is compared with the one of standard coating after the annealing.

The higher refractive index can be used to develop the high-reflective coating reducing the number of layer without affect the reflectivity and thank to the optimization, to change the thickness ration of the high-refractive-index material respect to the lower-index. In both cases, the thickness of the dissipative layer will be lower, leading hence to a lower coating thermal noise.

In order to evaluate if the higher refractive index allows to obtain a high-reflective coating with lower coating thermal noise, $\lambda/4$ and optimized stacks made with $SiO_2$ and $Nb_2O_5$ or Nb:$TiO_2$ have been sent to the MIT to perform direct measurements of coating thermal noise.

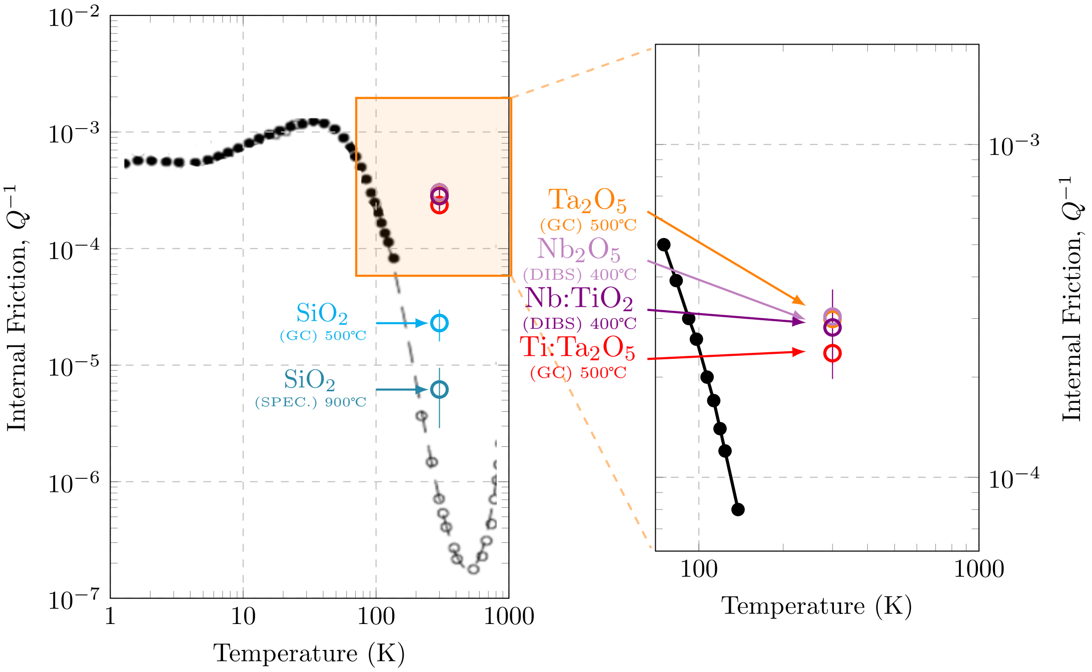

**Figure 4.54:** Nb:TiO$_2$ and Nb$_2$O$_5$ coating loss angle at 100 Hz after annealing, measured at room temperature, compared with other coatings. In the plot, also the fused-silica internal friction [112], acquired at 1.5 MHz, is showed. The zoom allows to better compare the dissipative materials.

## 4.7 Zr:Ta$_2$O$_5$ Coating

It is now clear that the heating treatment play an important role in the reduction of the internal stress of coating and hence in the reduction of internal friction. Under this respect, besides the increasing of the refractive index, it would be interesting to find an amorphous oxide to mix with Ta$_2$O$_5$ in order to increase the annealing temperature and possibly reduce the coating loss angle.

One of the main aspect of the studied mixtures is the higher crystallization temperature, likely achieved through the different atomic structure of the dopant. Accordingly to preliminary results obtained by the LIGO Scientific Collaboration, ZrO$_2$ is a valid option other than TiO$_2$. In fact, despite the refractive index of ZrO$_2$ is comparable to the one of Ta$_2$O$_5$ [140], we will see that the Zr:Ta$_2$O$_5$ (with 13-14% of Zr concentration with respect to Ta) has been annealed at 700℃ for 10 hours avoiding crystallization.

### 4.7.1 Mechanical Properties

In figure 4.55a the Zr:Ta$_2$O$_5$ coating loss angle deposited by the CG and after in-air annealing at 500℃, 600℃ and 700℃ for 10 hours is shown; it can be observed from the figure that the annealing reduces the coating loss angle. In table 4.16 the fit results are summarised. It is interesting to observe from table 4.16 that at each annealing, the $b$ parameter of Zr:Ta$_2$O$_5$ increases with the annealing temperature. Thus, it can be interesting to extrapolate the values of the loss angle at 100 Hz. By doing this, at 100 Hz we obtain a loss angle of about $\phi_{\mathrm{Zr:Ta_2O_5}} = 1.8 \cdot 10^{-4}$ for Zr:Ta$_2$O$_5$, compared to $\phi_{\mathrm{Ti:Ta_2O_5}} = 2.4 \cdot 10^{-4}$ for Ti:Ta$_2$O$_5$ with a reduction of a factor $\sim 1.3$ (the difference in frequency trend can be observed in figure 4.55b). Furthermore, the higher annealing

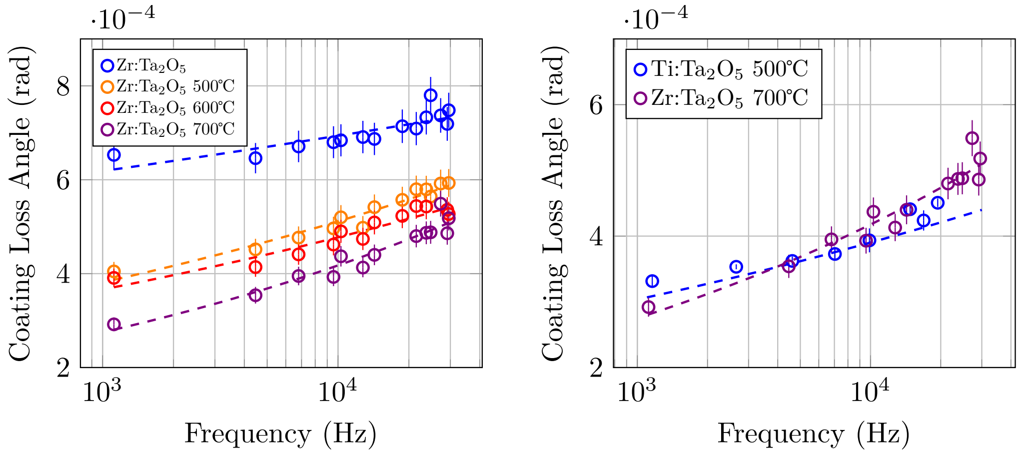

**(a)** Annealing.

**(b)** Comparison.

**Figure 4.55:** Coating loss angle of Zr:$Ta_2O_5$. (a) the results for different in-air post-deposition annealing up to 700℃ for 10 hours. (b) the comparison with the coating loss angle of standard Ti:$Ta_2O_5$ annealed at 500℃ for 10 hours.

| Zr:$Ta_2O_5$ | $Y$ (GPa) | $\nu$ | $a$ ($10^{-4}$ rad Hz$^{-b}$) | $b$ |
|---|---|---|---|---|
| GC | 120 ± 3 | 0.32 ± 0.01 | 4.4 ± 0.4 | 0.05 ± 0.01 |
| GC 500℃ | – | – | 1.58 ± 0.15 | 0.13 ± 0.01 |
| GC 600℃ | – | – | 1.7 ± 0.2 | 0.115 ± 0.012 |
| GC 700℃ | – | – | 0.79 ± 0.11 | 0.181 ± 0.015 |

**Table 4.16:** Young's modulus $Y$, Poisson ratio $\nu$, and $a$, $b$ parameters of the model $af^b$ for Zr:$Ta_2O_5$ deposited with GC and after the annealing at 500℃, 600℃ and 700℃ for 10 hours.

temperature would be beneficial also for the $SiO_2$ coating in a high-reflecting stack of $SiO_2$ and Zr:$Ta_2O_5$, leading to a stack with lower coating loss angle and hence to a lower coating thermal noise.

### 4.7.2 Optical Properties

The coating has been analysed by spectroscopic ellipsometry before the heating treatment and a spectrophotometric measurement has been made after the annealing at 500℃. For sake of clarity, in figure 4.56 the $(\Psi, \Delta)$ data are shown for the 60° angle of incidence. It can be observed that the quality data degrades in the UV region just after the energy gap around 4 eV. For this reason, parameters related to the properties in that region such as the Urbach energy have a large uncertainty. The fit curve refer to the Cody-Lorentz model and in figure 4.57a the refractive index and extinction coefficient are shown as function of energy, whereas in figure 4.57b the Cody plot highlights the energy gap.

In table 4.17 the final results are summarised, including the analysis done with spectrophotometry on reflectance measurements for the sample annealed at 500℃. As expected, the annealing reduces the refractive index in the NIR region. Furthermore, the energy gap is comparable to the one of $Ta_2O_5$ coating.

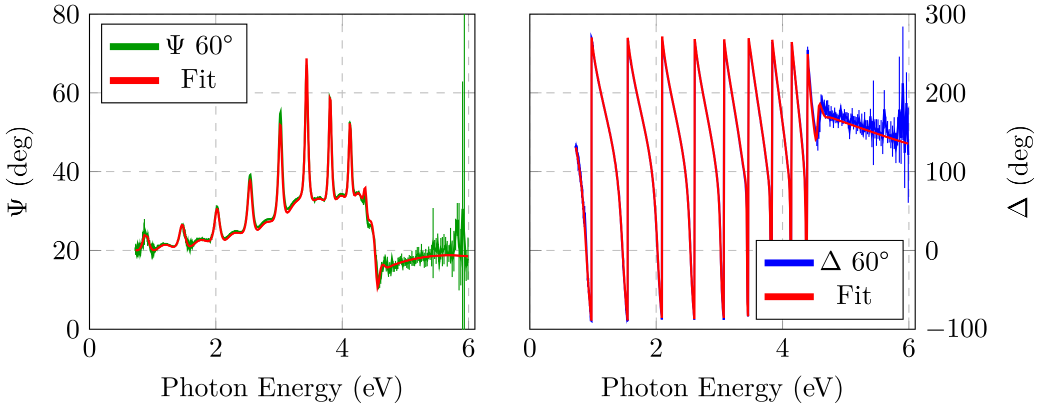

**(a)** Zr:Ta$_2$O$_5$, Ψ.   **(b)** Zr:Ta$_2$O$_5$, Δ.

**Figure 4.56:** Ψ (green), Δ (blue) data of as deposited Zr:Ta$_2$O$_5$ coating, measured with VASE ellipsometer. The data are compared with the best fit (red) obtained by CL model.

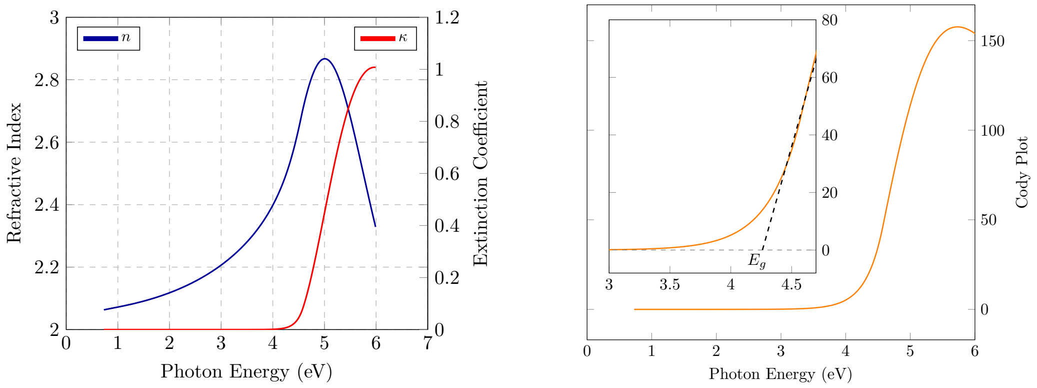

**(a)** Optical functions.   **(b)** Cody plot.

**Figure 4.57:** (a) Optical function $n$ and $\kappa$ for Zr:Ta$_2$O$_5$ coating obtained by the Cody-Lorentz model. (b) Cody plot; the dashed line highlights the linear trend of $(\alpha(E)n(E)/E)^{1/2}$ to better extrapolate the energy gap value.

| Zr:Ta$_2$O$_5$ | $n$@1064 nm | $n$@1550 nm | $\rho$ (g/cm$^3$) | $E_g$ (eV) | $E_U$ (meV) |
|---|---|---|---|---|---|
| GC (ellip.) | 2.09 ± 0.01 | 2.07 ± 0.01 | 6.9 ± 0.1 | 4.1 ± 0.1 | 130 ± 30 |
| GC 500°C (spectro.) | 2.03 ± 0.04 | – | - | - | - |

**Table 4.17:** Refractive index $n$ at wavelength of interest ($\lambda = 1064$ nm for LIGO and Virgo detectors, $\lambda = 1550$ nm of future detectors such as the Einstein Telescope), density $\rho$, energy gap $E_g$ and Urbach energy $E_U$ of Zr:Ta$_2$O$_5$ samples before and after the annealing at 500°C. Before the annealing the values has been carried out by spectroscopic ellipsometry characterization, after the annealing by spectrophotometry.

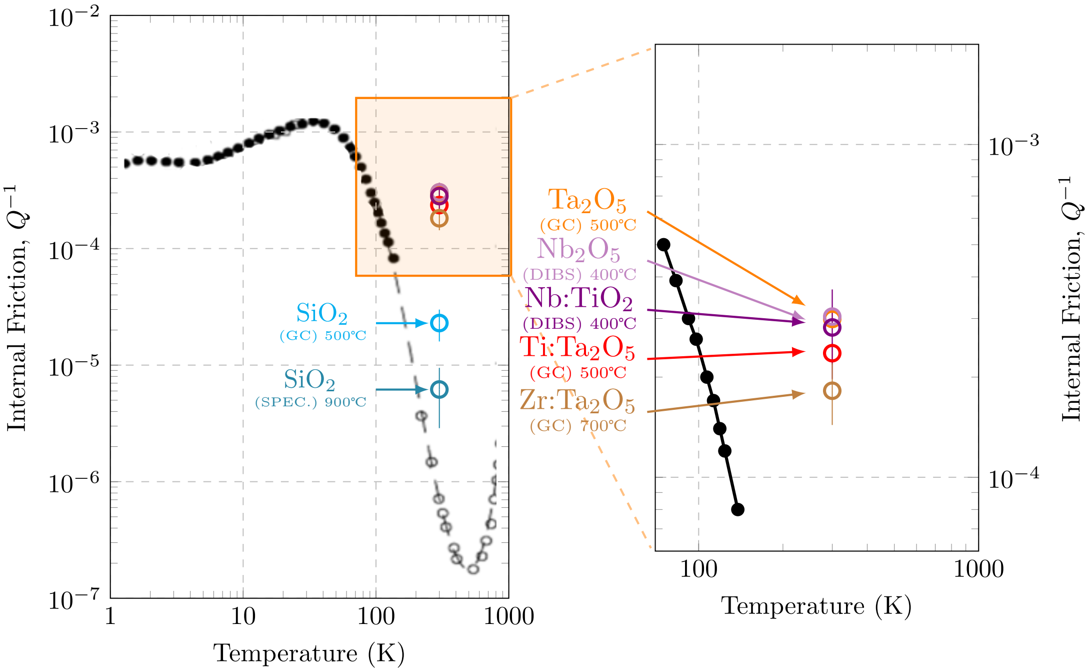

**Figure 4.58:** $Zr:Ta_2O_5$ coating loss angle at 100 Hz after the annealing at 600°C and 700°Ccompared with other coatings. 500°C, measured at room temperature. In the plot, also the fused-silica internal friction [112], acquired at 1.5 MHz, is showed. The zoom allows to better compare the higher dissipative materials.

### 4.7.3 Summary

The $Zr:Ta_2O_5$ mixture has been developed with the purpose of increasing the annealing temperature of Tantala coating, avoiding the crystallization. The main objective has been achieved, testing the sample up to 700°C. The resulting coating presents optical and mechanical properties similar to the tantala coating in term of refractive index, energy gap and coating loss angle between $10^3 - 10^4$ Hz. However, the higher annealing temperature allows to reach a lower coating loss angle, and the particular frequency trend set a reduction of a factor $\sim 1.3$ with respect to the standard $Ti:Ta_2O_5$ at 100 Hz, where the gravitational-wave detectors are limited by the coating thermal noise. In high-reflecting stack, the higher annealing temperature would beneficial also for silica coating, leading to a reduction of the total coating loss angle.

In figure 4.58, the coating loss angle at 100 Hz of $Zr:Ta_2O_5$ after the annealing at 700°C is compared with the previous analysed coatings.

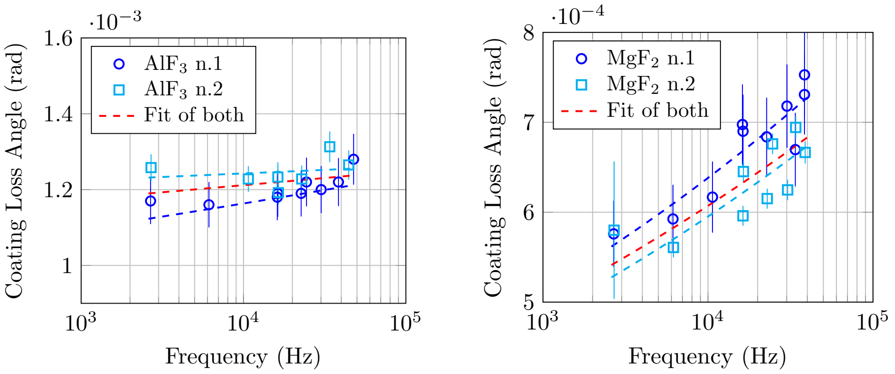

**(a)** AlF$_3$. **(b)** MgF$_2$.

**Figure 4.59:** Coating loss angle of IBS as deposited fluorides. (a) AlF$_3$, (b) MgF$_2$. The dashed lines represent the frequency trend $af^b$. The red line is the fit of both samples.

| IBS Coating | $a$ ($10^{-4}$ rad Hz$^{-b}$) | $b$ |
|---|---|---|
| AlF$_3$ sample 1 | 9 ± 2 | 0.03 ± 0.02 |
| AlF$_3$ sample 2 | 12 ± 2 | 0.006 ± 0.015 |
| AlF$_3$ total | 10.7 ± 1.5 | 0.014 ± 0.015 |
| MgF$_2$ sample 1 | 2.7 ± 0.4 | 0.095 ± 0.016 |
| MgF$_2$ sample 2 | 2.6 ± 0.7 | 0.09 ± 0.03 |
| MgF$_2$ total | 2.8 ± 0.5 | 0.09 ± 0.02 |

**Table 4.18:** Young's modulus $Y$, Poisson ratio $\nu$, and $a$, $b$ parameters of the model $af^b$ for MgF$_2$ and AlF$_3$ deposited by IBS.

## 4.8 MgF$_2$ and AlF$_3$ Coating

Fluorides like magnesium fluoride (MgF$_2$) and aluminium fluoride (AlF$_3$) present very low refractive index in the NIR region, including the operational wavelength of laser for gravitational-wave detectors. They could be a valid option for replacing SiO$_2$ in high-reflective coatings, in order to increase the refractive index contrast and reduce the total coating thickness, hence the coating thermal noise.

The fluorides coatings investigated are MgF$_2$ and AlF$_3$ deposited by ion beam sputtering at the Laser Zentrum Hannover (LZH). The main problem of such coatings is the possible oxidation during air exposition. For this reason, between each measurements the samples where stored in vacuum to prevent the oxidation.

### 4.8.1 Mechanical Properties

In figure 4.59 the coating loss angle of two samples of MgF$_2$ and AlF$_3$ is shown. The distribution of loss values in families has not been observed. On the other hand, it is clearly visible the frequency trend $af^b$. In table 4.18 the results obtained on samples analysed independently and considering their total measurements are listed.

Comparing the coating loss angle of the best as-deposited fluoride samples with the one of as-deposited SiO$_2$ CG (figure 4.60), it can be observed that both MgF$_2$ and AlF$_3$ have a higher coating loss angle.

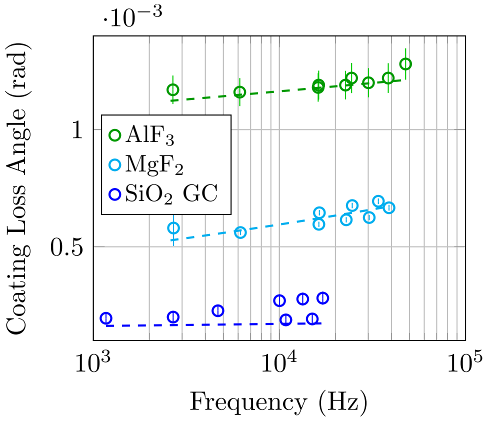

**Figure 4.60:** Coating loss angle of IBS as deposited fluorides compared with the as deposited $SiO_2$ CG. The dashed lines represent the frequency trend $af^b$.

### 4.8.2 Optical Properties

The $MgF_2$ and $AlF_3$ coating presented a little thickness non-uniformity, observed by measuring the samples at different positions. In figure 4.61 the comparison between the $\Psi$ measurements taken at two locations of the coating is shown. It can be observed that the distance between the maximum is different, confirming a different coating thickness in the two areas. A difference in thickness of about 4 nm for $MgF_2$ and 10 nm for $AlF_3$ have been found, due to the low thickness uniformity. The average value of the thickness was 208 nm and 211 nm for $MgF_2$ and $AlF_3$ respectively. Under this respect, these coatings have been analysed considering mainly the VASE ellipsometer, which has a smaller light spot.

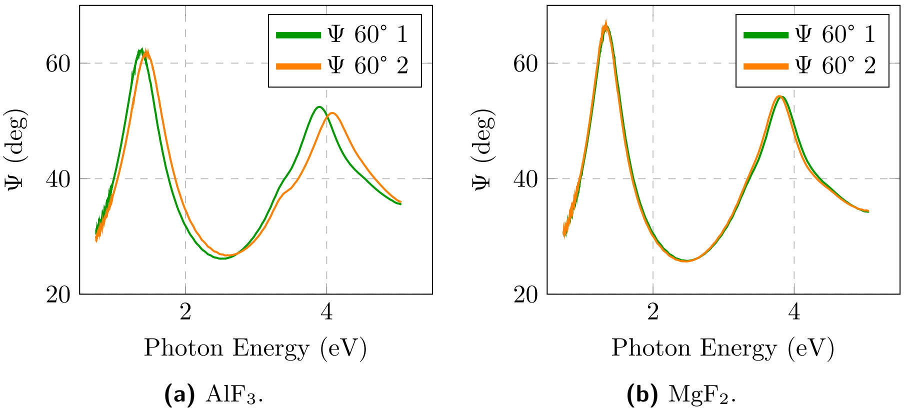

**(a)** $AlF_3$.

**(b)** $MgF_2$.

**Figure 4.61:** $\Psi$ data of (a) $AlF_3$ and (b) $MgF_2$ coating measured at 60° in two different areas of the coating.

In figure 4.62 the $(\Psi, \Delta)$ of $MgF_2$ and $AlF_3$ are shown. Fluorides should be ideally transparent in the energy region covered by our ellipsometers. For example, the band gap of crystalline $MgF_2$ is 10.8 eV [141] and one would expect a similar band gap for amorphous coating. For this reason, the 2-poles function has been used to represent the $(\Psi, \Delta)$ data. However, as it can be observed in figure 4.62, the model does not work for these coatings. In particular, the $\Psi$ data are well reproduced only in the NIR region, whereas the $\Delta$ data are substantially different from the simulated curves. In

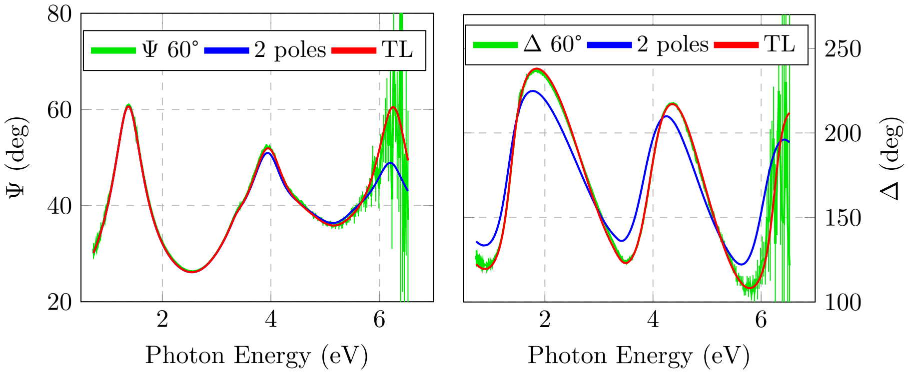

**(a)** AlF$_3$. **(b)** AlF$_3$.

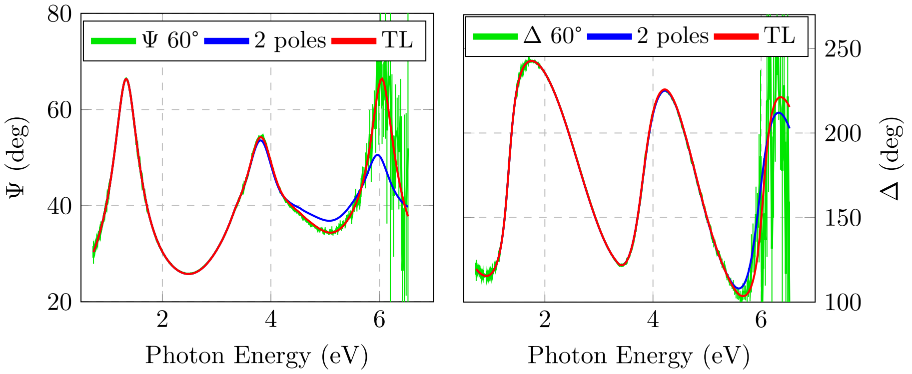

**(c)** MgF$_2$. **(d)** MgF$_2$.

**Figure 4.62:** $(\Psi, \Delta)$ data of (a), (b) AlF$_3$ and (c), (d) MgF$_2$ coating measured at 60° compared with model curves. The blue curves represent the 2 poles function, the red curves are the 2-poles with TL oscillator.

order to fit the data, absorption in the UV region must be taken into account. Under this respect, a TL oscillator has been added to the 2-poles function and, as it can be observed in figure 4.62, the model matches well the $(\Psi, \Delta)$ data for both MgF$_2$ and AlF$_3$ coating. The values of the refractive index and density are listed in table 4.19.

In figure 4.63 the dielectric functions of MgF$_2$ and AlF$_3$ coating obtained from 2-poles and TL models are compared. The $\varepsilon_1$ of the two models is similar in the NIR region whereas presents differences in the UV region. Furthermore, it has to be noted that for AlF$_3$ coating (figure 4.63a), a Gaussian oscillator has been added to the model to improve the MSE and hence the quality of the fit. Note that the absorption in the UV region is relatively weak. These absorptions could be related for example to colour centers, probably formed during the deposition of films which involves energetic

| Coating | $n$@1064 nm | $n$@1550 nm | $\rho$ (g/cm$^3$) |
|---|---|---|---|
| AlF$_3$ | 1.36 ± 0.01 | 1.36 ± 0.01 | 2.3 ± 0.6 |
| MgF$_2$ | 1.41 ± 0.01 | 1.40 ± 0.01 | 2.7 ± 0.2 |

**Table 4.19:** Refractive index $n$ at wavelength of interest ($\lambda = 1064$ nm for LIGO and Virgo detectors, $\lambda = 1550$ nm of future detectors such as the Einstein Telescope) and density $\rho$ of as deposited fluorides samples.

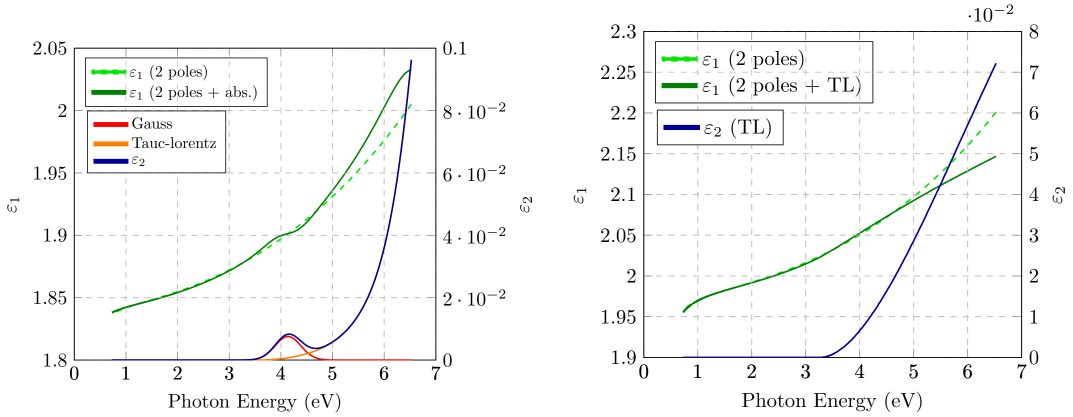

**(a)** $AlF_3$.

**(b)** $MgF_2$.

**Figure 4.63:** $(\varepsilon_1, \varepsilon_2)$ of (a) $AlF_3$ and (b) $MgF_2$ coating. The dashed curves represent the dielectric function obtained by the 2-poles model. For $AlF_3$ the $\varepsilon_2$ is a superposition of Gaussian and TL oscillators.

particles [142, 143].

Finally, it has to be noted that in both cases a thickness of about 6-8 nm for the Bruggeman EMA layer, which accounts for the roughness, has been found. This values has to be compared with the $\sim$ 200 nm of the coating thickness. Under this respect, 4% of roughness is considerable, especially in the UV region.

### 4.8.3 Summary

The fluorides coatings $MgF_2$ and $AlF_3$ deposited by ion beam sputtering have been analysed with the purpose of replace $SiO_2$ coating in high-reflective mirrors.

In order to reproduce the optical data, a weak absorption in the UV region had to be included in the model. This could be related to the presence of colour centers, likely formed during the IBS deposition.

The coating loss angle of both $MgF_2$ and $AlF_3$ is higher than all the previous coatings. This can be observed in figure 4.64, where the loss angles of $MgF_2$ and $AlF_3$ at 100 Hz is shown.

It has been shown that $SiO_2$ coatings have higher loss at cryogenic temperature [97, 144]. This is a limit if we want to use it in Bragg reflectors for cryogenic detectors. In this respect, it would be interesting to investigate fluorides at lower temperature, where the TLS distribution could be different than that of silica.

Work is ongoing to characterize the impact of annealing on their absorption and internal friction; soon we will also measure their low-temperature internal friction, for possible implementation in future interferometers.

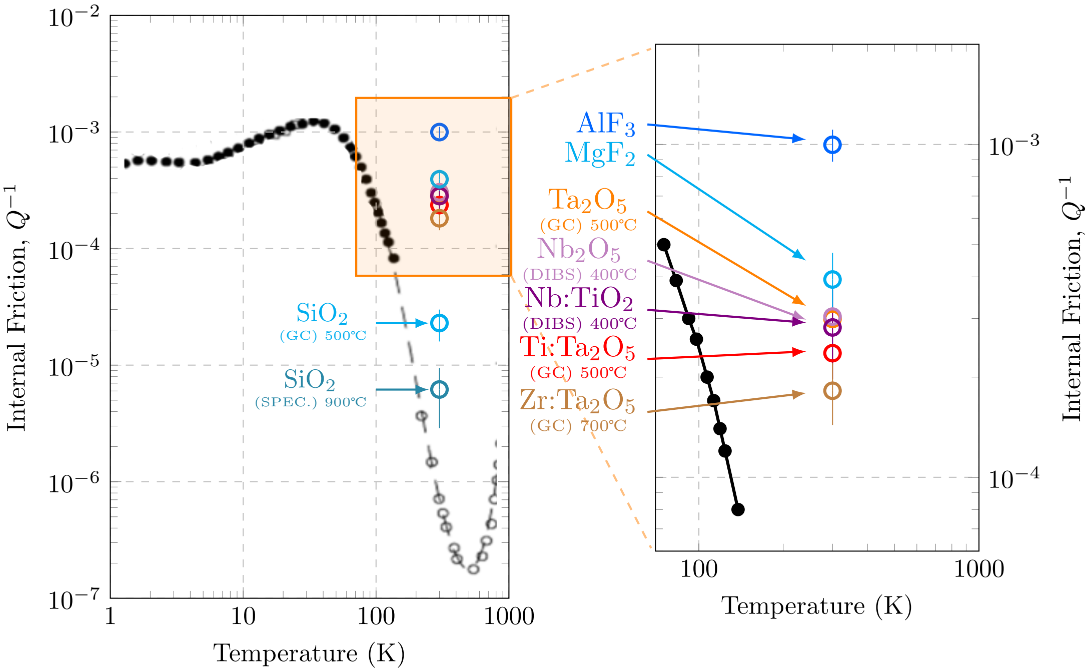

**Figure 4.64:** $MgF_2$ and $AlF_3$ coating loss angle at 100 Hz, measured at room temperature, compared with other coatings. In the plot, also the fused-silica internal friction [112], acquired at 1.5 MHz, is showed. The zoom allows to better compare the dissipative materials.

## 4.9 SiC Coating

The main reason leading to the investigation of silicon carbide (SiC) coating is related to the high refractive index in the NIR. Furthermore, SiC is a high-coordination number solid: the idea is to verify if this high coordination number solid has the tendency to reduce the TLS number and hence the mechanical loss. For this preliminary study, the poly-crystalline form 3C-SiC has been investigated.

SiC is a semiconductor with rigid stoichiometry (50% Si and 50% C) where the atoms are tetrahedrally bonded with covalent bonds. This material is the best known example of polymorph. The polymorph nature of SiC arises from the large number of combinations of stacking of Si-C bilayers. Staking Si-C bilayer along the c axis, in different combinations (A, B and C), different polymorph are obtained (figure 4.65a). In each layer, the silicon (or carbon) atoms have a close-packed hexagonal arrangement (figure 4.65b).

The main problem in growing SiC is the very high temperature required to realize single crystal material. For example, 4H-SiC and 6H-SiC need very high process temperatures (about 2000°C) to produce samples for commercial use. On the other hand, 3C-SiC is the thermodynamically stable and it can be grown at lower temperatures (i.e. below 1500°C). Furthermore, 3C-SiC has a diamond structure and if the coating is grown along the $c = \langle 0001 \rangle$ axis, it is isotropic along the coating surface. Under this respect, spectroscopic ellipsometry has been used to study the optical properties of 3C-SiC.

The samples have been provided by the Laboratoire des Multimatériaux et Interfaces (LMI) using chemical vapour deposition (CVD) technique around 900 – 1000°C. In order to use Silicon as substrate, the etching process with flowing HCl removes the oxide layer, than the carbonization is needed in order to deposit a first layer of the order

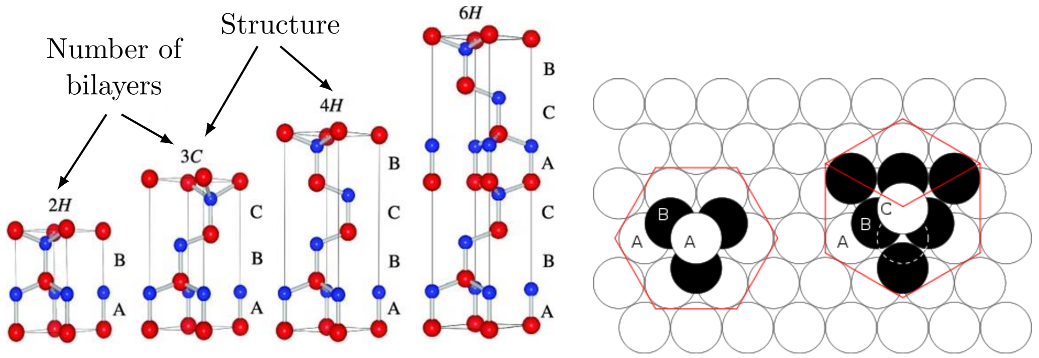

**(a)** Polytypes. **(b)** Arrangement.

**Figure 4.65:** (a) Different possible polytypes of SiC. The red atoms are Si atoms, the blue atoms are the C atoms. (b) Hexagonal arrangement.

of 1 nm in order to avoid the mismatch lattice between 3C-SiC and Silicon substrate. The coating has been deposited on 1" diameter silicon wafer and, as can be observed in figure 4.66, the coating shows a non-uniform deposition.

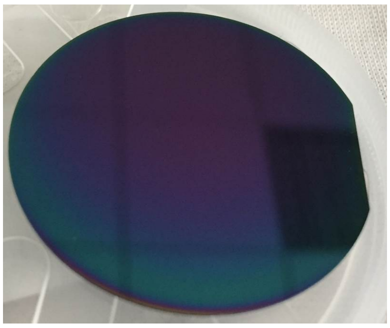

**Figure 4.66:** 3C-SiC deposited on a silicon substrate.

### 4.9.1 Optical Properties

The carbonization layer has been analysed with prior dedicated measurements. In figure 4.67 the $(\Psi, \Delta)$ data of carbonization layer are shown. It can be observed that the data are similar to the $(\Psi, \Delta)$ data of Silicon substrate because of the very thin layer on top. We can use a generalized oscillator model to reproduce the imaginary part of the dielectric function, obtaining a model Kramers-Kronig (KK)-consistent. However, it is important to describe as well as possible this system in order to use this model as substrate for the SiC coating. In figure 4.67 the data are compared to the fit curves.

In figure 4.68 the $(\Psi, \Delta)$ data of 3C-SiC coating are shown. As can be observed in figure 4.66, the sample presents a non uniform coating. In this respect the VASE ellipsometer is to be preferred respect to M2000 which has a larger light spot. However, the $(\Psi, \Delta)$ data presented a degradation in the UV region and for this reason, the data are presented up to 5.5 eV. The analysis shows a weak absorption also in the NIR region, for this reason a simple Cauchy or 2-poles model can not be used to represent the data in that region. A three layers model has been used to represent the optical properties, the first represents the model used to describe the carbonization layer, the second a generalized oscillator to describe the SiC coating and a surface layer. The latter was modelled through a Bruggeman effective medium approximation (EMA) layer, which accounts for a roughness of about $\sim 2$ nm over a film thick $155 \pm 2$ nm. In particular,

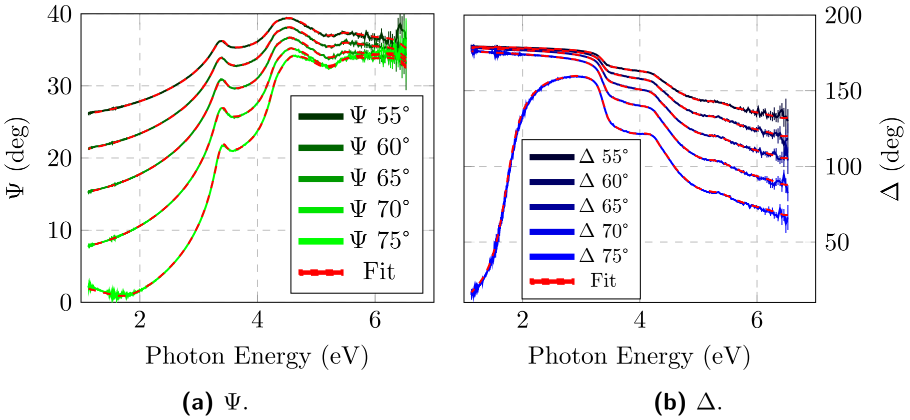

**(a)** Ψ. **(b)** Δ.

**Figure 4.67:** (Ψ, Δ) data and fit curves (red) for the carbonization layer on a silicon substrate.

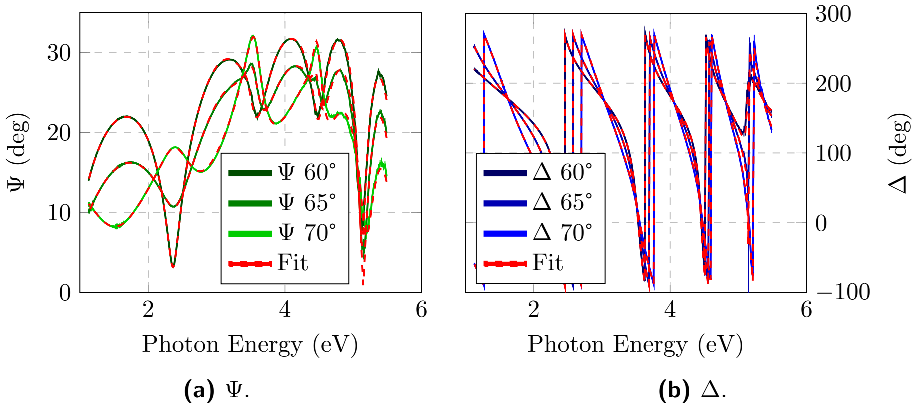

**(a)** Ψ. **(b)** Δ.

**Figure 4.68:** (Ψ, Δ) data and fit curves (red) for the carbonization layer on a silicon substrate.

five Gaussian oscillators and a pole around ∼ 7 eV have been used to describe the optical properties of the SiC coating.

In figure 4.69a the real and imaginary part of the dielectric function are shown, highlighting the several Gaussian oscillators used to build the optical model. In figure 4.69b the comparison of the result obtained by the analysis on VASE and M2000 data is shown. The results are different and this could be related to higher sensitivity of M2000 ellipsometer to the non-uniformity of the coating which may depolarize the light and affect the data.

### 4.9.2 Summary

SiC presents a refractive index much higher than the standard coating currently adopted in gravitational-wave detectors. The refractive index results $n \sim 2.57 \pm 0.01$ at 1064 nm and $n \sim 2.57 \pm 0.02$ at 1550 nm, in agreement with the values obtained in literature [145] ($n \sim 2.58$ at 1064 nm and $n \sim 2.57$ at 1550 nm). The main problem is the high optical absorption; the extinction coefficient is of the order of $10^{-2}$, to compare with the $\sim 10^{-7}$ of standard coatings for gravitational-wave detector.

The analysed coating was crystalline, however it would be interesting to investigate SiC deposited by IBS in order to obtain an amorphous coating with potentially lower

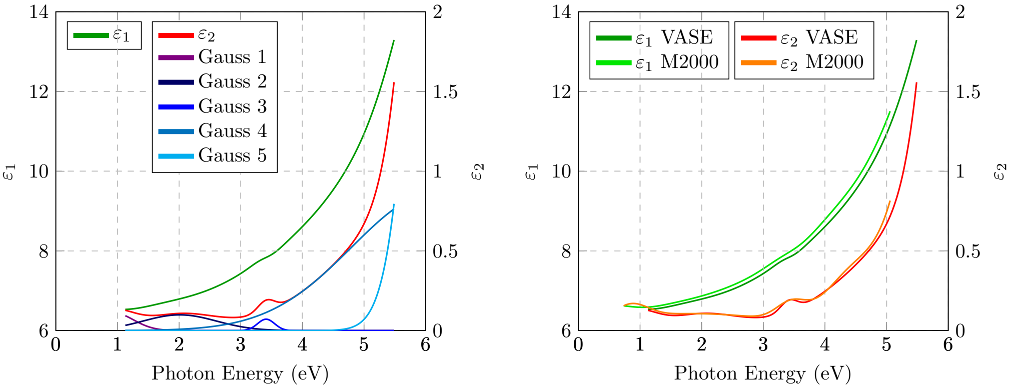

**(a)** Dielectric function.

**(b)** Comparison.

**Figure 4.69:** Real and imaginary part of the dielectric function. (a) The result obtained by the analysis on VASE data. (b) Comparison between the result obtained separately on VASE and M2000 data.

optical absorption.

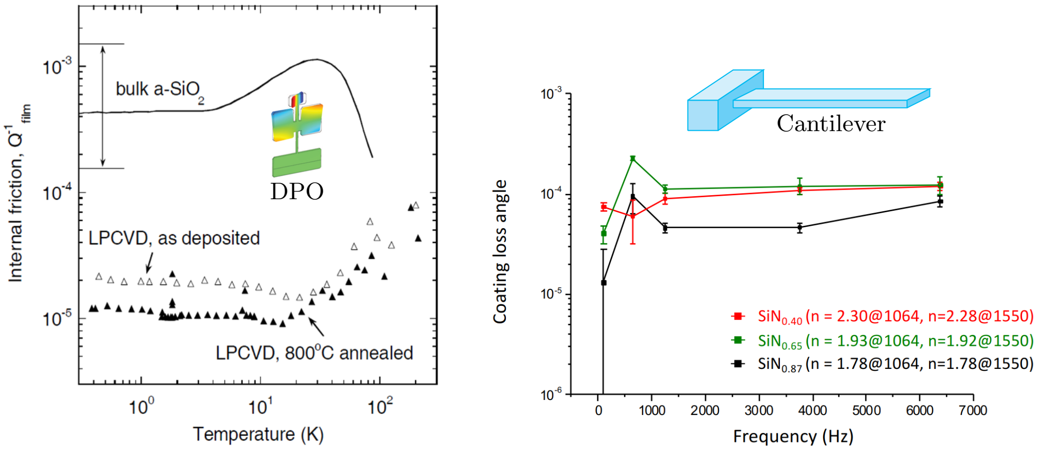

**(a)** DPO. **(b)** Cantilever.

**Figure 4.70:** Si$_3$N$_4$ CVD coating loss angle measured using two different systems. (a) Measurements at different temperatures of LPCVD a-SiN$_x$ using the double-paddle oscillators (DPOs) [146]. (b) Measurements at room temperature of different stoichiometry SiN$_x$ using a cantilever silica blade [147].

## 4.10 Si$_3$N$_4$ Coating

Silicon nitride (Si$_3$N$_4$) is a high-coordination solid with potentially low mechanical loss. Amorphous silicon nitride (a-SiN$_x$) thin films, are commonly deposited by chemical-vapor deposition (CVD) techniques. In figure 4.70a the internal friction of a-SiN$_x$ of a recent work [146], deposited by low-pressure chemical-vapor deposited (LPCVD), is shown. It can be observed that the coating loss angle is reduced by the increasing of deposition temperature (up to 800°C in figure 4.70a) and that this coating is particularly promising for application at low temperature. Furthermore, in figure 4.70b the coating loss angle of CVD SiN$_x$ of another recent work [147] are presented. The authors noted the presence of H in the coating, which concentration has an impact on the optical and mechanical properties. It can be observed that different stoichiometry yields different optical (the refractive index varies from 1.8 to 2.3) and mechanical properties (the loss angle varies almost of a factor 2). Furthermore, SiN$_x$ presented in figure 4.70 shows a coating loss angle at room temperature lower than the one of Ti:Ta$_2$O$_5$ and an higher refractive index.

CVD SiN$_x$ might suffer from high optical absorption ($\kappa \sim 1 - 5 \cdot 10^{-5}$) due to hydrogen contamination [148]; moreover, their thickness uniformity still remains to be tested against the stringent requirements of gravitational-wave detectors. Thus we chose to develop IBS SiN$_x$ coatings and test their loss versus the annealing temperature [116].

### 4.10.1 Mechanical Properties

In figure 4.71a the coating loss angle of first IBS SiN$_x$ samples ($A_1$ and $A_2$) deposited at room temperature is shown [116]. It can be observed that it is not possible to distinguish between family modes because in most of the cases, only one of the mixed modes could be measured. However, a frequency trend is observed. The fit results are summarised in table 4.20.

For all the samples the elastic constants have been carried out by fitting the measured dilution factor $D$ with simulations. In figure 4.72 the fit result for as deposited

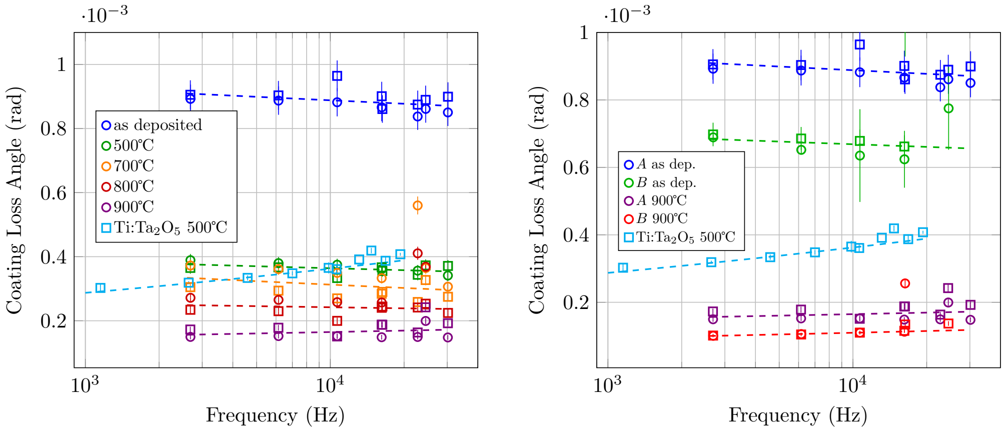

**(a)** $A_1$ and $A_2$ samples.

**(b)** Comparison.

**Figure 4.71:** Coating loss angle of IBS SiN$_x$ at different post-deposition annealing temperature. The circles and squares refer to two different samples. The dashed lines represent the frequency trend $af^b$ obtained considering both samples. (a) $A_1$ and $A_2$ samples [116]. (b) Comparison between $A_1$, $A_2$, $B_1$ and $B_2$ samples.

| IBS SiN$_x$ | $Y$ (GPa) | $\nu$ | $a$ ($10^{-4}$ rad Hz$^{-b}$) | $b$ |
|---|---|---|---|---|
| $A$ as dep. | – | – | 10 ± 1 | -0.017 ± 0.010 |
| $A$ 500°C | – | – | 4.6 ± 0.6 | -0.025 ± 0.013 |
| $A$ 700°C | – | – | 4.9 ± 1.8 | -0.05 ± 0.04 |
| $A$ 800°C | – | – | 2.9 ± 0.9 | -0.02 ± 0.03 |
| $A$ 900°C | – | – | 1.2 ± 0.6 | 0.04 ± 0.05 |
| $B$ as dep. | $250 \pm 30$ | $0.24 \pm 0.03$ | 7.8 ± 1.3 | -0.017 ± 0.019 |
| $B$ 900°C | – | – | 0.59 ± 0.02 | 0.067 ± 0.005 |

**Table 4.20:** Young's modulus $Y$, Poisson ratio $\nu$, and $a$, $b$ parameters of the model $af^b$ for SiN$_x$ coatings.

$B_1$ SiN$_x$ coating as representative sample.

One interesting feature of SiN$_x$ coating is the possibility to anneal the samples at high temperature without crystallization. This allows to obtain a coating loss angle lower than the standard Ti:Ta$_2$O$_5$. However, after the annealing at 800°C, the $A_1$ and $A_2$ samples present defects (figure 4.73). These defects are characterized by a sinusoidal stress relief patterns usually called "buckling waves", which are well-known in literature and are observed also in other systems under different conditions [149]. Cracks are due to excessive stress and poor adhesion [150]. The nucleation and growth of these defects is caused by a very well-defined combination of internal strain, Young's modulus, coating thickness and adhesion energy. In particular, internal stress and adhesion determine the stability of the coating/substrate composite and therefore the lifetime of a coated sample. A defect will grow if the shear stresses at the boundary exceed the bonding forces between the layer and the substrate. Under this respect, the internal stress must be sufficiently high to cause buckling but must be lower than a critical value for unbound spread of the defect. The cracks suggest that the substrate and the coating should have very different elastic moduli. During the annealing, the

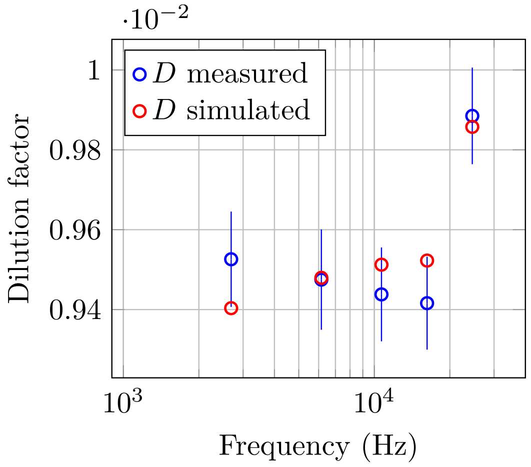

**Figure 4.72:** Fit of measured dilution factor (blue) with simulated values (red) for as deposited $B_1$ SiN$_x$ coating.

different thermal expansions lead to an internal stress large enough to cause the defects.

In figure 4.71b the coating loss angle of latest IBS SiN$_x$ ($B_1$ and $B_2$ samples) deposited at room temperature using different deposition parameters with respect to $A$ samples is shown. It is interesting to observe that the frequency trend is similar to the one showed by the $A_1$ and $A_2$ samples, but the level is different; $B_1$ and $B_2$ samples show lower coating loss angle. The fit values are summarised in table 4.20.

Another interesting detail is the behaviour of the coating loss angle of the different samples with the annealing. It is evident that when we approach the crystallization temperature, which is above 1300℃ [151], the difference between the loss angles decreases. The same behaviour has been observed for Ta$_2$O$_5$ coating, for which it is related likely with the structural limit observed by Raman measurements [116]. We did not observe cracks on latest $B_1$ and $B_2$ samples, even after the post deposition annealing at 900℃.

### 4.10.2 Optical Properties

In figure 4.74 the extinction coefficient $\kappa$ of IBS SiN$_x$ is shown as function of post-deposition annealing temperature. The measurements have been carried out using photothermal deflection technique [152]. The detection principle is based on the mirage effect, where a probe laser beam is deflected by change of the refractive index, due to the temperature gradient induced by absorption.

The obtained results show that, though lower than that of CVD coatings, their absorption is still too high ($10^{-6} < \kappa < 10^{-5}$) and we are presently working to further reduce this value.

### 4.10.3 Summary

We tested IBS SiN$_x$ deposited using different conditions. The results show SiN$_x$ coatings with different optical and mechanical properties. In particular, it has been observed that the coating loss angle of latest $B_1$ and $B_2$ samples is lower than the first $A_1$ and $A_2$ samples. However, this difference is reduced after the post-deposition annealing at 900℃. The coating loss angle after the annealing at 900℃, in the measured frequencies, is lower than the one of Ti:Ta$_2$O$_5$ annealed at 500℃ of a factor $\sim 2$ for $A_1$ and $A_2$ samples and $\sim 3$ for $B_1$ and $B_2$ samples. As can be observed in figure 4.75, this

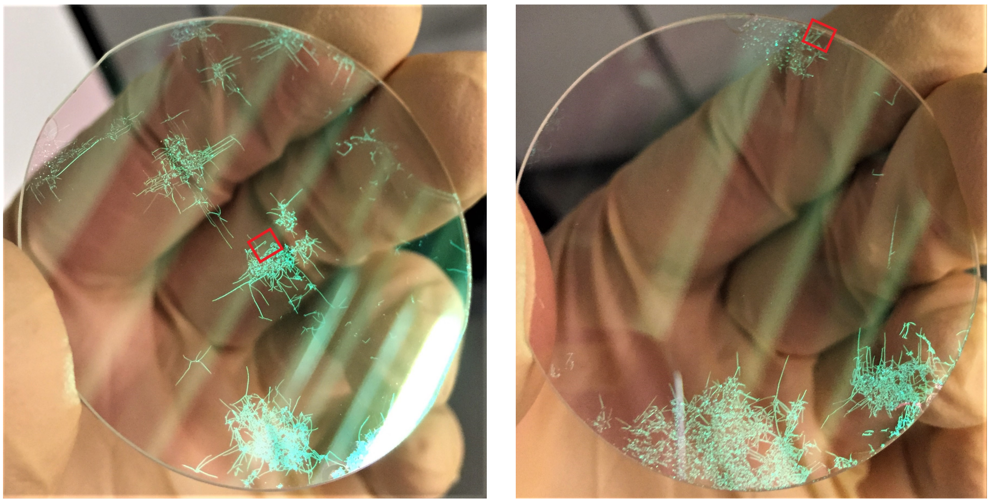

**(a)** $A_1$ sample. **(b)** $A_2$ sample.

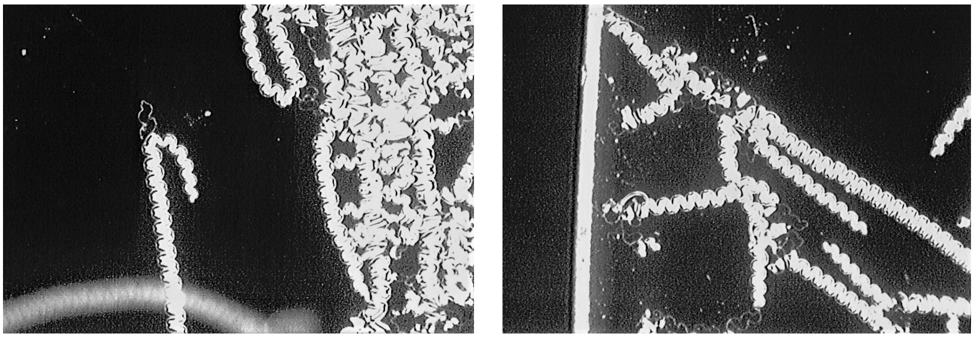

**(c)** $A_1$ sample (zoom). **(d)** $A_2$ sample (zoom).

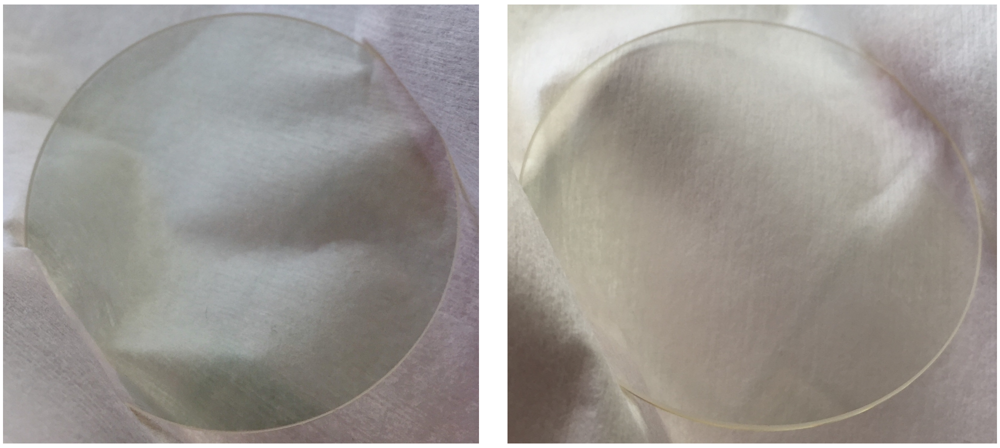

**(e)** $B_1$ sample. **(f)** $B_2$ sample.

**Figure 4.73:** IBS SiN$_x$ coating samples annealed at 800°C. (a) and (b) the first samples. (c) and (d) the optical microscopic observation of red squared area highlighted in (a) and (b) shows the sinusoidal stress relief patterns. (e) and (f) the latest samples annealed at 900°C.

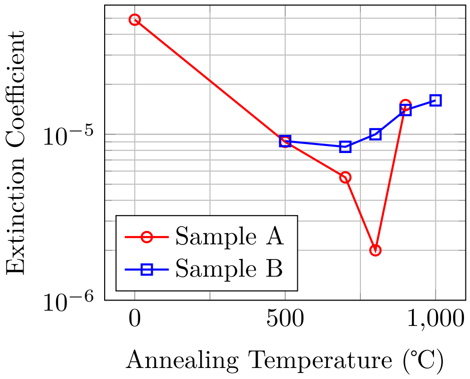

**Figure 4.74:** Extinction coefficient at 1064 nm of IBS SiN$_x$ coatings annealed at different temperature.

reduction at 100 Hz results of a factor $\sim 1.6$ for $A_1$ and $A_2$ samples and $\sim 2.8$ for $B_1$ and $B_2$ samples.

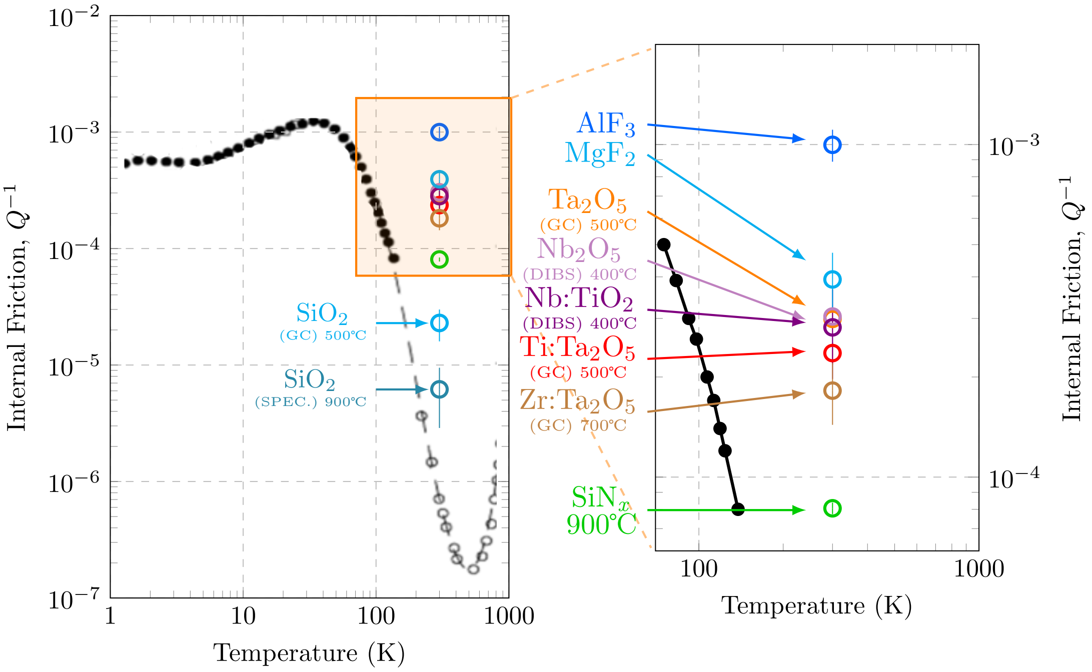

**Figure 4.75:** IBS SiN$_x$ coating loss angle at 100 Hz after the annealing at 900°C, measured at room temperature, compared with other coatings. In the plot, also the fused-silica internal friction [112], acquired at 1.5 MHz, is showed. The zoom allows to better compare the dissipative materials.

The main problem is related to the absorption at 1064 nm, which is higher than the absorption of coatings currently used in gravitational-wave detector ($\kappa \sim 10^{-7}$).

Another issue is the value of the Young's modulus $250 \pm 30$. Looking at equation (1.39) it is evident that the coating thermal noise depends also in the mismatch of the elastic moduli of the substrate and the coating. Since SiO$_2$ substrate has a Young's modulus of 72.2 GPa, SiN$_x$ Young's modulus could limit its use on SiO$_2$ substrates of room-temperature detectors. However, future cryogenic gravitational-wave detector might use a 1.550 $\mu$m laser wavelength and sapphire substrates, having a Young's modulus of 350 GPa. For this reason, since $\mathrm{SiN}_x$ is expected to show low coating loss angle at cryogenic temperature, it could be a valuable option for future cryogenic detectors if the absorption issue is solved.

Remarkable advantage of silicon nitride coatings is their much higher crystallization temperature: we could anneal our IBS $\mathrm{SiN}_x$ layers up to 900℃, without observing crystallization; since the crystallization temperature of our $\mathrm{SiO}_2$ coatings is 1000℃ [116], a high-reflective stack of $\mathrm{SiN}_x$ and $\mathrm{SiO}_2$ could be annealed at higher temperatures, decreasing also the loss of the $\mathrm{SiO}_2$ layers [116] and thus the resulting coating thermal noise of the whole stack itself.

## 4.11 Publications and Presentations of Results

I published or presented at several conferences most of the main results of this thesis. In particular, the first model of the edge effect on substrates has been described in [103]; then I presented a new study about the edge effect on substrates at the *LIGO-Virgo Collaboration (LVC) meeting* in Sonoma State University (USA, CA) and the improvement of this model including the edge effect on coatings at the *LVC meeting* in Maastricht University (NL). A paper with the final results and the model for coated samples will be published soon.

A paper about the correlation between the structure and the coating loss angle for $\mathrm{SiO}_2$ has been published [108].

I presented preliminary results about the coatings currently used in gravitational-wave detectors at the *12th Edoardo Amaldi Conference on Gravitational Waves* in Pasadena (USA, CA), published in [116]. A paper on the mechanical properties of these same coatings has been recently submitted for publication [153]. A paper on the optical properties of these same coatings has been published [109].

I presented the correlation between the Urbach energy and internal friction for the first time during the optical session of the *LVC meeting* in Lake Geneva (USA, WI) and during a *Coating Workshop* at the same meeting. Then, the correlation has been presented at the *8th International Conference on Spectroscopic Ellipsometry* in Barcelona(SE), for which a proceeding paper is under review. A paper about the correlation has been recently published [129].

Finally, some first results obtained from alternative coatings have been published [154] and presented by me at the *22nd International Conference on General Relativity and Gravitation/13th Edoardo Amaldi Conference on Gravitational Waves* in Valencia (ES), for which a paper will be submitted for publication. Other presentations and papers about the final results of this thesis work are planned.

Concerning theory and metrology, a paper on the analytical model of internal friction is under preparation and a paper regarding the estimation of the coating elastic constants has been submitted for publication [153].

# CONCLUSIONS

*"Be glad that you have some little knowledge of*
*something that you cannot penetrate.*
*Don't stop to marvel."*

Albert Einstein
LIFE Magazine, p.64 (2 May 1955)

At the end of 2015, the advanced-detectors started gravitational-wave astronomy; since then, 11 signals were detected during the observing run O1 and O2, and at the moment others signal alerts have been issued during the current observing run O3. Nowadays, the gravitational-wave detectors are entering an upgrading phase. One of the main goals is to reduce the so-called coating thermal noise which will limit the sensitivity of present and future detectors. There are different strategies in lowering coating thermal noise, and optical and mechanical characterizations are key ingredients in order to achieve this goal. In the following, the results obtained during this thesis work are listed.

**Substrates.** Silicon wafers have been used for optical investigation by reflection spectroscopic ellipsometry. The optical model developed here, based on several oscillators centered at the critical point of the joint density of states, gives a dielectric function which is in agreement with what can be found in literature.

Silica disk-shaped resonators have been used for mechanical characterizations. Silica substrates are affected by the so called *edge-effect*. The ageing of the loss angle due to this effect is erased by annealing and the vacuum storage of samples mitigates the effect.

**$SiO_2$.** Spurious loss at the coating edge has been observed. If not considered in the analysis, this edge effect could mask the actual coating loss angle.

The coating loss angle suggests a dependence in the mechanical loss on the deposition rate. However, the internal friction of silica coating at room temperature is still higher than the one of fused-silica (substrate silica) even after the annealing.

The evolution of internal friction and structure with respect to annealing showed a correlation between the $D_2$ peak in the Raman spectra, associated with the breathing mode of 3-ring structure, and the coating loss angle, measured at room temperature. Another unexpected result was the crystallization of the silica coating at 1000°C.

The optical measurements show a reduction of the refractive index after the annealing, accompanied by a reduction of density.

**$Ta_2O_5$.** Different deposition conditions yield coatings with different properties: the lowest deposition rate provides the coating with lower loss angle.

Moreover, as confirmed also by Raman measurements, post-deposition annealing at 500°C for 10h erases the deposition history.

The Young's modulus and Poisson's ratio do not show a clear dependence on deposition conditions within the explored range.

In order to minimize the internal friction, the mixing Ti:$Ta_2O_5$ has been investigated. It has been confirmed that Ti/Ta= 0.27 yielded minimum loss.

The mixed coating presents comparable elastic moduli to that of $Ta_2O_5$ but lower coating loss angle after the annealing. The coating loss angle of Ti:$Ta_2O_5$ after the annealing is reduced about 25% with respect to that of $Ta_2O_5$.

Concerning the optical properties of $Ta_2O_5$ and Ti:$Ta_2O_5$, it has been observed that the annealing does not affect the energy gap whereas it decreases the refractive index of about 1%, especially in the NIR region. The refractive index at 1064 nm of the Ti-doped coating after the annealing is higher almost 2% than that of pure tantala.

The Ti-doping causes a reduction of the energy gap which seems to be linearly related to the doping atomic ratio concentration of 0.27.

The effect of the annealing and the doping on the absorption measured in the Urbach tails spectral region is remarkable. In particular, similarly to the coating loss angle, the annealing and the doping reduce the Urbach energy, hence leading to a correlation between the Urbach energy and the coating internal friction. This correlation has been found for the first time in this thesis work.

**$Nb_2O_5$.** The refractive index of $Nb_2O_5$ is higher than that of Ti:$Ta_2O_5$ and this could lead to a thinner high-reflective stack and hence to a lower coating thermal noise.

The main objective of obtaining a high-refractive index coating from $TiO_2$ by Nb-doping, increasing the crystallisation temperature, has been achieved by Nb:$TiO_2$ with atomic ratio of Nb to Ti equal to 0.37.

The crystallization temperature of the Nb:$TiO_2$ is higher than 500°C, thus higher than that of pure $TiO_2$, which is between 250°C and 300°C, and of pure $Nb_2O_5$, which is above 400°C.

The refractive index of Nb:$TiO_2$ at 1064 nm is about 6% higher than that of Ti:$Ta_2O_5$. The high refractive index can be used to develop high-reflective coatings reducing the number of layers without affecting the reflectivity, possibly leading to a lower coating thermal noise.

The correlation between the Urbach energy and the coating internal friction has been confirmed in $Nb_2O_5$ too. Also in this case, the material was annealed and mixed with $TiO_2$.

The elastic moduli of Nb:$TiO_2$ are comparable with those of Ti:$Ta_2O_5$.

The lowest coating loss angle was obtained on Ti:$Nb_2O_5$ with atomic ratio of Nb to Ti equal to 0.37 and annealing temperature of 400°C. This minimum value is still higher than that of Ti:$Ta_2O_5$ coating annealed at 500°C.

**$MgF_2$ and $AlF_3$.** For the SE analysis, a relatively weak absorption had to be considered in the UV region, likely due to the presence of colour centers.

The coating loss angle of as deposited $MgF_2$ and $AlF_3$ is well higher than all the analysed as deposited oxides coatings at room temperature and have high optical absorption. Further investigations on the impact of annealing on their absorption and internal friction are ongoing; soon we will also measure their low-temperature internal friction, for possible implementation in future cryogenic detectors.

**SiC.** It presents a refractive index ~ 18% higher than the coatings currently adopted in gravitational-wave detectors. The main problem is the high extinction coefficient (of the order $10^{-2}$, to compare with $10^{-7}$ of standard coatings); it would be interesting to investigate SiC deposited by IBS in order to obtain an amorphous coating with potentially lower optical absorption.

Among all the investigated coatings Zr:$Ta_2O_5$ and $SiN_x$ provided the most promising results in term of internal friction, especially at 100 Hz, where the gravitational-wave detectors are limited by the coating thermal noise.

**Zr:$Ta_2O_5$.** This coating material has been proposed by the LIGO Scientific Collaboration. The main objective of increasing the annealing temperature of $Ta_2O_5$ by Zr-doping has been achieved, reaching 700°C.

The optical and mechanical properties are similar to the tantala coating in terms of refractive index, energy gap and coating loss angle between $10^3 - 10^4$ Hz.

The higher annealing temperature allows to reach a lower coating loss angle and the particular frequency trend gives a reduction of a factor ~ 1.3 with respect to the standard Ti:$Ta_2O_5$ at 100 Hz. The higher annealing temperature would beneficial also for silica coating in a high-reflecting stack, leading to a reduction of the total high-reflective coating loss angle.

**$SiN_x$.** Different deposition parameters provided different optical and mechanical properties. However, this difference is reduced after the post-deposition annealing at 900°C.

The coating loss angle after the annealing at 900°Cis lower than the one of Ti:$Ta_2O_5$, annealed at 500°C, in all the measured frequencies. This reduction at 100 Hz is ~ 2.8 for the latest IBS $SiN_x$ coatings.

The main issue is related to the absorption at 1064 nm, which is higher ($10^{-6} < \kappa < 10^{-5}$) than the absorption of coatings currently used in gravitational-wave detectors ($\kappa \sim 10^{-7}$). Further improvement of IBS SiNx are then needed, in order to decrease the optical absorption.

Another issue is the value of the Young's modulus ($250 \pm 30$ GPa). The coating thermal noise increases with the mismatch of the elastic moduli between the substrate and the coating. This is a problem since the $SiO_2$ substrate has a Young's modulus of 72.2 GPa. Future gravitational-wave detectors working at cryogenic temperature, will require substrates made of crystals. Among other option, sapphire is quite promising and its Young's modulus is ~ 350 GPa.

Further investigation of IBS SiNx deposited at high temperature and measurements at cryogenic temperature are planned.

Despite their different nature and annealing treatment, the coating loss angles of all measured high-index oxides (in particular the mixing with metals of 4th and 5th group) fall in the same range, from $1.5 \cdot 10^{-4}$ to $3.5 \cdot 10^{-4}$. This behaviour is in agreement with the many times cited universal behaviour of amorphous oxides [112].

Other important findings concern the method of analysis and fundamental properties of amorphous coatings.

**Analytical model of internal friction.** The analytical calculation of the internal friction of amorphous coatings has been worked out in the most general case of the potential barrier for the TLS. The obtained loss angle is in agreement with known results in literature about silica, in the limit of an exponential potential.

Further comparisons with other measured loss angle are needed in order to confirm the validity of this calculus.

**Edge effect.** A model which accounts for the extra mechanical loss of the edge has been developed during this thesis. This effect competes with the bulk and shear model and further investigation are needed in order to obtain better results in coating loss angle investigation.

**Protocol.** In order to mitigate the edge effect and to define the best treatments for all the samples, a protocol for loss measurements has been established, regarding the post-deposition annealing and vacuum storage of samples.

**Elastic constant estimation.** A non-destructive method, based on the measured dilution factor (ultimately based on the frequency shift of the resonator after the coating deposition), has been developed to estimate the elastic constants of coatings.

**Medium- long-range structure.** A correlation between the Urbach tails, evident in the optical absorption, and the internal friction, related to the mechanical properties, has been found. This correlation highlights the importance of the medum- long-range atomic organization in the mechanical quality of amorphous coatings.

APPENDIX A

# FLUCTUATION-DISSIPATION THEOREM

In the 1951 has been demonstrated a fundamental property of thermally activated fluctuations, where the power spectral density $S_{AA}$ of the observable $A$ is related to the imaginary part of the response function $\chi_{AA}$, by the so-called *dissipation-fluctuation theorem* [5]

$$S_{AA}(\omega) = 4\hbar \left( \frac{1}{2} + \frac{1}{e^{\beta\hbar\omega} - 1} \right) \Im \left[ \chi_{AA}(\omega) \right] \ , \tag{A.1}$$

where $\beta = (k_B T)^{-1}$ and $k_B$ is the Boltzmann's constant. The equation (A.1) can be written under the classic limit $\beta\hbar\omega \to 0$

$$S(\omega) = \frac{4k_B T}{\omega} \Im \left[ \chi(\omega) \right] \ . \tag{A.2}$$

In order to evaluate the response function $\chi(\omega)$, one may imagine to expose the observable $A$ to an external solicitation $F(t)$, so that $V(t) = -BF(t)$, which combines with an observable $B$ of the system. If the external solicitation is weak, from the linear response theory we obtain the Kubo relation [155]

$$\delta A(t) = \int_{-\infty}^{+\infty} \chi_{AB}(t - t') F(t') dt' \ , \tag{A.3}$$

where $\delta A(t)$ is the variation of the quantity $A$ and $\chi_{AB}(t)$ is the so-called *response function*

$$\chi_{AB}(t - t') = -\frac{i}{\hbar} \theta(t - t') \mathrm{Tr}(\rho [B, A(t)]) \ , \tag{A.4}$$

where $\theta(t - t')$ is the Heaviside function and $\rho$ is the matrix density of the system in thermodynamic equilibrium. If we consider a periodic solicitation, it is possible to rewrite the equation (A.3) using the admittance $\mathcal{Y}$ of the system

$$\delta \dot{A}(t) = \int_{-\infty}^{+\infty} \mathcal{Y}(t - t') F(t') dt' \ . \tag{A.5}$$

Using the frequency domain, it is possible to relates $\chi$ to $\mathcal{Y}$

$$\delta A(\omega) = \chi(\omega) F(\omega) \ , \tag{A.6}$$

$$-i\omega \delta A(\omega) = \mathcal{Y}(\omega) F(\omega) \ , \tag{A.7}$$

where

$$\mathcal{Y}(\omega) = -i\omega\chi(\omega) \ . \tag{A.8}$$

We can now express equation (A.2) as

$$S(\omega, T) = \frac{4k_B T}{\omega^2} \Re\left[\mathcal{Y}(\omega)\right] \ . \tag{A.9}$$

If we are interesting in the coating thermal noise in gravitational-wave detectors, we can consider as observable the displacement $A(t)$ of the mirror surface along the laser beam direction, averaged through the beam shape

$$A(t) = \int_S \zeta(x, y, t) B(x, y) dx dy \ , \tag{A.10}$$

where $\zeta(x, y, t)$ is the shape of the mirror surface at instant $t$ and $B(x, y)$ is the laser beam intensity profile (usually considered as Gaussian), with $\int B(x, y) dx dy = 1$. The external solicitation $V(t)$ is obtained using relation (A.10) in the Hamiltonian

$$\begin{aligned} V(t) &= -F_0(t) A(t) \\ &= -F_0(t) \int_S \zeta(x, y, t) B(x, y) dx dy \\ &= -\int_S \zeta(x, y, t) P(x, y, t) dx dy \ , \end{aligned} \tag{A.11}$$

where $F_0(t)$ has the dimension of a Force. The external force $F$ can be then expressed through the pressure $P(x, y, t) = F_0(t) B(x, y)$ applied on the mirror. It has to be noted that if $\zeta(x, y, t)$ is constant the total force on the mirror is not zero and the mirror start to move as a pendulum. For this reason, the observable is usually separated in two components: the pendulum and the mirror deformation. In the following we will consider $\zeta(x, y, t)$ as dependent on the spatial variables $x, y$. In order to use equation (A.9) it is necessary to evaluate the admittance $\mathcal{Y}(\omega)$, which is related to the dissipated energy. Indeed, using equation (A.3) the dissipated energy, which corresponds to the work done over a cycle $T = 2\pi/\omega$, for a periodic solicitation $F = F_0 \Re[e^{i\omega t}]$ reads

$$\begin{aligned} W_{\text{diss}} &= \int_0^T F(t) dA(t) = \int_0^T F(t) \dot{A}(t) dt \\ &= \int_0^T F(t) \Re[\mathcal{Y} F(t)] dt = \int_0^T F(t) \left( \frac{\mathcal{Y} F(t) + \mathcal{Y}^* F^*(t)}{2} \right) dt \\ &= \int_0^T F^2(t) \left( \frac{\mathcal{Y} + \mathcal{Y}^*}{2} \right) dt = \Re[\mathcal{Y}] \int_0^T F^2(t) dt \\ &= \Re[\mathcal{Y}] \frac{F_0^2}{4} \int_0^T (2 + e^{2i\omega t} + e^{-2i\omega t}) dt \\ &= \Re[\mathcal{Y}] \frac{F_0^2}{2} T = \Re[\mathcal{Y}] \frac{F_0^2 \pi}{\omega} \ . \end{aligned} \tag{A.12}$$

The thermal dissipation from (A.9) is then

$$S(\omega, T) = \frac{4k_B T}{\omega} \frac{W_{\text{diss}}}{F_0^2 \pi} \ . \tag{A.13}$$

# APPENDIX B

# $M_2$ FOR A TWO-LEVEL SYSTEM

In order to study the mechanical properties of amorphous solids related to the structure dynamics, the Debye equations (2.95) must be evaluated in the contest of two-level system. In particular, the imaginary part of the elastic modulus

$$M_2 = \delta M \frac{\omega \tau_u}{1+\omega^2 \tau_u^2} \tag{B.1}$$

$$M_2 = \delta M D(V) \,, \tag{B.2}$$

gives important hints on the dissipation energy, as expressed by the relation (2.104).

Following the theory of elasticity, we can relate $\delta M$ to the free energy $F$. looking at equation (2.78), the variation $\delta M$ can be evaluated by

$$\delta M = \frac{\partial \sigma_{ii}}{\partial u_{jj}} \,, \tag{B.3}$$

furthermore

$$\sigma_{ik} = \left( \frac{\partial F}{\partial u_{ik}} \right)_T \,, \tag{B.4}$$

and then

$$\delta M = \left. \frac{\partial^2 F}{\partial u_{ik}^2} \right|_{u_{ik}=0} \,. \tag{B.5}$$

For a system with TLS, one may use equation (2.74) and hence

$$\begin{aligned} \frac{\partial F}{\partial u_{ii}} &= \frac{\gamma}{2} \tanh \left( \frac{\Delta + \gamma u_{ii}}{2k_B T} \right) \,, \\ \frac{\partial^2 F}{\partial u_{ii}^2} &= \frac{\gamma^2}{4k_B T} \operatorname{sech}^2 \left( \frac{\Delta + \gamma u_{ii}}{2k_B T} \right) \,, \end{aligned} \tag{B.6}$$

which depends only on $\Delta$. For that reason, it is possible to evaluate the integral of equation (2.111) in $V$ as first.

The factor $D(V)$ which gives the Debye peak can be obtained considering the

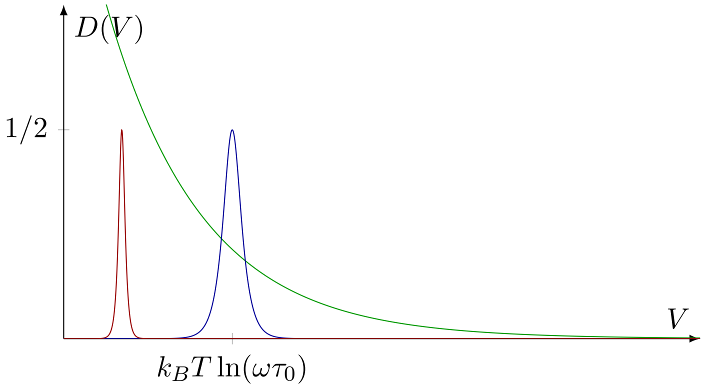

**Figure B.1:** Imaginary part of Debye function expressed by equation (B.7). The width depends on $k_B T$. The blue curve is obtained for $T = 290K$, $f = 1kHz$ and $\Delta = 0.2eV$. The red curve is obtained for $T = 100K$, $f = 1kHz$ and $\Delta = 0.2eV$. The green curve is the case of an exponential distribution of the barrier height $f(V) \propto e^{-V/V_0}$ in the TLS theory. For $k_B T \ll V_0$ the behaviour is similar to the delta function with amplitude 1/2 and by changing the temperature, it is possible to do a spectroscopic measurement of $f(V)$.

Arrhenius' law for the relaxation time, where $\tau = \tau_0' e^{V/k_B T}$. Under this respect

$$\begin{aligned} D(V) = \frac{\omega\tau}{1+\omega^2\tau^2} &= \frac{\omega\tau_0' e^{V/k_B T}}{1+\omega^2\tau_0'^2 e^{2V/k_B T}} \\ &= \frac{e^{[V/k_B T + \ln(\omega\tau_0')]}}{1+e^{2[V/k_B T+\ln(\omega\tau_0')]}} \\ &= \frac{1}{2\cosh\left(V/k_B T + \ln(\omega\tau_0')\right)}\,, \end{aligned} \tag{B.7}$$

which is shown in figure B.1.

# APPENDIX C

# ELASTIC ENERGY OF DISK RESONATOR

The elastic energy density for a disk-shaped resonator reads [156]

$$\begin{aligned} dE = \frac{Y}{1+\nu}\Bigg\{ & \frac{1}{2(1-\nu)}\left(\frac{\partial^2 w}{\partial r^2}+\frac{1}{r}\frac{\partial w}{\partial r}+\frac{1}{r^2}\frac{\partial^2 w}{\partial \theta^2}\right)^2 - \\ & + \Bigg[\frac{\partial^2 w}{\partial r^2}\left(\frac{1}{r}\frac{\partial w}{\partial r}+\frac{1}{r^2}\frac{\partial^2 w}{\partial \theta^2}\right) - \\ & + \left(\frac{\partial}{\partial r}\left(\frac{1}{r}\frac{\partial w}{\partial \theta}\right)\right)^2\Bigg]\Bigg\} z^2 dz r dr d\theta \,, \end{aligned} \tag{C.1}$$

where $Y$, $\nu$ are the Young's modulus and Poisson ratio respectively. In order to obtain the numerical values of the energy stored in a disk resonator, it is necessary to know the analytical expression of the deformation $w(r, \theta, t)$.

For a thin circular plate, the transversal displacement $w$ is obtained by the differential equation

$$S\nabla^4 w + \rho\frac{\partial^2 w}{\partial t^2} = 0 \,, \tag{C.2}$$

where $\rho$ is the superficial mass density of the disk, $\nabla^2$ is the Laplace operator in polar coordinates[1] and $S$ is the stiffness

$$S = \frac{Yh^3}{12(1-\nu^2)} \,, \tag{C.3}$$

where $h$ is the thickness of the disk. If we consider free vibrations, the displacement can be described by two factor, one depends to the resonant mode shape and the other one to the period of the deformation

$$w(r, \theta, t) = \zeta(r, \theta)\cos\omega t \,, \tag{C.4}$$

Using expression (C.4) in equation (C.2) we obtain

$$\left(\nabla^4 - \frac{\rho\omega^2}{S}\right)\zeta = 0 \,, \tag{C.5}$$

Defining $\mathcal{K}^4 = \frac{\rho\omega^2}{S}$ we obtain

$$\left(\nabla^4 - \mathcal{K}^4\right)\zeta = \left(\nabla^2 + \mathcal{K}^2\right)\left(\nabla^2 - \mathcal{K}^2\right)\zeta = 0 \,, \tag{C.6}$$

---

[1] The Laplacian in polar coordinate is $\nabla^2 = \frac{\partial^2}{\partial r^2} + \frac{1}{r}\frac{\partial}{\partial r} + \frac{1}{r^2}\frac{\partial^2}{\partial \theta^2}$.

with solutions

$$\begin{cases} \nabla^2\zeta_1 + \mathcal{K}^2\zeta_1 = 0 \,, \\ \nabla^2\zeta_2 - \mathcal{K}^2\zeta_2 = 0 \,. \end{cases} \tag{C.7}$$

We can express the displacement $\zeta(r,\theta)$ in therm of Fourier expansion over $\theta$ [157]

$$\zeta(r,\theta) = \sum_{n=0}^{\infty} \zeta_n(r)\cos(n\theta) + \sum_{n=1}^{\infty} \zeta_n^*(r)\sin(n\theta) \,, \tag{C.8}$$

so that we obtain the motion equations

$$\begin{cases} \frac{\partial^2}{\partial r^2}\zeta_{n,1} + \frac{1}{r}\frac{\partial}{\partial r}\zeta_{n,1} + \left(\mathcal{K}^2 - \frac{n^2}{r^2}\right)\zeta_{n,1} = 0 \,, \\ \frac{\partial^2}{\partial r^2}\zeta_{n,2} + \frac{1}{r}\frac{\partial}{\partial r}\zeta_{n,2} - \left(\mathcal{K}^2 + \frac{n^2}{r^2}\right)\zeta_{n,2} = 0 \,, \\ \frac{\partial^2}{\partial r^2}\zeta^*_{n,1} + \frac{1}{r}\frac{\partial}{\partial r}\zeta^*_{n,1} + \left(\mathcal{K}^2 - \frac{n^2}{r^2}\right)\zeta^*_{n,1} = 0 \,, \\ \frac{\partial^2}{\partial r^2}\zeta^*_{n,2} + \frac{1}{r}\frac{\partial}{\partial r}\zeta^*_{n,2} - \left(\mathcal{K}^2 + \frac{n^2}{r^2}\right)\zeta^*_{n,2} = 0 \,. \end{cases} \tag{C.9}$$

Equations (C.9) are the Bessel equations and the solutions read

$$\zeta_{n,1} = A_n J_n(\mathcal{K}r) + B_n Y_n(\mathcal{K}r) \,, \tag{C.10}$$

$$\zeta_{n,2} = C_n I_n(\mathcal{K}r) + D_n K_n(\mathcal{K}r) \,, \tag{C.11}$$

$$\zeta^*_{n,1} = A^*_n J_n(\mathcal{K}r) + B^*_n Y_n(\mathcal{K}r) \,, \tag{C.12}$$

$$\zeta^*_{n,2} = C^*_n I_n(\mathcal{K}r) + D^*_n K_n(\mathcal{K}r) \,, \tag{C.13}$$

$$\tag{C.14}$$

where $J_n$ and $Y_n$ are the Bessel functions of the first and second type whereas $I_n$ and $K_n$ are the modified Bessel functions of the first and second type, respectively. The coefficients $A_n$, $B_n$, $C_n$, $D_n$ and their conjugates depend on the shape of the resonant mode and are obtained from the boundary conditions. The displacement is then

$$\zeta(r,\theta) = \sum_{n=0}^{\infty}(\zeta_{n,1} + \zeta_{n,2})\cos(n\theta) + \sum_{n=1}^{\infty}(\zeta^*_{n,1} + \zeta^*_{n,2})\sin(n\theta) \,. \tag{C.15}$$

Considering the circular symmetry of the system and a homogeneous disk, if the center of the disk is the origin of the polar coordinates the functions $Y(\kappa r)$ and $K(\kappa r)$ are not to be considered in order to avoid infinite displacement and infinite stress in $r = 0$. Furthermore, considering the symmetry along the diameter, the solutions in $\sin(n\theta)$ can be discarded. In this respect, the displacement reads

$$\zeta(r,\theta) = \sum_{n=0}^{\infty}\left(A_n J_n(\mathcal{K}r) + C_n I_n(\mathcal{K}r)\right)\cos(n\theta) \,, \tag{C.16}$$

where $A_n$ and $C_n$ are obtained by the boundary conditions, which in the case of free-edge vibrating plate correspond to zero bending and twisting moments at the edge of the disk [158]. Considering the maximum displacement at $t = 0$, $w(r,\theta,t=0) = \zeta(r,\theta)$, it is possible to obtain the expression of the energy density and to solve numerically the integral for each resonance mode.

If we consider a disk coated on both sides, we can evaluate the integral of equation (C.1) over $z$ direction and obtain the expression of the energy stored in the substrate

$E_s$ and in the coating $E_c$

$$E_s = \frac{1}{2}\frac{Y_s h^3}{12(1-\nu_s^2)}\left\{(\nabla^2 w)^2 - 2(1-\nu_s)\Big[w''(r,\theta)\Big]\right\} r dr d\theta \,, \tag{C.17}$$

$$E_c = \frac{Y_c h^2 t}{4(1-\nu_c^2)}\left\{(\nabla^2 w)^2 - 2(1-\nu_c)\Big[w''(r,\theta)\Big]\right\} r dr d\theta \,, \tag{C.18}$$

where $h$ is the thickness of the substrate, $t$ is the thickness of the coating and

$$w''(r,\theta) = \left[\frac{\partial^2 w}{\partial r^2}\left(\frac{1}{r}\frac{\partial w}{\partial r} + \frac{1}{r^2}\frac{\partial^2 w}{\partial \theta^2}\right) - \left(\frac{\partial}{\partial r}\left(\frac{1}{r}\frac{\partial w}{\partial \theta}\right)\right)^2\right] . \tag{C.19}$$

A deformation can be decomposed in bulk, where the dilatation changes the volume of the sample, and shear, where the deformation does not affect the volume. The free energy density can be written as [156]

$$E = \frac{1}{2}(\lambda + \frac{2}{3}\mu)u_{ll}^2 + \mu({}_{ik} - \frac{1}{3}\delta_{ik}u_{ll})^2 \tag{C.20}$$

$$= \frac{1}{2}K u_{ll}^2 + \mu({}_{ik} - \frac{1}{3}\delta_{ik}u_{ll})^2 \,, \tag{C.21}$$

where $u_{ik}$ are the elements of the strain tensor, $\lambda$, $\mu$ are the Lamé's coefficients and $K = \lambda + \frac{2}{3}\mu$ is the bulk modulus, which are related to the Young's modulus and Poisson ratio

$$Y = \frac{9K\mu}{3K+\mu} \,, \qquad \nu = \frac{1}{2}\frac{3K - 2\mu}{(3K+\mu)} \,, \quad \text{so that} \quad K = \frac{1}{3}\frac{Y}{(1-2\nu)} \,. \tag{C.22}$$

The first term of equation (C.21) is the energy related to the bulk modulus and can be expressed in polar coordinate by considering

$$u_{rr} = \frac{\partial u_r}{\partial r} \,, \tag{C.23}$$

$$u_{\theta\theta} = \frac{1}{r}\frac{\partial u_\theta}{\partial \theta} + \frac{u_r}{r} \,, \tag{C.24}$$

$$u_{zz} = \frac{\partial u_z}{\partial z} \,, \tag{C.25}$$

with

$$u_r = -z\frac{\partial w}{\partial r} \,, \tag{C.26}$$

$$u_\theta = -\frac{z}{r}\frac{\partial w}{\partial \theta} \,, \tag{C.27}$$

$$u_z = w \,. \tag{C.28}$$

Thence

$$dE_{\text{Bulk}} = \frac{1}{2}K u_{ll}^2 \tag{C.29}$$

$$= \frac{1}{6}\frac{Y}{(1-2\nu)}\left(-z\frac{\partial^2 w}{\partial r^2} - \frac{z}{r^2}\frac{\partial^2 w}{\partial \theta^2} - \frac{z}{r}\frac{\partial w}{\partial r}\right)^2 dz dr d\theta \tag{C.30}$$

$$= \frac{Y}{6(1-2\nu)}(\nabla^2 w)^2 z^2 dz dr d\theta \,. \tag{C.31}$$

# BIBLIOGRAPHY

[1] R. Hulse and J. Taylor, "Discovery of a pulsar in a binary system," *Neutron stars, black holes, and binary X-ray sources*, vol. 48, p. 433, 1975.

[2] J. H. Taylor and J. M. Weisberg, "A new test of general relativity-gravitational radiation and the binary pulsar psr 1913+ 16," *The Astrophysical Journal*, vol. 253, pp. 908–920, 1982.

[3] B. Abbott, R. Abbott, T. Abbott, M. Abernathy, F. Acernese, K. Ackley, C. Adams, T. Adams, P. Addesso, R. Adhikari, *et al.*, "Observation of gravitational waves from a binary black hole merger," *Physical Review Letters*, vol. 116, no. 6, p. 061102, 2016.

[4] P. R. Saulson, "Thermal noise in mechanical experiments," *Physical Review D*, vol. 42, no. 8, p. 2437, 1990.

[5] H. B. Callen and R. F. Greene, "On a theorem of irreversible thermodynamics," *Physical Review*, vol. 86, no. 5, p. 702, 1952.

[6] M. Punturo *et al.*, "The einstein telescope: a third-generation gravitational wave observatory," *Classical and Quantum Gravity*, vol. 27, p. 194002, sep 2010.

[7] T. Kessler *et al.*, "A sub-40-mhz-linewidth laser based on a silicon single-crystal optical cavity," *Nat. Photon.*, vol. 6, pp. 687–692, Oct 2012.

[8] A. D. Ludlow *et al.*, "Optical atomic clocks," *Rev. Mod. Phys.*, vol. 87, pp. 637–701, Jun 2015.

[9] M. Aspelmeyer *et al.*, "Cavity optomechanics," *Rev. Mod. Phys.*, vol. 86, pp. 1391–1452, Dec 2014.

[10] L. Pinard *et al.*, "Mirrors used in the ligo interferometers for first detection of gravitational waves," *Appl. Opt.*, vol. 56, pp. C11–C15, Feb 2017.

[11] D. R. M. Crooks *et al.*, "Experimental measurements of coating mechanical loss factors," *Classical and Quantum Gravity*, vol. 21, pp. S1059–S1065, feb 2004.

[12] A. E. Villar *et al.*, "Measurement of thermal noise in multilayer coatings with optimized layer thickness," *Phys. Rev. D*, vol. 81, no. 12, p. 122001, 2010.

[13] M. Maggiore, *Gravitational Waves (Volume 1): Theory and Experiments*, vol. 1. Oxford university press, 2008.

[14] K. D. Kokkotas, “Gravitational wave physics,” *Encyclopedia of Physical Science and Technology,*, vol. 7, pp. 67–85, 2002.

[15] P. R. Saulson, *Fundamentals of interferometric gravitational wave detectors.* World scientific, 1994.

[16] LIGO Scientific Collaboration and Virgo Collaboration, “Gwtc-1: A gravitational-wave transient catalog of compact binary mergers observed by ligo and virgo during the first and second observing runs,” *Phys. Rev. X*, vol. 9, p. 031040, Sep 2019.

[17] B. J. Meers, “Recycling in laser-interferometric gravitational-wave detectors,” *Phys. Rev. D*, vol. 38, pp. 2317–2326, Oct 1988.

[18] A. Brillet *et al.*, *Advanced techniques: recycling and squeezing*, p. 369–405. Cambridge University Press, 1991.

[19] LIGO Scientific Collaboration, “Advanced ligo,” *Classical and Quantum Gravity*, vol. 32, no. 7, p. 074001., 2015.

[20] Virgo Collaboration, “Advanced virgo: a second-generation interferometric gravitational wave detector,” *Classical and Quantum Gravity*, vol. 32, no. 2, p. 024001., 2015.

[21] KAGRA Collaboration, “Interferometer design of the kagra gravitational wave detector,” *Phys. Rev. D*, vol. 88, p. 043007, Aug 2013.

[22] LIGO Scientific Collaboration and Virgo Collaboration, “Observation of gravitational waves from a binary black hole merger,” *Phys. Rev. Lett.*, vol. 116, p. 061102, Feb 2016.

[23] H. Grote, “The GEO 600 status,” *Classical and Quantum Gravity*, vol. 27, p. 084003, apr 2010.

[24] The LIGO Scientific Collaboration, the Virgo Collaboration, the 1M2H Collaboration, the Dark Energy Camera GW-EM Collaboration, the DES Collaboration, the DLT40 Collaboration, the Las Cumbres Observatory Collaboration, The VINROUGE Collaboration and the MASTER Collaboration, “A gravitational-wave standard siren measurement of the hubble constant,” *Nature*, vol. 551, pp. 85–88, Nov 2017. Letter.

[25] C. S. Unnikrishnan, “Indigo and ligo-india: scope and plans for gravitational wave research and precision metrology in india,” *International Journal of Modern Physics D*, vol. 22, no. 01, p. 1341010, 2013.

[26] B. Sathyaprakash *et al.*, “Scientific objectives of einstein telescope,” *Classical and Quantum Gravity*, vol. 29, p. 124013, jun 2012.

[27] B. P. Abbott *et al.*, “Exploring the sensitivity of next generation gravitational wave detectors,” *Classical and Quantum Gravity*, vol. 34, p. 044001, jan 2017.

[28] K. Danzmann *et al.*, “Lisa—laser interferometer space antenna: A proposal in response to the esa call for l3 mission concepts,” *Albert Einstein Inst. Hanover, Leibniz Univ. Hanover, Max Planck Inst. Gravitational Phys., Hannover, Germany, Tech. Rep*, 2017.

[29] G. Cella and A. Giazotto, "Invited review article: Interferometric gravity wave detectors," *Review of Scientific Instruments*, vol. 82, no. 10, p. 101101, 2011.

[30] P. R. Saulson, "Physics of gravitational wave detection: Resonant and interferometric detectors," *XXVI SLAC Summer Institute on Particle Physics*, 1998.

[31] P. Amico *et al.*, "Monolithic fused silica suspension for the virgo gravitational waves detector," *Review of scientific instruments*, vol. 73, no. 9, pp. 3318–3323, 2002.

[32] F. Piergiovanni *et al.*, "The dynamics of monolithic suspensions for advanced detectors: A 3-segment model," *Journal of Physics: Conference Series*, vol. 228, p. 012017, may 2010.

[33] Y. Levin, "Internal thermal noise in the ligo test masses: A direct approach," *Phys. Rev. D*, vol. 57, pp. 659–663, Jan 1998.

[34] M. L. Gorodetsky, "Thermal noises and noise compensation in high-reflection multilayer coating," *Physics Letters A*, vol. 372, no. 46, pp. 6813–6822, 2008.

[35] G. M. Harry *et al.*, "Thermal noise in interferometric gravitational wave detectors due to dielectric optical coatings," *Classical and Quantum Gravity*, vol. 19, pp. 897–917, feb 2002.

[36] M. Cerdonio *et al.*, "Thermoelastic effects at low temperatures and quantum limits in displacement measurements," *Physical Review D*, vol. 63, no. 8, p. 082003, 2001.

[37] M. Fejer *et al.*, "Thermoelastic dissipation in inhomogeneous media: loss measurements and displacement noise in coated test masses for interferometric gravitational wave detectors," *Physical Review D*, vol. 70, no. 8, p. 082003, 2004.

[38] V. Braginsky *et al.*, "Thermo-refractive noise in gravitational wave antennae," *Physics Letters A*, vol. 271, no. 5, pp. 303–307, 2000.

[39] B. P. Abbott *et al.*, "Prospects for observing and localizing gravitational-wave transients with advanced ligo, advanced virgo and kagra," *Living Reviews in Relativity*, vol. 21, no. 1, p. 3, 2018.

[40] M. Punturo *et al.*, "The einstein telescope: a third-generation gravitational wave observatory," *Classical and Quantum Gravity*, vol. 27, no. 19, p. 194002, 2010.

[41] T. Kessler *et al.*, "A sub-40-mhz-linewidth laser based on a silicon single-crystal optical cavity," *Nature Photonics*, vol. 6, p. 687, Sep 2012. Article.

[42] G. D. Cole *et al.*, "Tenfold reduction of brownian noise in high-reflectivity optical coatings," *Nature Photonics*, vol. 7, p. 644, Jul 2013. Article.

[43] G. D. Cole *et al.*, "High-performance near- and mid-infrared crystalline coatings," *Optica*, vol. 3, pp. 647–656, Jun 2016.

[44] F. Brückner *et al.*, "Realization of a monolithic high-reflectivity cavity mirror from a single silicon crystal," *Phys. Rev. Lett.*, vol. 104, p. 163903, Apr 2010.

[45] Virgo Collaboration, "Advanced virgo technical design report," *Virgo Technical Documentation System*, 2012.

[46] L. Pinard *et al.*, "Bulk absorption measurement at 1064 nm of the new heraeus ultra pure fused silica used for the advanced virgo test mass: effect of the annealing," *Virgo Note*, 2010.

[47] Z. Yan *et al.*, "Rayleigh scattering, absorption, and birefringence of large-size bulk single-crystal sapphire," *Applied optics*, vol. 45, no. 12, pp. 2631–2637, 2006.

[48] M. Born and E. Wolf, *Principles of Optics: Electromagnetic Theory of Propagation, Interference and Diffraction of Light.* Cambridge University Press, 7th ed., 10 1999.

[49] M. Principe, "Reflective coating optimization for interferometric detectors of gravitational waves," *Optics express*, vol. 23, no. 9, pp. 10938–10956, 2015.

[50] F. Beauville *et al.*, "The virgo large mirrors: a challenge for low loss coatings," *Classical and Quantum Gravity*, vol. 21, no. 5, p. S935, 2004.

[51] T. Accadia *et al.*, "Virgo: a laser interferometer to detect gravitational waves," *Journal of Instrumentation*, vol. 7, no. 03, p. P03012, 2012.

[52] G. M. Harry *et al.*, "Titania-doped tantala/silica coatings for gravitational-wave detection," *Classical and Quantum Gravity*, vol. 24, no. 2, p. 405, 2006.

[53] S. Adachi, *Optical properties of crystalline and amorphous semiconductors: Materials and fundamental principles.* Springer Science & Business Media, 2012.

[54] J. Tauc, *Amorphous and liquid semiconductors.* Springer Science & Business Media, 2012.

[55] V. A. Lobastov *et al.*, "Four-dimensional ultrafast electron microscopy," *Proceedings of the National Academy of Sciences*, vol. 102, no. 20, pp. 7069–7073, 2005.

[56] S. R. Elliott, *Physics of Amorphous Materials.* Longman, London, 1990.

[57] J. Singh and K. Shimakawa, *Advances in amorphous semiconductors.* CRC Press, 2003.

[58] P. W. Anderson, "Absence of diffusion in certain random lattices," *Phys. Rev.*, vol. 109, pp. 1492–1505, Mar 1958.

[59] F. Urbach, "The long-wavelength edge of photographic sensitivity and of the electronic absorption of solids," *Phys. Rev.*, vol. 92, pp. 1324–1324, Dec 1953.

[60] N. Mott, "Electrons in disordered structures," *Advances in Physics*, vol. 16, no. 61, pp. 49–144, 1967.

[61] N. F. Mott and E. A. Davis, *Electronic processes in non-crystalline materials.* OUP Oxford, 2012.

[62] H. Tompkins and E. A. Irene, *Handbook of ellipsometry.* William Andrew, 2005.

[63] J. D. Jackson, *Classical electrodynamics.* Wiley, 1999.

[64] A. Ibrahim and S. Al-Ani, "Models of optical absorption in amorphous semiconductors at the absorption edge — a review and re-evaluation," *Czechoslovak Journal of Physics*, vol. 44, no. 8, pp. 785–797, 1994.

[65] R. Klazes *et al.*, “Determination of the optical bandgap of amorphous silicon,” *Philosophical magazine B*, vol. 45, no. 4, pp. 377–383, 1982.

[66] D. Aspnes, A. Studna, and E. Kinsbron, “Dielectric properties of heavily doped crystalline and amorphous silicon from 1.5 to 6.0 ev,” *Physical Review B*, vol. 29, no. 2, p. 768, 1984.

[67] J. I. Pankove, *Hydrogenated Amorphous Silicon: Optical Properties.* Semiconductors and Semimetals Vol. 21, part B, Academic Press, 1984.

[68] G. D. Cody *et al.*, “Disorder and the optical-absorption edge of hydrogenated amorphous silicon,” *Phys. Rev. Lett.*, vol. 47, pp. 1480–1483, Nov 1981.

[69] Y. Pan *et al.*, “Atomistic origin of urbach tails in amorphous silicon,” *Phys. Rev. Lett.*, vol. 100, p. 206403, May 2008.

[70] D. A. Drabold *et al.*, “Urbach tails of amorphous silicon,” *Phys. Rev. B*, vol. 83, p. 045201, Jan 2011.

[71] I. Studenyak *et al.*, “Urbach rule in solid state physics,” *Int. J. Opt. Appl.*, vol. 4, pp. 76–83, 01 2014.

[72] Y. Pan *et al.*, “Topological and topological-electronic correlations in amorphous silicon,” *Journal of Non-Crystalline Solids*, vol. 354, no. 29, pp. 3480 – 3485, 2008.

[73] L. D. Landau and E. M. Lifshitz, *Course of theoretical physics.* Elsevier, 2013.

[74] E. Pineda, “Theoretical approach to poisson ratio behavior during structural changes in metallic glasses,” *Phys. Rev. B*, vol. 73, p. 104109, Mar 2006.

[75] A. S. Nowick, *Anelastic relaxation in crystalline solids*, vol. 1. Elsevier, 2012.

[76] P. W. Anderson *et al.*, “Anomalous low-temperature thermal properties of glasses and spin glasses,” *Philosophical Magazine*, vol. 25, no. 1, pp. 1–9, 1972.

[77] K. Binder and W. Kob, *Glassy materials and disordered solids: An introduction to their statistical mechanics.* World Scientific, 2011.

[78] R. Zeller and R. Pohl, “Thermal conductivity and specific heat of noncrystalline solids,” *Physical Review B*, vol. 4, no. 6, p. 2029, 1971.

[79] K. Gilroy and W. Phillips, “An asymmetric double-well potential model for structural relaxation processes in amorphous materials,” *Philosophical Magazine B*, vol. 43, no. 5, pp. 735–746, 1981.

[80] W. Phillips, “Tunneling states in amorphous solids,” *Journal of Low Temperature Physics*, vol. 7, no. 3, pp. 351–360, 1972.

[81] J. Jäckle *et al.*, “Elastic effects of structural relaxation in glasses at low temperatures,” *Journal of Non-Crystalline Solids*, vol. 20, no. 3, pp. 365–391, 1976.

[82] A. Anderson *et al.*, *Amorphous solids: low-temperature properties*, vol. 24. Springer Science & Business Media, 2012.

[83] J. Wiedersich *et al.*, “Light scattering spectra of fast relaxation in silica and $\mathrm{ca}_{0.4}\mathrm{k}_{0.6}(\mathrm{no}_3)_{1.4}$ glasses,” *Phys. Rev. B*, vol. 64, p. 064207, Jul 2001.

[84] F. Travasso *et al.*, "Low-frequency losses in silica glass at low temperature," *Materials Science and Engineering: A*, vol. 521-522, pp. 268 – 271, 2009.

[85] H. Fujiwara, *Spectroscopic ellipsometry: principles and applications.* John Wiley & Sons, 2007.

[86] R. Kleim *et al.*, "Systematic errors in rotating-compensator ellipsometry," *JOSA A*, vol. 11, no. 9, pp. 2550–2559, 1994.

[87] G. Jellison Jr and F. Modine, "Parameterization of the optical functions of amorphous materials in the interband region," *Applied Physics Letters*, vol. 69, no. 3, pp. 371–373, 1996.

[88] A. Ferlauto, G. Ferreira, J. M. Pearce, C. Wronski, R. Collins, X. Deng, and G. Ganguly, "Analytical model for the optical functions of amorphous semiconductors from the near-infrared to ultraviolet: Applications in thin film photovoltaics," *Journal of Applied Physics*, vol. 92, no. 5, 2002.

[89] L. V. R. de Marcos and J. I. Larruquert, "Analytic optical-constant model derived from tauc-lorentz and urbach tail," *Opt. Express*, vol. 24, pp. 28561–28572, Dec 2016.

[90] J. I. Larruquert and L. V. R. de Marcos, "Procedure to convert optical-constant models into analytic," *Thin Solid Films*, vol. 664, pp. 52 – 59, 2018.

[91] C. M. Herzinger and B. D. Johs, "Dielectric function parametric model, and method of use," 1998. US Patent 5,796,983.

[92] O. Stenzel, *The Physics of thin film optical spectra.* Springer, 2005.

[93] S. Reid *et al.*, "Mechanical dissipation in silicon flexures," *Physics Letters A*, vol. 351, no. 4, pp. 205 – 211, 2006.

[94] M. Granata *et al.*, "Mechanical loss in state-of-the-art amorphous optical coatings," *Phys. Rev. D*, vol. 93, p. 012007, Jan 2016.

[95] E. Cesarini *et al.*, "A "gentle" nodal suspension for measurements of the acoustic attenuation in materials," *Review of Scientific Instruments*, vol. 80, no. 5, p. 053904, 2009.

[96] E. Cesarini *et al.*, "Mechanical characterization of 'uncoated' and '$ta_2o_5$-single-layer-coated' $sio_2$ substrates: results from gens suspension, and the coach project," *Classical and Quantum Gravity*, vol. 27, no. 8, p. 084031, 2010.

[97] M. Granata *et al.*, "Internal friction and young's modulus measurements on $sio_2$ and $ta_2o_5$ films done with an ultra-high q silicon-wafer suspension," *Archives of Metallurgy and Materials*, vol. 60, no. 1, pp. 365 – 370, 2015.

[98] A. Cadez and A. Abramovici, "Measuring high mechanical quality factors of bodies made of bare insulating materials," *Journal of Physics E: Scientific Instruments*, vol. 21, no. 5, p. 453, 1988.

[99] S. Moaveni, *Finite Element Analysis Theory and Application with ANSYS.* Prentice Hall, 3rd ed., 4 2007.

[100] H. J. McSkimin, "Measurement of elastic constants at low temperatures by means of ultrasonic waves–data for silicon and germanium single crystals, and for fused silica," *Journal of Applied Physics*, vol. 24, no. 8, pp. 988–997, 1953.

[101] P. Lautenschlager *et al.*, “Temperature dependence of the dielectric function and interband critical points in silicon,” *Phys. Rev. B*, vol. 36, no. 9, pp. 4821–4830, 1987.

[102] C. Herzinger *et al.*, “Ellipsometric determination of optical constants for silicon and thermally grown silicon dioxide via a multi-sample, multi-wavelength, multi-angle investigation,” *Journal of Applied Physics*, vol. 83, no. 6, pp. 3323–3336, 1998.

[103] G. Cagnoli *et al.*, “Mode-dependent mechanical losses in disc resonators,” *Physics Letters A*, vol. 382, no. 33, pp. 2165 – 2173, 2018.

[104] J. Wiedersich, S. V. Adichtchev, and E. Rössler, “Spectral shape of relaxations in silica glass,” *Phys. Rev. Lett.*, vol. 84, pp. 2718–2721, Mar 2000.

[105] F. Travasso *et al.*, “Low-frequency internal friction in silica glass,” *EPL (Europhysics Letters)*, vol. 80, no. 5, p. 50008, 2007.

[106] W. Jin, R. K. Kalia, P. Vashishta, and J. P. Rino, “Structural transformation in densified silica glass: A molecular-dynamics study,” *Phys. Rev. B*, vol. 50, pp. 118–131., Jul 1994.

[107] A. Pasquarello and R. Car, “Identification of raman defect lines as signatures of ring structures in vitreous silica,” *Phys. Rev. Lett.*, vol. 80, pp. 5145–5147., Jun 1998.

[108] M. Granata *et al.*, “Correlated evolution of structure and mechanical loss of a sputtered silica film,” *Phys. Rev. Materials*, vol. 2, p. 053607, May 2018.

[109] A. Amato *et al.*, “Optical properties of high-quality oxide coating materials used in gravitational-wave advanced detectors,” *Journal of Physics: Materials*, vol. 2, p. 035004, jun 2019.

[110] C. Bundesmann *et al.*, “Stress relaxation and optical characterization of tio2 and sio2 films grown by dual ion beam deposition,” *Thin Solid Films*, vol. 516, no. 23, pp. 8604 – 8608, 2008.

[111] D. Souche *et al.*, “Visible and infrared ellipsometry study of ion assisted sio2 films,” *Thin Solid Films*, vol. 313-314, pp. 676 – 681, 1998.

[112] K. Topp and D. G. Cahill, “Elastic properties of several amorphous solids and disordered crystals below 100 k,” *Zeitschrift für Physik B Condensed Matter*, vol. 101, pp. 235–245, Mar 1996.

[113] S. D. Penn *et al.*, “Mechanical loss in tantala/silica dielectric mirror coatings,” *Classical and Quantum Gravity*, vol. 20, pp. 2917–2928, jun 2003.

[114] C. Comtet *et al.*, “Proc. 42th rencontres de moriond on gravitational waves and experimental gravity,” 2009.

[115] R. Flaminio *et al.*, “A study of coating mechanical and optical losses in view of reducing mirror thermal noise in gravitational wave detectors,” *Classical and Quantum Gravity*, vol. 27, p. 084030, apr 2010.

[116] A. Amato *et al.*, “High-reflection coatings for gravitational-wave detectors: State of the art and future developments,” *Journal of Physics: Conference Series*, vol. 957, no. 1, p. 012006, 2018.

[117] G. Vajente *et al.*, "Effect of elevated substrate temperature deposition on the mechanical losses in tantala thin film coatings," *Classical and Quantum Gravity*, vol. 35, p. 075001, feb 2018.

[118] M. R. Abernathy *et al.*, "Investigation of the young&#x2019;s modulus and thermal expansion of amorphous titania-doped tantala films," *Appl. Opt.*, vol. 53, pp. 3196–3202, May 2014.

[119] L. Pinard *et al.*, "Mirrors used in the ligo interferometers for first detection of gravitational waves," *Appl. Opt.*, vol. 56, pp. C11–C15, Feb 2017.

[120] S. Gras and M. Evans, "Direct measurement of coating thermal noise in optical resonators," *Phys. Rev. D*, vol. 98, p. 122001, Dec 2018.

[121] M. Prato *et al.*, "Gravitational waves detector mirrors: Spectroscopic ellipsometry study of ta2o5 films on sio2 substrates," *Thin Solid Films*, vol. 519, no. 9, pp. 2877–2880, 2011.

[122] H. Tang *et al.*, "Electrical and optical properties of tio2 anatase thin films," *Journal of Applied Physics*, vol. 75, no. 4, pp. 2042–2047, 1994.

[123] M. Nakamura *et al.*, "Hydrophilic characteristics of rf-sputtered amorphous tio2 film," *Vacuum*, vol. 59, no. 2, pp. 506 – 513, 2000. Proceedings of the Fifth International Symposium on Sputtering and Plasma Processes.

[124] J. Dong and D. A. Drabold, "Atomistic structure of band-tail states in amorphous silicon," *Phys. Rev. Lett.*, vol. 80, pp. 1928–1931, Mar 1998.

[125] D. A. Drabold, "Topics in the theory of amorphous materials," *The European Physical Journal B*, vol. 68, pp. 1–21, Mar 2009.

[126] R. Bassiri *et al.*, "Correlations between the mechanical loss and atomic structure of amorphous tio2-doped ta2o5 coatings," *Acta Materialia*, vol. 61, no. 4, pp. 1070 – 1077, 2013.

[127] J. P. Trinastic *et al.*, "Molecular dynamics modeling of mechanical loss in amorphous tantala and titania-doped tantala," *Phys. Rev. B*, vol. 93, p. 014105, Jan 2016.

[128] T. Damart and D. Rodney, "Atomistic study of two-level systems in amorphous silica," *Phys. Rev. B*, vol. 97, p. 014201, Jan 2018.

[129] A. Amato *et al.*, "Observation of a correlation between internal friction and urbach energy in amorphous oxides thin films," *Scientific Reports*, vol. 10, p. 1670, 2020.

[130] B. Shyam *et al.*, "Measurement and modeling of short and medium range order in amorphous ta2o5 thin films," *Scientific Reports*, vol. 6, p. 32170, Aug 2016. Article.

[131] K. Prasai *et al.*, "High precision detection of change in intermediate range order of amorphous zirconia-doped tantala thin films due to annealing," *Phys. Rev. Lett.*, vol. 123, p. 045501, Jul 2019.

[132] R. A. Barrio, F. L. Galeener, E. Martínez, and R. J. Elliott, "Regular ring dynamics in $ax_2$ tetrahedral glasses," *Phys. Rev. B*, vol. 48, pp. 15672–15689, Dec 1993.

[133] S. Xue *et al.*, “Effects of post-thermal annealing on the optical constants of zno thin film,” *Journal of Alloys and Compounds*, vol. 448, no. 1, pp. 21 – 26, 2008.

[134] K. Boubaker, “A physical explanation to the controversial urbach tailing universality,” *The European Physical Journal Plus*, vol. 126, p. 10, Jan 2011.

[135] S. D. Penn *et al.*, “Mechanical loss in tantala/silica dielectric mirror coatings,” *Classical and Quantum Gravity*, vol. 20, pp. 2917–2928, jun 2003.

[136] M. R. Abernathy *et al.*, “Investigation of the young’s modulus and thermal expansion of amorphous titania-doped tantala films,” *Appl. Opt.*, vol. 53, pp. 3196–3202, May 2014.

[137] A. E. Villar *et al.*, “Measurement of thermal noise in multilayer coatings with optimized layer thickness,” *Phys. Rev. D*, vol. 81, p. 122001, Jun 2010.

[138] S. Gras *et al.*, “Audio-band coating thermal noise measurement for advanced ligo with a multimode optical resonator,” *Phys. Rev. D*, vol. 95, p. 022001, Jan 2017.

[139] S. Gras and M. Evans, “Direct measurement of coating thermal noise in optical resonators,” *arXiv preprint arXiv:1802.05372*, 2018.

[140] M. Jerman *et al.*, “Refractive index of thin films of sio2, zro2, and hfo2 as a function of the films’ mass density,” *Appl. Opt.*, vol. 44, pp. 3006–3012, May 2005.

[141] K. R. Babu *et al.*, “Structural, thermodynamic and optical properties of mgf2 studied from first-principles theory,” *Journal of Solid State Chemistry*, vol. 184, no. 2, pp. 343 – 350, 2011.

[142] V. Mussi *et al.*, “Surface nanostructuring and optical activation of lithium fluoride crystals by ion beam irradiation,” *Applied Physics Letters*, vol. 88, no. 10, p. 103116, 2006.

[143] R. Montereali *et al.*, “Visible photoluminescence of aggregate colour centres in lithium fluoride thin films for low-energy proton beam radiation detectors at high doses,” *Journal of Luminescence*, vol. 200, pp. 30 – 34, 2018.

[144] P. G. Murray *et al.*, “Ion-beam sputtered amorphous silicon films for cryogenic precision measurement systems,” *Phys. Rev. D*, vol. 92, p. 062001, Sep 2015.

[145] E. D. Palik, *Handbook of optical constants of solids*, vol. 3. Academic press, 1998.

[146] X. Liu *et al.*, “Elastic properties of several silicon nitride films,” *MRS Proceedings*, vol. 989, pp. 0989–A22–01, 2007.

[147] H. wei Pan *et al.*, “Silicon-nitride films deposited by pecvd method on silicon substrate for next generation laser interference gravitational wave detector,” in *Optical Interference Coatings 2016*, p. MB.12, Optical Society of America, 2016.

[148] H.-W. Pan *et al.*, “Silicon nitride films fabricated by a plasma-enhanced chemical vapor deposition method for coatings of the laser interferometer gravitational wave detector,” *Phys. Rev. D*, vol. 97, p. 022004, Jan 2018.

[149] J. Seth *et al.*, “Influence of the deposition gas mixture on the structure and failure modes of diamondlike carbon films,” *Journal of Vacuum Science & Technology A*, vol. 10, no. 2, pp. 284–289, 1992.

[150] G. Gille and B. Rau, "Buckling instability and adhesion of carbon layers," *Thin Solid Films*, vol. 120, no. 2, pp. 109 – 121, 1984.

[151] H. Schmidt *et al.*, "Thermal stability and crystallization kinetics of sputtered amorphous si3n4 films," *Thin Solid Films*, vol. 450, no. 2, pp. 346 – 351, 2004.

[152] A. C. Boccara *et al.*, "Sensitive photothermal deflection technique for measuring absorption in optically thin media," *Opt. Lett.*, vol. 5, pp. 377–379, Sep 1980.

[153] M. Granata *et al.*, "Amorphous optical coatings of present gravitational-wave interferometers," *arXiv preprint arXiv:1909.03737*, 2019.

[154] M. Granata *et al.*, "Progress in the measurement and reduction of thermal noise in optical coatings for gravitational-wave detectors," in *Optical Interference Coatings Conference (OIC) 2019*, p. FA.1, Optical Society of America, 2019.

[155] R. Kubo, "Statistical-mechanical theory of irreversible processes. i. general theory and simple applications to magnetic and conduction problems," *Journal of the Physical Society of Japan*, vol. 12, no. 6, pp. 570–586, 1957.

[156] L. D. Landau and E. Lifshitz, "Theory of elasticity, vol. 7," *Course of Theoretical Physics*, vol. 3, p. 109, 1986.

[157] A. W. Leissa, "Vibration of plates," tech. rep., OHIO STATE UNIV COLUMBUS, 1969.

[158] M. Amabili *et al.*, "Natural frequencies and modes of free-edge circular plates vibrating in vacuum or in contact with liquid," *Journal of Sound and Vibration*, vol. 188, no. 5, pp. 685 – 699, 1995.